Alumina based nanocomposites by precipitation

Chen Xu

The Queen's College

A Thesis submitted for the degree of Doctor of Philosophy

University of Oxford

Hilary Term, 2014

Alumina based nanocomposites by precipitation

Chen Xu Doctor of Philosophy

The Queen's College Hilary Term, 2014

Abstract

This project addressed two main problems pertaining to Al_2O_3-$FeAl_2O_4$ nanocomposites developed via solid state precipitation: the mechanisms for precipitation in ceramic solid solution via reduction reaction, and the mechanisms for the improved mechanical properties and wear resistance of the developed Al_2O_3-$FeAl_2O_4$ nanocomposites.

A model was proposed for precipitation in ceramic solid solutions via reduction reactions (the PRCS model). The thermodynamics of reduction reactions during aging treatments under various atmospheres were calculated and discussed relative to the second phase precipitate formation. Attempts were made to measure the corresponding diffusion kinetics using a new theory developed here based on volume fraction profiles of second phase particles in the aged samples. It was found that the measured apparent oxygen vacancy diffusivities conform well to the oxygen vacancy grain boundary diffusion coefficients reported in the literature, and the measured apparent matrix diffusivity conforms well to the Fe^{3+} ion matrix diffusion coefficients reported in literature. Based on the thermodynamics calculations, diffusion kinetics and some essential mechanisms that were discussed, the PRCS model was proposed. This has two aspects: macroscopic and microscopic. The macroscopic aspect of PRCS model was mainly used to explain the general aspects of microstructure and the distribution of intergranualar second phase particles. The microscopic aspect of the PRCS model was mainly used to explain the precipitation of intragranualar nanoparticles.

The mechanical properties, thermal residual stress and wear resistance of selected Al_2O_3-$FeAl_2O_4$ nanocomposites were measured. The results revealed that the Al_2O_3-$FeAl_2O_4$ possessed improved flexural strength (by around 30%) and abrasive wear resistance (by a factor of around 5) with respect to monolithic alumina. Several mechanisms were proposed to explain the improvements in both mechanical properties and wear resistance. Compressive residual stress was found in the surface layer of Al_2O_3-$FeAl_2O_4$ nanocomposites due to the thermal expansion coefficient mismatch between surface layer and bulk parts. Such residual stress was also interpreted as the main reason for the improvements in both mechanical properties and wear resistance.

Acknowledgements

I would like to express my most sincere gratitude towards my supervisor Professor Richard I. Todd for providing valuable guidance and inspirations through the three and half years of my research in Oxford. He provides me all the necessary support for completion of the thesis, despite of his busy schedule.

I would like to thank Mrs Gabriella Chapman, Dr Chris Salter and all EM support staff who gave me valuable training and help in the past three and half years. They are always so nice and helpful. I can always learn EM knowledge from them.

I would like to thank everybody in the RIT group (Andrew Norton, Dingyue Shi, Mi Du, Geoffrey Otieno, Noor Yahya, Claire Dancer, Xiaodan Sun, Teresa Rodríguez Suárez and Yuanfei Gao) for providing assistance and valuable advice.

I would like to thank Mrs Lyn Richmond and Mrs Marion Beckett, who gave me the kindest help on matters relating to department. I would like to thank Mr Steve Lett, for his patient training and useful advice on EM sample preparation.

I am grateful to the fund bursaries of Oxford University-Chinese Education Ministry joint scholarship for providing me financial support for my DPhil studies.

At last, I would like to thank my parents, who raised me up and gave me the chance to study abroad since my teenage. They provided me encouragements and all financial support when needed for my study in UK. I was definitely a naughty kid as viewed in Chinese tradition when I was young, but they gave me the best that they can give.

Preface

The work presented in this thesis was carried out by the author in the Department of Materials, University of Oxford, under the supervision of Professor Richard I. Todd. The work in this thesis is original and no part of this thesis has been previously submitted for a degree at this or other university. The approximate number of words in this thesis is 32000.

Parts of the work described here have been presented as poster presentation at the 13th ECERS International Conference, Limoges, France, June 2013:

Xu, C. and Todd, R.I, Alumina based nanocomposites by precipitation.

Dedicated to

My Parents

And those people who supported me in my past 25 years from birth to PhD!

Table of Contents

Chapter 1 Introduction

1.1 Driving force for the development of ceramic nanocomposites

In the past several decades, engineering ceramics have received significant attention as structural material candidates. Compared with metals, they have advantages such as high thermal resistance, good chemical stability, high hardness and so on. [1,2,3] Based on these qualities, engineering ceramics are promising materials for applications used under conditions of high temperature, wear and chemical attack that are too severe for metals. However, both oxide ceramics and non-oxide ceramics have relatively low fracture toughness. This is the major limit of ceramics. [1,3,4,5]

Therefore, significant scientific efforts have been directed mainly towards toughening of engineering ceramics in the past decades. Before 1991, the majority of such research focused on *composite technology*, which involves incorporating micro-size second phases such as whiskers and fibers within the ceramic matrix.[6,7,8,9] It was reported that micro-size ceramic fillers could effectively toughen ceramics though with orientation dependence.[6,7,8,9] For example, Prewo and Brennan[6] demonstrated that with continuous high strength micro-size SiC fibers which were aligned preferentially, the fracture toughness of glass ceramics can be increased substantially up to 20 $MPa \cdot m^{0.5}$ (crack plane normal to orientation of the fibers). Becher and Wei[9] reported fracture toughness increases in alumina reinforced with aligned SiC whiskers from 4.6 ± 0.4 $MPa \cdot m^{0.5}$ to 5.6 ± 0.8 $MPa \cdot m^{0.5}$ with crack plane parallel to orientation of the whiskers and to 8.7 ± 0.9 $MPa \cdot m^{0.5}$ with crack plane normal to the orientation of the whiskers. Although the increased toughness in composites is beneficial for increasing strength, micro-size reinforcements introduce weaker interfaces which could increase the critical flaw size and hence decrease the strength to some extent.[10]

In the last two decades, a new design concept has attracted significant interest—'*ceramic nanocomposites*'. Niihara[5] first claimed a relatively large improvement in fracture strength, moderate enhancement in toughness and a higher maximum operating temperature in both oxide and non-oxide nanostructured ceramics (Table 1.1). This is a unique microstructure: micro-size ceramic matrix grains with nano-size ceramic reinforcements[5], e.g nanotubes, nanosheets, nanoparticles, nanofibers. (Figure 1.1)

Table 1.1 Improvement of the mechanical properties observed for the ceramic nanocomposites[5]

Composite system	Fracture Toughness ($MPa \cdot m^{0.5}$)	Strength ($MPa \cdot m^{0.5}$)	Maximum operating temperature (℃)
Al_2O_3/SiC	3.5→4.8	350→1520	800→1200
Al_2O_3/Si_3N_4	3.5→4.7	350→850	800→1300
MgO/SiC	1.2→4.5	340→700	600→1400
Si_3N_4/SiC	4.5→7.5	850→1550	1200→1400

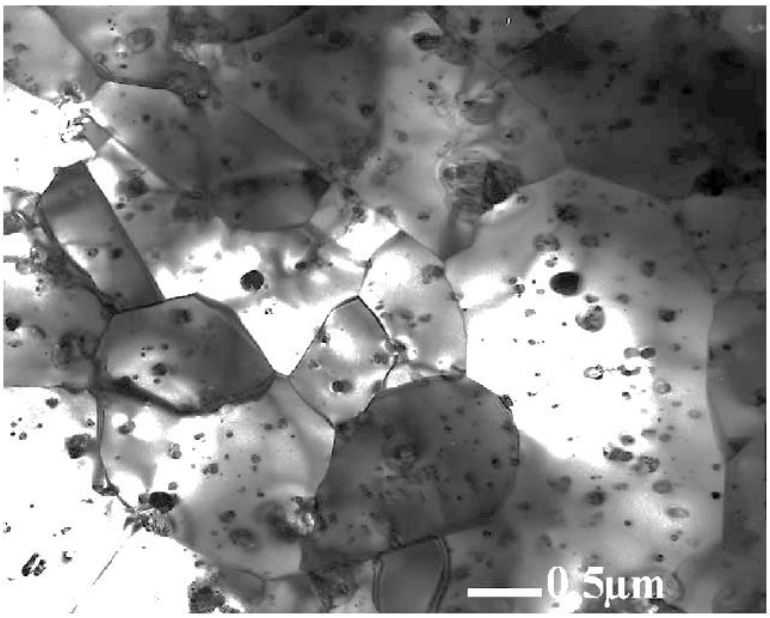

Figure 1.1 Bright field TEM micrograph of the Al_2O_3/SiC nanocomposite [11]

1.2 Driving force for developing particulate reinforced alumina based nanocomposites (PRABN)

Among various oxide ceramics, alumina is one of the most widely used materials in a range of structural and wear resistant applications, such as thermal/electrical insulators, biomedical implants, kiln furniture and so on.[1,7] Alumina can exist in many metastable polymorphs, besides the only thermodynamically stable crystal structure, i.e the α-Al_2O_3 corundum structure which is based on a hexagonal close-packed (HCP) anion sub-lattice.[12] Despite its low fracture toughness (3-3.5MPa $m^{0.5}$) and low fracture strength (typically 350MPa), alumina has a very high melting point (around 2100 °C), high Young's modulus (380-400GPa) and high hardness (16-18GPa), along with considerable wear resistance and excellent resistance to chemical attack and oxidation.[12] Hence it is understandable that a majority of research on nanocomposites has been directed towards alumina[12-30].

Despite the debate as to what extent nanoparticles can improve the properties of alumina (Table 1.2), there is an agreement among these investigations that the nanoparticles in alumina can lead to improved fracture strength (typically, up to around 600MPa) combined with a modestly improved fracture toughness (to about 4 $MPam^{1/2}$)[13], which triggered significant further research activities in PRABN. The general characteristics of PRABN compared with monolithic alumina ceramics can be summarized as:

- Moderate to significant strength improvements (Table 1.2);
- Moderately fracture toughness increase (Table 1.2);
- Fracture mode change from intergranular fracture to transgranular fracture in alumina based nanocomposites (Figure 1.2);[14-30]
- Improvements in several other mechanical properties such as hardness[14], wear resistance[15], thermal shock resistance[16], and creep resistance[17].

Table 1.2 A brief survey of to what extent SiC nanoparticles can improve the strength and fracture toughness in Al_2O_3/SiC nanocomposites

Researchers	Improvement in strength (%)	Improvement in fracture toughness (%)
Niihara [5]	200	28
Zhao et al[18]	36	24
Carroll et al[14]	50	19.8/-15
Gao et al[19]	180	14
Sternitzke et al[20]	50	0
Borsa et al[21]	30	0
Wang et al[22]	40	40
Ferroni et al[23]	100	0
Sun et al[24]	100	0

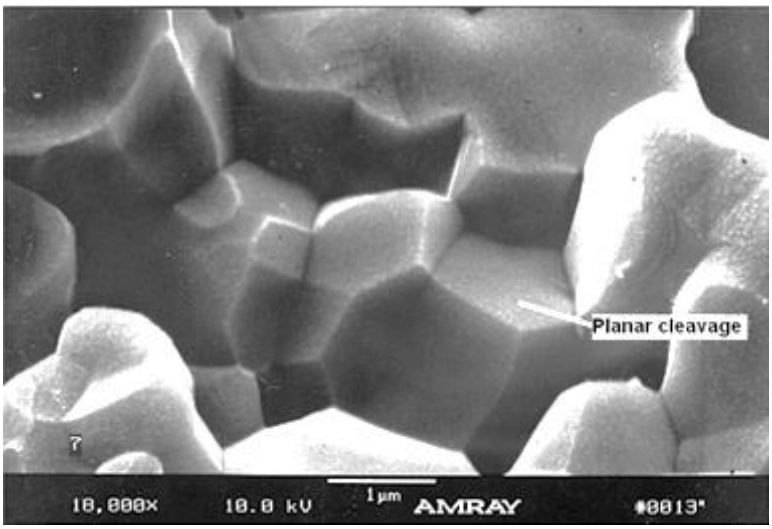

(a) Monolithic alumina

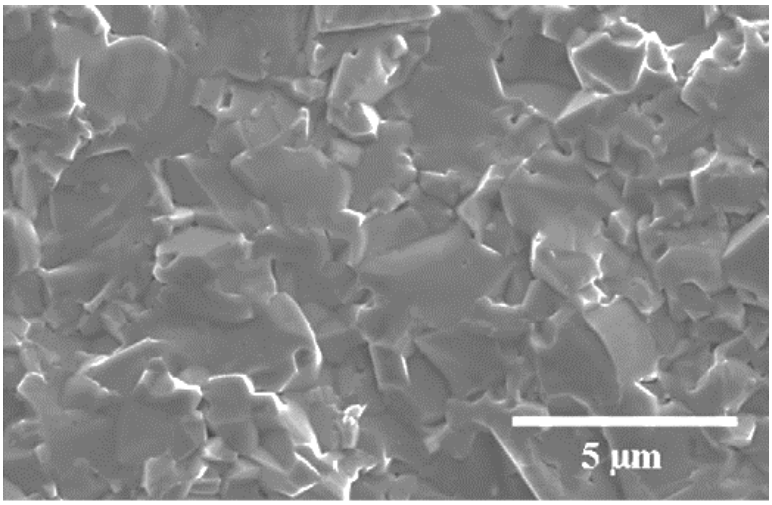

(b) Nanocomposites

Figure 1.2 Fracture surfaces of monolithic alumina [25] (a) and nanocomposites [26] (b). This shows that an intergranular fracture mode exists in the monolithic alumina with planar cleavages while there is a change to transgranular fracture mode in alumina based nanocomposites.

1.3 Development of alumina based nanocomoposites by solid solution precipitation

The traditional 'mixing-densification' of nano-powders methods for producing ceramic nanocomposites involve the utilization of pressure assisted sintering (e.g. hot pressing)[27] and novel sintering techniques (e.g. plasma assisted sintering)[28]. However, due to the high fabrication expenditure, sample shape and dimension limits, neither pressure assisted

sintering nor novel sintering techniques has been adopted as commercial processes for mass scale production of PRABN (this will be discussed further in Chapter 2). In order to stimulate commercial application of PRABN, a new idea utilizing pressureless sintering has recently been developed, which is 'nanocomposites by precipitation' (NBP). [26] This is an in-situ processing design for PRABN. The rationale behind this idea is to dissolve ceramics with aliovalent cations in alumina to form fully dense solid solutions using pressureless sintering in air, and then to age the solid solutions in reducing atmospheres to reduce the solvent cations from high valence to low valence. Usually, the low valence solvent cations can not be accommodated in the Al_2O_3 lattices, therefore second phase particles will precipitate out. [26] Particles with a desirable size, morphology and dispersion can be obtained by careful control of the precipitation process. If this idea is successful, it can avoid the expensive advanced sintering techniques by minimizing the densification inhibition caused by refractory non-oxide reinforcements.[26]

However, there is not much literature on the subject of developing in-situ formation of particles in alumina. This may be at least partly due to the fact that most cation ions have negligible solubility in alumina, since their larger ionic radius and/or different charge compared with aluminium ions, which makes them could neither be accommodated in substitional nor interstitional solution.[26] One of the earliest indications of precipitation from supersaturated alumina solid solution is the formation of needle shaped precipitates (TiO_2) in star sapphire. [29,30] However, the needles formed are usually hundreds of micrometre in length, and the volume fraction of the second phase particles is also extremely limited (no more than 1 vol%). Another system, i.e. Al_2O_3/ $FeAl_2O_4$ nanocomposites, has been developed to achieve higher amounts of spinel nanoparticles in PRABN. Fe_2O_3 was dissolved in Al_2O_3 and then an aging treatment with reducing conditions was employed to reduce Fe^{3+} (of dissolved Fe_2O_3) to Fe^{2+}, which produced a relatively large volume fraction of $FeAl_2O_4$ precipitates (up to 20

vol%) [26]

Nevertheless, although Al_2O_3/ $FeAl_2O_4$ nanocomposites seems a more promising NBP system, the thermodynamics of reduction reactions, diffusion mechanisms and mechanisms for the microstructural developments involved in the aging still remain unclear. Understanding these mechanisms is essential for designing PRABN microstructures by 'in-situ method'. Furthermore, some efforts have been made to investigate the 'microstructure-mechanical properties' relationship for Al_2O_3/ $FeAl_2O_4$ nanocomposites, but a more systematic and comprehensive work is demanded to consider more factors that may influence the mechanical behaviours.

1.4 Structure of the thesis

In this project, Al_2O_3/ $FeAl_2O_4$ nanocomposites were produced by pressureless sintering. Broadly, this research aims to investigate the thermodynamics, diffusion kinetics and mechanisms behind microstructural evolution in Al_2O_3-Fe_2O_3 system under varying reducing atmospheres, and try to understand the corresponding 'microstructure-mechanical property' relationship for Al_2O_3/ $FeAl_2O_4$ nanocomposites.

Chapter 2: the objective of this chapter is mainly to review the previous studies on diffusion mechanisms in alumina, and improvements in both mechanical properties and tribological properties of PRABN. Some background of PRABN will be illustrated to justify the reasons for developing 'in-situ' method.

Chapter 3: this chapter will give a full description of the experimental methods utilised in this project.

Chapter 4: this chapter mainly describes how varying as-sintered microstructures and processing parameters influence the specimen microstructures after aging treatment. The thermodynamics, diffusion kinetics and mechanisms for microstructural developments during aging are discussed. A model for precipitation in ceramic solid solution induced by

reductions (PRCS model) was proposed, and applied to explain the microstructural development during aging.

Chapter 5: this chapter presents the mechanical properties and wear resistance measured from selected samples. The mechanisms for the change in mechanical properties and tribological properties are discussed.

Chapter 6: this chapter will summarize the main conclusions obtained in this project, and propose future work plans.

Reference

[1] R. W. Davidge, Mechanical Behavior of Ceramics, Cambridge University Press, Cambridge (1979).

[2] W. T. Liao, Flexural Strength of Creep Feed Ground Ceramics: General pattern, Ductile–Brittle Transition and MLP Modelling, International Journal of Machine Tools and Manufacture, 38, 257-275 (1998).

[3] S. Reschke, C. Bogdanow, Engineering Ceramics: New Perspectives through Value-Added Multi-functionality, Key Engineering Materials, 175, 1-10 (1999).

[4] S. Choi, H. Awaji, Nanocomposites: a New Material Design Concept. Science and Technology of Advanced Materials, 6, 2-10 (2005).

[5] K. Niihara, New Design Concept of Structural Ceramics-Ceramic Nanocomposites, The Centennial Memorial Issue of The Ceramic Society of Japan, 99, 974-982 (1991).

[6] K. M. Prewo, J. J. Brennan, High-Strength Silicon Carbide Fiber-Reinforced Glass-Matrix Composites, Journal of Materials Science, 15, 463-468 (1980)

[7] P. M. Ajayan, Nanocomposite Science and Technology, Wiley-VCH, Weinheim (2003).

[8] R. W. Rice, Mechanisms of Toughening in Ceramic Composites, Proceedings of the 5th Annual Conference on Composites and Advanced Ceramic Materials: Ceramic Engineering and Science, 2, 661-701 (1981).

[9] P. F. Becher, G. C. Wei, Toughening Behavior in SiC-Whisker-Reinforced Alumina, Journal of the American Ceramic Society, 67, C267-C269 (1984).

[10] E. Yasuda, T. Akatsu, Y. Tanabe, Influence of Whiskers' Shape and Size on Mechanical Properties of SiC Whisker-Reinforced Al_2O_3, Journal of the Ceramic Society of Japan, 99, 52–58(1991).

[11] S. Bajwa, W. M. Rainforth, W. E. Lee, Sliding Wear Behaviour of SiC–Al_2O_3 Nanocomposites, Wear, 259, 553-561 (2005).

[12] W. D. Kingery, H. K. Bowen, D. R. Uhlmann, Introduction to Ceramics, John Wiley & Sons , London (1976).

[13] T. Ohji, Y. K. Jeong, Y. H. Choa, K. Niihara, Strengthening and Toughening Mechanisms of Ceramic Nanocomposites, Journal of the American Ceramic Society, 81, 1453–1460 (1998).

[14] L. Carroll, M. Sternitzke, B. Derby, Silicon Carbide Particle Size Effects in Alumina based Nanocomposites, Acta Materialia, 44, 4543-4552 (1996).

[15] R. W. Davidge, P. C. Twigg, F. L. Riley, Effects of Silicon Carbide Nano-phase on the Wet Erosive Wear of Polycrystalline Alumina, Journal of the European Ceramic Society, 16, 799-802(1996).

[16] K. Niihara, A. Nakahira, Strengthening and Toughening Mechanisms in Nanocomposite Ceramics, Annales de Chimie et de Physique, 16, 479-486 (1991).

[17] A. Nakahira, High Temperature Creep and Deformation Behaviour of Al_2O_3/SiC Nanocomposites, Annales de chimie et de physique, 18, 403–408 (1993).

[18] J. H. Zhao, L. C. Stearns, M. P. Harmer, H. M. Chan, G. A. Miller, R. F. Cook, Mechanical Behavior of Alumina–Silicon Carbide Nanocomposites, Journal of the American Ceramic Society, 76, 503-510 (1993).

[19] L. Gao, H. Z. Wang, J. S. Hong, H. Miyamoto, K. Miyamoto, Y. Nishikawa, S. D. D. L. Torre, Mechanical Properties and Microstructure of Nano-SiC–Al_2O_3 Composites Densified by Spark Plasma Sintering, Journal of the European Ceramic Society,19,609-613 (1999).

[20] M. Sternitzke, Review: Structural Ceramic Nanocomposites, Journal of the European Ceramic Society, 17, 1061-1082 (1997).

[21] C. E. Borsa, S. Jiao, R. I. Todd, R. J. Brook, Processing and Properties of Al_2O_3/SiC nanocomposites, Journal of Microscopy, 177, 305–312 (1995).

[22] H. Z. Wang, L. Gao, L. H. Gui, J. K. Guo, Preparation and Properties of Intragranular Al_2O_3-SiC Nanocomposites, Nanostructured Materials, 10, 947-953 (1998).

[23] L. P. Ferroni, G. Pezzotti, Evidence for Bulk Residual Stress Strengthening in Al_2O_3/SiC Nanocomposites, Journal of the American Ceramic Society, 85, 2033-2038 (2002).

[24] X. D. Sun, J. G. Li, S. W. Guo, Z. M Xiu, K. Duan, X. Z. Hu, Intragranular Particle Residual Stress Strengthening of Al_2O_3–SiC nanocomposites, Journal of the American Ceramic Society, 88, 1536-1543 (2005).

[25] H. Tan, W. Yang, Toughening Mechanisms of Nanocomposite Ceramics, Mechanics of Materials, 30, 111-123 (1998).

[26] A. Mukhopadhyay, R. I. Todd, Effect of Yttria Doping on the Microstructure and Mechanical Properties of Al_2O_3-$FeAl_2O_4$ Nanocomposites Developed via Solid State Precipitation, Journal of the European Ceramic Society, 30, 2905-2915 (2010).

[27] M. Parchovianský, D. Galusek, J. Sedláček, P. Švančárek, M. Kašiarová, J. Dusza, P. Šajgalík, Microstructure and Mechanical Properties of Hot Pressed Al_2O_3/SiC Nanocomposites, Journal of the European Ceramic Society, 33, 2291-2298 (2013).

[28] J. H. Chae, K. H. Kim, Y. H. Choa, J. I. Matsushita, J. W. Yoon, K. B. Shim, Microstructural Evolution of Al_2O_3–SiC Nanocomposites during Spark Plasma Sintering, Journal of Alloys and Compounds, 413, 259-264 (2006).

[29] D. S. Phillips, A. H. Heuer, T. E. Mitchell, Precipitation in Star Sapphire: I. Identification of the Precipitate, Philosophical Magazine A, 42, 385-404 (1980).

[30] S. E. Hsu, W. Kobes, M. E. Fine, Strengthening of Sapphire by Precipitates Containing Titanium, Journal of the American Ceramic Society, 50, 149-151(1967).

Chapter 2 Literature Review

2.1 Mechanisms for mechanical property improvements

The majority of research after Niihara et al[1] has been directed to investigating the mechanisms for mechanical property improvements and wear behavior of nanocomposites. This research can be categorized into four aspects: fracture mode change, strengthening, toughening and wear behavior.

2.1.1. Fracture mode change

Since the pioneering work by Niihara[1], there are generally four mechanisms proposed to explain the fracture mode change: *matrix weakening by residual stress*, *grain boundary strengthening*, *reduction of intergrain stress*, and *deflection by intergranular particles*. The former three mechanisms are based on *residual stress*, while the fourth mechanism is based on *crack/particle interaction*.

2.1.1.1. Reisidual stress

Niihara et al[2] first used the concept of residual stress to explain the fracture mode change in PRABN. It was speculated that tensile hoop stresses would develop around intragranular SiC particles in the Al_2O_3/SiC nanocomposites system resulting from the thermal expansion mismatch between the matrix and particles when cooling from fabrication temperatures.[1] This could 'weaken' the matrix grains, being referred as *'matrix weakening'*. An intergranular crack may be attracted into the grain by such tensile stresses, hence resulting in a fracture mode change. In addition, the higher

stiffness of the SiC particles situated on the grain boundary may also assist deflecting the crack into the bulk of the grains. [1,2,3,4,5]

Nevertheless, according to the 'matrix weakening theory', since the crack propagation will be promoted into the matrix grains in tension, the strength of PRABN is expected to decrease, but this is obviously contrary to the fact that many researchers including Niihara et al (themselves)[2] reported an increased strength in the Al_2O_3/SiC nanocomposites. Furthermore, the contribution of tensile hoop stresses around the embodied particles to the stress intensity is also related to the interparticle spacing. Todd's calculations[6] showed that in an Al_2O_3/SiC nanocomposite with average tensile hoop stresses $\bar{\sigma}_h = 90$MPa and interparticle spacing d= 400nm, the contribution of tensile hoop stresses to stress intensity, K_h, is 0.09MPa·m$^{0.5}$, which is only 2.5% of the fracture toughness of alumina (about 3.5 MPa·m$^{0.5}$). Therefore the contribution of of tensile hoop stresses is small and may not be sufficient for the mechanism proposed by Niihara et al[2] to work.

Another mechanism considering residual stress due to the CTE difference between SiC particles and the alumina was proposed, i.e. grain boundary strengthening. Several researchers[7,8,9] found that grain pull-out was significantly reduced in Al_2O_3/SiC nanocomposites during polishing machining or abrasive wear, indicating a grain boundary strengthening. Residual stress calculations by different researchers[10,11,12,13] all suggested that besides a tensile stress within matrix grain as the tangential component of the matrix residual stresses, compressive stress in the radial direction is also created at the grain boundary by intragranular particles. It was suggested that the local compressive residual stress on grain boundaries located between nearest-neighbor particles could strengthen the grain boundaries (Figure

2.1). However, there wasn't much experimental evidence in these papers showing to what extent the grain boundaries can be 'strengthened'. Furthermore, the particles position in Figure 2.1 is unrealistic and this model doesn't work quantitatively.

The third mechanism based on residual stress was proposed by Todd et al[14], who emphasizes the role of the thermal expansion anisotropy. A residual stress measurement using neutron diffraction revealed that the addition of 5wt% SiC nanoparticles in alumina reduced the intergrain stress resulting from thermal expansion anisotropy between two adjacent grains only by about 7%. It was suggested that the tensile intergrain stresses can aid the deflection of cracks along weak grain boundaries inclined to the macroscopic crack path. Therefore Todd et.al argued that such a reduction in the intergrain stresses favors the transition to transgranular fracture. It was suggested that matrix weakening, the reduction in intergrain stress and the presence of dislocation arrays all favored the observed fracture mode transition as normal in Al_2O_3/SiC nanocomposites, even though these effects are weak when considered in isolation. Nonetheless, this mechanism is somewhat speculative, in that its applicability has so far not been tested in other systems.

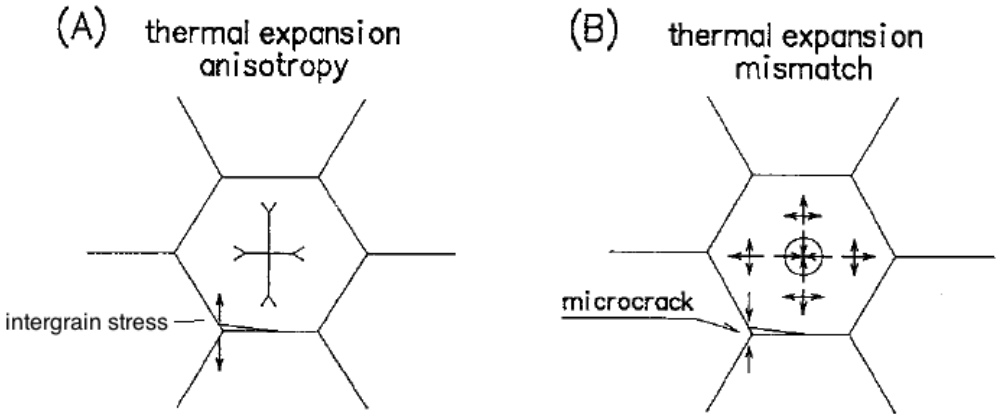

Figure 2.1 schematic illustration of the residual stress fields generated at grain boundaries and on a grain-boundary microcrack (A) thermal expansion anisotropy in monolithic alumina induces tensile stress in the direction normal to grain boundaries, known as intergrain stress, which could assist microcrack along grain boundaries; (B) thermal expansion mismatch in Al_2O_3/SiC nanocomposites with intragranular nanoparticles, induce a compression stress normal to grain boundaries which could strengthen the grain boundaries and inhibit the microcrack, and a tensile stress parallel to grain boundaries which could weaken the matrix grains.[9]

2.1.1.2. Deflection by intergranular particles

Jiao et al[15,16] challenged the residual stresses models in 2.1.1.1, suggesting that fracture mode change in Al_2O_3/SiC system is due to intergranular SiC particles instead of intragranular particles. An examination based on TEM of cracks showed that stress-induced microcracking around nanosized SiC does not occur and cutting of intragranular SiC particles is also absent (Figure 2.2)[15], thus it was suggested that residual stress induced by SiC intragranular particles is insufficient to ensure the crack deflection, while intergranualr particles may promote transgranular fracture.

Jiao et al measured the grain boundary-interface dihedral angles from TEM micrographs[16], and calculated the ratio of Al_2O_3/SiC interfacial energy to the alumina grain boundary energy on the basis of an energy balance condition. These results,

together with estimation of surface energies, showed that the Al_2O_3/SiC interfacial fracture energy is over twice the grain boundary fracture energy. Thus it was suggested that the grain boundaries are strengthened by intergranualr SiC particles due to the stronger interfaces, which favours transgranular cracks. The TEM observation of crack/particle interaction also suggested that the intergranular cracks are deflected into grains by intergranular particles inclined to the average direction of crack propagation (Figure 2.3)[15]. These observations further emphasis the dominant role of intergranular particle in fracture mode change.

This mechanism was supported by Winn and Todd[17], who suggested that it is the intergranular particles that are the most important in achieving grain boundary strengthening in PRABN, and that a small amount of SiC (1vol%) nanoparticles in alumina could strengthen the grain boundary sufficiently to deflect cracks away into grains, hence resulting in a fracture mode change.

Nonetheless, TEM images are difficult to interpret. With only 2D observation, thin TEM samples can't provide the whole crack front information, and the measurement of dihedral angles is somewhat speculative as equilibrium may not have been achieved. Therefore, this mechanism may need further investigation.

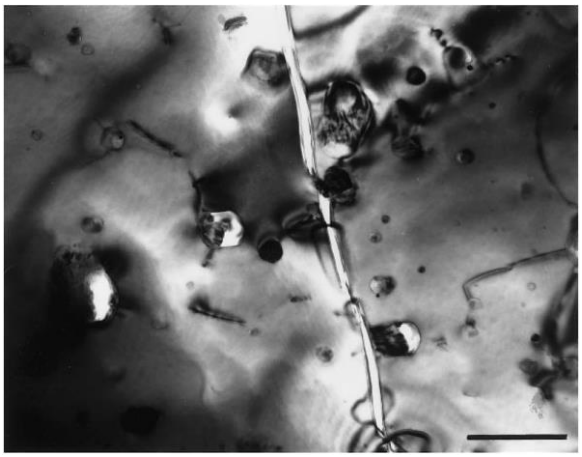

Figure 2.2 TEM image under high magnification showing no crack deflection by intragranular SiC particles in Al_2O_3/5wt% SiC nanocomposites.[15] Scale bar=500nm.

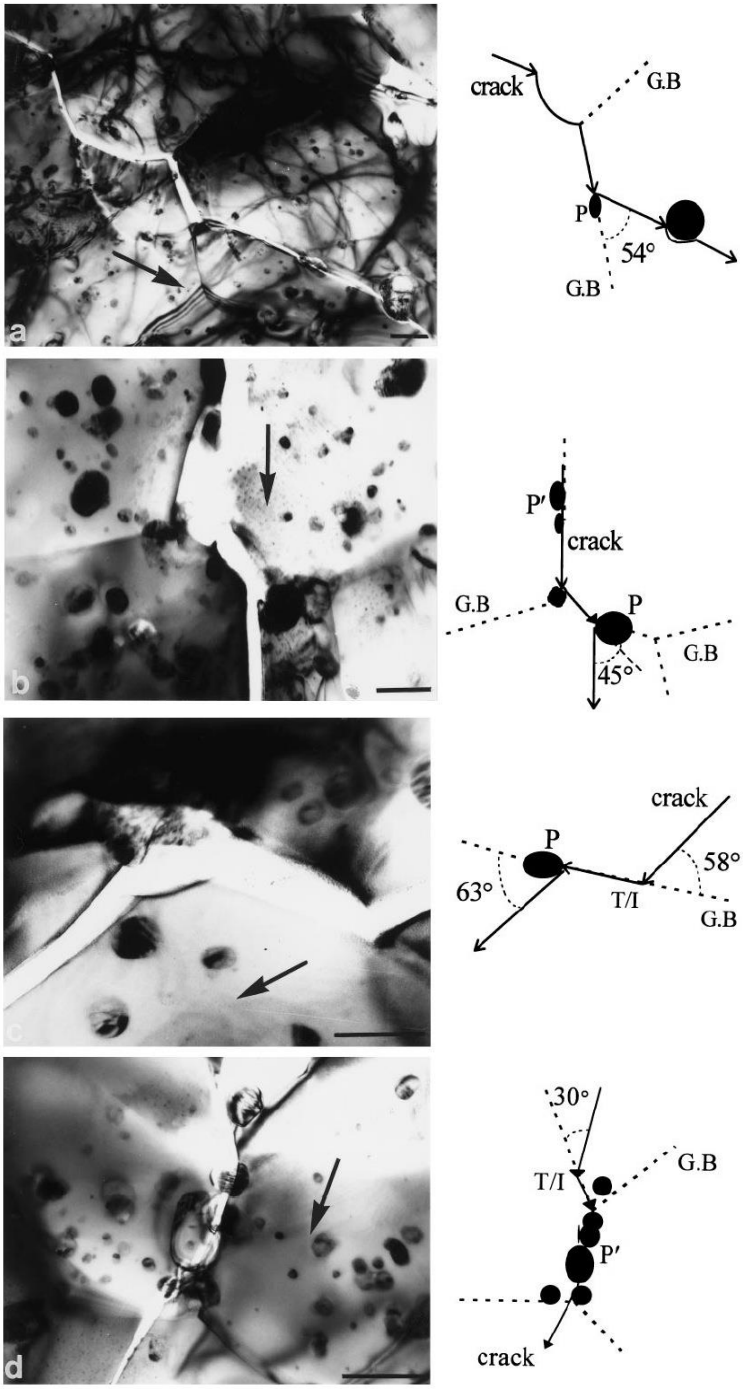

Figure 2.3 TEM images and corresponding schematic drawings showingcrack/particle interactions in Al_2O_3/5 wt% SiC nanocomposites. Scale bar =500nm. Dotted lines represent grain boundaries (G.B) and solid lines represent cracks. Angles of deflection are also shown. The average direction of crack propagation is indicated by a large arrow in each micrograph. [15]

2.1.1.3. Discussion

It was reported that Al_2O_3/SiC nanocomposites fracture transgranularly at temperatures as high as 1200 ℃, at which temperature the thermal residual stress must relax, thus the contribution of thermal residual stress should be ruled out for transgranular fracture at high tempertatures.[1,2] Therefore although thermal residual stress exists in Al_2O_3/SiC nanocomposites at low temperatures, it may play a minor role in fracture mode change at low temperatures.

In terms of the particle position, with experimental results and theoretical calculations, it was suggested that intergranular particles may dominate fracture mode and the effect of intragranular particles should be ruled out. However, studies on deflection by intergranular particles were mostly based on TEM and SEM characterization, while both of which could only provide 2D information and the EM sample preparation may influence crack behaviour.

It is possible that both residual stress mechanisms (especially the intergrain stress reduction mechanism) and deflection by intergranular particles are operative in changing the fracture mode in PRABN. Future investigations may help clarify which one is dominant, including (1) fabrication of alumina nanocomposites containing only particles within grains or grain boundaries. (2) more accurate quantification of the compressive stress on grain boundaries created only by intragranular nanoparticles; (3) the measurement of intergrain stresses of monolithic alumina etc.

2.1.2. Toughening mechanisms

As shown in Table 2 in Chapter 1, compared with strength, reports of the fracture toughness for PRABN are quite controversial. Several authors have reported a modest toughness increase in PRABN compared with monolithic alumina, while others did not find any appreciable enhancement or even reported a reduction in fracture toughness. Such varying reports may partially explain the diversity of toughening mechanisms proposed.

2.1.2.1. Early reports on toughening mechanism

In Niihara's pioneering paper[1], it was speculated that the modest toughness increase measured by means of SENB (single edge notched beam) was a result of crack deflection due to the nano-sized SiC particles. However, increase in fracture toughness caused by crack deflection estimated by Faber and Evans gives no more than 12% improvement.[18] In this model the local stress field at and near the matrix/particle interface is ignored. Apparently, this is insufficient to account for the maximum fracture toughness increase in Al_2O_3/SiC nanocomposites (40%, Table 1.2).

Zhao et al[19] attributed the observed toughening in Al_2O_3/SiC nanocomposites measured by indentation-strength method exclusively to the compressive surface stress induced by machining. However, without detailed investigation of microstructures this model is speculative and no subsequent research showed any support to this model yet.

Furthermore, Borsa et al[20] and Carroll et al[21] found no toughness increases in similar composites by the indentation fracture toughness measurement. The dispute among these reports may be due to the limited accuracy of the indentation method. More

recently, there are generally two main mechanisms proposed to explain the observed modest fracture toughness increase: fracture mode change and crack bridging.

2.1.2.2. Fracture mode change

The fracture mode change discussed in 0, was proposed as one explanation for the modest fracture toughness improvement in PRABN. This mechanism is based on the relative fracture energies of the two fracture types estimated by Hansson et al[22]:

For an ideally intergranular and transgranular fracture, the fracture energies can be given by: $G_{ig} = 2\gamma_s - \gamma_{gb}$, $G_{tg} = 2\gamma_s$ respectively, where ig stands for intergranular fracture, tg stands for transgranular fracture, γ_s stands for surface energy, γ_{gb} stands for grain boundary energy. [22] Assuming that the fracture surfaces have identical geometries, the ratio of fracture energies is $\frac{G_{tg}}{G_{ig}} = \frac{2\gamma_s}{2\gamma_s - \gamma_{gb}} = \frac{1}{1-\frac{\gamma_{gb}}{\gamma_s}}$.

Handwerker et al[23] estimated the ratio of $\frac{\gamma_s}{\gamma_{gb}}$ by measuring the equilibrium dihedral angle, θ, formed by a grain boundary at the surface (Figure 2.4). Thus at equilibrium: $2\gamma_s \cos\frac{\theta}{2} = \gamma_{gb}$.The measured θ was = 106 °in alumina. [22] Then it can be calculated that $\frac{\gamma_{gb}}{\gamma_s}$ = 1.2 and $\frac{G_{tg}}{G_{ig}}$ = 2.5. Therefore, based on the assumption that the ratio of the real fracture energies is the same as the ratio of these ideal fracture energies, the increase in fracture toughness due solely to an intergranular to transgranular fracture mode change yields: $\frac{K_{IC,tg}}{K_{IC,ig}} = (\frac{G_{tg}}{G_{ig}})^{0.5}$=1.58.[22] This value (58% improvement) may prove adequate for the observed maximum toughening in the Al_2O_3/ SiC nanocomposites. However, in this calculation, the toughness increase applies to two surfaces with identical geometry, while account must be taken of any accompanying change of

geometry due to crack deflection. Therefore a modification was made: $\frac{K_{IC,tg}}{K_{IC,ig}} = 1.58 \times f_d$, where f_d is the deflection factor. It has been widely demonstrated that transgranular fracture may result in higher toughness and strength than intergranular fracture for the same matrix materials[15,16,24,25]. Jiao et al[15,16] also suggested that the generation of cleavage steps in transgranular fracture can absorb fracture energy and may be the main cause of the toughening in Al_2O_3/SiC nanocomposites.

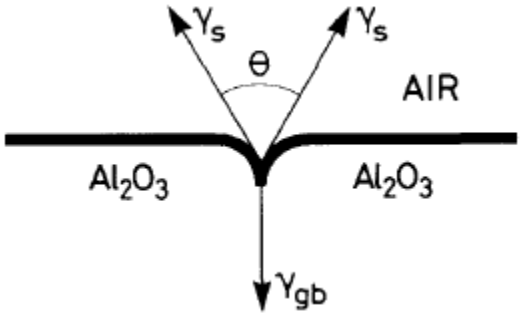

Figure 2.4 Balance of surface and grain boundary energy at equilibrium for a thermally etched grain boundary groove.[22]

It might be argued that Hansson et al's model[22] ignored the fact that the fracture energy along different lattice planes can be quite different. For example, the study on fracture of single crystal sapphire proved that (001) plane of alumina has the highest fracture surface energy, while the fracture surface energy for other planes is reasonably constant[26]. However, since most transgranular fractures in alumina do not happen on the (001) plane[3-16], the effect of the (001) plane on the transgranular fracture energies of alumina might be minor. Secondly, it seems Hansson et al's model[22] only illustrated why fracture mode change would increase the fracture toughness of materials, but it could not explain why the fracture mode change would happen since this model indicates that intergranular fracture is more preferable. It has been reported that local hindrance such as residual stress, strong grain boundary

bonding and difference in Young's modulus could result in fracture mode change[3-16], however, none of these factors have been considered in Hansson et al's model[22].

2.1.2.3. Crack bridging

Another toughening mechanism for PRABN is crack bridging, by which crack-face shielding results from the intact particles bridging a propagating crack behind the crack tip. (Figure 2.5) This model is also developed on the premise that the fracture mode in PRABN is transgranular.

It has been established experimentally that cracks in brittle materials undergo local shape and velocity changes in the vicinity of second phase particles,[27] especially when the particles have higher fracture toughness than the matrix. When the primary cracks meet the particles, its path is normally impeded and hence bows out between the particles, while the particles bridge the crack when the crack front has bypassed them. This could give a shielding effect until either the particle itself or the particle/matrix interface is first fractured.[27] Although a SiC particle (the most widely used nanoparticles in PRABN) is a brittle material, which implies that the shielding zone is quite limited, it was suggested that perfect SiC nanoparticle crystal has an extremely high strength, and the particle/matrix interface is quite strong. Thus the high shielding stress could compensate the very limited shielding zone. In such a case, the bridging could be effective and hence a steep increase in fracture resistance. In other words, the fracture toughness therefore will increase rapidly with a very short crack extension. Furthermore, since both the particles and the particle/matrix interface are much stronger than the grain boundary itself, the material can be strengthened.[27]

This mechanism was proposed by Ohji et al, who made a direct crack path observation in alumina-17 vol% SiC nanocomposites using TEM (Figure 2.6) [28] which provides some evidence that crack bridging could possibly operate in PRABN. This coincides with fracture surface observations for the same nanocomposites (Figure 2.7) where the SiC particles protrude from the fracture surface.

However, although Figure 2.8[28] was given by Ohji et al to provide some evidence that the particles bridged the crack after the crack front bypassed them, a careful examination of the picture shows that the particle/matrix interface has cracked. Many assumptions in Ohji et al's model[28] such as good lattice matches and perfect crystal are not always valid in real nanocomposites. This model also assumed that SiC has infinite toughness which is actually untrue. Furthermore, TEM images are usually difficult to interpret and TEM sample preparation also may extend the cracks. Jiao et al[15] also showed that the Al_2O_3/SiC nanocomposites do not show R-curve behaviour, thus particle bridging toughening mechanism seems not important in this case. Therefore, the validity of Ohji et al's model is still uncertain.

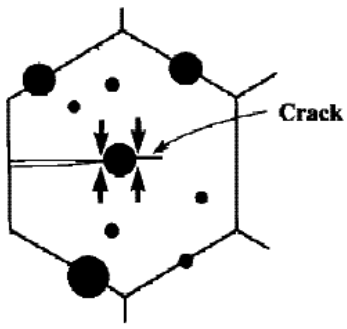

Figure 2.5 Schematic of crack propagations. The intergranular particles strongly bond the matrix/matrix interfaces; a crack extension along the grain boundaries is suppressed. Cracks are mostly deflected into matrix grains in PRABN, which induces the crack to extend to the particles and leads to the particle bridging toughening. [28]

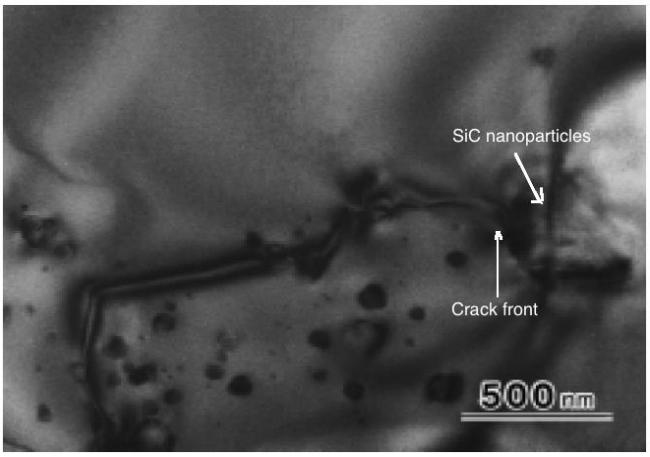

Figure 2.6 TEM graph for direct crack path observation in 17 vol% SiC--alumina nanocomposites. Crack propagation is from left to right. [28]

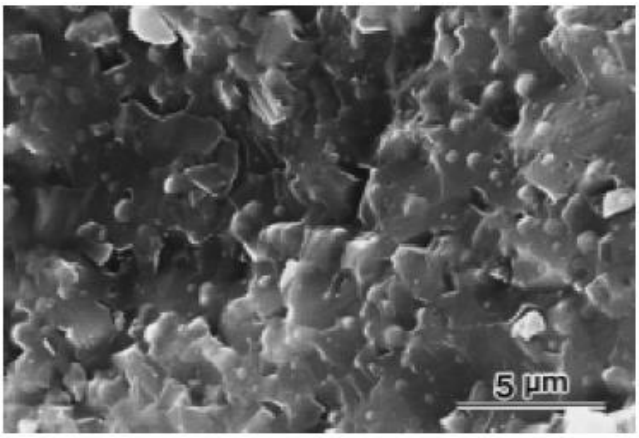

Figure 2.7 SEM micrograph for fracture surface observation for 17vol% SiC-alumina nanocomposites.[28]

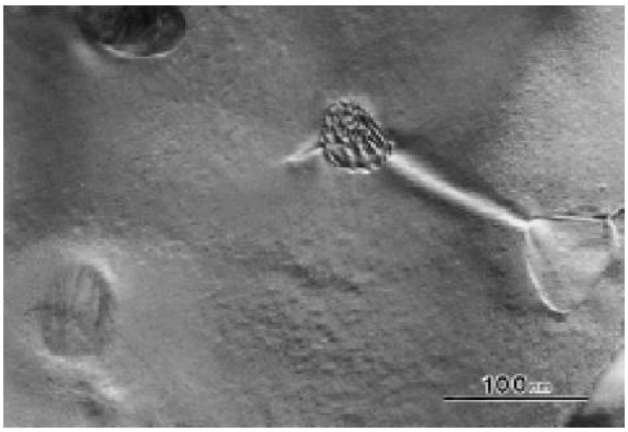

Figure 2.8 Crack interaction with a particle in the area close to the crack front. Crack propagation is from right to left. This micrograph shows one of the expanded cracks and its interaction with particles in the area near the crack front. In the vicinity behind the crack tip neither crack penetration through the particles nor propagation along the interfaces was observed. [28]

2.1.3. Strengthening mechanisms

The results published in the last two decades showed that the dispersion of ceramic nanoparticles does increase the strength at room temperature, but the extent varies among different investigations (Table 2 in Chapter 1). Most mechanisms developed in the last two decades to explain the observed strengthening in PRABN were based on flaw size reduction.[1-19]

2.1.3.1. Flaw Size Reduction

The theoretical strength of ceramics can be interpreted as the stress to break atomic bonds or to shear along a plane. However, the observed strengths of ceramics are usually much less than the theoretical strength. The fundamental reason lies on the fact that fracture of ceramics is mostly initiated by a critical flaw, at which the local stress is much higher than the macroscopic stress.

In terms of the fracture mechanics, both fracture toughness increase and flaw size reduction could increase strength of ceramics. Since toughening induced by micro-

size particle reinforcement is usually inadequate to account for the corresponding strengthening (Chapter1, section 1.2), it is understandable that most strengthening mechanisms for PRABN are directed towards how nanoparticle addition results in flaw size reduction.

However, none of these strengthening mechanisms has achieved widespread acceptance. [1-19] Besides the fact that slight differences in processing could lead to very different mechanical behaviour, this may be at least partially due to the fact that nanoparticle additions in PRABN could affect the flaw size in contradictory ways. For instance, crack extension along grain boundaries could be suppressed by intergranular nanoparticles, hence limiting the size of flaws lying on grain boundaries and resulting in a strength improvement.[15,16] On the other hand, intergranular particles could introduce matrix thermal tension which may enhance the crack formation during cooling and machining, i.e, results in larger initial flaws.[1,2,3,19] Therefore, it is understandable that the evaluations of how nanoparticle addition influence the flaw size is always difficult.

2.1.3.2. Flaw size reduction due to matrix refinement

Niihara first attributed his observed notable strength improvement mainly to flaw size reduction caused by matrix grain refinement. [1,2] With finer matrix grains, the size of flaws lying both along grain boundaries and within the grains could be further limited. Using the toughness and strength data in Niihara's publication[1,2], the flaw size estimated from the Griffith equation is 31 μm in the polycrystalline alumina, but only 3 μm in the Al_2O_3/5vol% SiC nanocomposites after annealing. Such flaw size reduction in PRABN was proposed as the source of strengthening in PRABN, and the matrix refinement was suggested as the reason for flaw size reduction. This

calculation was based on strength and toughness data and assumed that Griffith equation is applicable in this case, while further microscopy characterization for flaws after fracture is needed to support this theory.

There are generally two other reasons proposed for matrix refinement. One is the formation of subgrain boundaries (Figure 2.9).[2,3,21] Subgrain boundaries form as a result of pinning and pile-up of dislocations at intragranular SiC particles due to the thermal expansion mismatch between alumina matrix and SiC particles, which was believed as effective refinement of the matrix grains for strengthening.[2] However this theory was questioned by Fang et al[29]whose theoretical calculation suggested that the level of the residual stresses due to the expansion mismatch is insufficient to induce the amount of plastic deformation required for subgrain formation, and their TEM studies (Figure 2.10) showed that only a small amount of subgrain boundaries could be found. Another problem with the idea of subgrain boundaries is that the flaw size is 3 μm or even above in Niihara's work [1,2], which is much larger than the subgrain size.

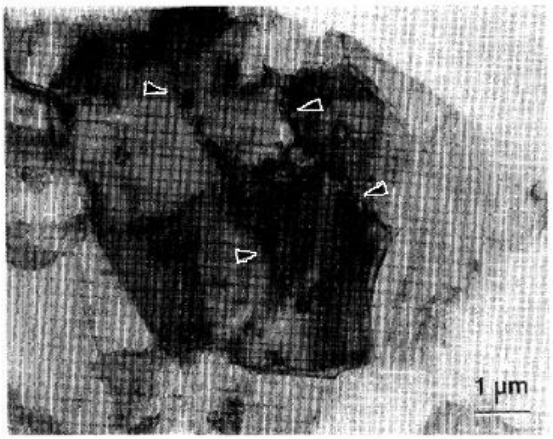

Figure 2.9 The subgrain boundaries observed within the matrix grains of Al_2O_3/SiC nanocomposites. Arrows indicates the existence of subgrain boundaries[2]

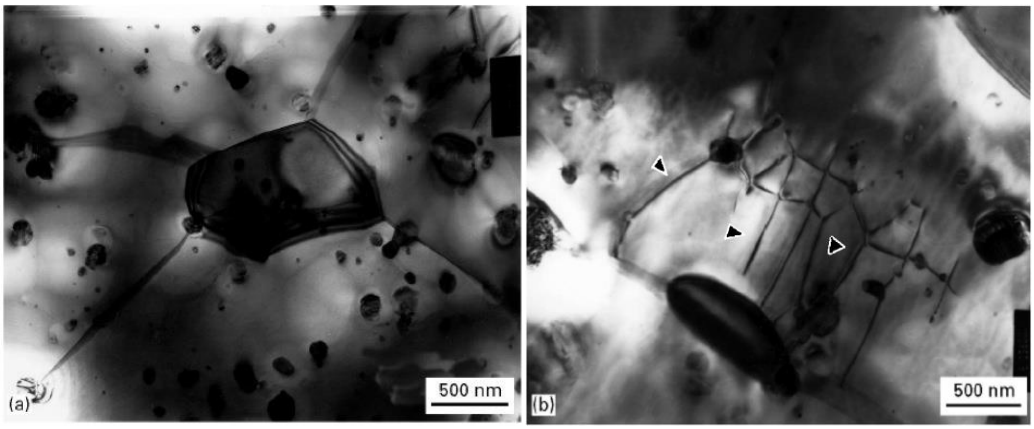

Figure 2.10 TEM bright-field images of 5 vol% SiC-Al2O3 nanocomposite showing (a) the absence of deformation structure in most areas (b) and the presence of a low density of dislocations in isolated regions. This showed that only small amount of dislocations present in matrix, nowhere were any sub-grains observed. Arrows indicate the existence of dislocations[29]

Instead of sub-grain formation, subsequent research tended to attribute the microstructure refinement to particle pinning, especially Zener grain boundary pinning[30], which is a grain growth inhibition mechanism: $D = \frac{d}{V_f}$, where *D* stands for grain size, d stands for particle size, and V_f stands for volume fraction. Borsa's results[20] (Figure 2.11) showed an agreement with Zener's model in two ways: 1, larger particle volume fraction leads to finer grains, i.e smaller $\frac{1}{V_f}$ corresponds to smaller matrix grain size D; 2, the gradient of the line in a plost of D vs $\frac{1}{V_f}$, corresponding to *d* in Zener model, is 230nm which is close to the average SiC particles size 200nm used in Borsa et al's study.

However, some reports showed disagreements with Zener's pinning model. For instance, Stearns et al [31] reported that 5vol% ultra-fine SiC particles could significantly retard grain growth of alumina, but the grain size is larger than the prediction of the Zener model. Study by Carroll et al[21] also showed that the matrix

grain size was independent of the SiC particle size for the same SiC volume fraction (5vol%), but this may be due to the fact that the grains did not reach the maximum size yet.

Therefore, it can be concluded that there is no well accepted model explaining how nanoparticle additions affect microstructure refinement and hence result in strengthening. In addition, there is not a clear consensus yet on the effect of particle size and particle fraction on the mechanical properties, though both topics were addressed in Borsa et al's work[20].

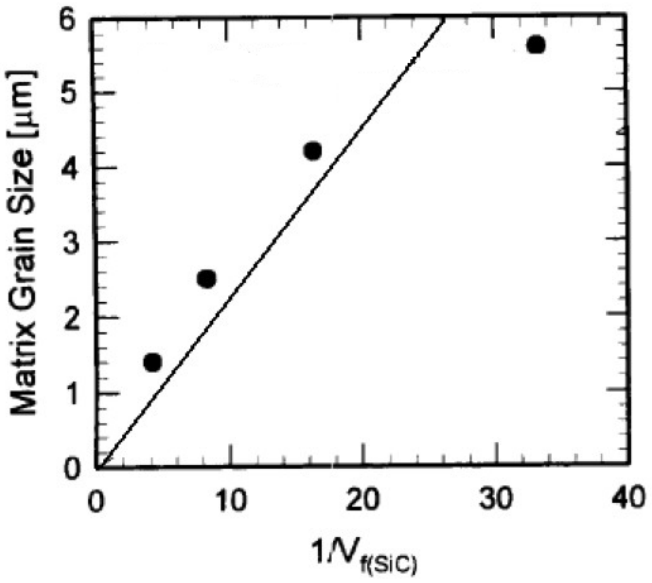

Figure 2.11 Matrix grain size as a function of the inverse of the SiC volume fraction for Al2O3-SiC nanocmoposties, where the black dot s present the experimental data, drawn straight line is a tendline for those dots. [20]

2.1.3.3. Flaw size reduction due to processing

Zhao et al[19] and Carroll et al[21] proposed that a flaw size reduction in PRABN could result from processing and sample preparation, while nanoparticles only play an indirect role in such flaw size reduction.

Zhao et al[19] suggested that only PRABN samples that have been surface-ground and then annealed could obtain high strength. The annealing treatment was believed to have relaxed the compressive surface stresses induced by the grinding process, and also help heal surface flaws and reduce intrinsic flaw size, both of which could result in strengthening. Wu et al[32] have shown that the annealing effect was associated with a chemical process on the nanocomposite surface which has been tentatively identified as an oxidation leading to:

$$SiC(s)+O_2 \rightarrow SiO(g)+CO(g) \quad (2.1)$$

$$2SiO(g)+3Al_2O_3(s)+O2 \rightarrow 3\ Al_2O_3 \cdot 2SiO_2 \quad (2.2)$$

However, Zhao et al's conclusion excluded the consideration of microstructure, and neglected the fact that in Niihara's work[1] samples were polished after grinding to remove the effect of residual stress caused by grinding. Furthermore, Zhao et al did not measure the residual stress in their specimens. Therefore, this story is somewhat speculative.

Later work by Carroll et al[21] incorporated the consideration of microstructure. All samples with similar grain size showed different strength depending on different processing, but there is no clear dependence of strength on SiC particle size. Carroll et al proposed that processing routes directly affect the size and the volume density of the flaws, thus directly affecting the strength of the nanocomposites.[21] In this case,

SiC particles just act as a grinding medium in processing, and SiC particle size has no effect on strength.

However, it appears that the way that Carroll et al deduce the strengthening mechanism is not rigorous because: (1), how different processing influences the flaws remains unknown; (2), the type and size of processing flaws could vary with different SiC particle size even for the same processing procedures, and thus may further influence strength; (3), the fracture toughness decreases with decreased SiC particle size in their own work. Therefore, it seems that SiC particles work not just as a grinding medium and particle size may also have an impact upon strength though such impact is difficult to interpret.

2.1.3.4. Flaw size reduction by residual stress

As Todd et al[14] suggested, a reduction in the intergrain stresses in nanocomposites due to intergranular nanoparticles, can cause large strength increases by reducing the critical flaw size. This can be explained as follows (Figure 2.12): (1), both grinding and intergrain residual stress could make a contribution to the stress intensity at the crack tip; (2), as the crack grows, the grinding contribution diminishes. In contrast, the intergrain residual stress intensity is proportional to the square root of crack length, and increases as the crack grows; (3), therefore, the total stress intensity K_{alum} undergoes a minimum. [14] If this minimum value is higher than the local fracture toughness K_c, the crack continues to grow unarrested until it encounters a compressive grain boundary at c_{alum}. So if the intergrain stress is reduced, the minimum total stress intensity in nanocomposites may fall below K_c, so that the crack arrests while it is still small, i.e the flaw size is limited, giving a higher strength.

However, as mentioned in 2.1.1.2, Todd's intergrain theory is somewhat speculative and has not been tested in other system yet.

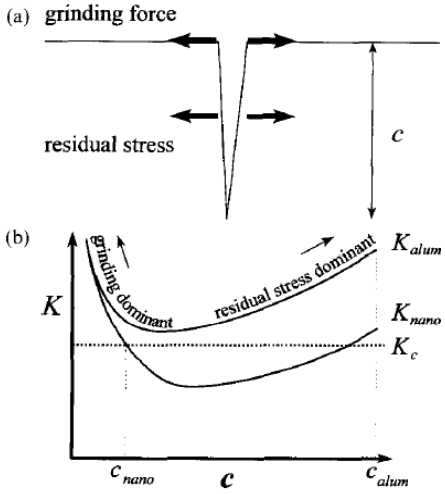

Figure 2.12 (a) Loading of a surface crack in alumina during grinding or polishing and (b) schematic illustration of total stress as crack grows in pure alumina (K_{alum}) and in a nanocomposite with reduced intergrain residual stresses (K_{nano}).[14]

2.1.4. Comments on the strengthening and toughening mechanisms for PRABN

From the discussion above, it is clear that none of mechanisms discussed has gained widespread acceptance as a strengthening and/or toughening mechanism, and none of them provides quantitative expressions to predict the mechanical behaviours of PRABN.

One of the main barriers to the understanding of the mechanical property improvements in PRABN is the fact that slight differences in processing could lead to the different mechanical behaviors of PRABN. For instance, one possible explanation for the fact that none of the subsequent research investigations could reproduce Niihara's superior results is the fact that Niihara used better particle dispersion techniques.[1-32]

Limited accuracy of microstructural and/or mechanical characterisation methods could also contribute to different interpretations of the mechanical behaviours of PRABN. For instance, neither TEM nor SEM can provide full 3D information about microstructure and/or cracks, while EM sample preparation could also introduce cracks in the specimen. The indentation toughness technique is used in many PRABN related investigations, and is actually a widely disputed method for estimating fracture toughness.[33]

Another possibility could be that these mechanical improvements are contributed by different mechanisms operating simultaneously. Fracture is a very complicated process, upon which many factors such as microstructure, residual stress, interfacial energy, critical flaw size and so on, could have an influence. Furthermore, all these features could be influenced by processing variables to some extent, which further emphasises the significance of processing routes. Most PRABN related investigations only consider one or some of these factors. It is reasonable to say that to obtain a whole picture of the mechanical behaviour of PRABN, none of the factors should be ignored in modelling.

2.2 Abrasive wear mechanisms of nanocomposites

2.2.1. Early studies on wear resistance of ceramics

Nearly 30 years ago it was postulated that wear rate of ceramics is controlled by hardness and especially by its fracture toughness. The fracture toughness was considered to be a primary parameter to relate to the wear loss.[34] However, in wear processes of polycrystalline alumina ceramics the fracture occurs on the scale of individual grain size or less, microcracks propagate along the grain boundaries of

individual grains, resulting in grain dislodgement and pull-out.[35] Therefore, fracture toughness measured by macroscopic extension of cracks should not represent the type of fracture that occurs during the wear process. Studies have also found that the wear resistance of nanocomposites is much higher than that of the corresponding monolithic alumina with the comparable grain size, where the indentation fracture toughness of the nanocomposites is only moderately higher than the monolithic alumina.[36] Similarly, the requirement of high hardness as a prerequisite for high abrasive wear resistance of hard ceramics was questioned by Roberts[37], who revealed that the depths of cracks produced by hard abrading particles in ceramic counterfaces decreased with decreasing counterface hardness. Any direct relationship between the wear resistance and mechanical properties of hard polycrystalline materials is therefore questionable.

2.2.2. Early models proposed for wear resistance of ceramics

Both brittle fracture controlled abrasive wear (including intergranular and transgranular fracture) and plasticity controlled abrasive wear have been reported.[38,39,40]

To further understand intergranular microfracture controlled material removal during wear, Cho et al[38] developed a fracture mechanics model to account for the intergranular grain pull-out during wear, and Liu et al[39] further modified this model. The critical condition for the onset of local microfracture in wear is that the superposed stress intensity factors equal the intrinsic grain-boundary toughness K_c^b. The mode could be expressed as: [38,39]

$$c_o = \beta \times l \tag{2.3}$$

$$\Psi(\beta \times l)^{0.5}(\sigma_T + \sigma_R + \sigma_D) = K_c^b \tag{2.4}$$

In which Ψ is a crack-geometry factor, β is a scaling coefficient, c_o is the initial flaw size, l is the grain size, σ_T is the tensile stress due to the applied stress field under sliding contact, σ_R is the residual stress due to the thermal expansion coefficient anisotropy of alumina, σ_D is the tensile stress due to accumulated damage. From this equation, it can be found that the wear rate is linearly dependent of the grain size.

A quantitative relationship between the wear rate, ν, and the area fraction of pullout, f_{po}, can be developed by assuming that the plasticity controlled abrasive wear of this load bearing area obeys the simple model in which[41,42]:

$$Q=\frac{KW}{H} \tag{2.5}$$

where Q is the volume of material removed per unit sliding distance under a normal load W, H is the hardness of the surface and K is a constant depending on the geometry of the particles and the fraction of the material displaced by an abrasive particle that is removed.

2.2.3. Wear behaviour of nanocomposites

Although a lot of research has been directed towards nanocomposites' strengthening and toughening effects, the most remarkable and reproducible benefits offered by the nanocomposites are their tribological properties, where significantly improved wear resistances compared with pure alumina have been widely reported.[43] Zhao et al[19] first reported that alumina/SiC nanocomposites are easier to polish to a good surface finish than pure alumina of similar grain size, which was also confirmed by subsequent research.[44] Zhao et al attributed the improved strength to a reduced surface defects size due to better processing. Unfortunately, the finishing process they used for their machined and unmachined surfaces was not specified in detail. Nevertheless, if nanocomposite strengthening is mainly a surface phenomenon, it

should also modify the wear properties. Thus this triggered further interest in investigating the tribological properties of nanocomposites.

One of the most important features of wear behavior of Al_2O_3/SiC nanocomposites is the improved wear resistance.[44,45] An improved surface finish was then found after severe surface grinding[45]and it has been found that the nanocomposites suffered much less surface fracture and grain pull-out than pure polycrystalline alumina. Todd et al[17] first reported that the worn surfaces of nanocomposites showed a mixture of intergranular and transgranular fracture. This was confirmed by subsequent research[46,47]. Despite the intensive papers mentioned above on the improved wear resistance in nanocomposites, none of them gave any plausible explanation for the improved wear resistance.

2.2.4. Mechanisms proposed for the wear resistance improvements in nanocomposites

There are three noticeable mechanisms proposed for the improved wear resistance in nanocompmosites, which are reviewed here.

Although Chen et al[47] implied that the improved wear resistance in their Al_2O_3/SiC nanocomposites during sliding wear might be a result of improved grain boundary strength of the nanocomposites, there was no direct evidence showing the grain boundary strength was improved in their nanocomposites. Rodr ́guez et al[46] suggested that the improved wear resistance of nanocomposites compared with monolithic alumina during sliding wear is because of the transition to transgranular fracture and the abrasion and plastic deformation wear processes in the nanocomposites, but did not give any plausible explanation for such transition.

Via quantitative surface fractography of the worn surfaces, Ortiz-Merino and Todd[43] suggested that the primary cause of the improved wear resistance and better surface finish of 2 vol% SiC nanocomposites was a reduction in the size of individual surface pullouts owing to the geometrical effect of the fracture mode change induced by the SiC particles. (Figure 2.13)[43] A secondary effect with high SiC contents was a reduction in the pull-out formation rate, which was suggested to be a result of the suppression of twinning and dislocation pileups by intragranular SiC particles. This was based on observations of Wu et al[48], who observed the sub-surface damage following diamond grinding in alumina/SiC nanocomposites and alumina by TEM, and found that twin formation was suppressed in the nanocomposites. Ortiz-Merino and Todd's results were explained using a simple model for mixed plasticity and brittle fracture controlled wear. A key prediction of this explanation is that the wear behavior of nanocomposites should be independent of grain size if the fracture mode is transgranular during the wear. This prediction was then confirmed by Limpichaipanit and Todd[49] who also supported the idea that cracking is suppressed because intragrnular SiC nanoparticles block the formation of long twins and/or dislocation pileups during plastic deformation. Mukhopadhyay and Todd[50] also supported the twining suppression mechanism. However, the twinning suppression mechanism would be more convincing if any of these researchers had made TEM observations on the sub-surface damage with foils carefully prepared with near the as-worn surfaces.

In conclusion, although lots of effort has been directed towards the mechanisms for improvement of wear resistance of Al_2O_3/SiC nanocomposite, there isn't any well accepted mechanism. However, the reduction in grain pull-out size due to

trangranular fracture and suppression of twinning and dislocation pileups by intragranular SiC particles both seem to be important mechanisms.

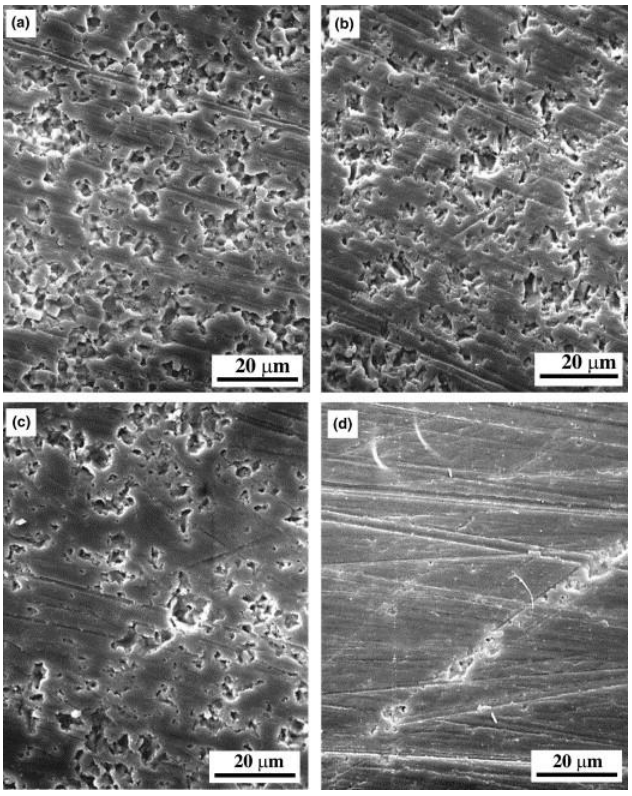

Figure 2.13 A selection of worn surfaces of alumina and composites showing pullout by brittle fracture and load bearing area with scratches indicative of plasticity-controlled wear. (a) A1, fine grained AKP50 alumina, predominantly intergranular fracture within the pullouts. (b) A5, fine grained ALM44 alumina, more transgranular fracture than for A1. (c) C3, 2% SiC nanocomposite, majority of transgranular fracture. (d) C1, 10% SiC nanocomposite, low density of small pullouts, associated with a minority of the scratches.[43]

2.2.5. The laminate structure designed for improving wear resistance in nanocomposites

It has been found that the surface compressive stresses due to coefficient of thermal expansion (CTE) mismatch in layered structures can result in improved wear

resistance due to the suppression of cracking.[51] Therefore Dancer et al developed functionally graded Al_2O_3-SiC nanocomposites utilizing the surface compressive stress caused by residual stress distribution to improve wear resistance.[52] In another paper, Dancer et al[53] constructed two-layer samples consisting of alumina faced with a layer of 10 vol% SiC $–Al_2O_3$ nanocomposite, and suggested that the observed improved wear resistance compared with 10 vol% SiC $–Al_2O_3$ nanocomposite is mainly a result of compressive residual stress on the 10 vol% SiC $–Al_2O_3$ nanocomposite layer due to CTE mismatch. However, none of the residual stress models in Dancer et al's paper perfectly matches the measured residual stress, and the error range of the measured Cr^{3+} fluorescence R1 peak position shift seems a bit large.

2.3 Development of PRABN via precipitation from Alumina-Matrix solid solution

2.3.1. Challenges caused by nanopowders

Due to the large specific surface area of the ceramic nanocpoweder, the high driving force for agglomeration leads to one of the most significant problems associated with nanocomposites processing. Although high energy ball milling and sol-gel technique were used to prevent agglomeration, the results are still frustrating.[54] Such agglomeration might dominate the densification behavior, and result in slower overall densification, enhanced grain growth and higher porosity.

One widely used techniques for preventing nanopowder agglomeration is to introduce surface charges by the use of certain surfactant which are generally organic molecules. This could create electrostatic repulsion between particles in dispersion during the synthesis stage.[54] Although surfactant has been proved to reduce the

agglomeration to some extent, it requires much smaller organic molecules than those conventional ones. The method of drying precursor powders is also found critical for agglomeration control. Freeze drying[55], colloidal processing[54], replacement of water by organic solvents prior to drying[56] have also been employed widely to avoid agglomerate. Post-synthesis deagglomeration techniques such as centrifugation, ultrasonication and ball milling have also been employed widely [54].

2.3.2. The sintering techniques and the origin of PRABN via precipitation

As described in Chapter 1, due to the high fabrication expenditure, sample shape and dimension limits[57,58,59,60 ,61,62], both pressure assisted sintering and novel sintering techniques have not been adopted as commercial processes for mass scale production of PRABN. Since pressureless sintering (PS) is one of the most industry-friendly and cost-effective methods widely used to sinter ceramics, efforts have been directed towards developing fully dense PRABN with PS. Although with some sintering aids such as Y_2O_3 or CeO_2[63,64], it has been reported that pressureless sintering allows near theoretical densification of Al_2O_3/SiC nanocomposites at modest sintering temperatures (1450-1650 ℃), such benefits are limited to a very narrow composition-processing window. Such nanocomposites contained only no more than 2vol% reinforcements if full density is required.

In order to stimulate commercial application of PRABN, a new idea utilizing PS has recently been developed, which is 'nanocomposites by precipitation' (NBP). The rationale behind this idea has been described in Chapter 1.[9] If this idea is successful, it can avoid the usage of expensive advanced sintering techniques, and meantime minimize the densification inhibition usually caused by non-oxide reinforcement.

Nevertheless, up to date, there is not much literature on the subject of developing in-situ formation of particles in alumina， and only two NBP systems have been recently developed. This may be at least partly due to the fact that most cations have negligible solubility in alumina, since their ionic radius and/or different charge compared with aluminum ions, which makes them could neither be accommodated in substitional nor interstitional solution. [65] One of the earliest indications of precipitation from supersaturated alumina solid solution is the formation of needle shaped precipitates (TiO_2) in star sapphire. [66,67] However, the needles formed are usually hundreds of micrometre in length and the volume fraction of precipitates is very limited.[68]

Based on the early studies, Wang et al[69] constructed a process to produce lens shaped $MgAl_2O_4$ precipitates with diameters of 100 nm and thicknesses of 10 nm in alumina. (Figure 2.14 and Figure 2.15) The solid solution $(Al_{1-2x},Ti^{4+}_x,Mg_x)O_3$ was formed by heating an Al_2O_3-TiO_2-MgO mixture in an oxidizing atmosphere.

$$Al_2O_3+MgTiO_3 \rightarrow (Al_{1-2x}, Ti_x^{4+},Mg_x)_2O_3(ss) \quad (2.6)$$

$(Al_{1-x}, Ti_x^{3+})_2O_3$ solid solution and $MgAl_2O_4$ precipitates were obtained by heating Al_2O_3-TiO_2 in a reducing atmosphere.

$$Al_2O_3+TiO_2+H_{2(g)} \rightarrow (Al_{1-x}, Ti_x^{3+})_2O_3(ss)+H_2O_{(g)} \quad (2.7)$$

$$(Al_{1-2x}, Ti_x^{4+},Mg_x)_2O_3(ss) + H_{2(g)} \rightarrow (Al_{1-x}, Ti_x^{3+})_2O_3(ss)+ MgAl_2O_4+H_2O_{(g)} \quad (2.8)$$

However, only a maximum of 2 mol% ($MgO+TiO_2$) can be incorporated during solution treatment due to the solubility limit. This limits the volume fraction of the second phase particles that can be precipitated out during the aging treatment. Nevertheless, Wang et al's work provides an idea that the precipitation of spinel from supersaturated alumina solid solution may be used as a basic model to develop

PRABN using PS. Since spinel structure is based on a FCC close-packed oxygen sublattice, different from alumina (HCP),[69] spinel can precipitate out from alumina solid solution once it forms.

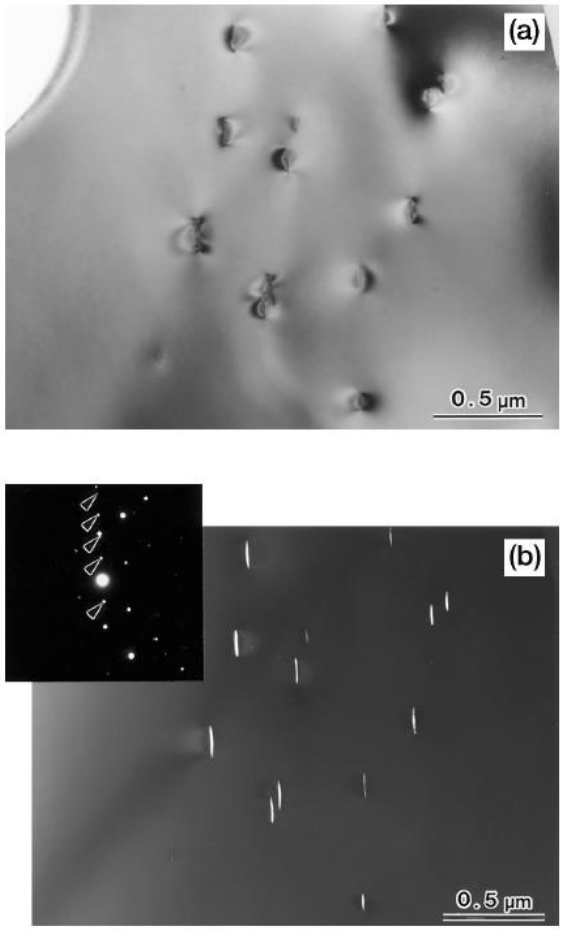

Figure 2.14 TEM photographs of the specimen after precipitate heating of the (Al,Ti,Mg)2O3 solid solution at 1400℃ for 0.5 h: (a) bright field and (b) dark field with the electron diffraction pattern around a precipitate (arrows show magnesium aluminum spinel).[69]

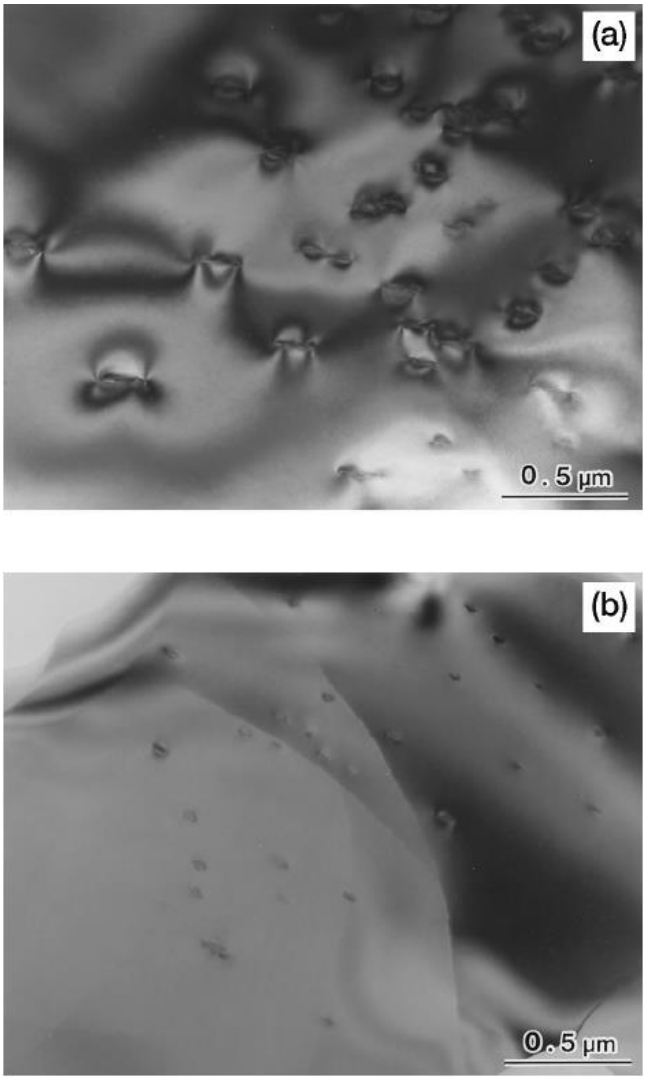

Figure 2.15 TEM photographs of the specimens after precipitate heating the (Al,Ti,Mg)2O3 solid solution (as shown in the Fig. 3) under various conditions: (a) 1400 ℃ for 5 h and (b) 1300 ℃ for 5 h. [69]

More recently, Al_2O_3/ $FeAl_2O_4$ nanocomposites have been developed by Mukhopadhyay et al[65] to achieve higher amount of spinel nanoparticles in PRABN. The synthesis of Al_2O_3/ $FeAl_2O_4$ nanocomposites via precipitation was also developed by Santanach et al[70,71] but by expensive technique SPS. This is based on the following facts: since Fe_2O_3 belongs to the same space group as α-alumina and possesses substantial solubility in alumina at moderately high temperatures (about 15 mol% at 1410 ℃, Figure 2.16) in air, this allows the formation of dense alumina

based solid solutions containing more than 10wt% of Fe_2O_3.[65] Furthermore, under reducing conditions Fe^{3+} (in dissolved Fe_2O_3) can be reduced to Fe^{2+}, which being aliovalent to Al^{3+}, possesses very limited solubility in alumina. Thus aging of Al_2O_3-Fe_2O_3 solid solutions under reducing conditions such as 4% H_2/N_2 could produce PRABN with relatively large volume fraction of $FeAl_2O_4$ precipitate.

The chemical reactions for precipitation were proposed in sequence as follows:

$$Fe_2O_3+Al_2O_3+H_2 \rightarrow FeAl_2O_4+H_2O \quad (2.9)$$

$$FeAl_2O_4+H_2 \rightarrow Fe+Al_2O_3+H_2O \quad (2.10)$$

The aim of the investigation by Mukhopadhyay et al [65] was to produce only spinel nanoparticles. It was reported the microstructure of the aged samples consists of a surface layer where both $FeAl_2O_4$ and Fe metallic particles exist, and a bulk part where intergranular and intragranular $FeAl_2O_4$ particles formed (Figure 20). It has been observed that the resultant PRABN possesses considerably improved fracture toughness (by about 45%), flexural strength (by about 50%) and wear resistance (by 200%) with respect to monolithic polycrystalline Al_2O_3. The observed fracture mode change from intergranular to transgranular coincided was believed to be a result of intragranular nanoparticles.

Nonetheless, the thermodynamics regarding to the second phase formation was not addressed in Mukhopadhyay et al's work. The diffusion kinetics was neither clear. The mechanism of the microstructural developments during the aging remained unknown. Furthermore, the corresponding strengthening and toughening mechanism were not clear and subject to further investigation.

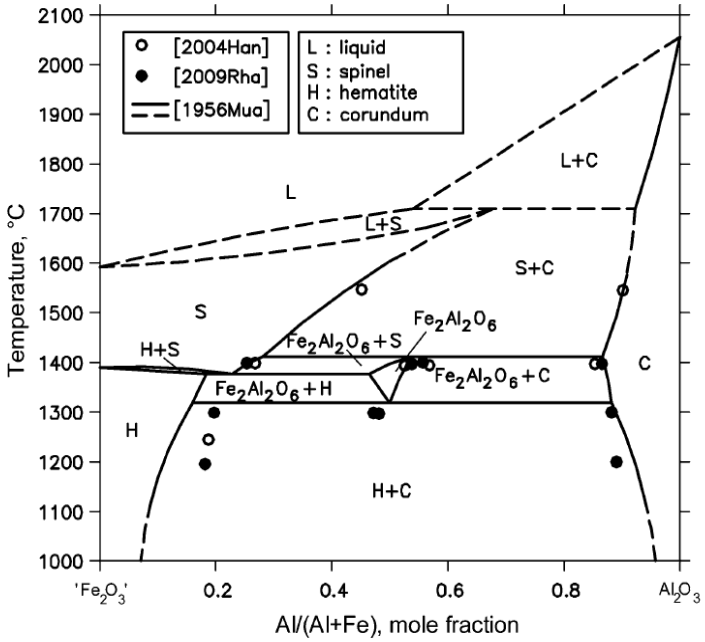

Figure 2.16 Al-Fe-O pseudo-binary section in air along the Fe_2O_3-Al_2O_3 system in 1 atm pressure.[72]

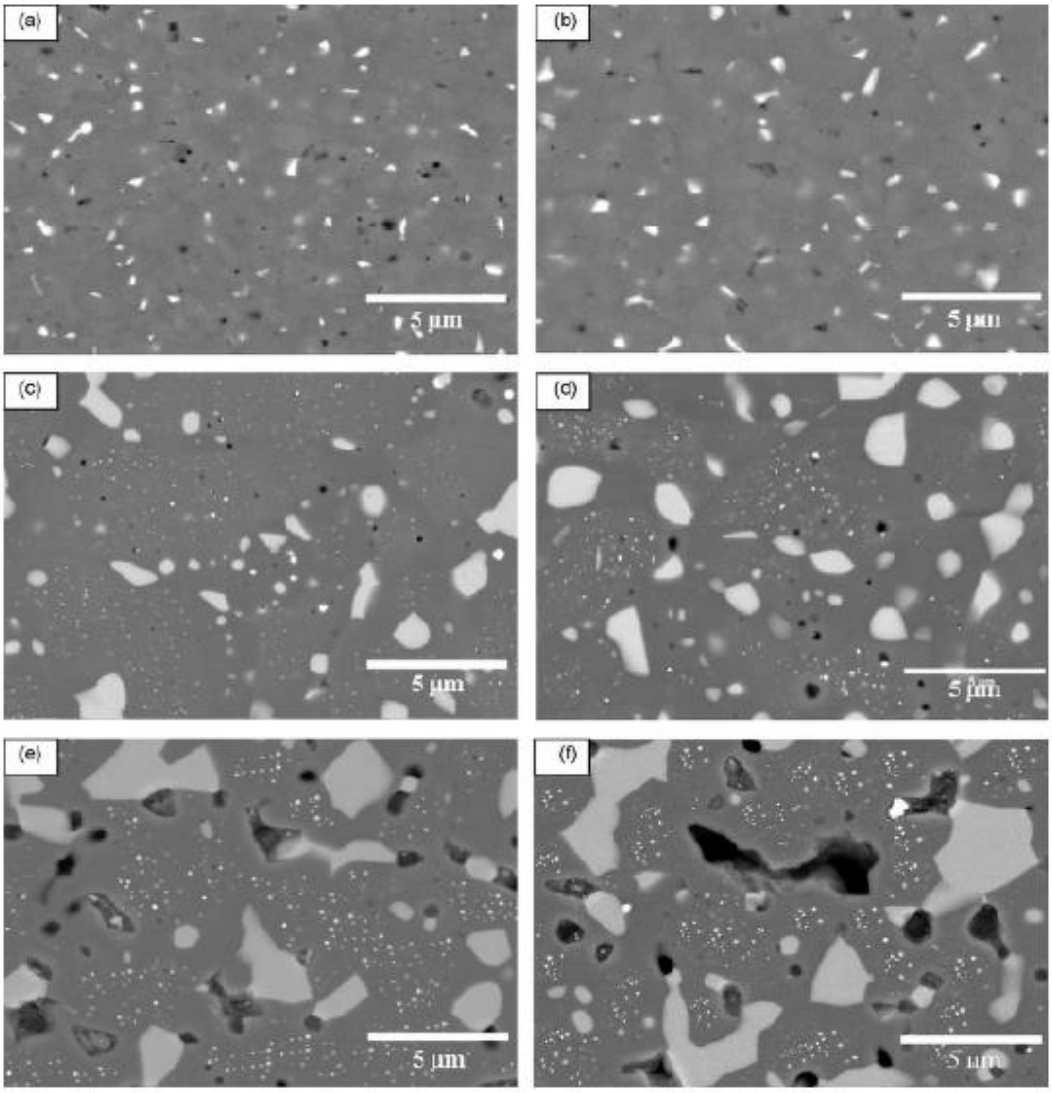

Figure 2.17 Back scattered SEM (BSE-SEM) images corresponding to the bulk microstructural developments on aging of (a) A10FY solid solution (yttria-doped) at 1450 ◦C for 0 h; (b) A10F solid solution (yttria-free) at 1450 ◦C for 0 h; (c) A10FY at 1450 ◦C for 20 h; (d) A10F at 1450 ◦C for 20 h and (e) A10FY at 1550 ◦C for 10 h and (f) A10F at 1550 ◦C for 10 h.[65]

2.4 Diffusion in Alumina:

One of the primary objectives of this project is to investigate the diffusion kinetics during the aging treatment of $Al_2O_3/FeAl_2O_4$ nanocomposites which would strongly influence the precipitation, thus it would be beneficial to review the diffusion phenomenon in alumina.

2.4.1. Hydrogen diffusion and permeation in alumina.

There is currently no well accepted hydrogen diffusion data in alumina yet. Values of hydrogen diffusion coefficients in alumina from different research works are not consistent.[73-78] Although this could be at least partially explained by different diffusion characterization techniques used in different research groups, difficulties in understanding the diffusion mechanism are still shared by all research groups.

Theoretically, the effective radius of the hydrogen molecule of about 0.125 nm probably makes it too large to squeeze through the close-packed alumina structure as a molecule. [73,74] And the pressure exponent of permeation coefficients of hydrogen in alumina is 0.53 nm, not as would be expected from molecular permeation.[73,74] Thus it seems unlikely that hydrogen transported as molecules in alumina, and hydrogen diffusion in alumina is usually assumed to take place by transport of either hydrogen ions or atoms..

It has been emphasized that bare protons (H^+) are unlikely to move without an associated water molecule.[75] Since a bare proton experiences no repulsive force from any adjacent neutral or negatively-charged species, it is able to enter and embed itself in the electron cloud of an oxygen ion in alumina and no ordinary influence can dislodge it.[75] Therefore, the associated activation energy should be high and diffusion rate should be low. However, low activation energy and high diffusion rates for H_2

diffusion in alumina have been reported by several authors (Table 2.1). Thus it seems that the proton story is not realistic. Roberts et al[74] suggested an atomic rather than molecular transport of hydrogen through alumina. This was supported by Serral et al[77] and Begeal[78]. The permeation and diffusion coefficients of hydrogen in polycrystalline alumina measured by these researchers are consistent with earlier results for single crystals,[76] hence it seems that grain boundaries and small closed pores did not contribute significantly to accelerated permeation of hydrogen in sintered alumina. Diffusion coefficients for grain boundary and matrix should therefore be equal. Furthermore, the activation energy for gas-phase hydrogen dissociation (406 kJ/mol) is higher than the permeation activation energy measured (318 kJ/mol), indicating that permeating hydrogen probably derives from dissociation of absorbed hydrogen in the alumina matrix instead of atomic hydrogen created in the gas phase.

Table 2.1 Examples of diffusion data of hydrogen in alumina

Reference	Q(kJ/mol)	Temp range (℃)	Method	Crystal form
Serra et al[77]	81	1000-1400	Permeation	Polycrystalline
Roberts et al[74]	318	1200-1450	Permeation	Polycrystalline
Begeal[78]	132	250-600	Permeation	Polycrystalline
Hauffe et al[79]	97	1000-1200	Reducution	Polycrystalline

Serra et al[77] reported the lowest activation energy (82kj/mol) and the highest diffusion coefficients for hydrogen permeation in alumina. The measured activation energy is in reasonable agreement with activation energy measured by Begeal[78] (132 kJ/mol). Hauffe et al[79] measured the reduction of cobalt ions dissolved in alumina by

hydrogen, and reported around 97 kJ/ mol is obtained, which is also not far from Serral et al's results[77]. However, it should be noted that the permeation data in Begeal's work is for hydrogen permeating through an alumina layer coated on alloys, and the presence of alloys seems to influence permeation, so the resulting permeation data can't be directly used for measurement of the activation energy for hydrogen diffusion in alumina.

Although these low activation energies measured for H_2 suggested that hydrogen transports in alumina by atomic mechanism, the data showed large scatter. Part of the reason could be due to different materials, measuring techniques and gases used. Another problem associated with measuring diffusion rate of H_2 is the low diffusion rate of H_2 in alumina, which can increase the complexity and enlarge the error range of the measurements. Therefore, the diffusion rate of H_2 in alumina still remains uncertain.

2.4.2. Oxygen diffusion in alumina

Table 2.2 Oxygen diffusion data in alumina, S stands for single crystalline, P stands for polycrystalline.

Reference	Log D_o (cm^2/s)	Q(kJ/mol)	Temp range(℃)	Method	Crystal form
Reed et al[80]	5.81	787	1585-1840	TP	S
Reddy et al[81]	2.43	615	1477-1677	NP	S
Oishi et al[87]	3.27	665	1580-1700	XI	S
Cawley et al [82]	1.18	572	1415-1627	NP	S
Prot et al[85]	2.31	636	1500-1720	SP	S
Lagerof et al[83]	0.83	588	1200-1460	DA	S
Oishi et al [84]	0.3	460	1350-1750	XI	P
Prot et al[85]	10.84	800	1460-1723	CA	P

*SP: Profile measured with SIMS

TP: Tracer profile

NP: Nuclear resonance profile

XI: Integrated amount after isotopic exchange

DA: Kinetics of annealing dislocation loops

CA: Chemical analysis

Since 1960 when oxygen self-diffusion was first measured in alumina, several investigations of oxygen diffusion in undoped alumina have been conducted.[80-85] Different oxygen matrix diffusion coefficients and activation energies measured from single crystal alumina have been reported by different laboratories, as summarized in Table 2. The mean of these six activation energies is 644 kJ/mole with a standard deviation of 78 kJ/mole, which falls within the range expected from the experimental error, so it is assumed that the oxygen diffusion mechanisms in these studies are

comparable. In most of those studies, oxygen diffusion was suggested to take place by a vacancy mechanism.

The more than one order of magnitude differences between the original oxygen diffusion coefficients (D_o) from those laboratories, could at least partially result from different experimental diffusion profiles forming methods. Another reason could be the different surface conditions of the alumina samples used in different laboratories. For example, Oishi et al[84] reduced the surface roughness and damage by chemical polishing and argon milling, compared with their earlier studies. Then much lower diffusion coefficients were found for the smoother and less damaged samples. It was suggested that surface roughness, cracks and damage could strongly influence the absolute values of the measured diffusion coefficients.

Another source for the varying oxygen vacancy diffusion data in alumina could be the impurities which can influence the diffusion. However, it is difficult to determine the influence. One reason could be that impurities are so variable between samples used by different laboratories. Another reason could be that they are quite uncontrollable, for example, samples held in the furnace at high temperatures can pick up impurities, such silicon, sodium, and calcium which might have been vaporized from the furnace refractories. [73]

Prot et al[85] reported an activation energy for the grain boundary and sub-boundary diffusion greater than the activation energy for the matrix diffusion, which is different from others who believed that the activation for oxygen grain boundary diffusion is lower than the matrix diffusion. They attributed the high activation energy for oxygen grain boundary diffusion to the interaction between the diffusing species and the segregated impurities, but this sounds too speculative. Furthermore, it

seems that they overemphasized the effect of impurity interaction and ignored the fact that the vacancies on grain boundaries may assist the diffusion and reduce the energy barrier. Therefore Prot et al's story is too speculative.

Diffusion data presented by Stubican and Osenbach[86] indicates that the mechanism of diffusion in alumina grain boundaries is a dislocation pipe mechanism, which is much faster than matrix diffusion. It has been found that the diffusion coefficients of oxygen in polycrystalline alumina are usually orders of magnitude higher than that in single crystalline alumina.[86] Oishi and Kingery [87] showed a time dependence of measured diffusion coefficients and much lower activation energy in polycrystalline alumina, suggesting an enhanced diffusion in a boundary region having an appreciable capacity for material exchange.

In conclusion, it is held by many researchers that oxygen diffusion coefficients along grain boundaries and subboundaries are much higher than in the matrix, even though there are disagreements on activation energies in the matrix and along grain boundaries. Different penetration profile forming techniques and materials could be part of the reasons for the discrepancies.

2.4.3. Aluminum diffusion in alumina

Compared with reports on oxygen diffusion in alumina discussed above, reports of Al ion diffusion in alumina are far fewer. One of the reasons lies on the fact that the only available isostope of aluminum is Al^{26}, which makes diffusion coefficients measurements very limited.

Aluminum ion diffusion exhibits a single activation energy over the range of temperatures studied by Paladino and Kingery in 1962 [88] , which probably corresponds to intrinsic behavior. The activation energy for aluminum ion matrix

diffusion measured in their study was 477 kJ/mol, which is about three quarters of oxygen matrix diffusion as listed in Table 2.2, and the diffusion coefficients were about three to four orders of magnitude larger at 1600 ℃ than those of oxygen. Some researchers' diffusion data of aluminum ions showed much greater ion mobility than that of oxygen, which is consistent with ionic size considerations.[73]

Paladino and Coble[89] found that the aluminum diffusion in alumina was not strongly dependent upon the presence of grain boundaries, nor does it depend much on crystal orientation for reasonably high symmetry structures. However, this is in contrary to some reports suggesting that the presence of grain boundaries does enhance the cation diffusion in alumina.[74]

In a more recent study directed by LeGall and Lesage[90] in 1994, diffusion coefficients of aluminum in single crystalline alumina were reported, giving an activation energy of 510 kJ/mole. Nevertheless, although the absolute original aluminum diffusion values are within experimental error of oxygen diffusion coefficients measured by Prot and Monty[85] in 1996, the data points in LeGall and Lesage's report were far fewer from being reliable.

2.4.4. Iron diffusion in alumina

Iron is often present as a contaminant in systems where alumina is used. Izbekov and Gorbunova[91] first studied iron diffusion in alumina in the late 1950's. However, their results did not lead to useful conclusions due to uncertainties regarding impurity and grain boundary effects involved.

Lloyd and Bowen[92] studied the diffusivity of iron as a function of temperature, oxygen partial pressure and impurity concentration in single crystal alumina in 1981, using Fe^{59} as tracer element. They proposed a vacancy mechanism for iron diffusion

in their study, but also noted the existence of competing diffusion mechansims since there is an oxygen pressure dependence of diffusion. An activation energy 280 kJ/mole was reported. However, only Mg and silicon as impurities were studied in Lloyd and Bowen's study, and the results are too scattered to determine the influence of impurities.[92]

Lesage et al[93,94] found that iron diffuses much faster by dislocations in doped alumina, and gave an equation for iron diffusion in alumina:

$$D_{Fe} = 3.64 \times 10^{-5} \exp\left(\frac{300kJ/mol}{RT}\right) \quad (2.11)$$

Despite similar activation energies (280 kJ/mol and 300 kJ/mol) measured by the above two laboratories, the absolute diffusion coefficients of iron in single crystal alumina from the above two different laboratories do not agree very well, differing by a factor of about 22 at 1200 ˚C in ambient air.

In conclusion, given by the limited research conducted so far, the diffusion data of iron in alumina are not well established yet, nor are diffusion mechanisms of iron in alumina clear yet.

2.4.5. Conductivity in alumina

Almost all mechanisms of conductivity for Alumina proposed so far involve electron and hole migration.[76] Conductivity measurements for high purity alumina in vacuum by Heldt and Haase[95] gave an activation energy of 2.57eV over the temperature range from 550 ˚C to 1465 ˚C, which is in good agreement with the activation energy of 2.5 eV for extrinsic oxygen ion self-diffusion in single crystal alumina given by Oishi and Kingery.[87] The two together imply that conductivity in alumina is dominantly ionic conductivity based on oxygen ion motion over that entire

temperature range. However, it should be noted that Oishi and Kingery's results showed a relatively large scatter, in which different activation energies were reported. Conductivity results in argon[76] gave a high temperature activation energy of 2.85 eV and a low temperature activation energy of 0.66 eV. The former activation energy is in reasonable agreement with the value of 2.97 eV obtained by Pappis and Kingery[96] from electrical conductivity measurements conducted on single crystalline alumina in an atmosphere of pure oxygen gas. Thermoelectric electromotive force measurement results indicated that in 1 atmosphere oxygen conduction in alumina occurred predominantly via positive current carriers, while with 10^{-10} atmosphere thermoelectric electromotive force measurements indicated negative current carriers.[76] However, although thermoelectric electromotive force measurements can give the sign of the predominant current carrier, it could not give evidence to determine whether it is electronic or ionic conduction. [76]

Actually, the most direct and reliable approach used to determine the nature of the conductivity is potential measurements, which is difficult to obtain data and so far has only been conducted once by Schmalzried[97]. He stated that both ionic and electronic conduction occurred below 1323℃. The mixed conduction may result from the chemical reactions of the gaseous components other than O_2 with alumina.

In conclusion, both alumina conductivity data and potential measurements lead to a consistent picture possessing features that can be satisfactory explained by ionic conduction mechanisms, though oxygen self-diffusion data for alumina showed some scatter.

2.5. Conclusions and priorities for future work

Research on PRABN is rich with interesting and unanswered questions. The work reviewed here describes the significant debates surrounding the strengthening, toughening mechanisms and mechanisms for improved wear resistance in PRABN, and a precipitation method to produce PRABN to avoid using expensive sintering techniques was introduced. The diffusion in alumina has also been briefly reviewed.

On the basis of the review on PRABN presented above, the following conclusions can be drawn:

1. Generally, the PRABNs could exhibit a superior strength and wear resistance compared with monolithic polycrystalline alumina, but it does not seem a promising way to improve the toughness since none of the investigation yet has shown a toughness increase more than 40%.
2. There is no unified opinion on the strengthening, toughening mechanisms or the mechanisms for improved wear resistance for PRABN. This may be at least partly due to the slight differences during processing, different microstructure and/or mechanical property characterization techniques. It is also suggested that different mechanisms may work simultaneously.
3. Due to the nature of alumina and refractory particles, it is difficult to use PS to consolidate mixture of particles and alumina powders to obtain fully dense solid. Some pressure assisted sintering techniques and the use of high temperatures or sintering aids have proved successful obtaining fully dense ceramics without severe grain growth. However, the high expense or limited particle volume fraction inhibits them from being commercial.

4. Some success in alumina/spinel micro-/nano-composites via precipitation indicates that it can be a model for developing PRABN commercially. Studies on alumina/ $FeAl_2O_4$ nanocomposites via precipitation demonstrated considerably improved fracture toughness (by about 45%) and flexural strength (by about 50%) with respect to monolithic Al_2O_3. However, this method needs long aging time and the surface layers need be removed by grinding/polishing, which makes it expensive. Furthermore, the thermodynamic and kinetic data of the precipitation process are both absent, and the factors controlling the kinetics and the reaction mechanisms are still unknown.
5. Both the diffusion of hydrogen, oxygen, aluminum ions and iron ions in alumina, and the conductivity of alumina have been reviewed. The kinetics data between different researchers show a large scatter which may be caused by different measuring techniques used, but there are some agreements on the diffusion mechanisms.

Future work is needed for more systematic mechanical property measurement and microstructure characterization, to give deeper understanding in strengthening/toughening mechanisms in PRABN. More detailed study on the thermodynamic, diffusion kinetics and precipitation mechanisms for Al_2O_3/ $FeAl_2O_4$ nanocomposite is also needed.

Reference

[1] K. Niihara, New Design Concept of Structural Ceramics-Ceramic nanocomposites, The Centennial Memorial Issue of The Ceramic Society of Japan, 99, 974-982 (1991).

[2] K. Niihara, A. Nakahira, M. Inoue, Sintering Process and Mechanical Properties for Oxide-based Nanocomposites, Materials Research Society Proccedings, 271, 589–593 (1992).

[3] I. Levin, W. D. Kaplan, D. G. Brandon, Residual Stresses in Alumina-SiC Nanocomposites, Acta Metallurgica, 42, 1147-1154 (1994).

[4] J. Seising, Internal Stresses in Ceramics, Journal of the American Ceramic Society, 44, 419-419 (1961).

[5] M. Taya, S. Hayashi, A. S. Kobayashi, H. S. Yoon, Toughening of a Particulate-Reinforced Ceramic Matrix Composite by Thermal Residual Stress, Journal of the American Ceramic Society, 73, 1382–1391 (1990).

[6] R.I. Todd, Alumina/SiC Nanocomposites: Big Things from Small Packages, 21st Century Ceramics, The University Press Cambridge, UK (1996).

[7] B. Basu, T. Venkateswaran, D. Y. Kim, Microstructure and Properties of Spark Plasma Sintered ZrO_2/ZrB_2 Nano-ceramic Composites, Journal of the American Ceramic Society, 89, 2405–2412 (2006)

[8] M. Sternitzke, B. Derby, R. J. Brook, Alumina/Silicon Carbide Nanocomposites by Hybrid Polymer/Powder Processing: Microstructures and Mechanical Properties, Journal of the American Ceramics Society, 81, 41–48 (1998).

[9] H. Z. Wang, L. Gao, J. K. Guo, The Effect of Nanoscale SiC Particles on the Microstructure of Al_2O_3 Ceramics, Ceramics International, 26, 391-396 (2000).

[10] L. P. Ferroni, G. Pezzotti, Evidence for Bulk Residual Stress Strengthening in Al_2O_3/SiC Nanocomposites, Journal of the American Ceramic Society, 85, 2033–2038 (2002).

[11] X. D. Sun, J. G. Li, S. W. Guo, Z. M. Xiu, K. Duan, X. Z. Hu, Intragranular Particle Residual Stress Strengthening of Al_2O_3–SiC Nanocomposites, Journal of the American Ceramic Society, 88, 1536–1543 (2005).

[12] B. Lv, F. C. Zhang, H. H. Luo, M. Zhang, Inter-phase Microstress on the Grain Boundary in Al_2O_3/SiC Nanocomposites, Scripta Materialia, 64, 260-263 (2001).

[13] G. Pezzotti, W. H. Müller, Strengthening Mechanisms in Al_2O_3/SiC Nanocomposites, Computational Materials Science, 22, 155-168 (2001).

[14] R. I. Todd, M. A. M. Bourke, C. E. Borsa, R. J. Brook, Neutron Diffraction Measurements of Residual Stresses in Alumina/SiC Nanocomposites, Acta Materialia, 45, 1791-1800 (1997).

[15] S. Jiao, M. L. Jenkins, R. W. Davidge, Electron Microscopy of Crack/Particle Interactions in Al_2O_3/SiC Nanocomposites. Journal of Microscopy, 185, 259–264 (1997).

[16] S. Jiao, M. L. Jenkins, R. W. Davidge, Interfacial Fracture Energy-mechanical Behaviour Relationship in Al_2O_3/SiC and Al_2O_3/TiN nanocomposites, Acta Materialia, 45, 149-156 (1997).

[17] A. J. Winn, R. I. Todd, Microstructural Requirements for Alumina-SiC Nanocomposites, British Ceramic Transactions, 98, 219-224 (1999).

[18] K. T. Faber, A. G. Evans, Crack Deflection Processes: I. Theory, Acta Metallurgica, 31, 565-576 (1983).

[19] J. H. Zhao, L. C. Stearns, M. P. Harmer, H. M. Chan, G. A. Miller, R. F. Cook, Mechanical Behavior of Alumina–Silicon Carbide Nanocomposites, Journal of the American Ceramic Society, 76, 503–510 (1993).

[20] C. E. Borsa, S. Jiao, R. I. Todd, R. J. Brook, Processing and Properties of Al_2O_3/SiC Nanocomposites, Journal of Microscopy, 177, 305–312 (1995).

[21] L. Carroll, M. Sternitzke, B. Derby, Silicon Carbide Particle Size Effects in Alumina Based Nanocomposites, Acta Materialia, 44, 4543–4552 (1996).

[22] T. Hansson, R. Warren, J. Wasén, Fracture Toughness Anisotropy and Toughening Mechanisms of a Hot-pressed Alumina Reinforced with Silicon Carbide Whiskers, Journal of the American Ceramic Society, 76, 841–848 (1993).

[23] C. A. Handwerker, J. M. Dynys, R. M. Cannon, R. L. Coble, Dihedral Angles in Magnesia and Alumina: Distribution from Surface Thermal Grooves, Journal of the American Ceramic Society, 73, 1371–77 (1990).

[24] R. F. Cook, Segregation Effects in the Fracture of Brittle Materials: Ca-Al_2O_3, Acta Metallic Materialia, 44, 4543-4552 (1990).

[25] R. L. Stewart, M. Iwasa, R. C. Bradt, Room Temperature K_{IC} Values for Single Crystal and Polycrystalline $MgAl_2O_4$, Journal of the American Ceramic Society, 64, C22-C23 (1981).

[26] S. M. Widerhorn, Fracture of Sapphire, Journal of the American Ceramic Society, 52, 485-491 (1969).

[27] D. J. Green, Fracture Toughness Predictions for Crack Bowing in Brittle Particulate Composites, Journal of the American Ceramic Society, 66, C4-C5 (1983).

[28] T. Ohji, Y. K. Jeong, Y. H. Choa, K. Niihara, Strengthening and Toughening Mechanisms of Ceramic Nanocomposites., Journal of the American Ceramic Society, 81, 1453-1460 (1998).

[29] J. X. Fang, M. P. Harmer, H. M. Chan, Evaluation of Subgrain Formation in Al_2O_3-SiC Nanocomposites, Journal of Materials Science, 32, 3427-3433 (1997).

[30] M. Hillert, Inhibition of Grain Growth by Second Phase Particles, Acta Metallurgica, 36, 3177-3181 (1988).

[31] L. C. Stearns, J. H. Zhao, M. P. Harmer, Processing and Microstructure Development in Al_2O_3-SiC Nanocomposites, Journal of the European Ceramic Society, 10, 473-477 (1992).

[32] H. Z. Wu, C. W Lawrence, S. G. Roberts, B. Derby, The Strength of Al_2O_3/SiC Nanocomposites After Grinding and Annealing, Acta Materialia, 46, 3839-3848 (1998).

[33] G. R. Anstis, P. Chantikul, B. R. Lawn, D. B. Marshall, A Critical Evaluation of Indentation Techniques for Measuring Fracture Toughness: I, Direct Crack Measurements, Journal of the American Ceramic Society, 64, 533–538 (1981).

[34] A. G. Evans, D. B. Marshall, Fundamentals of Friction and Wear of Materials: Wear Mechanisms in Ceramics, American Society for Metals, New York (1980).

[35] H. H. K. Xu, S. Jahanmir, Y. Wang, Effect of Grain Size on Scratch Interactions and Material Removal in Alumina, Journal of the American Ceramic Society, 78, 881–891 (1995).

[36] J. Sedláček, D. Galusek, P. Švančárek, R. Riedel, A. Atkinson, X. Wang, Abrasive wear of Al_2O_3–SiC and Al_2O_3–(SiC)–C Composites with Micrometer- and

Submicrometer-sized Alumina Matrix Grains, Journal of the European Ceramic Society, 28, 2983-2993 (2008).

[37] S. G. Roberts, Depths of Cracks Produced by Abrasion of Brittle Materials, Scripta Materialia, 40, 101–108 (1999).

[38] S. J. Cho, B. J. Hockey, B. R. Lawn, S. J. Bennison, Grain Size and R-curve Effects in the Abrasive Wear of Alumina, Journal of the American Ceramic Society, 72, 1249–1252 (1989).

[39] H. Liu, M. E. Fine, Modeling of Grain-Size-Dependent Microfracture-Controlled Sliding Wear in Polycrystalline Alumina, Journal of the American Ceramic Society, 76, 2393–2396 (1993).

[40] Y. S. Wang, C. He, S. M. Hsu, P.I. Lacey, In Proceedings of the Japan International Tribology Conference, Japanese Society of Tribologists, 2, 1225–1230 (1990).

[41] F. P. Bowden, D. Tabor, The Friction and Lubrication of Solids, Oxford University Press, Oxford (1950).

[42] I. M. Hutchings, Tribology: Friction and Wear of Engineering Materials, Edward Arnold, London (1992).

[43] J. L. Ortiz-Merino, R. I. Todd, Relationship between Wear rate, Surface Pullout and Microstructure during Abrasive Wear of Alumina and Alumina/SiC Nanocomposites, Acta Materialia, 53, 3345-3357 (2005).

[44] H. Kara, S. Roberts, Polishing Behavior and Surface Quality of Alumina and Alumina/Silicon Carbide Nanocomposites, Journal of the American Ceramic Society, 83, 1219–1225 (2000).

[45] C. N. Walker, C. E. Borsa, R. I. Todd, R. W. Davidge, R. J. Brook, Fabrication, Characterization and Properties of Alumina Matrix Nanocomposites, British Ceramic Proccedings, 53, 249-264 (1994).

[46] J. Rodr ́guez, A. Mart ́n, J. Y. Pastor, J. LLorca, J. F. Bartolom ́, J. S. Moya, Sliding Wear of Alumina/Silicon Carbide Nanocomposites, Journal of the American Ceramic Society, 82, 2252-2254 (1999).

[47] H. J. Chen, W. M. Rainforth, W. E. Lee, The Wear Behaviour of $A1_2O_3$-SiC Ceramic Nanocomposites, Scripta Materilia, 42, 555-560 (2000).

[48] H. Wu, S. G. Roberts, B. Derby, Residual Stress and Sub-Surface Damage in Machined Alumina and Alumina/Silicon Carbide Nanocomposites Ceramics, Acta Materialia, 49, 507-517 (2001).

[49] A. Limpichaipanit, R. I. Todd, The Relationship between Microstructure, Fracture and Abrasive Wear in Al_2O_3/SiC Nanocomposites and Microcomposites Containing 5 and 10% SiC, Journal of the European Ceramic Society, 29, 2841-2848 (2009).

[50] A. Mukhopadhyay, R. I. Todd, Relationship between Microstructure and Abrasive Wear Resistance of Al_2O_3-$FeAl_2O_4$ Nanocomposites Produced via Solid State Precipitation, Journal of the European Ceramic Society, 31, 339-350 (2011).

[51] G. de Portu, L. Micele, G. Pezzotti, Laminated Ceramic Structures from Oxide Systems, Composites: Part B, 37, 556-567 (2006).

[52] C. E. J. Dancer, M. Achintha, C. J. Salter, J. A. Fernie, R. I. Todd, Functionally Graded Alumina-Silicon Carbide Components, Scripta Materialia, 67, 281-284 (2012).

[53] C. E. J. Dancer, N. A. Yahya, T. Berndt, R. I. Todd, G. de Portu, Effect of Residual Compressive Surface Stress on Severe Wear of Alumina–Silicon Carbide Two-Layered Composites, Tribology International, 74, 87–92 (2014).

[54] A. Mukhopadhyay, B. Basu, Consolidation-Microstructure-Property Relationships in Bulk Nanocomposites and Ceramic Nanocomposites: a Review, International Materials Review, 52, 257-288 (2007).

[55] M. Sternitzke, Review: Structural Ceramics Nanocomposites, Journal of the European Ceramic Society, 17, 1061-1082 (1997).

[56] D. J. Chen, M. J. Mayo, Densification and Grain Growth of Ultrafine 3 mol% Y_2O_3-ZrO_2 Ceramics, Nanostructural Materials, 2, 469-478 (1993).

[57] D. Galusek, J. Sedlacek, P. Svancarek, R. Riedel, R. Satet, M. Hoffmann, The Influence of Post-sintering HIP on the Microstructure, Hardness, and Indentation Fracture Toughness of Polymer-derived Al_2O_3–SiC nanocomposites, Journal of the European Ceramic Society, 27, 1237–1245 (2007).

[58] S. H. Risbud, C. H. Shan, A. K. Mukherjee, M. J. Kim, J. S. Bow, R. A. Holl, Retention of Nanostructure in Aluminum Oxide by Very Rapid Sintering at 1150 ℃, Journal of Material Research, 10, 237–239 (1995).

[59] R. S. Mishra, A. K. Mukherjee, K. Yamazaki, K. Shoda, Effect of TiO_2 Doping on Rapid Densification of Alumina by Plasma Activated Sintering, Journal of Material Research, 11, 1144–1148 (1996).

[60] R. S. Dobedoe, G. D. West, M. H. Lewis, Spark Plasma Sintering of Ceramics: Understanding Temperature Distribution Enables More Realistic Comparison with Conventional Processing, Advances in Applied Ceramics, 104, 110-116 (2005).

[61] A. M. Thompson, H. M. Chan, M. P. Harmer, R. E. Cook, Crack Healing and

Stress Relaxation in Al_2O_3-SiC Nanocomposites, Journal of the American Ceramic Society, 78, 567-571 (1995).

[62] R. S. Mishra, J. A. Schneider, J. F. Shackelford, A.K. Mukherjee, Plasma Activated Sintering of Nanocrystalline γ-Al_2O_3, Nanostructured Materials, 5, 525–544 (1995).

[63] S.K.C. Pillai, B. Baron, M. J. Pomeroy, S. Hampshire, Effect of Oxide Dopants on Densification, Microstructure and Mechanical Properties of Alumina-Silicon Carbide Nanocomposite Ceramics Prepared by Pressureless Sintering, Journal of the European Ceramic Society, 24, 3317-3326 (2004).

[64] A. M. Cock, I. P. Shapiro, R. I. Todd, S. G. Roberts, Effects of Yttrium on the Sintering and Microstructure of Alumina-Silicon Carbide Nanocomposites, Journal of the American Ceramic Society, 88, 2354-2361 (2005).

[65] A. Mukhopadhyay, R. I. Todd, Effect of Yttria Doping on the Microstructure and Mechanical Properties of Al_2O_3-$FeAl_2O_4$ Nanocomposites Developed via Solid State Precipitation, Journal of the European Ceramic Society, 30, 2905-2915 (2010)

[66] D. S. Phillips, A. H. Heuer, T. E. Mitchell, Precipitation in Star Sapphire: I. Identification of the Precipitate, Philosophical Magazine A, 42, 385-404 (1980).

[67] S. E. Hsu, W. Kobes, M. E. Fine, Strengthening of Sapphire by Precipitates Containing Titanium, Journal of the American Ceramic Society, 50, 149–151 (1967).

[68] R. A. Langensiepen, R. E. Tressler, P. R. Howell, A Preliminary Study of Precipitation in Ti^{4+}-Doped Polycrystalline Alumina, Journal of Materials Science, 18, 2771-2776 (1983).

[69] Y. Wang, T. Fujimoto, H. Maruyama, K. Koga, Precipitation of Magnesium Aluminum Spinel from Alumina-Matrix Solid Solution: I. Fundamental Concept and

Precipitation Behavior, Journal of the American Ceramic Society, 83, 933–936 (2000).

[70] J. Gurt Santanach, C. Estournès, A. Weibel, A. Peigney, G. Chevallier, C. Laurent, Spark Plasma Sintering as a Reactive Sintering Tool for the Preparation of Surface-Tailored Fe–$FeAl_2O_4$–Al2O3 Nanocomposites, Scripta Materialia, 60, 195-198 (2009).

[71] J. Gurt Santanach, C. Estournès, A. Weibel, A. Peigney, G. Chevallier, Ch. Laurent, Mechanical and Tribological Properties of Fe/Cr-$FeAl_2O_4$-Al_2O_3 nano/micro Hybrid Composites prepared by Spark Plasma Sintering, Scripta Materialia, 64, 777-780 (2011).

[72]V. Raghavan, Al-Fe-O (Aluminum-Iron-Oxygen), Journal of Phase Equilibria and iffusion, 31, 367-367(2010).

[73] R. H. Doremus, Diffusion in alumina, Journal of Applied Physics, 100, 101-301 (2006);

[74] R. M. Roberts, T. S. Elleman, H. Palmour, K. Verghese, Hydrogen Permeability of Sintered Aluminium Oxide, Journal of the American Ceramic Society, 62, 495-499 (1979).

[75] F.M. Ernsberger, Proton Transport in Solids, Journal of Non-Crystalline Solids, 38, 557-561 (1980).

[76] M. O. Dauies, Nasa Technical Notes: Transport Phenomena in Aluminum Oxide, Lewis Research Center, Cleveland (1965).

[77] E. Serra, A. Calza Bini, G. Cosoli, L. Pilloni, Hydrogen Permeation Measurements on Alumina, Journal of the American Ceramic Society, 88, 15-18 (2005).

[78] D. R. Begeal, Hydrogen and Deuterium Permeation in Copper Alloys, Copper-Gold Brazing Alloys, Gold, and the In Situ Growth of Stable Oxide Permeation Barriers, Journal of Vacuum Science and Technology, 15, 1146-1154 (1978).

[79] K. H. Hauffe, S. R. Morrison, S. A. Jansson, Z. A. Foroulis, High Temperature Gas-Metal Reactions in Mixed Environment, The Metallurgical Society of American Institute of Mining, Metallurgical, and Petroleum Engineers, Boston (1973).

[80] D. J. Reed, B. J. Wuensch, Ion-Probe Measurement of Oxygen Self-Diffusion in Single-Crystal Al_2O_3, Journal of the American Ceramic Society, 63, 88-92(1980).

[81] K. P. R. Reddy, A. R. Cooper, Oxygen Diffusion in Sapphire, Journal of the American Ceramic Society, 65, 634–638 (1982).

[82] J. D. Cawley, J. W. Halloran, A. R. Cooper, Oxygen Tracer Diffusion in Single-Crystal Alumina, Journal of the American Ceramic Society, 74, 2086–2092 (1991).

[83] K. P. D. Lagerlof, T. E. Mitchell, A. H. Heuer, Lattice Diffusion Kinetics in Undoped and Impurity-Doped Sapphire (α-Al_2O_3): a Dislocation Loop Annealing Study, Journal of the American Ceramic Society, 72, 2159–2171 (1989).

[84] Y. Oishi, K. Ando, N. Suga, W. D. Kingery, Effect of Surface Condition on Oxygen Self-Diffusion Coefficients for Single-Crystal Al_2O_3, Journal of the American Ceramic Society, 66, C130–C131 (1983).

[85] D. Prot, M. L. Gall, B. Lesage, A. M. Huntz, C. Monty, Self-diffusion in α-Al_2O_3: IV. Oxygen Grain-Boundary Self-diffusion in Undoped and Yttria-Doped Alumina Polycrystals, Philosophical Magazine A, 73, 935-949 (1996).

[86] V. S. Stubican, J. W. Osenbach, Influence of Anisotropy and Doping on Grain Boundary Diffusion in Oxide Systems, Solid State Ionics, 12, 375-381 (1984).

[87] Y. Oishi, W. D. Kingery, Intrinsic Oxygen Diffusion, Journal of Chemical Physics, 33, 480-480 (1960).

[88] A. E. Paladino, W. D. Kingery, Aluminum-Ion Diffusion in Aluminum Oxide, Journal of Chemical Physics, 37, 957–962 (1962).

[89] A. E. Paladino, R. L. Coble, Effect of Grain Boundaries on Diffusion-Controlled Processes in Aluminum Oxide, Journal of the American Ceramic Society, 46, 133-136 (1963).

[90] M. LeGall, A. M. Huntz, B. Lesage, C. Monty, Self-diffusion in Al_2O_3: I. Aluminum Diffusion in Single Crystals, Philosophical Magazine A, 70, 761-761 (1994).

[91] V. I. Izbekov, K. M. Gorbunova, Investigation of Iron Diffusion in Corundum and Rutile by Means of the 'Fe Indicator, The Physics of Metals and Metallography, 7, 71–77 (1959).

[92] I. K. Lloyd, H. K. Bowen, Iron Tracer Diffusion in Aluminum Oxide, Journal of the American Ceramic Society, 64, 744–747(1981) .

[93] B. Lesage, A. M. Huntz, G. Petot-ervas, Transport Phenomena in Undoped and Chromium-or Yttrium-Doped alumina, Radiation Effects and Defects in Solids, 75, 283–299 (1983).

[94] B. Lesage, A. M. Huntz, Diffusion du Chrome et du Fer Dans L'alumine α Monocristalline, Scripta Metallurgica, 14, 1143-1146 (1980).

[95] K. Heldt, G. Haase, Der Elektrische Widerstand von Reinem Hochvakuumgesintertem Aluminiumoxyd, Zeitschrift für angewandte Mathematik und Physik, 6, 157-160 (1954).

[96] J. Pappis, W. D. Kingery, Electrical Properties of Single-Crystal and Polycrystalline Alumina at High Temperatures, Journal of the American Ceramic Society, 44, 459-464 (1961).

[97] H. Schmalzried, Ionen und Elektronenleitung in binären Oxiden und ihre Untersuchung mittels EMK-Messungen, Max-Planck-Institut für physikalische Chemie, 38, 87–102 (1963).

Chapter 3 Experimental Details

3.1 Synthesis of Al_2O_3-Fe_2O_3 Powders

45g high purity (around 99.995%), fine (particle size around 200 nm) α-Al_2O_3 powders (AKP-50,Sumitomo, Japan) were mixed with 25.25g $Fe(NO_3)_3$ $9H_2O$ (purity >98%, Sigma Aldrich, UK) in ethanol to form slurries. The weight ratio of powder to ethanol was 1 to 3. Instead of adding Fe_2O_3 directly, $Fe(NO_3)_3$ $9H_2O$ was used due to its high solubility in ethanol, which could enhance the homogenization of the target solid solution. The $Fe(NO_3)_3$ solutions contained the requisite amount of the salt that would result in doping levels corresponding to Al_2O_3-10wt% Fe_2O_3 as the final solid solution. In order to prevent abnormal grain growth during sintering and to achieve near theoretical densification, 250ppm MgO powders (99.95%; 120nm, UBE, Japan) was added to the slurries. 0ppm and 2500ppm of MgO were also added to some of the slurries to study the effect MgO dopant level. 847.8ppm Y_2O_3 was also added to the slurry in the form of $Y(NO_3)_3$ $9H_2O$, in order to minimise precipitation of intergranular particles and maximise intragranular particle precipitation.[1] Both $Fe(NO_3)_3$ $9H_2O$ and $Y(NO_3)_3$ $9H_2O$ are soluble in ethanol. The slurry was dispersed using an ultrasonic probe (Kerry, UK) for 15 minutes to enhance homogenization, and then ball milled on a ball milling machine (Pascall Engineering, UK) for 24 hours in bottles made of polyethylene, using high purity (99.99%) alumina balls. After ball milling the slurries were dried in a rotatory evaporator (VWR, UK) at a temperature of 60 ℃ in vacuum.

After drying in the rotatory evaporator, the powders were in a wet ‘mud’ form. This is at least partially because of the crystallised water in $Fe(NO_3)_3$ $9H_2O$. The rotatory evaporator could remove ethanol at 60 ℃, but could not remove water completely. The ‘mud’ was placed in an oven (RHF1600, Carbonite Furnaces, UK) at a temperature of 100 ℃ for 1 hour to dry off completely, and then ground strongly using an alumina mortar and pestle (Sigma-Aldrich,

UK). However, the dried mud was too hard to be ground to a fine powder in this way. Due to the high surface tension of residual water, small particles can be drawn strongly together (Figure 3.1) when water was evaporated in the oven at temperature of 100 °C, which results in the fact that aggregations can hardly be broken.

The dried and ground 'mud' was then heated in an oven (RHF1600, Carbonite Furnaces, UK) at 10 ℃/min up to 600°C and held there for 1.5 hour to decompose the ferric nitrate to Fe_2O_3 completely (also known as calcination). The calcination temperature and times were decided from TGA/DSC tests (Figure 3.2). It can be seen from Figure 3.2 that above 500°C there is almost no weight change. Therefore, all the iron nitrates had decomposed into Fe_2O_3 when the temperatures were above 500°C. In order to break the hard aggregations resulting directly from the rotatory evaporation step and obtain finer Al_2O_3-10wt% Fe_2O_3 solid solution powders, the calcined 'mud' was mixed with ethanol again and ball milled for 24 hours in bottles made of polyethylene on the same ball milling machine, using high purity (99.99%) alumina balls. After ball milling, the slurry was dried completely by the same rotatory evaporator again. The dried powders were then gently ground using an alumina mortar and pestle and passed through a 150 um sieve.

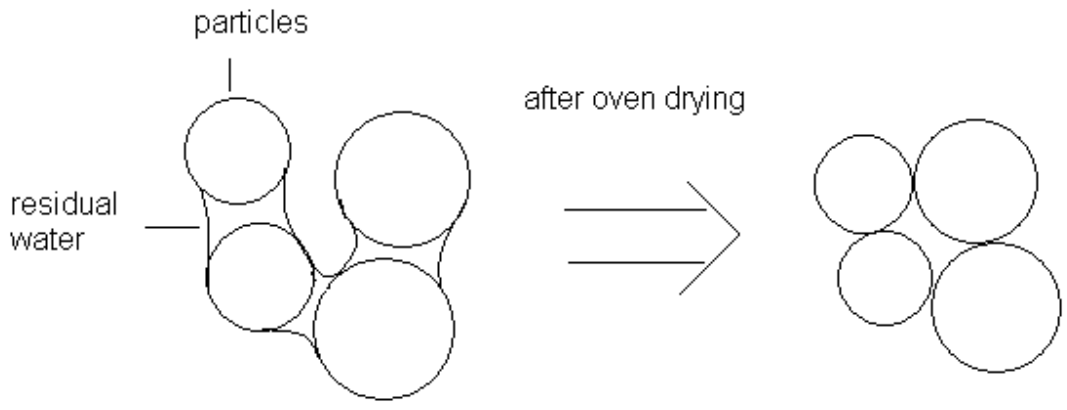

Figure 3.1 Schematic presentation of particles before and after oven drying.

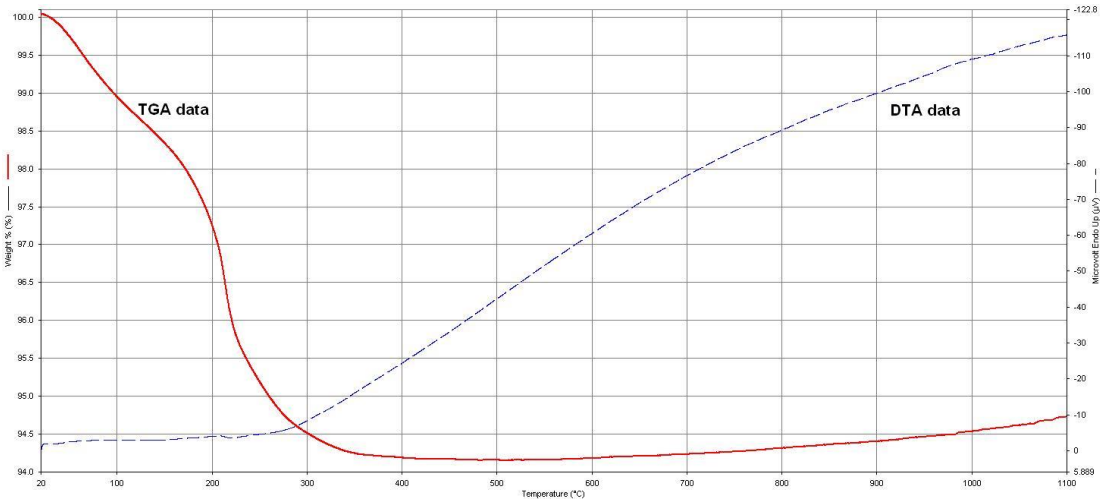

Figure 3.2 TGA results from 20 ˚C to 1100 ˚C for as-dried powder.

3.2 Sintering and aging treatment

Green compact making involved two steps. Firstly, powders were pressed into 32 mm discs at 56MPa by uniaxial cold pressing. Secondly, the discs were double sealed in plastic bags, and further pressed at 150 MPa by cold isostatic pressing.

Green compacts were sintered pressurelessly in air inside an alumina tube furnace (Lenton, UK) at 1450˚C for 5 hours. Both heating rate and cooling rate were 10 ℃/min. The as-sintered pellets were around 28 mm in diameter, with thickness varying from 0.8 mm to 4 mm. Pellets with varying thickness were produced in order to study the influence of dimensions on the diffusion kinetics. According to the Al_2O_3–Fe_2O_3 phase diagram, more than 10wt% (equals 6.61 mol%) Fe_2O_3 is soluble in Al_2O_3 at 1450 ˚C (Figure 2.16). The combination of sintering temperature and time were designed to achieve full dissolution and homogeneous distribution of Fe^{3+} in the cation sub-lattice of Al_2O_3 and near theoretical density.

The second step in the heat treatment scheme (aging treatment) was the generation of second phase particles during heat treatment of Al_2O_3–10wt% Fe_2O_3 solid solutions under different reducing/inert gas atmospheres (4% H_2/N_2, 1% H_2/N_2, 4% CO/N_2, pure argon) at different

temperatures (1250–1550°C) and for different durations up to 20 hours.

3.3 Sintered density characterization

The sintered densities of all sintered samples were measured using Archimedes' principle. Firstly, all samples were put in an oven at 150 °C for 2 hours to obtain a dry weight as m_{dry}. Secondly, all samples were immersed in boiling distilled water for 1 hour to fill any open pores. Thirdly, all samples were weighed as immersed in distilled water to be weighed as m_{wet}. Finally samples were dried with damp filter paper to remove surface water, and then weighed as m_{damp}. The relative density ρ, can be calculated as:

$$\rho = [\frac{m_{dry}}{m_{damp} - m_{wet}}] \times \rho_{H2O} \div \rho_t \times 100\% \quad (3.1)$$

Where ρ_{H2O} is the density of distilled water, and ρ_t is the theoretical density of sample. The relative density is expressed as a percentage of theoretical density. The theoretical density of 10wt% Al_2O_3–Fe_2O_3 solid solution was determined using XRD data by a previous study.[2]

3.4 Phase Evolution and Microstructure Characterization

The as-sintered/aged samples were cut along a diameter by a slow speed saw machine (Buehler, UK), and polished with 25, 9, 6, 3 and 1 micron diamond suspensions (Kermet, UK) in order to produce optically reflective ceramographic surfaces representative of the samples' cross section. Polishing of all samples was performed on Buehler Automet 300 (UK) or Logitech PM2 (UK) semi-automatic lapping and polishing machines. The phase identifications were performed by X-ray diffraction (XRD) in a θ-2θ diffractometer (Philips, Netherlands) at a collection rate of 2 °/min using Cu Kα radiation.

The polished as-sintered/as-aged samples were thermally etched in the original atmospheres at a temperature 50 ℃ below the heat treatment temperatures for 15 minutes to reveal the grain boundaries followed by cooling at 10 ℃/min. Carbon coatings were applied on the polished surfaces of thermally etched samples to make them conductive. The microstructures

of all the polished surfaces (including aged samples) were observed using a field emission scanning electron microscope (EOL JSM 840A, Japan) operated at 20 kV. SEM images were taken to estimate the grain size using the linear intercept method. The measured intercept lengths were multiplied by 1.56 to obtain equivalent spherical diameters. For each sample, the grain size was measured from over 200 grains obtained from more than 6 SEM pictures.

Back Scattered Electron (BSE) pictures were also taken on the cross-sections of polished aged samples at different distance from the surface in steps of 100 μm, i.e one picture per hundred μm. Based on the BSE images, volume fraction and particle size of iron spinel particles were determined based on area measurement using the ImageJ image processing software, as a function of distance from the surface. All particle size values were measured from over 100 particles, and volume fractions at each step were measured from areas of more than 0.04 mm^2. Elemental analysis was performed using EDS attached to the SEM.

Sample preparation for transmission electron microscope (TEM) observations involved mechanical thinning of 3 mm discs, followed by grinding and polishing of both sides on a Gantan dimple grinder. The final step in TEM sample preparation was ion-beam milling in the Gatan PIPS. Observations were performed using 200kV JEOL 2000FX, equipped with EDS systems.

3.5 Mechanical property characterization

3.5.1. Hardness

For evaluating the hardness (H_v) of the monolithic alumina, solid solution and the surface layers of aged samples, Vickers indentations (AVK-C1/C2, Mitutoyo, US) were obtained on the lightly polished surfaces with indentation loads (P) 5 kg and for loading times of 15s.

3.5.2. Four point bending tests

Flexural strengths were measured using rectangular cross-section beams tested in a four-point bending testing set on a universal testing machine (Dension-Mayes, UK). The configuration

of the test was shown in Figure 3.3. The as-cut samples were polished on both narrow long faces and one broad long face using 25, 9, 6, 3 and 1μm diamond slurries. The final specimen dimensions were around 13mm(l)×2.5mm(w)×2mm(t). The cross head loading rate was 5 N/min, and the inner and outer spans were 5.8 and 10mm respectively.

The flexural strength σ_f can be calculated using the following equation[3]:

$$\sigma_f = \frac{3 \times F_{max} \times a}{W \times t^2} \tag{3.2}$$

Where F_{max} is the maximum load detected by the machine, W is the beam width, t is the specimen thickness and a is as defined in Figure 3.3. The reported values are the average of at least 6 independent measurements.

The fracture surfaces of the broken samples were observed by SEM (JSM 840A and JSM 5510). Prior to SEM observations, the fractured samples were cleaned in an ultrasonic bath using acetone and then sputter coated with carbon.

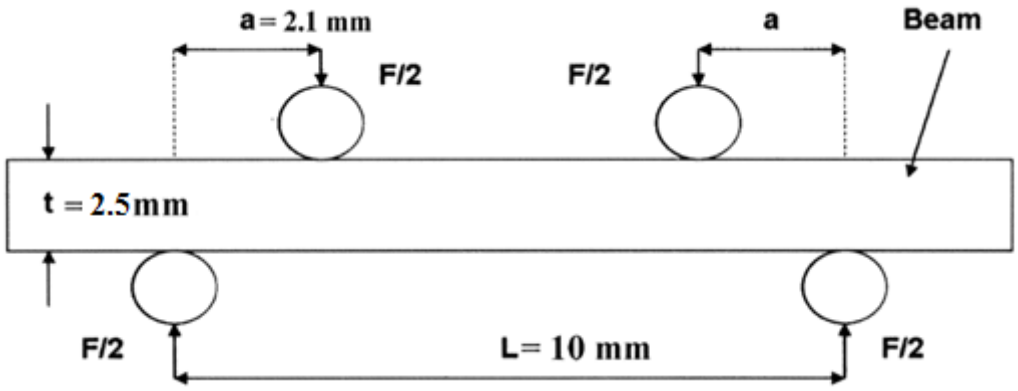

Figure 3.3 Schematic representation of the 4-point bending set up.[1]

3.5.3. Residual stress measurement

The different phase compositions of the surface layers from the bulk parts of the aged samples were thought to leave surface residual stress. A set of measurements were made to

investigate the residual stress distributions in the aged samples via a piezospectroscopic technique, which relates the R1 Cr^{3+} fluorescence peak position to the stress in the sample. The equipment utilized here was a 1000 series Renishaw Raman microscope (Renishaw, UK) with a 50 mW He-Ne laser. All measurements were taken with confocal settings using a 100x objective lens. Spectra were curve-fitted using the WiRE software package (version 3.2, Renishaw, UK) and average values of the R1 peak position were calculated for each sample.

A line scan was made through a polished cross section of the specimen (scan 1 in Figure 3.4). To provide a stress free reference, a second line scan was made on the bulk part of as-polished cross section with the two 'effective surface layers' on both sides removed (scan 2 in Figure 3.4). The two line scans are made on the same position in the bulk part. The shifts of R1 Cr^{3+} fluorescence peak position between two line scans were measured. A stress in these samples occurs due to the composition difference between the surface layer and the bulk part which causes a thermal expansion coefficient (TEC) difference between them.

The stresses along the lines scanned are approximately uniaxial since the experiments measured the stress on the cut, free surface of the specimen, and the stress normal to the plane of the 'sandwich structure' is expected to be small. Therefore, a relationship between the change in frequency of the R1 peak $\Delta\nu$ and the uniaxial stress in the bulk part σ_{b-uni} could be proposed in Equation 3.3[4]:

$$\sigma_{b-uni} = \frac{3}{\Pi_H}\Delta\nu \tag{3.3}$$

The hydrostatic piezospectroscopic coefficient Π_H is 7.59 $cm^{-1}GPa^{-1}$ for polycrystalline texture-free alumina. The 'effective surface layer' of samples aged in 4% H_2/N_2 mentioned in the residual stress measurement, is the layer where the Fe concentration is relatively low and experiences compressive residual stress, 'surface layer' in Chapter 4 means the layer where metallic intergranular Fe particles particles exists. Usually the thickness of 'effective surface layer' is higher than the thickness of surface layer, because some areas in the bulk part

mentioned in Chapter 4 contained relatively low second phase particles though there is no metallic particles, i.e. a relatively low Fe concentration and should experience compressive residual stress. The thickness of 'effective surface layer' and the corresponding bulk part could be measured from the SEM images.

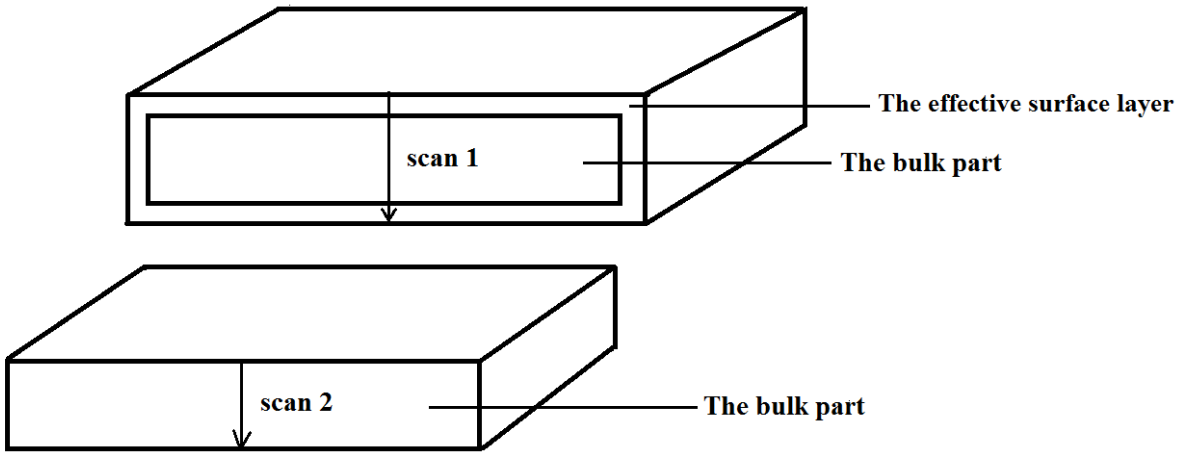

Figure 3.4 The geometry of the cross sections, the position and direction of the residual stress measurements.

3.5.4. Abrasive wear test

A micro-scale abrasive wear tester (TE 66, Phoenix Tribology, UK) was used to measure the wear resistance of all samples. The samples were loaded by a pre-conditioned chrome steel ball (25 mm in diameter) with a dead weight of 5 N. The supplied abrasive slurry consists of silicon carbide particles (4.3 μm, grade F1200, Washington Mills, UK) suspended in distilled water (concentration 0.35 g/cm^3) and doped with Dispex A40 dispersant. A magnetic stirring was used in the slurry supply to prevent particle sedimentation, and the slurry was dispersed drop-wise at a constant rate onto the surface of the rotating ball. The total sliding distance used in each test was 58.8 m (750 ball rotations) and the relative sliding speed was around 0.19 ms^{-1}. The tests were interrupted at every 125 ball rotations to record the wear diameters using an optical microscope attached to the wear tester. The final wear diameters were also examined after the test using scanning electron microscopy (JEOL JSM 840A).

The wear volume *V* was calculated using the following formula: [5]

$$V = \frac{\pi b^4}{64\,R} \tag{3.4}$$

where *b* is the crater diameter and *R* is the ball radius. This relationship assumes that the shape of the crater is conformal to the shape of the ball. The wear volume *V* is related to the sliding distance *S* and applied load *N* by the Archard wear law:

$$V = kSN \tag{3.5}$$

where *k* is the wear coefficient. A linear plot of *V* against *SN* can then be plotted from Equation 3.5, with gradient equal to the wear coefficient (*k*). The wear resistance *1/k* was then calculated. The worn surfaces were observed by SEM (JEOL JSM 840A). Prior to SEM observations, the worn samples were cleaned in ultrasonic bath using ethanol and then sputter coated with carbon. Similar to the estimations concerning the area fraction and sizes of the second phase particles from BSE-SEM images, the area fractions and sizes of pull-outs caused by brittle fracture on the worn surfaces were measured using software ImageJ.[6]

3.5.5. Indentation polish tests

Vickers Indentations were obtained using 5kg (49N) load on the polished surfaces of monolithic alumina, solid solution and selected aged samples. The indented surfaces were then polished with 1μm diamond slurry (Kemet, UK) using the automated grinding polishing machine (Buehler Automet 300, UK) until only the very tip of the original indentation. SEM (JEOL JSM 840A) was used to observe the details of the polished indentation.

Reference

[1] A. Mukhopadhyay, Fabrication and Properties of Oxide Nanocomposites Containing Uniformly Dispersed Second Phase, DPhil Thesis, Oxford University, UK (2010).

[2] T. Butler, In situ Ceramic Nanocomposites by Solid State Precipitation, MSc thesis, Oxford University, UK (2011).

[3] J. B. Wachtman, W. R. Cannon, M. J. Matthewson, Mechanical Properties of Ceramics, John Wiley & Sons, New York (2009).

[4] J. He, David, R. Clarke, Determination of The Piezospectroscopic Coefficients for Chromium Doped Sapphire, Journal of the American Ceramic Society, 78, 1347-1353 (1995).

[5] K. L. Rutherford, I. M. Hutchings, Theory and Application of a Micro-scale Abrasive Wear Test, Journal of Testing and Evaluation, 25, 259-269 (1997).

[6] J. L. Ortiz-Merino, R. I. Todd, Relationship between Wear Rate, Surface Pullout and Microstructure during Abrasive Wear of Alumina and Alumina/SiC Nanocomposites, Acta Materialia, 53, 3345–3357 (2005).

Chapter 4 Thermodynamics, Diffusion kinetics and Mechanisms responsible for the Precipitation

4.1 Introduction

This chapter firstly describes the results of how varying processing parameters influence the specimen microstructures after aging. The results indicate that the second phase precipitation is diffusion controlled. In the discussion section, the thermodynamics of reduction reactions involved during aging treatment are firstly discussed. The diffusions and mechanisms involved during the aging are then discussed. Based on the discussion above, a model named PRCS corresponding to microstructural development during aging is proposed. Finally, PRCS is applied to interpret the results of microstructural developments under different processing conditions.

The sample identification used in this chapter is explained as follows. There are four symbols in the identification, the first symbol implies the composition, the second symbol implies aging temperature, and the last symbol implies the aging time. For examples, H1-1550-20 means sample aged in atmosphere 1% H_2/N_2 at 1550˚C for 20 hours (Table 4.1).

Table 4.1 Symbol identification for atmospheres

Atmosphere	4% H_2/N_2	1% H_2/N_2	4% CO/N_2	Argon
Symbol	H4	H1	CO	Ar

4.2 Results

4.2.1. Phase Evolution

By the means of X-ray diffraction, the phase evolution through the whole processing schedule, including calcination, solution treatment and aging was revealed. A few selected XRD patterns, recorded with as sintered monolithic alumina, un/as-calcined Al_2O_3-Fe_2O_3 powders, sintered solid solution, and samples aged at 1450 ℃ for different durations are compared in Figure 4.1. It should be mentioned that all XRD patterns corresponding to the as sintered and aged samples, were obtained from cut and polished cross-section surfaces.

Pattern 1 shows the XRD pattern of monolithic alumina. Pattern 2 in response to solid solution powders before calcination, only shows the peaks of alumina since $Fe(NO_3)_3$ is amorphous. Pattern 3 revealed that after calcination at 600 ℃ for 1 hour, the $Fe(NO_3)_3$ precursor has decomposed to α-Fe_2O_3, thus the powder contains both α-Al_2O_3 and α-Fe_2O_3 XRD peaks. After being pressed into pellets and solid solution treatment, the peaks corresponding to α-Fe_2O_3 disappeared, and only peaks of α-Al_2O_3 can be detected, which means the specimen is fully Al_2O_3-Fe_2O_3 solid solution (Pattern 4). Both pattern 5 and pattern 6 show the existence of $FeAl_2O_4$ after aging treatment, but the intensities of $FeAl_2O_4$ are not very high since only 10wt% Fe_2O_3 was incorporated in the solid solution. The XRD results show that aging of Al_2O_3-Fe_2O_3 solid solution under 4%H_2/N_2 leads to the precipitation of $FeAl_2O_4$ as the product from reduction reactions.

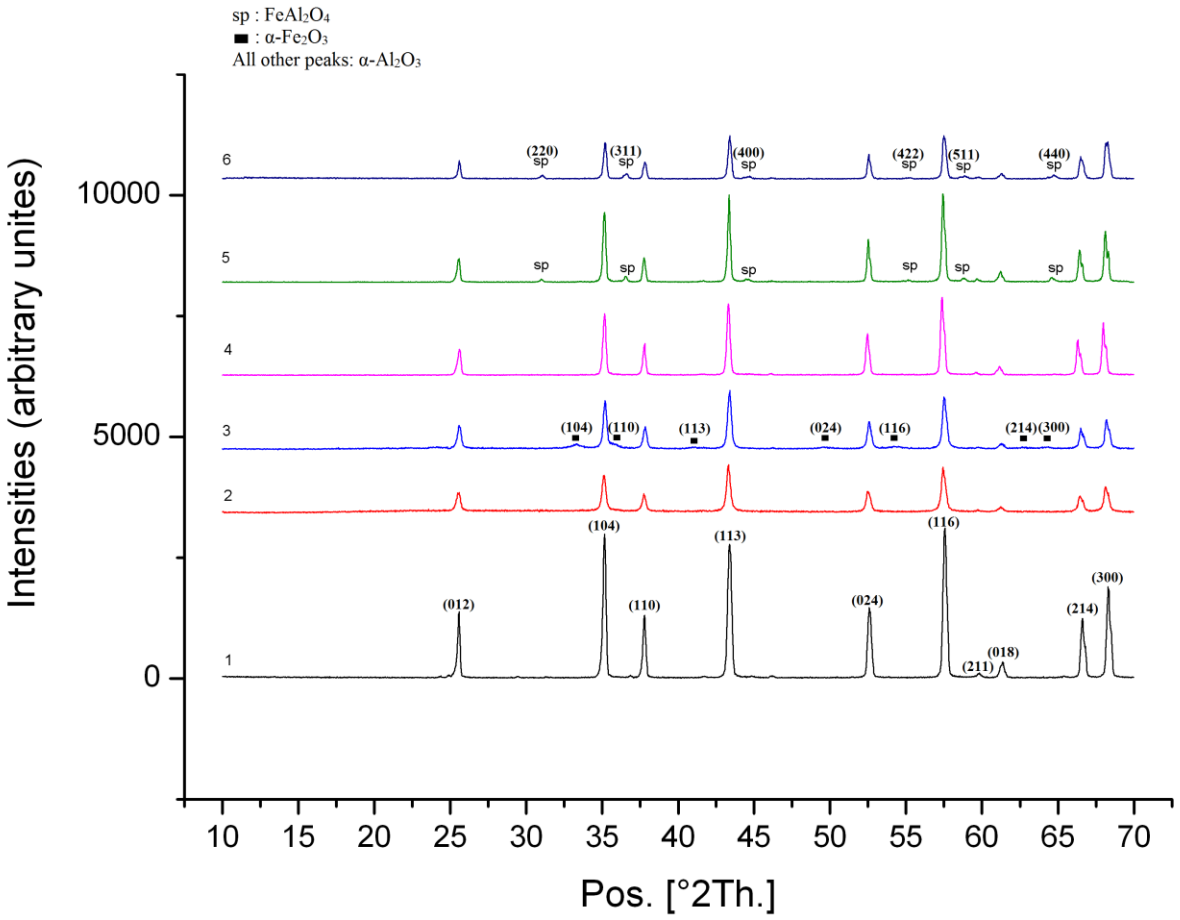

Figure 4.1 X-ray diffraction patterns recorded with ground and polished surfaces of various samples: (1) monolithic alumina; (2) solid solution powder before calcining; (3) solid solution powder after calcining; (4) as sintered solid solution; (5) sample H4-1450-20; (6) sample H4-1450-10.

4.2.2. As sintered microstructures

Density measurements showed that the sintered density of monolithic alumina was around 99.1% of the theoretical full density (3.98 g/cm^3) [1], while the sintered density of 10 wt% Fe_2O_3-Al_2O_3 solid solution was about 98.5% of theoretical full density (4.078g/cm^3) [2]. Figure 4.2 shows the microstructures of different as sintered samples. Figure 4.2(a) shows the microstructure of monolithic alumina, which mainly exhibits an equiaxed grain shape. Figure 4.2b shows some residual porosity in the solid solution and the most pores sit along grain boundary, indicating that pore-boundary separation did not happen during sintering. Although 0.025 wt% MgO was added to ease the problem, abnormal grain growth still

occurred, as a few elongated grains were 10 micron in size, while the average grain size of most grains was only around 2.7 μm. Grains in the solid solution samples are not equiaxed compared with that in the monolithic alumina, at least some of them are anisotropic grains, i.e. a bimodal microstructure.

Figure 4.2(c) shows the existence of small amount of particles along grain boundaries in some regions of the solid solution. EDX results (Table 4.2) showed that besides elements of Al, Fe and O, those particles contain Si and Ca elements, both of which may come from the impurities during processing. Besides those 'impurity particles', there is no evidence of any other secondary phase detected on the BSE images of the as-sintered Al_2O_3- Fe_2O_3 samples. The absence of significant amounts of secondary phase either along the matrix grain boundaries or within the matrix grains was confirmed with TEM investigation (Figure 4.2(d)). Along with XRD results, these observations indicate that most Fe_2O_3 has been dissolved into the solid solution. Such results are in agreement with preceding published work.[3]

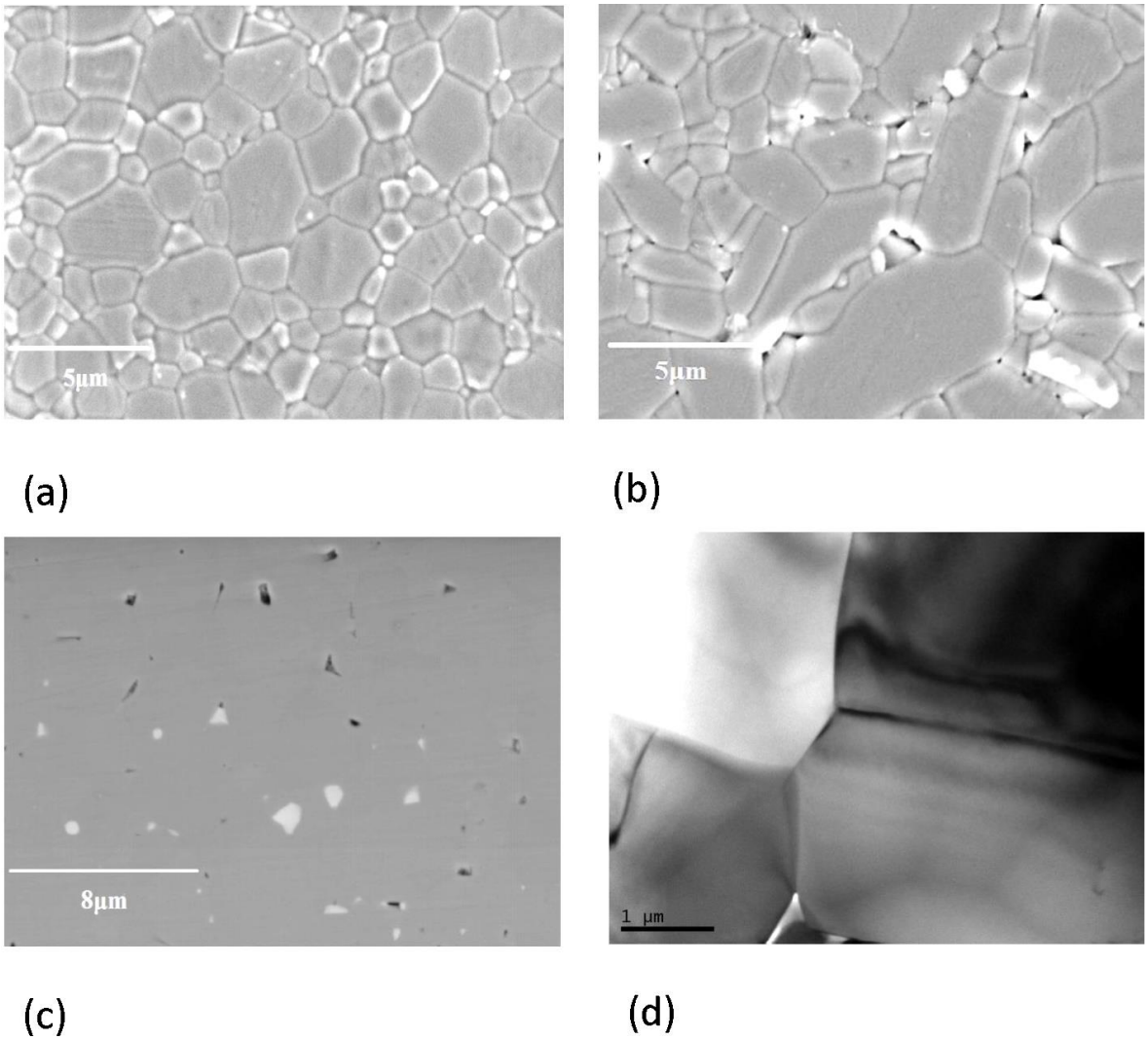

Figure 4.2 SEM-SEI image of thermally etched surfaces of (a) as sintered monolithic alumina; (b), SEM-BSE images for (c) as sintered solid solution; (d) Bright field TEM image corresponding to as sintered solid solution, confirming the absence of significant amount of secondary phase along the matrix grain boundaries or within the grains.

Table 4.2 EDX results corresponding to the white particles in Figure 2(c)

Site	Form (%)	O	Al	Fe	Ca	Si
white particles in Figure 4.**2**(c)	Weight	36.0 ±2.2	44.3 ±3.1	1.19 ±0.6	6.30 ±1.5	12.30 ±0.9

4.2.3. Microstructure development on aging

4.2.3.1. Microstructure pattern

Figure 4.3(a) presents a general microstructure pattern for most aged samples, in which microstructures consist of two parts: a surface layer and a bulk part. The surface layer (Figure 4.3(b)), which is directly in contact with the atmosphere, had higher porosity than the bulk part (Figure 4.3(c-f)).

The chemical compositions of the micro-sized second phase particles produced during aging treatment were identified by EDX analysis. The results (Figure 4.3 and Table 4.3) showed that the chemical composition of bright particles in the aged materials are different from the chemical composition of grey particles. The grey particles were usually surrounded by dark areas (marked as 4 in Figure 4.3(d)). EDX results revealed that the light regions usually contain a considerable amount of iron but lower than the 7 wt% of solid solution, while the dark regions barely contain any Fe atom (referred as 'iron free zone').(Table 4.3) Mukhopadhyay and Todd's study using TEM analysis[3] on the same composites has demonstrated that the bright particles in Figure 4.3 are metallic Fe particles while the grey particles in Figure 4.3 are $FeAl_2O_4$ particles. The metallic iron phase was not found in the XRD patterns because the concentration of metallic Fe in the cut and polished cross-sections of aged samples is too low to detect.

Very fine particles (noted in the white circle in Figure 4.3(b)) were found in the surface layers of all samples aged in 4% H_2/N_2, which were confirmed as intragranular Fe nanoparticles (bright particles) and intragranular $FeAl_2O_4$ nanoparticles (dark particles) by Mukhopadhyay and Todd using TEM analysis on the same composites[3]. It was found that in the bulk parts of samples aged in 4% H_2/N_2, areas within a critical distance from the surface layer/bulk part interface contained both intergranular particles and intragranular nanoparticles (Figure 4.3(f)), while the areas with distance larger than the critical distance contained only

intergranular micro-size $FeAl_2O_4$ particles (Figure 4.3(e)). Such critical distance was referred as P_{crit}. For clarification, two more definitions are made here (Figure 4.4): P_{surf} refers to the thickness of surface layer, P_{nano} refers to the depth to which the intragranular nanoparticles can be found (in some samples intragranular nanoparticles exist not only in the surface layer but also in the bulk part of the samples). It can be deduced that $P_{nano}= P_{surf} +P_{crit}$. Both P_{nano} and P_{surf} varied in different aged samples. The measurements of P_{surf} and P_{nano} were both made on BSE-SEM images such as Figure 4.3(b,e-f). It is difficult to give an accurate estimation of volume fraction and particle size of the nanoparticles due to their low concentration, inhomogeneous distribution and small sizes. However, the intragranular particles on BSE-SEM images such as Figure 4.3(b,f) have been confirmed as nano-size $FeAl_2O_4$ and Fe particles by previous work[3], thus it is credible to measure P_{nano} on BSE-SEM images such as Figure 4.3(b,f).

It was found that the microstructures of surface layers of samples aged in different atmospheres were different. Samples aged under 4% H_2/N_2 and a few samples aged in 1% H_2/N_2 contained intragranular and intergranular Fe particles, intragranular and intergranular $FeAl_2O_4$ particles, while the surface layers of most samples aged in 1% H_2/N_2 and all samples aged in the 4% CO/N_2 and argon only contained intergranular $FeAl_2O_4$ particles or even no particles. Furthermore, it has been found that the chemical level of element Fe in the matrix of surface layers in all aged samples was much less than 7 wt% of the solid solution, indicating that most iron in the surface layer has either gone to the particles or evaporated.

The bulk parts of most samples aged under 4% H_2/N_2 contained both intragranular and intergranular $FeAl_2O_4$ particles. The bulk parts of samples aged in 1% H_2/N_2, 4% CO/N_2 and argon were similar: only contained intergranular $FeAl_2O_4$ particles without any intragranular $FeAl_2O_4$ particles. It should be noted that in all aged samples, the particle size of

intergranular $FeAl_2O_4$ particles in the bulk part is much larger than that of the surface layer, which is probably because of the evaporation.

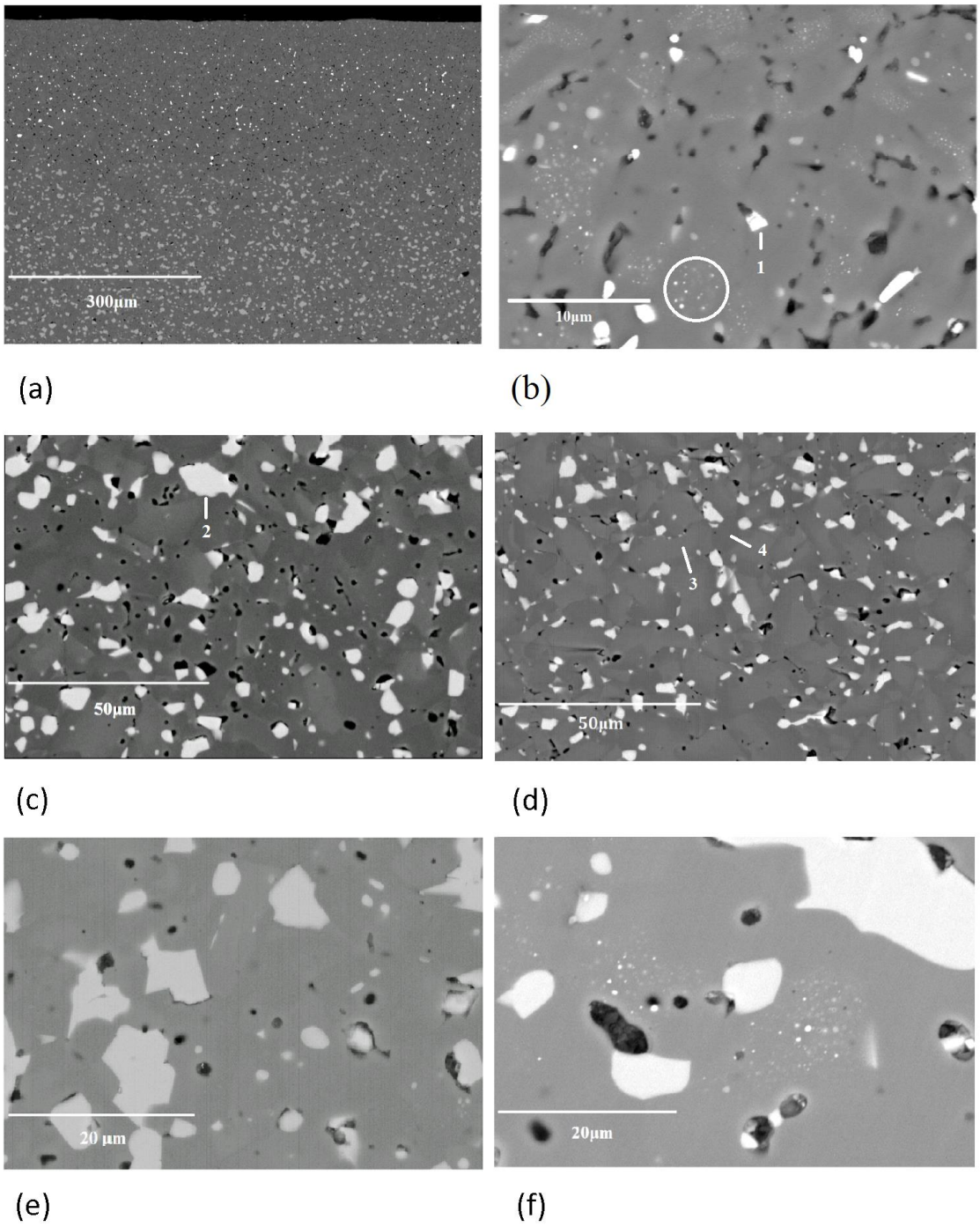

Figure 4.3 BSE images obtained from the polished surfaces (cross-section) of : (a) sample aged at 1450 ℃ for 20 hours; (b) 100 μm below the gas/solid interface, aged at 1450°C for 20 hours; (c) 400 μm below the gas/solid interface, aged at 1450 ℃ for 20 hours; (d) 400 μm below the gas/solid interface, aged at 1350 ℃ for 20 hours; (e) higher magnification picture of 400 μm below the gas/solid interface, aged at 1450°C for 20 hours; (f) 400 μm below the gas/solid interface, aged at 1550 ℃ for 20 hours.

Table 4.3 Examples of EDX results corresponding to the sites in Figure 4.3.

Spectrum	Form (%)	O	Al	Fe
Spectrum 1	Weight			100
Spectrum 2	Weight	31.25 ±2.5	32.96 ±2.7	35.37 ±4.0
Spectrum 3	Weight	39.46 ±2.5	54.46 ±3.9	6.02 ±1.5
Spectrum 4	Weight	42.22 ±3.6	56.32 ±4.6	1.46 ±0.5

Figure 4.4 Schematic presentation of definitions of P_{crit}, P_{surf} and P_{nano}. The grey region represents the surface layer, the dashed line represents the boundary between regions containing nanoparticles and regions containing no nanoparticles (the region above the dashed line are regions containing nanoparticles, the regions below the dashed line are regions containing no nanoparticles). It can be seen that the surface layer are usually included in the regions containing nanoparticles.

4.2.3.2. The effects of aging temperature

It can be seen that with elevated aging temperature/longer aging duration, both P_{surf} and P_{nano} increased (Table 4.4 and Table 4.5).There was no surface layer in samples aged at 1250 ˚C. Figure 4.5 gives the volume fraction profiles and particle size distributions of intergranular $FeAl_2O_4$ particles in samples aged for 20 hours in 4% H_2/N_2. Since the volume fraction of

intragranular nanoparticles are very low compared with that of intergranular particles in all samples and the nanoparticles are highly dispersed, both of which made the measurements of nanoparticles very difficult, the volume fraction of nanoparticles would not be measured in this project. The volume fraction profiles of sample H4-1250-20, H4-1350-20 and H4-1450-20 follow a similar pattern: as distance from the gas/solid interface increases, the volume fraction increases from zero and then reaches a peak, after which it gradually decreases. In sample H4-1550-20, however, the volume fraction profile kept almost constant after the peak point. It is very clear that with more elevated aging temperatures, the intergranular particle volume fraction was elevated.

Figure 4.5 (b) shows that the particle size generally increased as the aging temperature was elevated. In all samples, the particle size increases along with the distance from the gas/solid interface and then becomes almost constant after the peak point.

Table 4.4 Surface layer thickness (P_{surf}) of samples aged under 4% H_2/N_2 for different durations at different temperatures.

P_{surf},μm	0.5	5	10	20
H4-1350	20±4	60±7	140±12	180±16
H4-1450	70±6	160 ±11	205 ±15	220 ±16
H4-1550	80 ±8	240±18	325±20	400±29

Table 4.5 P_{nano} of samples aged under 4% H_2/N_2 for different durations at different temperatures.

P_{nano}, μm	0.5	5	10	20
H4-1350	20±4	60±7	160±11	205±13
H4-1450	80±7	180±15	235±20	260±18
H4-1550	100±8	350±25	600±30	1250

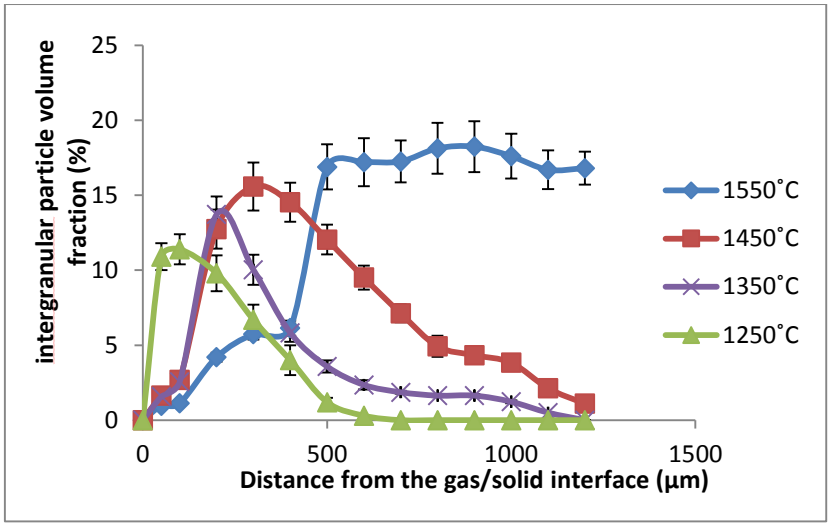

(a)

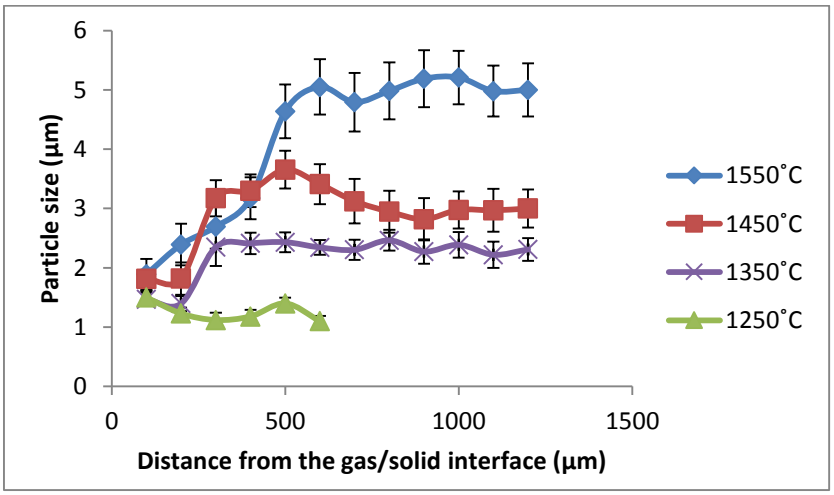

(b)

Figure 4.5 (a) Intergranular spinel particle volume fraction profiles of samples aged at different temperatures for 20 hours (b) Particle size distribution of intergranular spinel particles in samples aged at different temperatures for 20 hours. The samples here are all 2.5 mm thick.

4.2.3.3. The effects of aging duration

Table 4.4 and Table 4.5 show that both the surface layer thickness and P_{nano} increasd significantly from 0.5 hours to 5 hours respectively, but did't not change significantly after 5 hours.

Figure 4.6(a) shows that with increased aging durations, the $FeAl_2O_4$ volume fractions of samples aged at 1450 ℃ under 4% H_2/N_2 increased with longer aging durations. However, the peak volume fraction kept almost constant after 5 hours. In all samples, the particle size increased along with the distance from the gas/solid interface and then kept constant or gradually decreased after a peak point. Generally, the particle size increased with longer aging durations, but just increased slightly after 5 hours (Figure 4.6 and Figure 4.7).

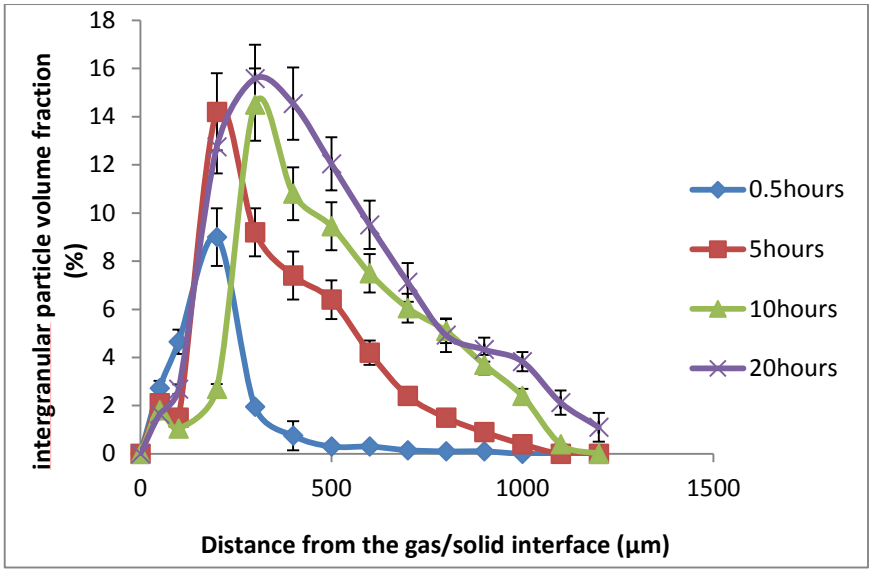

(a)

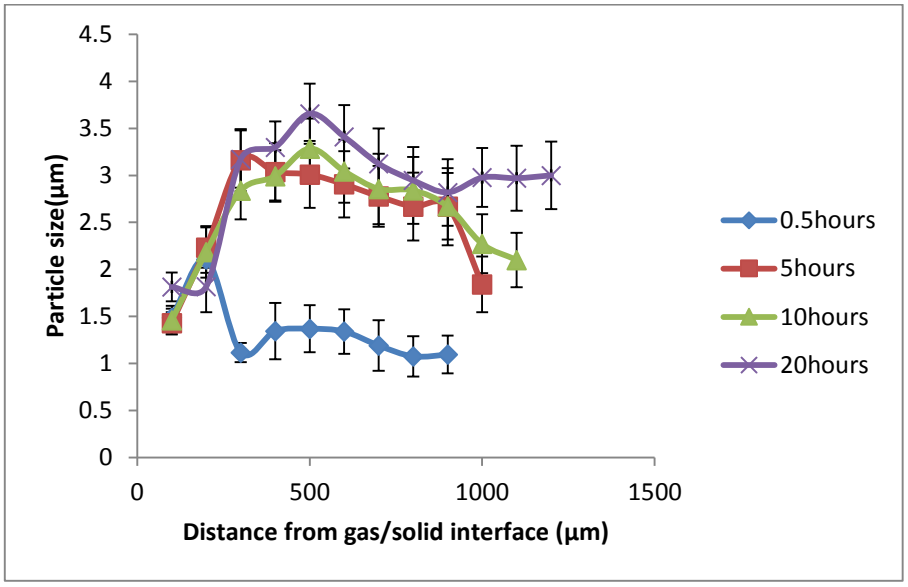

(b)

Figure 4.6(a) Intergranular spinel particle volume fraction profiles of samples aged under 4% H_2/N_2 atmosphere at 1450 ˚C for different aging times (b) Particle size distribution for samples aged at 1450 ˚C for different durations. The samples here are all 2.5 mm.

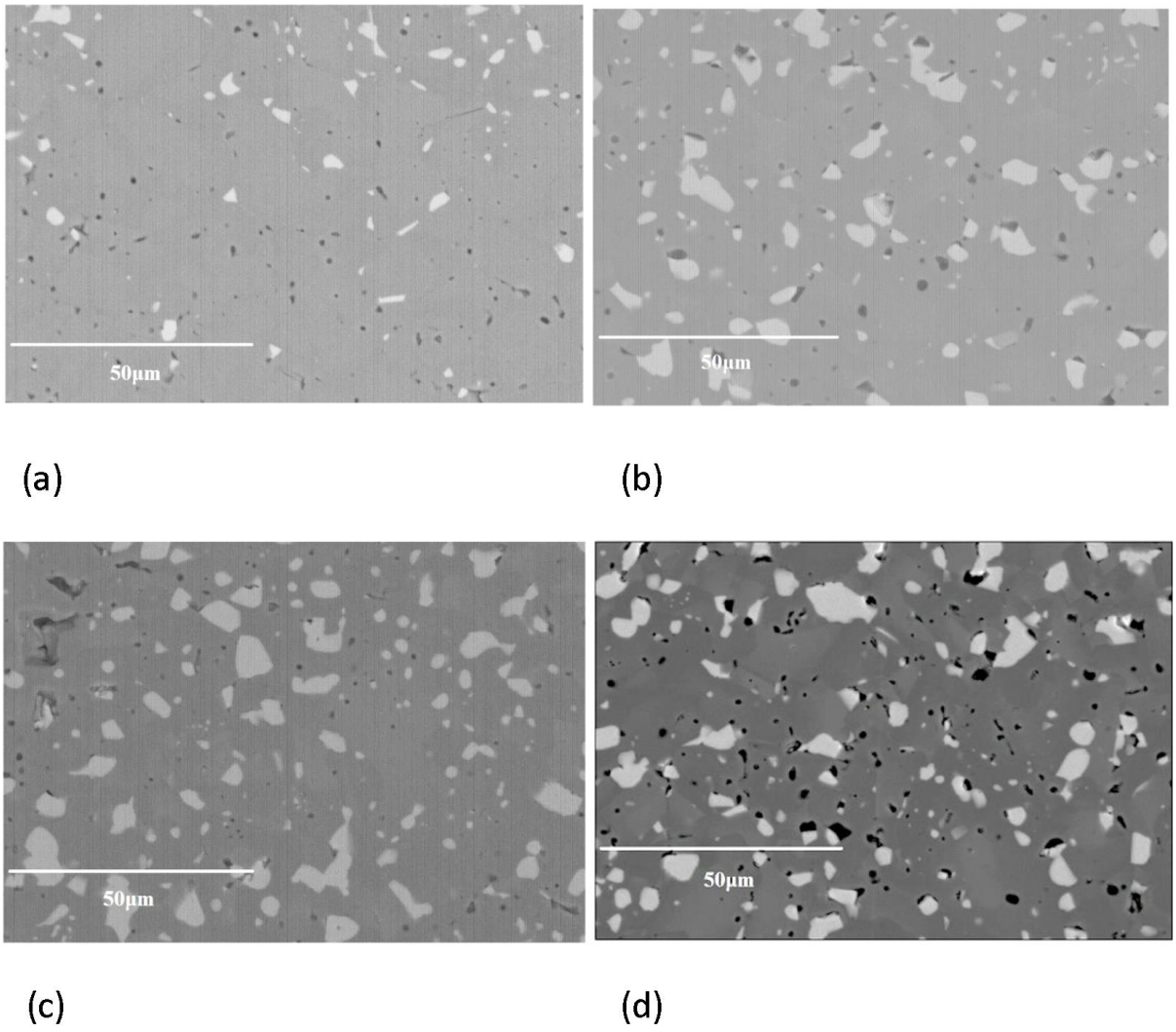

Figure 4.7 BSE images obtained from samples aged at 1450 ˚C under 4% H_2/N_2 gas for (a) 0.5 hours, (b) 5 hours,(c) 10 hours and (d) 20 hours.

4.2.3.4. The effects of atmosphere

This section reports the results of samples aged under 1% H_2/N_2, 4% CO/N_2 and argon at 1450 ℃ for 20 hours. It has been found that most the microstructures of samples aged in different atmospheres consist of a surface layer and a bulk part (Figure 4.8). The microstructures of the bulk parts in samples aged under different atmospheres are similar as they only contain intergranular $FeAl_2O_4$ particles. However, the microstructures of surface layers in samples aged under different atmospheres are different, which has been described in

section 4.2.3.1. Furthermore, it should be noted that unlike sample H4-1450-20, P_{nano} of sample H1-1450-20 is just 70 μm, much less than the surface layer thickness. (Table 4.6)

The intergranular particle volume fraction profiles of sample H1-1450-20 and CO-1450-20 follow the same pattern as that of sample H4-1450-20 (Figure 4.9). However, the intergranular particle volume fraction profile measured from sample Ar-1450-20 is not the same as samples aged under other reducing atmospheres: the particle volume fraction shows little variation after the peak point, and the intergranular particle volume fraction of sample Ar-1450-20 is much lower than that of sample H4-1450-20.

The intergranular particle size distributions and particle morphology of sample H1-1450-20, CO-1450-20 and Ar-1450-20 are all very similar to sample H4-1450-20.

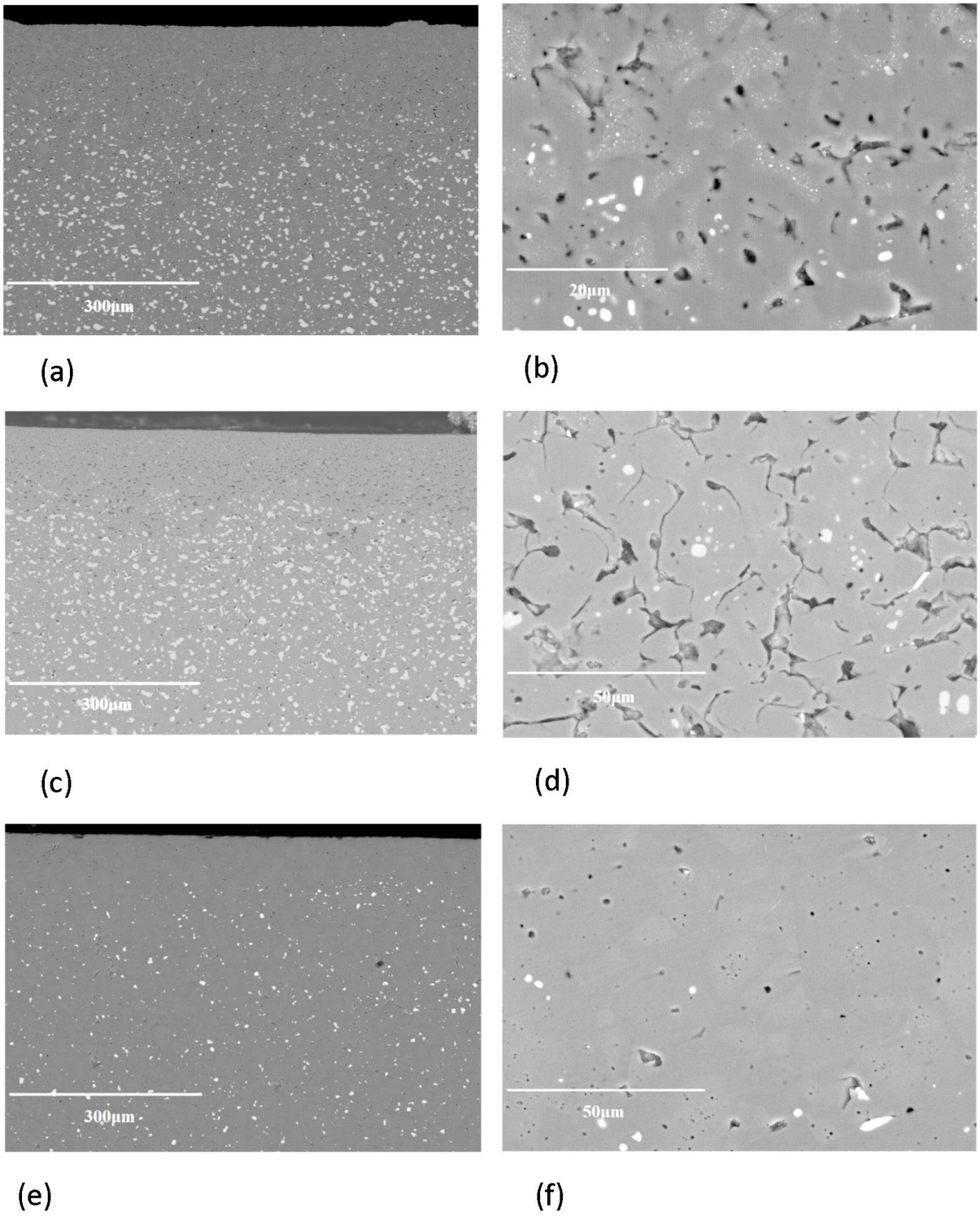

Figure 4.8 BSE images of (a) sample H1-1450-20: (b) sample H1-1450-20, near the gas/solid interface; (c) sample CO-1450-20: (d) sample CO-1450-20, near the gas/solid interface; (a) sample Ar-1450-20: (b) sample Ar-1450-20, near the gas/solid interface;

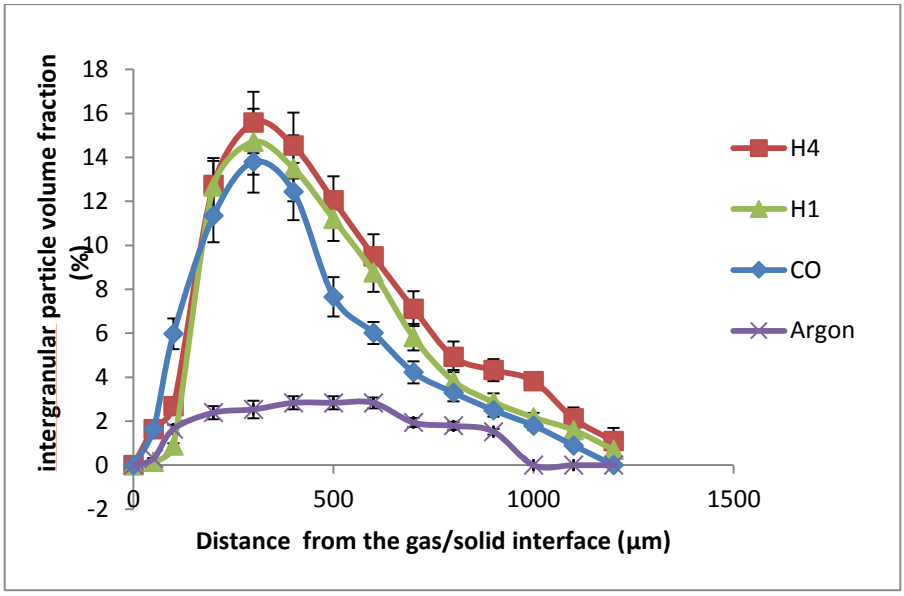

(a)

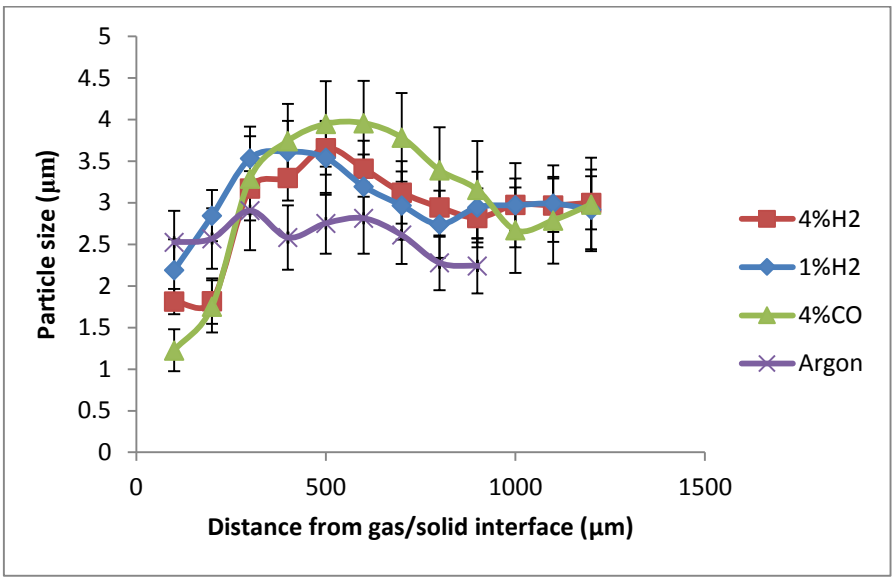

(b)

Figure 4.9 (a) Intergranular spinel particle volume fraction profiles and (b) particle size of samples aged under different atmospheres at 1450 ˚C for 20 hours. The samples here are all 2.5 mm thick.

Table 4.6 The Surface layer thickness and penetration length of nanoparticles in samples aged in different atmospheres at 1450˚C for 20hours.

Atmospheres	4%H_2/N_2	1%H_2/N_2	4%CO/N_2	Argon
P_{surf}(µm)	220 ±16	150 ±10	120 ±8	80 ±6
P_{nano} (µm)	260 ±18	70 ±6	0	0

4.2.3.5. The effects of varying gas flow rate

Table 4.7 gives the sample identification of samples aged at 1450˚C for 20 hours under 4% H_2/N_2 but with different gas flow rate. Figure 4.10(a) indicates indicates that the intergranular particle volume fraction profiles in the bulk part are similar between 200ml and 100ml, while both of which are higher than 10m. The particles size of intergranular $FeAl_2O_4$ particles was also independent of gas flow rates. Figure 4.10(b) also showed that particles size of intergranular $FeAl_2O_4$ particles was also independent of gas flow rates. However, Table 4.8 shows that both the surface layer thickness and P_{nano} increased with increased gas flow rates. It was also found that the surface layer of sample 10ml barely contains any Fe metallic particles.

Table 4.7 sample ID for samples aged at 1450 ˚C for 20 hours but with different gas flow rate

Gas flow rate (ml/min)	200	100	10
Sample ID	200ml	100ml	10ml

Table 4.8 Parameters of samples aged at 1450 ˚C for 20 hours but with different gas flow rate.

Gas flow rate (ml/min)	200	100	10
P_{surf} (μm)	220 ±16	170 ±13	100 ±9
P_{nano} (μm)	260 ±18	200 ±15	60 ±5

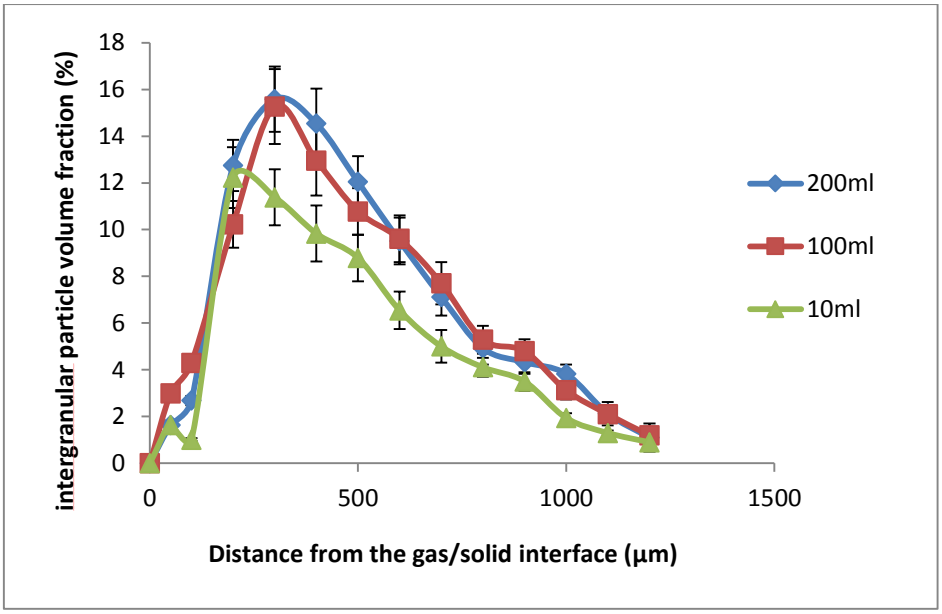

(a)

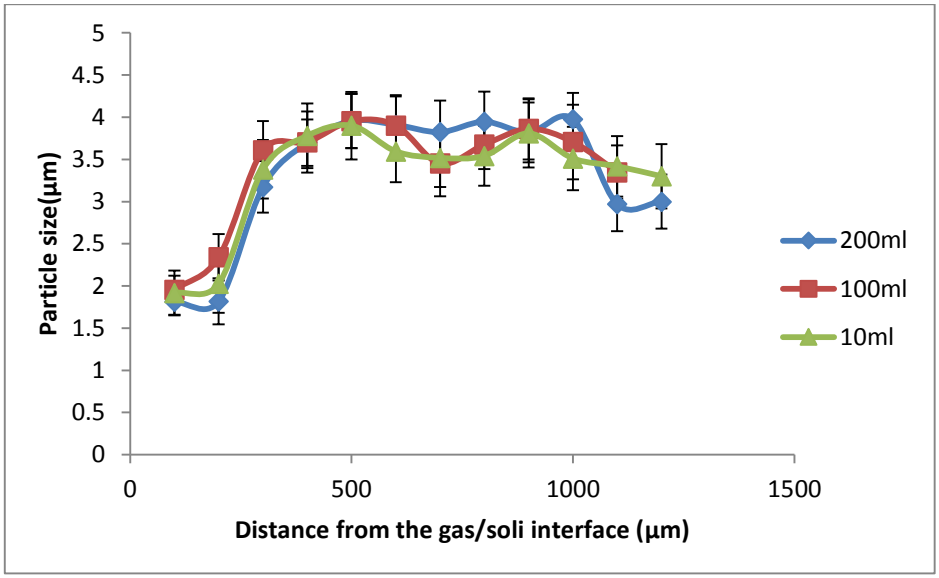

(b)

Figure 4.10(a) Volume fraction profiles of intergranular $FeAl_2O_4$ particles in samples aged at 1450 ℃ for 20 hours under 4% H_2/N_2 with different gas flow rates.(b)Particle size of intergranular $FeAl_2O_4$ particles in samples aged at 1450 ℃ for 20 hours under 4% H_2/N_2 with different gas flow rates. The samples here are all 2.5 mm thick.

4.2.3.6. The effects of varying dopant level

The grain sizes of as-sintered samples doped with different amount of MgO are shown in Figure 4.11. It can be seen that with a higher amount of MgO, the grain size of sintered Al_2O_3-10wt% Fe_2O_3 solid solution became smaller. The role of MgO in inhibiting Al_2O_3 grain size during sintering was mainly attributed to its ability to lower the grain boundary mobility.[4]

Table 4.9 showed that the grain size after aging treatment also increased with decreased dopant amount. In all cases, the grain size after aging is much larger than in the prior solid solution. This will be discussed in section 4.2.3.8. Both the surface layer thickness and and P_{nano} increased with increased amount of MgO dopant. Figure 4.12(a) shows that the intergranular spinel particle volume fraction of 0.25MgO and 0MgO shared a similar microstructure pattern as sample 0.025MgO (H4-1450-20). It can be seen that the volume fraction of $FeAl_2O_4$ generally increased with increased dopant level. Figure 4.12(b) shows the effect of MgO dopants on intergranular $FeAl_2O_4$ particle size distribution in sintered Al_2O_3-10wt% Fe_2O_3 solid solution. In the three samples, the particle size generally increased from the gas/solid interface until a peak point and then gradually decreased. It is clear that the particle size distributions in 0.025MgO and 0.25MgO are almost the same, while sample 0MgO has the largest particle size.

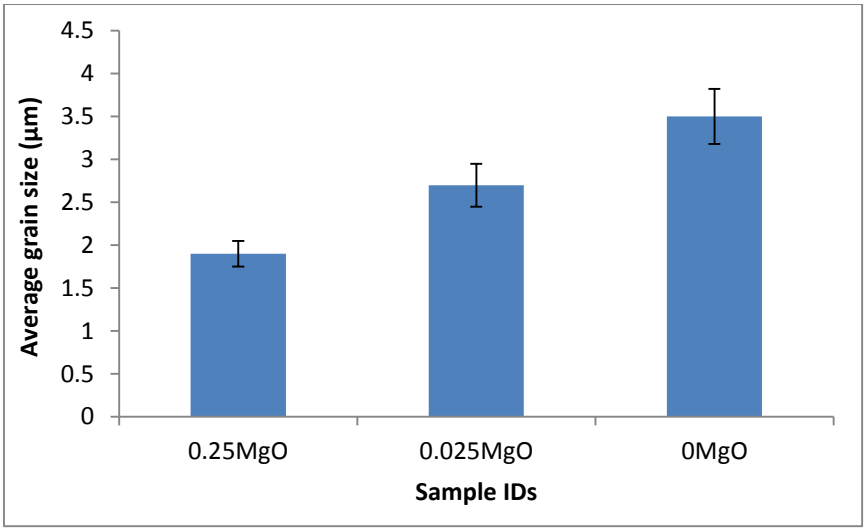

Figure 4.11 Grain sizes of samples doped with different amount of MgO and sintered at 1450 ℃ for 5 hours.

Table 4.9 The parameters of samples doped with different amount of MgO.

Dopant amount	0.25wt%	0.025wt%	0wt%
P_{surf} (μm)	300 ±25	220 ±16	140 ±11
P_{nano}(μm)	355 ±21	260 ±18	165 ±12
Grain size in the surface layer after aging treatment (μm)	11.7 ±1.8	15.2 ±2.5	16.4 ±3.4

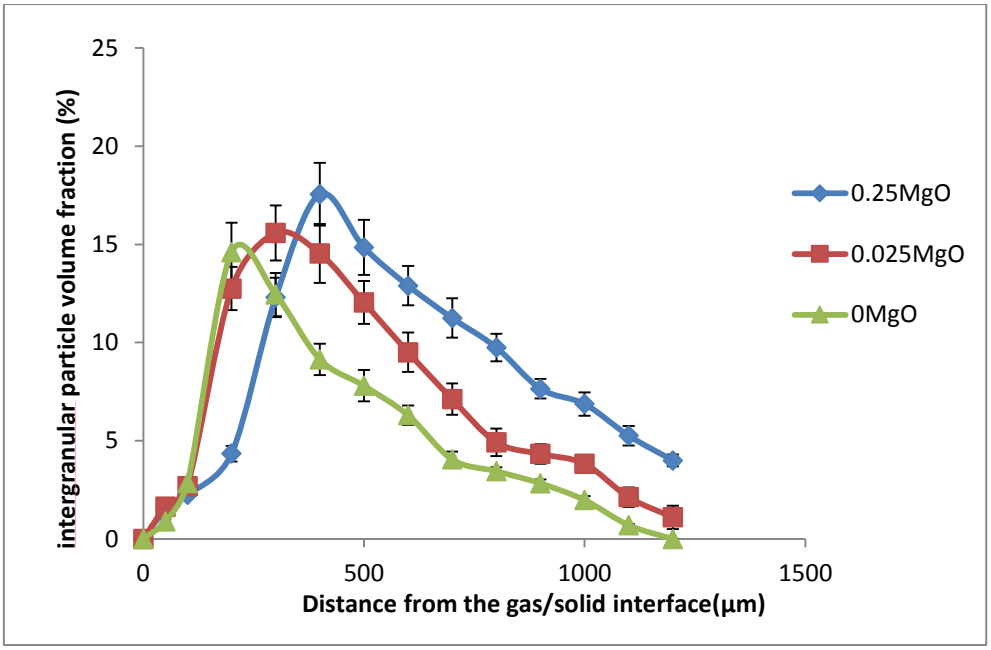

(a)

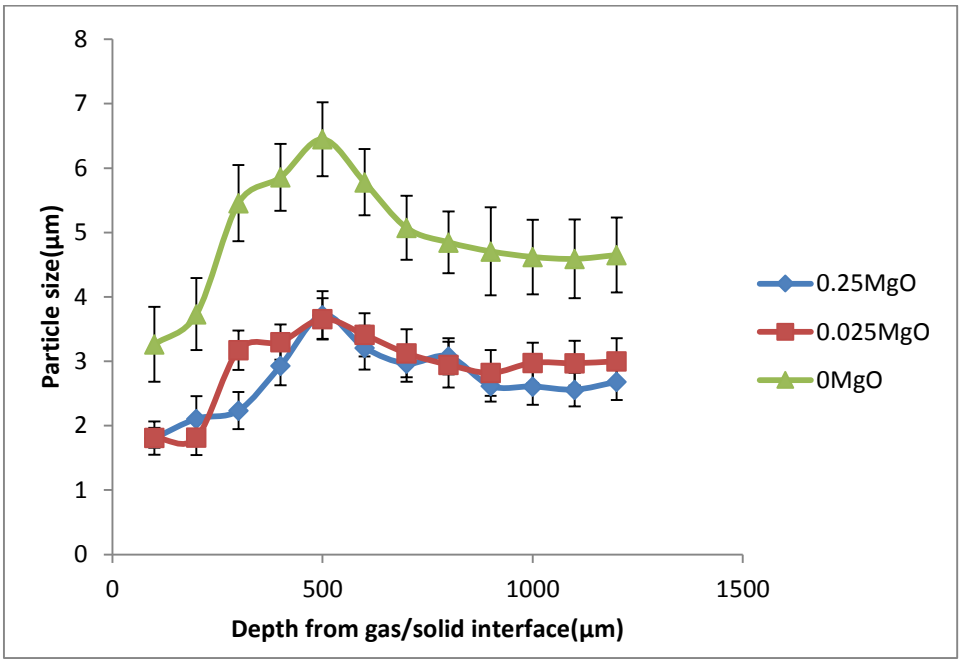

(b)

Figure 4.12 (a) $FeAl_2O_4$ particle volume fractions in samples doped with different amount of MgO and aged at 1450 ℃ for 20hours. (b) $FeAl_2O_4$ particle size distribution in samples doped with different amount of MgO and aged at 1450 ℃ for 20hours. The samples here are all 2.5 mm thick.

4.2.3.7. The effects of varying sample thickness

Figure 4.13(a) describes how specimen thickness affected intergranular spinel particle volume fraction profiles. It can be seen that the heights of the peaks generally increased with decreased thickness from 4mm (13.8%) to 1mm (18%). From Figure 4.13(b) it can be seen that the intergranular particle size distribution in samples with different thickness were very close to each other. Considering the standard error, it can be claimed that the intergranular $FeAl_2O_4$ particle size is independent of sample thicknesses.

As shown in Table 4.10, in samples aged at 1450 ℃ for 20 hours, both surface layer thickness and P_{nano} increased with reduced sample thickness. In sample 0.8mm, the intragranular $FeAl_2O_4$ particles exist throughout the whole sample thickness.

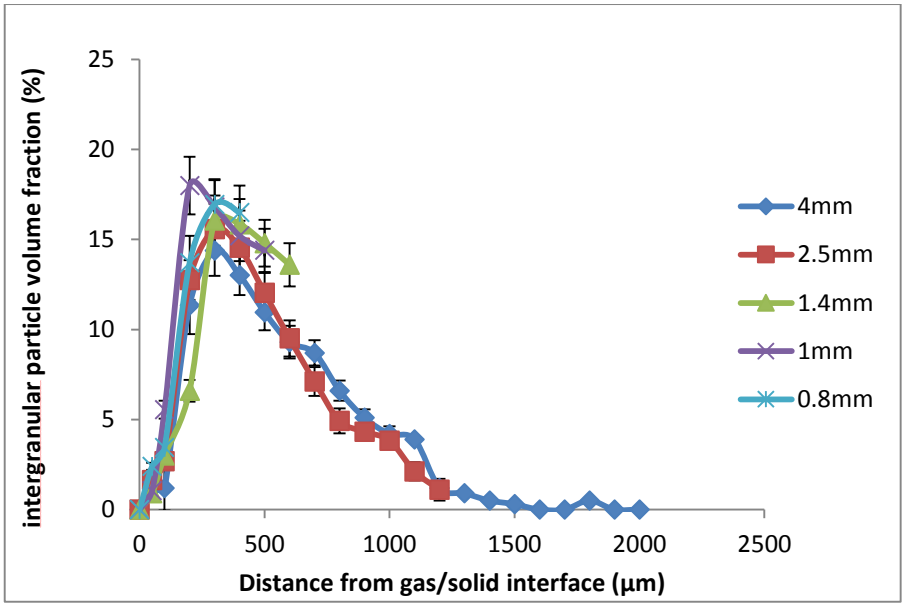

(a)

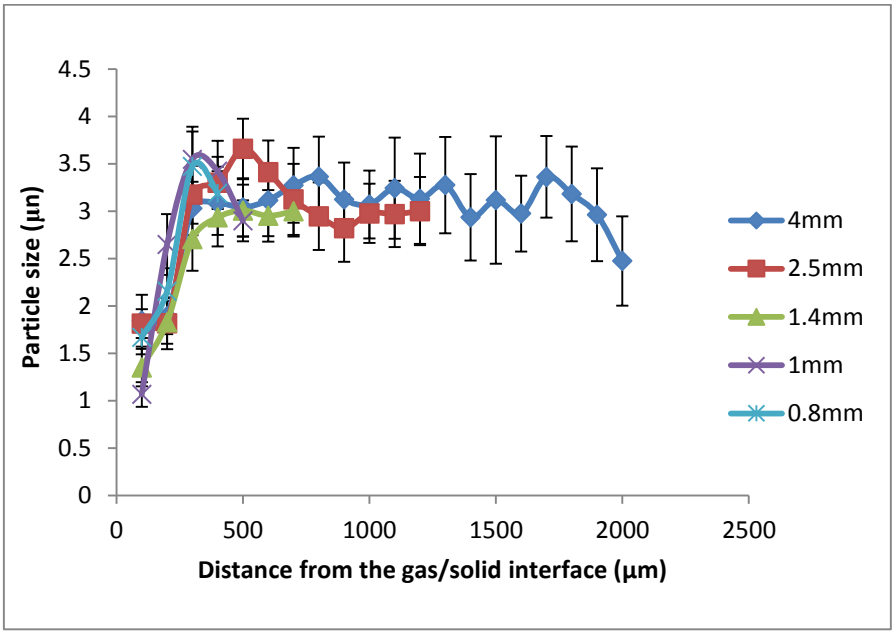

(b)

Figure 4.13 (a) $FeAl_2O_4$ particle volume fractions of samples with different thickness aged at 1450℃ for 20hours (b) $FeAl_2O_4$ particle size distributions of samples with different thickness aged at 1450℃ for 20hours.

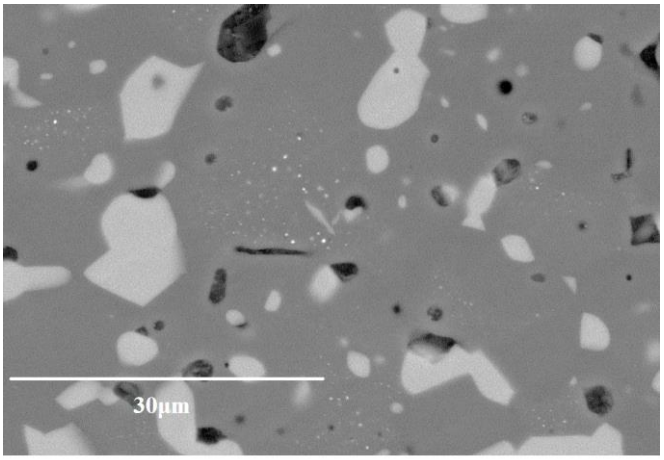

Figure 4.14 BSE images from sample 1.4mm with 400μm from the gas/solid interface.

Table 4.10 The parameters of samples with different thickness.

Sample thickness (mm)	0.8	1	1.4	2.5	4
P_{surf} (μm)	300±19	280±18	250±18	220±16	200±15
P_{nano} (μm)	400	500	700	260±18	200±15

4.2.3.8. Grain growth

Large grains were found in samples aged above 1450℃ in all atmospheres (Figure 4.15). Figure 4.16 gives the grain size of samples aged at 1450℃ for different durations in 4% H_2/N_2. It can be found that after 0.5 hours, the mean grain size increased significantly from 2.7 μm to around 7.1 μm, but remained 15 μm after 5 hours. This is very similar to the situation of average particle size as stated in section 4.2.3.3.

The rapid grain growth can be considered as a result of grain boundary migration induced by the presence of Fe^{2+} during aging treatment. As firstly reported by Gordon and Ikuma[5], doping of iron in alumina can increase the grain boundary diffusivity and that the diffusivity increases with decreasing oxygen partial pressure. This suggests that the diffusivity is related to Fe^{2+}. Tartaj et al[6] also suggested that grain boundary segregation of Fe^{2+} in alumina can significantly increase grain boundary mobility by creating positive defects (i.e. interstitial aluminium or oxygen ion vacancies) in response to the creation of Fe^{2+}, which results in

rapid grain growth. As reported by Phillips and Muan[7], Fe_2O_3 heated in air would start to lose oxygen at 1388 ℃. When heated at 1450 ℃ in air, iron is primarily in the trivalent state, but 2% of the total Fe^{3+} is reduced to Fe^{2+}.[8] The solubility of Fe^{2+} in alumina is very low (only 0.7 to 1.9wt% at 1450 ℃)[9], due to the fact that Fe^{2+} has larger ironic radius (0.64 Å) than Al^{3+}'s (0.53 Å) and a different charge. Since large amount of Fe^{3+} ions in the solid solution (7 wt%) would all be reduced to Fe^{2+} when aged at 1450 ℃ under 4% H_2/N_2, most of the produced Fe^{2+} ions would segregate to the grain boundaries. Therefore, the aging treatment resulted in the rapid grain growth.

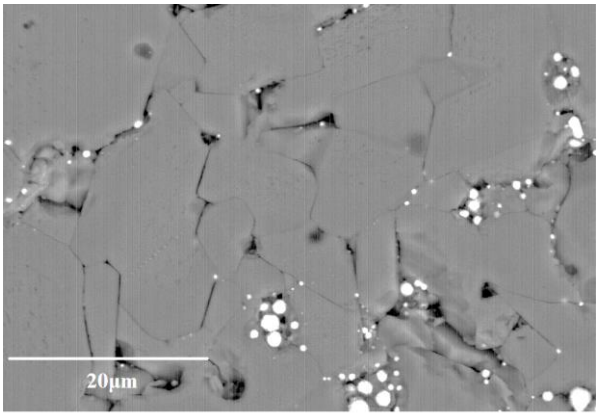

Figure 4.15 BSE images of sample H4-1450-10.

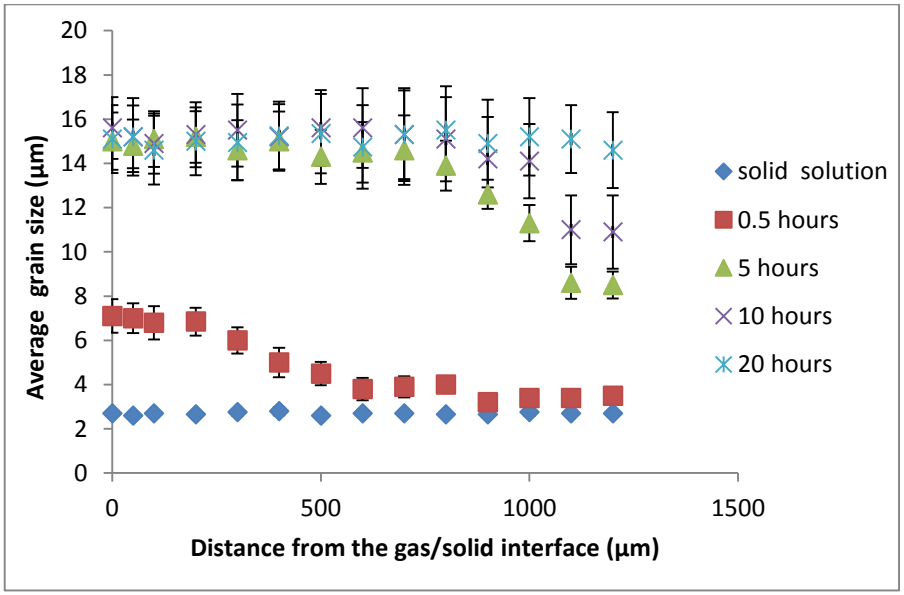

Figure 4.16 Grain size distribution of samples aged in 4% H_2/N_2 at 1450˚C for different durations. The samples here are all 2.5 mm thick.

4.3 Discussion

The thermodynamics of all reduction reactions will be calculated and discussed firstly. Then diffusion kinetics will be calculated and discussed. To fully understand the microstructural development, three essential mechanisms involved during the aging treatment will be discussed: the reduction reaction mechanisms at the gas/solid interface, the grain boundary diffusion and the origin of the 'iron free zone'.

With the discussion above, a model for precipitation by reduction of ceramic solid solutions (PRCS model) will be proposed to explain the microstructural developments during aging treatment.

4.3.1 Thermodynamics of Reduction reactions

Previous study has shown that $FeAl_2O_4$ particles could form in alumina at temperatures below 1050 ˚C in 4% H_2/N_2 gas[10]. Several reports[11,12] have demonstrated that reduction of dissolved Fe^{3+} in the Al_2O_3-Fe_2O_3 solid solutions during aging in reducing atmospheres could result in both chemical composition changes and precipitation of new phases ($FeAl_2O_4$ and Fe). Similar microstructural change has also been observed in this project under four different atmospheres: 4% H_2/N_2, 1% H_2/N_2, 4% CO/N_2 and Argon. 5 chemical reactions were proposed in the following section, based on the observations of microstructure in section 4.2.

The oxygen partial pressures of the four atmospheres used in this project are different, which could affect the concentration of oxygen vacancies produced in alumina[1]. Therefore the precipitation of second phase particles in the aged samples can be affected by the atmospheres. The differences in oxygen vacancy concentration under different atmospheres can be interpreted using a thermodynamics database.[13,14]

4.3.1.1 The Gibbs energy calculation

Although the partial pressure of H_2O produced in each atmospheres can't be measured, the Gibbs energy change of all reductions where the partial pressure of any gas involved is assumed as 0.1MPa can be calculated using a thermodynamics database.[13,14] Therefore, at temperature 1450 ℃, the Gibbs energy changes (driving force) in the following reactions could be calculated. Such driving force calculation could tell which reduction reaction is the most spontaneous under the same conditions. For clarification, the terms used in the following reactions and equations are defined here: ΔH^{o} is the standard enthalpy change of the corresponding reaction, $\Delta_f H(X)$ is the standard enthalpy of formation of X, ΔS^{o} is the standard entropy change of the corresponding reaction, $S^{o}(X)$ is the standard molar entropy of X, ΔG° is standard-state free energy of the corresponding reaction.

For reaction:

$$H_{2(g)} + Fe_2O_3 \rightarrow H_2O_{(g)} + FeO \tag{4.1}$$

$$\Delta H^{o} = 2\Delta_f H^{o}(FeO) + \Delta_f H^{o}\left(H_2O_{(g)}\right) - \Delta_f H^{o}(Fe_2O_3) - \Delta_f H^{o}\left(H_{2(g)}\right) \tag{4.2}$$

$$= [2 \times (-272) + (-241) - (-824) - (0)]\text{kJ/mol}$$

$$= 39\ \text{kJ/mol}$$

$$\Delta S^{o} = 2S^{o}(FeO) + S^{o}\left(H_2O_{(g)}\right) - S^{o}(Fe_2O_3) - S^{o}\left(H_{2(g)}\right) \tag{4.3}$$

$$= [2 \times (60.75) + (188.72) - (87.4) - (130.58)]\text{J/K} \cdot \text{mol}$$

$$= 92.24\ \text{J/K} \cdot \text{mol}$$

Therefore

$$\Delta G^{\circ} = \Delta H^{o} - T \cdot \Delta S^{o} = -119.93\ \text{kJ/mol} \tag{4.4}$$

Hence this reaction is spontaneous.

For reaction:

$$CO_{(g)} + Fe_2O_3 \rightarrow CO_{2(g)} + 2FeO \quad (4.5)$$

$$\Delta H^o = 2\Delta_f H^o(FeO) + \Delta_f H^o\left(CO_{2(g)}\right) - \Delta_f H^o(Fe_2O_3) - \Delta_f H^o\left(CO_{(g)}\right) \quad (4.6)$$

$$= [2 \times (-272) + (-393.5) - (-824\ ) - (-110.5)]\text{kJ/mol}$$

$$= -3\text{kJ/mol}$$

$$\Delta S^o = 2S^o(FeO) + S^o\left(CO_{2(g)}\right) - S^o(Fe_2O_3) - S^o\left(CO_{(g)}\right) \quad (4.7)$$

$$= [2 \times (60.7\ ) + (213.7\ ) - (87.4\ ) - (197.90\ )]\text{J/K} \cdot \text{mol}$$

$$= 49.9\ \text{J/K} \cdot \text{mol}$$

So

$$\Delta G^\circ = \Delta H^o - T \cdot \Delta S^o = -89.00\ \text{kJ/mol} \quad (4.8)$$

Hence this reaction is spontaneous.

For reaction:

$$Fe_2O_3 \rightarrow 0.5O_{2(g)} + 2FeO \quad (4.9)$$

$$\Delta H^o = 2\Delta_f H^o(FeO) + 0.5\ \Delta_f H^o\left(O_{2(g)}\right) - \Delta_f H^o(Fe_2O_3) \quad (4.10)$$

$$= [2 \times (-272\ ) + 0.5 \times (0) - (-824\ )]\text{kJ/mol}$$

$$= 280\ \text{kJ/mol}$$

$$\Delta S^o = 2S^o(FeO) + 0.5S^o(O_2) - S^o(Fe_2O_3) \quad (4.11)$$

$$= [2 \times (60.75\ ) + 0.5\ (205\ ) - (87.4\ )]\text{J/K} \cdot \text{mol}$$

$$= 136.6\ \text{J/K} \cdot \text{mol}$$

So

$$\Delta G^\circ = \Delta H^o - T \cdot \Delta S^o = 44.64\ \text{kJ/mol} \quad (4.12)$$

Hence this reaction is not spontaneous.

In terms of production of metallic Fe, the following two reactions could be considered:

$$3H_{2(g)} + Fe_2O_3 \rightarrow 2Fe + 3H_2O_{(g)} \quad (4.13)$$

$$\Delta H^o = 2\Delta_f H^o(Fe) + 3 \times \Delta_f H^o\left(H_2O_{(g)}\right) - \Delta_f H^o(Fe_2O_3) - 3 \times \quad (4.14)$$

$$\Delta_f H^o(H_{2(g)})$$

$$= [2 \times (0) + 3 \times (-241) - (-824) - 3 \times (0)]\text{kJ/mol}$$

$$= 101\text{kJ/mol}$$

$$\Delta S^o = 2S^o(Fe) + 3 \times S^o\left(H_2O_{(g)}\right) - S^o(Fe_2O_3) - 3 \times S^o(H_{2(g)}) \quad (4.15)$$

$$= [2 \times (27.28) + 3 \times (188.72) - (87.4) - 3 \times (130.58)]\text{J/K} \cdot \text{mol}$$

$$= 141.57\ \text{J/K} \cdot \text{mol}$$

Therefore

$$\Delta G^\circ = \Delta H^o - T \cdot \Delta S^o = -142.93\ \text{kJ/mol} \quad (4.16)$$

Hence this reaction is spontaneous.

For reaction:

$$3CO_{(g)} + Fe_2O_3 \rightarrow 2\,Fe + 3CO_{2(g)} \quad (4.17)$$

$$\Delta H^o = 2\Delta_f H^o(Fe) + 3 \times \Delta_f H^o\left(CO_{2(g)}\right) - \Delta_f H^o(Fe_2O_3) - 3 \times \Delta_f H^o\left(CO_{(g)}\right) \quad (4.18)$$

$$= [2 \times (0) + 3 \times (-393.5) — (824) - 3 \times (-110.5)]\text{kJ/mol}$$

$$= -25\ \text{kJ/mol}$$

$$\Delta S^o = 2S^o(Fe) + 3 \times S^o(CO_2) - S^o(Fe_2O_3) - 3 \times S^o(CO_{(g)}) \quad (4.19)$$

$$= [2 \times (27.28) + 3 \times (213.7) - (87.4) - 3 \times (197.9)]\ \text{J/K} \cdot \text{mol}$$

$$= -14.56\ \text{J/K} \cdot \text{mol}$$

Therefore

$$\Delta G^\circ = \Delta H^o - T \cdot \Delta S^o = -50.09\ \text{kJ/mol} \quad (4.20)$$

Hence this reaction is spontaneous.

The driving force ΔG^o for Reaction 4.1 is more negative than Reaction 4.5, and the driving force ΔG^o for Reaction 4.13 is more negative than Reaction 4.17. Thus it can be deduced that at 1450 ℃, more $FeAl_2O_4$ and metallic Fe particles will be produced in samples aged under 4% H_2/N_2 than 4% CO/N_2. Furthermore, since $\frac{[H_2]}{[H_2O]}$ is decreased from 4% H_2/N_2 to 1% H_2/N_2, less $FeAl_2O_4$ and metallic Fe particles will be produced in samples aged under 1% H_2/N_2 than under 4%H_2/N_2. Since Reaction 4.9 gives positive driving force, the amount of $FeAl_2O_4$ particles produced in argon should be the lowest, which conforms to the results stated in section 4.2.

4.3.1.2 The oxygen vacancy concentration at the gas/solid interface ($[V_o^{\cdot\cdot}]_{g/s}$) produced in different atmospheres

Using the Gibbs energy calculated above, the $[V_o^{\cdot\cdot}]_{g/s}$ produced in each atmospheres can be discussed. Firstly, four sets of chemical reactions using Kröger-Vink notation are proposed below.

(1). As reported by a previous study[3], the overall reduction reactions in 4% H_2/N_2 and 1% H_2/N_2 are:

$$Fe_2O_3 + 2Al_2O_3 + H_{2(g)} \rightarrow 2FeAl_2O_4 + H_2O_{(g)} \quad (4.21)$$

$$FeAl_2O_4 + H_{2(g)} \rightarrow Fe + H_2O_{(g)} + 2Al_2O_3 \quad (4.22)$$

In Kröger-Vink notation, the corresponding reduction reactions could be written as:

$$H_2 + O_O^x \rightarrow H_2O + V_O^{\cdot\cdot} + 2e^- \quad (4.23)$$

$$2Fe_{Al}^x + 4Al_{Al}^x + 8O_O^x + V_O^{\cdot\cdot} + 2e^- \rightarrow 2FeAl_2O_4 \quad (4.24)$$

$$FeAl_2O_4 + V_O^{\cdot\cdot} + 2e^- \rightarrow Fe + Al_2O_3 \quad (4.25)$$

(2). 4%CO/N_2:

$$CO+Fe_2O_3+2Al_2O_3 \rightarrow 2\ FeAl_2O_4+ CO_2 \quad (4.26)$$

$$CO+ O_O^x \rightarrow CO_2+V_O^{\bullet\bullet}+2e^- \quad (4.27)$$

(3). Argon:

$$2Fe_2O_3+ 4Al_2O_3 \rightarrow 4FeAl_2O_4+ O_2 \quad (4.28)$$

$$O_O^x \rightarrow V_O^{\bullet\bullet}+0.5O_2+2e^- \quad (4.29)$$

It can be deduced that the oxygen vacancy created by the reduction reaction affects the precipitation of second phase particles. As the reaction temperature and corresponding partial pressures are fixed, the Van't Hoff equation[15] can be applied here:

$$\Delta G^\circ = -R \cdot T \cdot (lnK) \quad (4.30)$$

In Equation 4.30, ΔG° is the standard free energy change of the corresponding reaction, R is the gas constant, T is the reaction temperature, K is the equilibrium constant.

In Reaction 4.23,

$$K_{4.23} = \frac{[H_2O][V_O^{\cdot\cdot}]}{[H_2]} \quad (4.31)$$

where$K_{4.23}$is the equilibrium constant of Reaction 4.23;

In Reaction 4.27,

$$K_{4.27} = \frac{[CO_2][V_O^{\cdot\cdot}]}{[CO]} \quad (4.32)$$

where $K_{4.27}$is the equilibrium constant of Reaction 4.27;

Using the Gibbs energy calculated above, at a same temperature, $K_{4.23} = \frac{[H_2O][V_O^{\cdot\cdot}]}{[H_2]} > K_{4.27} = \frac{[CO_2][V_O^{\cdot\cdot}]}{[CO]}$. Therefore, if $\frac{[H_2]}{[H_2O]} = \frac{[CO]}{[CO_2]}$, $[V_o^{\bullet\bullet}]$ in samples aged under H_2 should be higher than that under CO. Thus it can be deduced that $[V_o^{\bullet\bullet}]_{g/s}$ in samples aged under 4% H_2/N_2 should be higher than aged in 4% CO/N_2. Furthermore, if $\frac{[H_2]}{[H_2O]}$ is decreased, $[V_o^{\bullet\bullet}]_{g/s}$ will correspondingly decreases, hence $[V_o^{\bullet\bullet}]_{g/s}$ in samples aged under 4% H_2/N_2 should be higher

than that aged under 1% H_2/N_2. Argon gives the least $[V_o^{\bullet\bullet}]_{g/s}$ in alumina since the oxygen partial pressure is the highest among those four atmospheres.

Since ΔS^o for Reaction 4.1 is much higher than that of Reaction 4.5, as temperature increases, the increase of ΔG for Reaction 1 will be higher than that of Reaction 4.5. Thus $[V_o^{\bullet\bullet}]_{g/s}$ in samples aged under 4% H_2/N_2 will be always higher than that of 4% CO/N_2.

In conclusion, more reducing gases led to higher concentration of oxygen vacanciy, thereby more $FeAl_2O_4$ and metallic Fe particles. This conforms the observations in the results section.

4.3.2 Diffusion kinetics

4.3.2.1. Diffusion coefficients measurement theory

a. Grain boundary diffusion in the bulk part

For convenience, the following terms are defined firstly: *D* refers to diffusion coefficient for a diffusion process, D_{surf} refers to the apparent diffusion coefficient of oxygen vacancy diffusion responsible for the formation of the surface layer, D_{bulk} refers to the apparent diffusion coefficient of oxygen vacancy diffusion in the bulk part of samples (responsible for the formation of intergranular spinel particles in the bulk part of samples).

Since the microstructure showed no difference with gas flow rate increased from 100ml to 200ml in all atmospheres, it is reasonable to say that $[V_O^{\bullet\bullet}]_{g/s}$ doesn't change from 100ml to 200ml. Thus a flow rate of 200ml should be sufficient to maintain $\frac{[H_2]}{[H_2O]}$, $\frac{[CO]}{[CO_2]}$ and $[O_2]$ respectively during the aging. In other words, when the gas flow rate is 200ml, $[V_O^{\bullet\bullet}]_{g/s}$ is a constant at a certain aging temperature.

As Reaction 4.23 shows, reduction reactions create an oxygen vacancy chemical concentration difference between the gas/solid interface (g/s interface) and the bulk of the samples, hence resulting in a diffusion process. Since $[V_O^{\bullet\bullet}]_{g/s}$ is a constant at the gas/solid

interface with the atmosphere, for short aging times the oxygen vacancy diffusion process could be regarded as a surface source of initial concentration $[V_O^{\bullet\bullet}]_{g/s}$, in contact with a semi-infinite volume of zero initial concentration, therefore the 2-D spatial and time distribution of oxygen vacancy concentration along with distance from the g/s interface, could be written as: [16]

$$C(x,t) = C_o + (C_S - C_o) \cdot erfc[\frac{x}{2\sqrt{D_{bulk} \cdot t}}] \tag{4.33}$$

Where $C(x,t)$ is the oxygen vacancy concentration function of distance from the gas/ solid (g/s) interface x and aging time t, C_o is the original oxygen vacancy concentration in the sample, C_S is the oxygen vacancy concentration at gas/s interface, $erfc[\frac{x}{2\sqrt{D_{bulk} \cdot t}}]$is the error function of $[\frac{x}{2\sqrt{D_{bulk} \cdot t}}]$ [16]. When oxygen vacancies and electrons move into the bulk of samples, both the formation of intergranular and intragranular particles may happen.

It has been found that the volume fraction profile of second phase particles, was sensitive to the atmosphere (section 4.2.3.4), gas flow rate (section 4.2.3.5), the grain size (section 4.2.3.6) and sample thickness. This indicated that the precipitation of second phase particles was diffusion controlled. Both electrons and oxygen vacancies are needed for the precipitation to occur, but it is assumed that electrons move faster than oxygen vacancies (Chapter 2 section 2.3.5), i.e the precipitation rate is controlled by the oxygen vacancy diffusion.

Therefore, it is reasonable to assume that the volume fraction of intergranular $FeAl_2O_4$ particles is linearly related to the oxygen vacancy concentration $C(x,t)$. This assumption will be discussed further in section 4.3.4.

$$\frac{f(x,t)}{f_o} = \frac{C(x,t)}{C_{s/b}} = \frac{(C_{s/b} - C_o) \cdot erfc[\frac{x}{2\sqrt{D_{bulk} \cdot t}}]}{C_{s/b}} + \frac{C_o}{C_{s/b}} \tag{4.34}$$

Where $f(x,t)$ is the volume fraction of $FeAl_2O_4$ particles with the distance x from the surface layer/ bulk part interface (S/B interface) at time t from the start of reaction, f_o is the maximum volume fraction of $FeAl_2O_4$ particles at S/B interface which is almost a constant at a certain temperature as shown in section 4.2.3.3, $C_{s/b}$ is the oxygen vacancy concentration at S/B interface and thereby should also be a constant. The $C_o << C_{s/b}$ and it doesn't contribute to formation of spinel particles. Therefore Equation 4.33 can be re-written as:

$$f(x,t) = f_o[\frac{x}{2\sqrt{D_{bulk} \cdot t}}] \tag{4.35}$$

If all Fe atoms form $FeAl_2O_4$, the volume fraction of $FeAl_2O_4$ would be around 21%, hence f_o can be set as 21% (the calculation will be shown in Appendix A). The microstructures in section 4.2 showed that the penetration of intergranular spinel particle formation is much faster than the rate of increase of the surface layer, thus the movement of the S/B interface could be neglected in this calculation.

b. Grain boundary diffusion in the surface layer and the matrix diffusion

As discussed above, the oxygen vacancy concentration at the g/s interface $[V_o^{\cdot\cdot}]_{g/s}$ is a constant with atmosphere at a certain temperature, thus the surface layer thickness should be equal to the distance between where the $[V_o^{\cdot\cdot}]=[V_o^{\cdot\cdot}]_{g/s}$ and where $[V_o^{\cdot\cdot}]=[V_o^{\cdot\cdot}]_{s/b}$. A diffusion coefficient (D_{surf}) could then be obtained by measuring the surface thickness against aging duration at each temperature if the surface layer thickness varies according to $t^{1/2}$ law, where t is the aging time.[16]

Similarly, assuming the electrons move faster than iron ions and the formation of 'iron free zone' is solely due to iron matrix diffusion, iron matrix diffusivity can be obtained by measuring the 'iron free zone' width with aging time, if the zone width varied according to a $t^{1/2}$ law, which corresponds to the ordinary law of diffusion from a solid solution grain core to a grain boundary.

4.3.2.2. Oxygen vacancy diffusion kinetics in 4%H_2/N_2

Using the error function and theories described in section 4.3.2.1, diffusion distance x^2 could be calculated from the surface thickness of samples aged for different times at different temperatures under 4 %H_2/N_2 atmosphere and shown in Figure 4.17. If z is 0.5, *erfc*(*z*)= 0.48. So referring to equation 6, if $\frac{f(x,t)}{f_o}$ =0.48, $x^2 = D_{bulk} \times t$. Therefore, the diffusion distance x^2 (where $\frac{f(x,t)}{f_o}$ is set as 0.48) could also be calculated from the intergranular spinel particle volume fraction profiles in the bulk part of the same samples (Figure 4.18). The apparent diffusion coefficients were obtained as the gradients of lines in both Figure 4.17 and Figure 4.18 (Table 4.11, Figure 4.19 and Figure 4.20). D_{bulk} is the apparent diffusion coefficient corresponding to intergranular spinel particle volume fraction profile against time measured in the bulk part. From Figure 4.20, an equation could be drawn:

$$D_{bulk} = 6.4 \times 10^{-4} \times exp(\frac{295kJ/mol}{RT}) \text{ m}^2/\text{s} \quad (4.36)$$

The corresponding activation energy Q_A=295 kJ/mol and pre-exponential constant D_0= 6.4 × 10^{-4} m^2/s could be obtained.

It was found that the thickening of the surface layer also approximately follows Fick's second law (Figure 4.17), thus a diffusion coefficient D_{surf} corresponding to surface layer thickening could be obtained. This indicates that the surface layer thickening is also a result of diffusion. From Figure 4.19, an equation could be drawn as:

$$D_{surf} = 1.69 \times 10^{-2} \times exp(\frac{327kJ/mol}{RT}) \text{ m}^2/\text{s} \quad (4.37)$$

The corresponding activation energy Q_A=327 kJ/mol and pre-exponential constant D_0=1.69 × 10^{-2} m^2/s could be obtained.

It can be seen that at each aging temperature, D_{surf} and D_{bulk} are comparable, and the activation energies corresponding to D_{surf} and D_{bulk} are very close. It is probably because both D_{surf} and D_{bulk} follow equation 4, though $z = \frac{x}{2\sqrt{Dt}}$ and the meaning of x are both different in

calculating D_{surf} and D_{bulk}. It is therefore reasonable to speculate that the oxygen vacancy diffusion mechanisms in both surface layer and bulk materials could be considered as the same one.

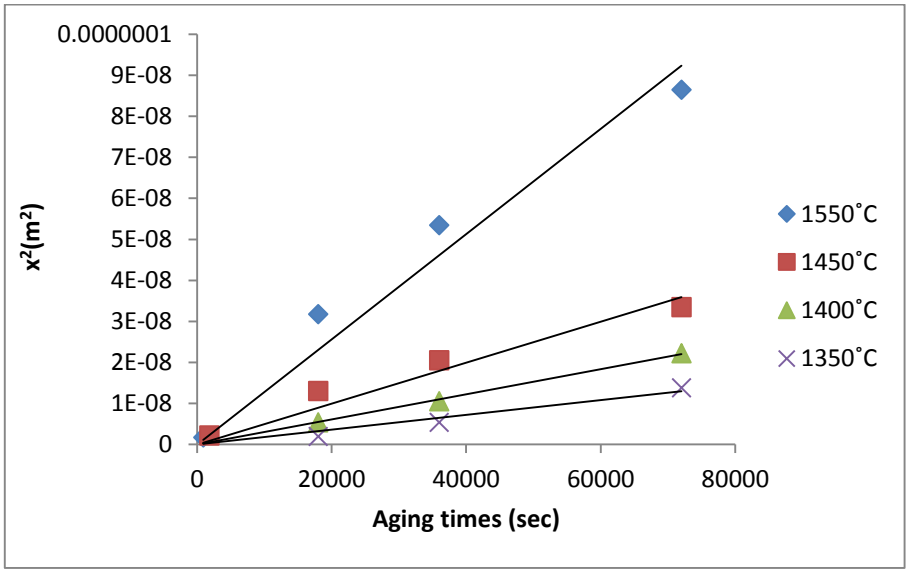

Figure 4.17 Diffusion distance against aging times in surface layer, for solid solution samples aged under 4% H_2/N_2 atmosphere at different temperatures.

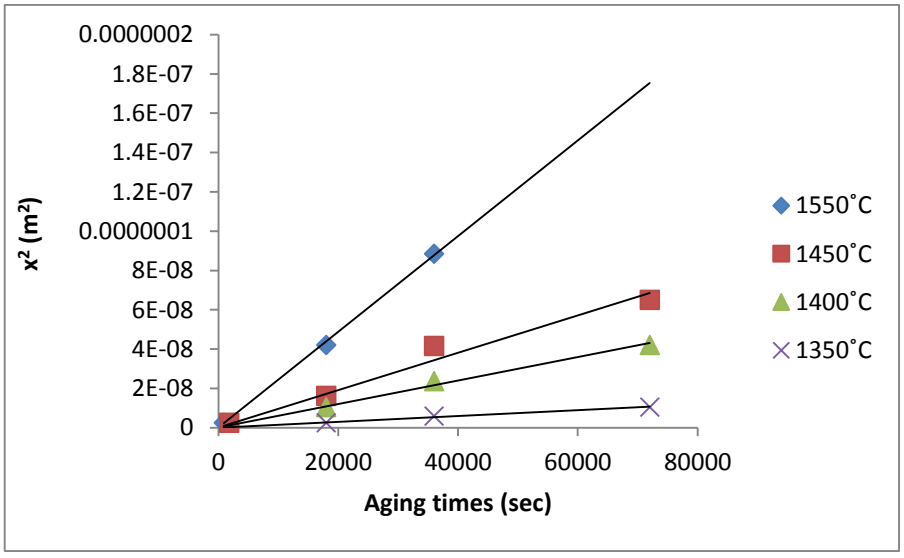

Figure 4.18 Diffusion distance against aging times in bulk part, for solid solution samples aged under 4 % H_2/N_2 atmosphere at different temperatures.

Table 4.11 D_{surf} and D_{bulk} for different aging temperatures.

Temperatures (℃)	1350	1400	1450	1550
D_{surf} (m^2/s)	1.20×10^{-13}	3.01×10^{-13}	7.5×10^{-13}	1.60×10^{-12}
D_{bulk} (m^2/s)	1.45×10^{-13}	3.25×10^{-13}	9.01×10^{-13}	2.27×10^{-12}

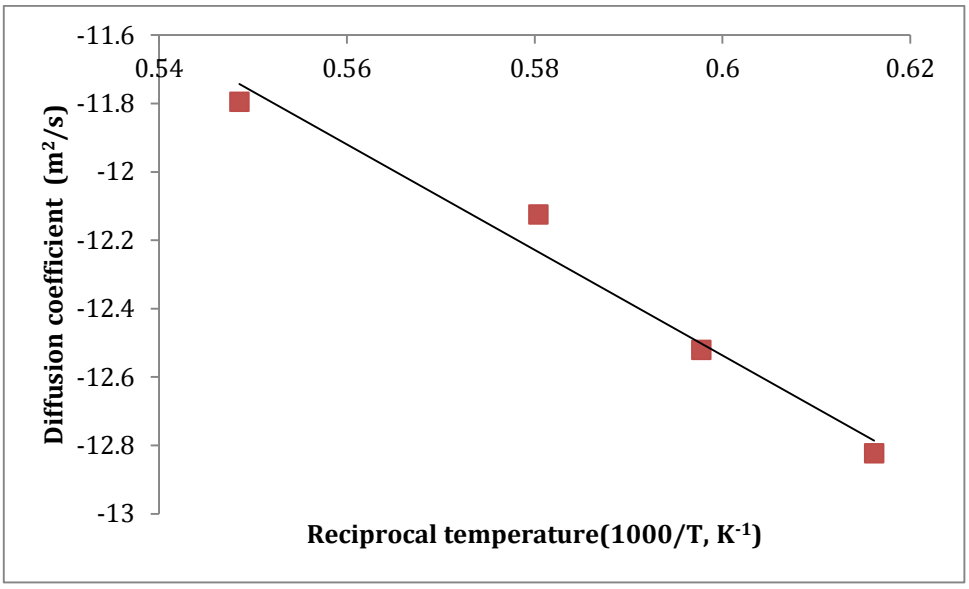

Figure 4.19 Temperature dependence of diffusion coefficients measured in surface layer.

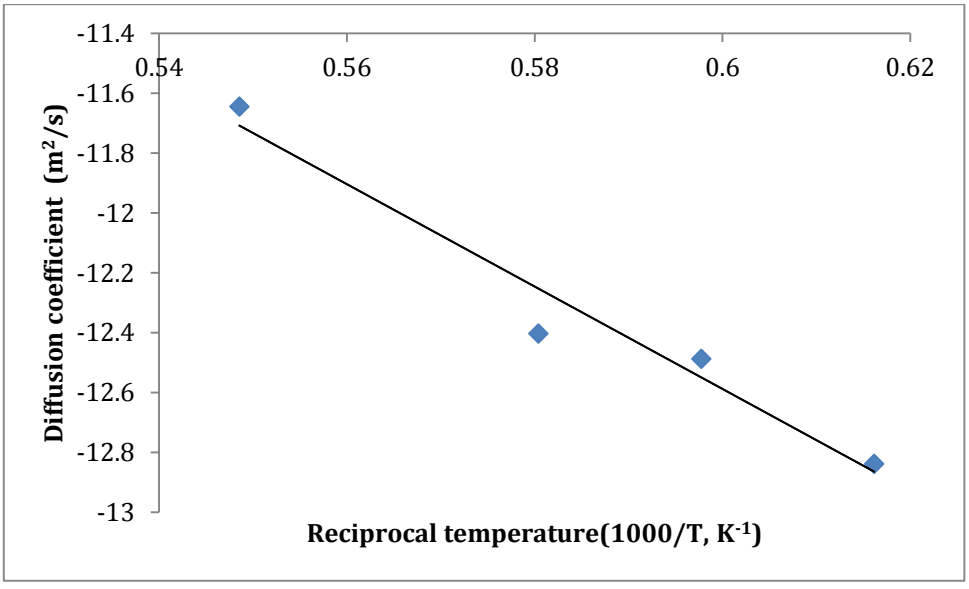

Figure 4.20 Temperature dependence of diffusion coefficients in bulk part.

4.3.2.3. Oxygen diffusion kinetics in the other three atmospheres

The values of D_{surf} and D_{bulk} in samples aged under atmosphere 1% H_2/N_2 and 4% CO/N_2 then could be measured using the same method used in samples aged under 4% H_2/N_2 in section 4.3.2.2. However, since the microstructures of the surface layer are different in different atmospheres and the evaporation of Fe atoms could make the f_o lower than 21%, f_o is taken differently in different atmospheres.

An equation could be drawn from Figure 4.21:

$$D_{bulk} = 7.6 \times 10^{-3} \times exp\left(\frac{-334kJ/mol}{RT}\right) \quad (4.38)$$

An equation could be drawn from Figure 4.22:

$$D_{bulk} = 1.8 \times 10^{-2} \times exp\left(\frac{-345kJ/mol}{RT}\right) \quad (4.39)$$

As shown in Table 4.12 and Table 4.13, despite the differences in pre-exponential coefficients, the activation energies of grain boundary diffusion measured from samples aged under 1% H_2/N_2 and 4 % CO/N_2 are comparable to 4%H_2/N_2. The average activation energies of oxygen vacancy matrix diffusion reported in literature is around 644 kJ/mol[17], and the average value of oxygen vacancy grain boundary diffusion is around 386 kJ/mol. These values are in a good agreement with values reported for oxygen vacancy grain boundary diffusion.

Samples aged under argon were less reduced, even at 1550 ℃ for 20 hours, compared with samples aged in other reducing atmospheres. Since the volume fractions of spinel particles in samples aged at both 1450 ℃ and 1350 ℃ under argon were very low, the measurement of corresponding diffusion coefficients would lack sufficient accuracy. The diffusion coefficient measured at 1550 ˚C under argon is around 5.0×10^{-13} m^2/s (Figure 4.23), which is less than a quarter of the value measured under 4% H_2/N_2 at the same temperature.

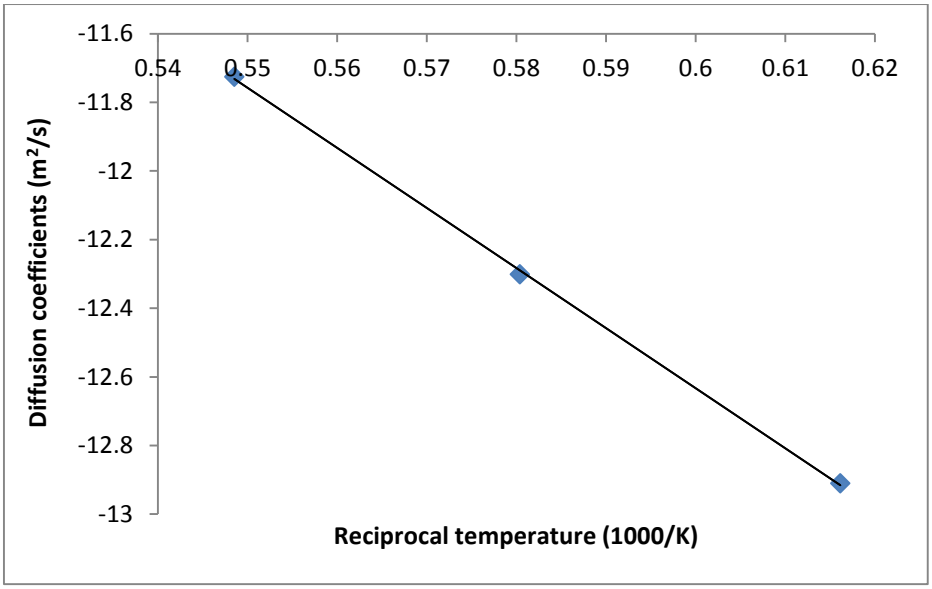

Figure 4.21 Temperature dependence of grain boundary diffusion coefficients in 4% CO/N_2.

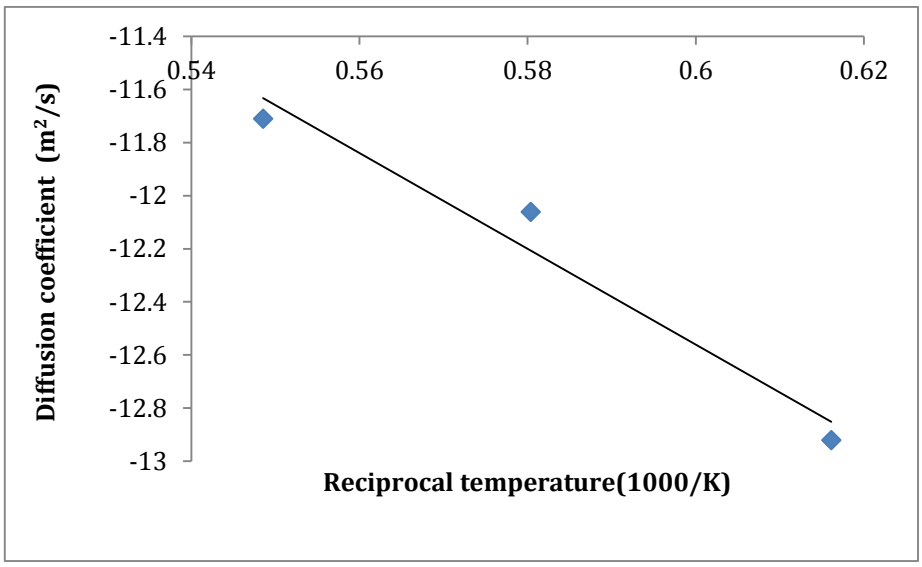

Figure 4.22 Temperature dependence of grain boundary diffusion coefficients in 1% H_2/N_2.

Table 4.12 Activation energy for samples aged under different atmospheres

Atmospheres	4% H_2/N_2	4% CO/N_2	1% H_2/N_2
Activation energy (kJ/mol)	327	334	345

Table 4.13 Pre-exponential coefficients measured at 1550 ˚C under different atmospheres

Atmospheres	4% H_2/N_2	4% CO/N_2	1% H_2/N_2	Argon
Diffusion coefficient(m^2/s)	2.3×10^{-12}	1.8×10^{-12}	2.0×10^{-12}	5.0×10^{-13}

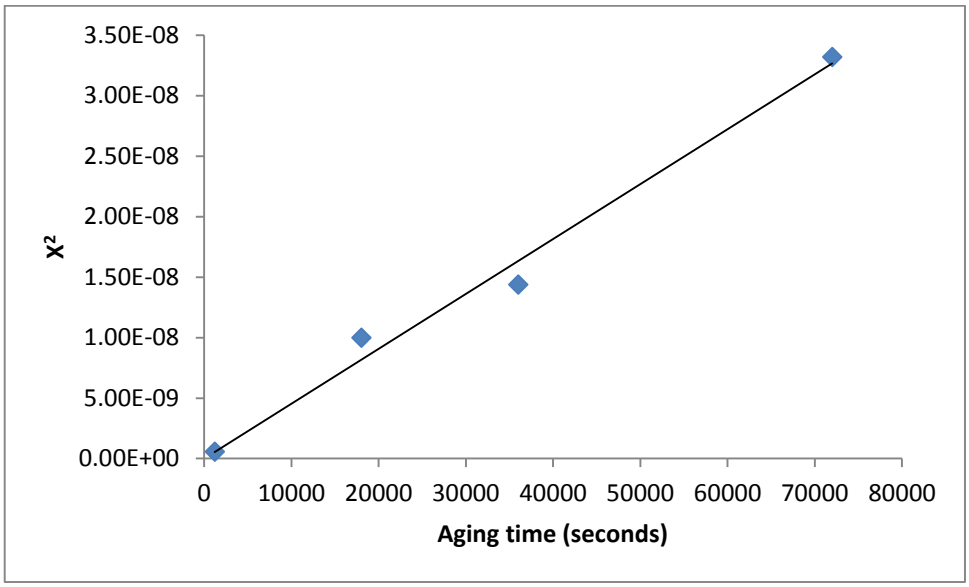

Figure 4.23 Diffusion distance against aging time for samples aged at 1550 ℃ under argon.

4.3.2.4. Matrix diffusion kinetics of Fe

It is assumed here that the 'iron free zones' in the grains are only lattice diffusion caused. Considering the 'iron free zone' around the matrix grains, an apparent lattice diffusion coefficient of iron in alumina matrix D_{Fe} could be obtained by measuring the 'iron free zone' width against aging time. The values in Table 4.14 are in the same order of magnitude of literature value of iron lattice diffusions. [18, 19]

Table 4.14 D_{Fe} for different aging temperatures measured in samples aged under 4%H_2/N_2

Temperatures (℃)	1350	1400	1450	1550
D_{Fe} (m^2/s)	9.60×10^{-18}	1.82×10^{-17}	3.13×10^{-17}	8.8×10^{-17}

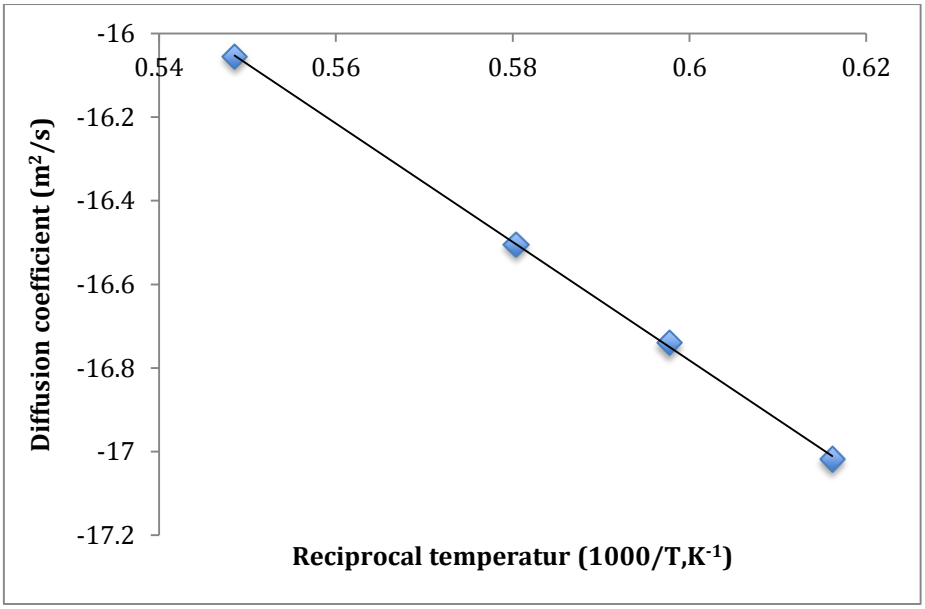

Figure 4.24 Temperature dependence of Fe matrix diffusion coefficients measured in samples aged under 4%H_2/N2.

An equation can be drawn from Figure 4.24:

$$D_{Fe} = 6.4 \times 10^{-4} \times exp\,(\frac{-280\text{kJ/mol}}{RT})\ \text{m}^2/\text{s} \tag{4.40}$$

This equation is in a good agreement with the Ahrrenius equation reported previously for the iron lattice diffusion in alumina.[18,19]The measured apparent iron matrix diffusivity in samples aged under 4% H_2/N_2 is in the same order of magnitude of the literature values for iron matrix diffusivity, and the activation energies are not far away from 300 kJ/mol as reported by Lesage et al[18].

Same as the samples aged in 4% H_2/N_2, the lattice diffusion coefficient of iron under the other three atmospheres were also measured in this project, and the corresponding D_{Fe} could be obtained using the same method. Values measured are summarized and compared with values measured under 4% H_2/N_2 in Table 4.15 and Figure 4.25.

Table 4.15 D_{Fe} in samples aged under different atmospheres at different temperatures.

Temperatures(℃)	1350	1450	1550
D_{Fe} (m^2/s) in 1%H_2	9.60×10^{-18}	3.13×10^{-17}	8.8×10^{-17}
D_{Fe} (m^2/s) in 4%CO	2.16×10^{-17}	7.04×10^{-17}	2.2×10^{-16}
D_{Fe} (m^2/s) in Argon	2.35×10^{-17}	5.5×10^{-17}	2.5×10^{-16}
D_{Fe} (m^2/s) in 4%H_2	9.6×10^{-18}	3.13×10^{-17}	8.8×10^{-17}

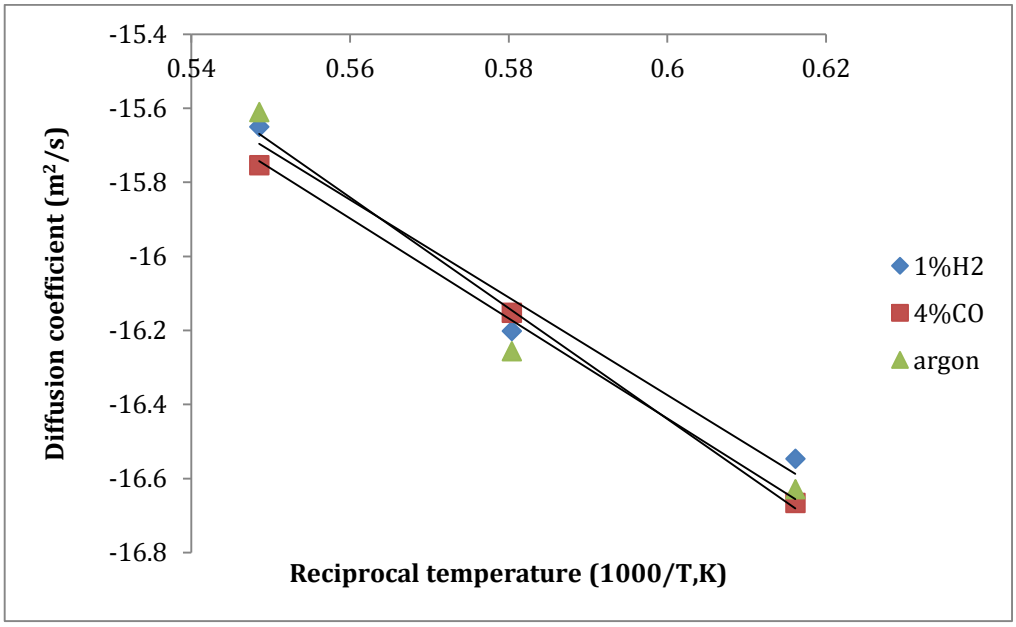

Figure 4.25 D_{Fe} in samples aged under different atmospheres at different temperatures

The following Ahhrenius equations describe the trend lines in Figure 4.25.

For 1% H_2/N_2:

$$D_{Fe} = 4.7 \times 10^{-9} \times exp\left(\frac{-312\text{kJ/mol}}{RT}\right) \text{m}^2/\text{s} \quad (4.41)$$

For 4% CO/N_2:

$$D_{Fe} = 3.5 \times 10^{-8} \times exp\left(\frac{-340\text{kJ/mol}}{RT}\right) \text{m}^2/\text{s} \quad (4.42)$$

For Argon:

$$D_{Fe} = 3.4 \times 10^{-8} \times exp\left(\frac{-345\text{ kJ/mol}}{RT}\right) \text{m}^2/\text{s} \quad (4.43)$$

All equations above are in a good agreement with Ahhrenius equations reported in literature for the iron lattice diffusion in alumina. The activation energies are not far away from 345 kJ/mol as reported by Lesage et al[18].

4.3.3 Mechanisms involved in aging treatments.

(a) The reduction reaction mechanisms at the gas/solid interface

As indicated in Chapter 2, the hydrogen diffusion in alumina is usually assumed to take place by transport of hydrogen atoms. Ernsberger[20] also proposed that protons can't exist in any solid even momentarily. It has been reported that hydrogen molecules will not dissociate significantly into atoms unless the temperature is above 3300K (3023℃).[21] Therefore it is unlikely that the hydrogen molecules would dissociate into atoms during the heat treatments in this project. Thus it seems reasonable to assume that during the aging treatments, hydrogen molecules would attach to the solid surface and induce Reaction 4.23.

The molecule size of CO and atomic size of O are both too large compared with the lattice parameters of alumina solid, thus it is impossible for CO and oxygen atoms to be transported as interstitials in the alumina lattice.[22] Therefore, it is probable that in 4% CO/N_2 the carbon mono-oxide would attach to the solid surface and induce the reduction reactions, while in argon, the oxygen ions in the solid solution will lose electrons and form oxygen molecules at the g/s interface.

(b) Oxygen Vacancy grain boundary diffusion

As the reduction reactions proceed at the g/s interface, the g/s interface will accumulate lots of oxygen vacancies and electrons, which creates a high chemical potential of oxygen vacancies and electronic potential at the g/s interface compared with the core of the samples. Thus the diffusion of oxygen vacancies and electronic conduction occurs down the chemical

potential. Oxygen vacancies have higher mobility than oxygen interstitials, thus the transport of oxygen is suggested to be mainly by vacancy mechanism.[1]

There are two routes for the diffusion of oxygen vacancies in polycrystalline alumina: matrix diffusion and grain boundary diffusion. Atoms/vacancies in grain boundaries have higher mobility than within grains, so usually grain boundaries provide a faster pathway for diffusion. As discussed in Chapter 2, the matrix diffusion of oxygen vacancies in alumina is much slower than the oxygen vacancy grain boundary diffusion. Hence it is probable that the oxygen vacancies diffuse towards the core of the sample mainly via grain boundary diffusion. The Fe^{3+} dissolved in the solid solution near the grain boundaries will be reduced to Fe^{2+} by the electrons on the grain boundaries (Reaction 4.24) and segregate to the grain boundaries to form intergranular $FeAl_2O_4$ particles which may then be reduced further to Fe metallic particles.[6]

As stated in section 4.3.2.1, it is probable that D_{surf} and D_{bulk} were the same one (D_{app}, D_{app} is the apparent oxygen vacancy grain boundary diffusivity in alumina in this project). As discussed above, oxygen vacancies are the only possible diffusion species that can be controlling the diffusion process from the gas/solid interface to the bulk. The activation energy of D_{app} is also very close to the literature values of oxygen vacancy grain boundary diffusion. Furthermore, as stated in section 4.3.2.1, although the values of D_{app} are different among different atmospheres, the values are in the same order of magnitude, and the corresponding activation energies measured are comparable. Therefore it is probable that the D_{app} represents the oxygen vacancy grain boundary diffusivity. However, D_{app} at 1450 ℃ is around 2 to 6 orders of magnitude greater than any oxygen vacancy grain boundary diffusion coefficients in polycrystalline alumina reported in the literature[19], depending on different materials and methodologies (mainly monolithic alumina and isotope tracing techniques).

Three reasons were proposed to explain the extremely high diffusion kinetics measured here compared with the literature.

The first reason is the high oxygen vacancy concentration produced during reduction reactions. As discussed in Chapter 2, the oxygen ion diffusion coefficients in both single crystalline and polycrystalline alumina in literature, were usually obtained by isotope tracer profiles, nuclear resonance profile and so on. However, the differences caused by different methodologies should be less than an order of magnitude. Although uncertain levels of impurities are present, alumina materials used in literature are usually monolithic so the extrinsic defect concentrations are limited.

Considering the equation of the diffusion coefficient:

$$D_v = \frac{1}{6}\boldsymbol{\Gamma}_v \alpha^2 \tag{4.44}$$

Where D_v is diffusion coefficient of vacancy, α is jumping distance, Γ_v is vacancy jumping frequency. Taking sample H4-1400-20 as an example, a maximum oxygen vacancy concentration of around 2.2×10^{-2} could be generated in the bulk part (the calculations are shown in Appendix A). Such oxygen vacancy concentration is far above the limit that under which point defects in solid solution are dilute enough that they will not interact with each other. [1,17] A single oxygen atom in samples during aging treatments, will be surrounded by more vacancies, hence the possibility of successful vacancy jumping will be higher, i.e. Γ_v would be increased. Therefore, the oxygen vacancy grain boundary diffusion could be significantly increased. In this case, Γ_v will be dependent on oxygen vacancy concentration. Furthermore, Fe^{3+} has a larger ionic radius than Al^{3+}, which would expand the crystal structure and hence results in a larger jumping distance α, though this effect might be small.[3] In addition, according to the reports by Lagerlof et al[23], the theoretical maximum oxygen vacancy diffusivity D_{1400} in the bulk part of samples aged at 1400 ℃ under 4% H_2/N_2 with an

oxygen vacancy concentration of 2.2×10^{-2} could be calculated as 1×10^{-13} m^2/s, which is not far away from 3.25×10^{-13} m^2/s as measured (the calculation will be shown in Appendix B).

The second reason may lie on the improved grain boundary mobility. As discussed in section 4.2.3.8, the segregation of Fe^{2+} to high-energy non-basal grain boundaries enhances the grain boundary mobility. Since the rapid grain growth was observed in the aged samples, it is reasonable to speculate that the increased grain boundary mobility could result in an enhancement of the oxygen vacancy grain boundary diffusion.

Thirdly, there may be a very thin glassy phase film on the grain boundary, which could enhance the oxygen vacancy transport. The BSE image (Figure 4.2(c)) showed the existence of second phase particles in the as-sintered solid solution, with a volume fraction of up to 1.5%. Besides elements of iron, aluminium and oxygen, EDX results confirmed that the particles also contained calcium, magnesium and silicon as described in 4.2.2. These impurities in the sample could come from two sources. The first source is the furnace tube. Although the furnace tube is made of Al_2O_3, it contains some impurities. At high temperatures, the tube could evaporate SiO_2 which affects the chemical composition of the atmosphere near the sample surface. Another source might be the powder processing. During aging, these impurity particles could cause the formation of silicate glasses along alumina grain boundaries even though they are only present in small amounts. It was suggestd that such intergranular glass would provide a faster transport path.[17] However, such a glass phase should be very thin so that can be hardly detected by SEM in the aged samples. Furthermore, the silicate glasses could form a liquid phase in high temperatures[1,24], thus both diffusivities of grain boundaries and the mobility of grain boundaries could be further significantly increased. Therefore, both the silicate glass and the liquid phase could improve the atomic mobility and hence increase the oxygen vacancy diffusivity.

In conclusion, it is probable that oxygen vacancy grain boundary diffusion is the main diffusion mechanism operating in different samples aged under different atmospheres.

(c) The origin of 'iron free zone'

There are two origins for the 'iron free zones'.

The first one is the iron ion matrix diffusion. The oxygen vacancies at the gas/solid interface are suggested to be transported mainly through the grain boundaries as described in (b). Fe^{3+} atoms adjacent to the grain boundaries could then be reduced to Fe^{2+}, resulting in a significant driving force for segregation of Fe^{2+} to the grain boundaries and then form spinel particles along the grain boundary. Thus the intergranular particles could deplete the iron atoms adjacent to grain boundaries and thus formed an 'iron free layer'. This would further lead to matrix diffusion of Fe^{3+} from within the grains towards the grain boundaries, which increased the 'iron free zone' size. (Figure 4.26) Referring to Figure 4.3, there are some blurred boundaries between dark regions and light regions indicating a diffusion process.

The second origin for 'iron free zones' is the migrating grain boundaries. The rapid grain growth suggested that the grain boundaries during the aging were be highly mobile. The highly mobile grain boundaries near the dark regions could move towards and absorb the light regions, thus the Fe^{3+} ions can be absorbed by the moving grain boundaries. Meanwhile, the absorbed Fe^{3+} at the grain boundaries can diffuse to the intergranular particles through grain boundary which is much faster than the matrix diffusion. Thus the dark region can be expanded much faster. Referring to Figure 4.3, it can be seen that some of the dark regions have a sharp boundries indicating a clear boundary between the light and dark regions, which is consistent with this argument.

As the grain size results revealed, there are two stages of grain growth during aging treatments: rapid grain growth and particle pinning. In the rapid grain growth stage, it is

probable that the moving grain boundaries dominated the formation iron free zone since it is faster than the iron ion matrix diffusion. In the particle pinning stage, the grain boundaries are pinned by the particles, thus the matrix diffusion should be the main origin of iron free zones.

As stated in section 4.3.2.4, the size of the iron-free zone follows solutions to Fick's second law in samples aged under all atmospheres, and the corresponding diffusivity equations measured are all in a good agreement with the Ahrrenius equation reported in the literature for the iron lattice diffusion in alumina[19]. This is probably because the iron matrix diffusion dominated the formation of iron free zone after 5 hours' aging.

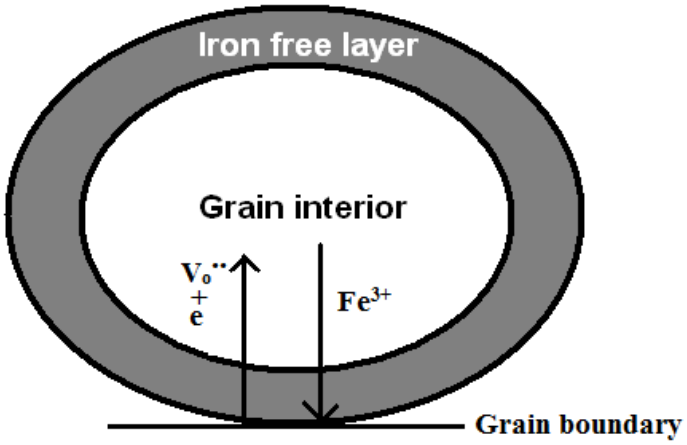

Figure 4.26 Diffusion processes within grains during aging treatment.

4.3.4 PRCS Model

Despite the differences in details, samples aged in argon, 1% H_2/N_2, and 4% CO/N_2 share a similar microstructural pattern as was found in 4% H_2/N_2 (section 4.2.3.4). This suggested that the microstructural developments in samples aged under different atmospheres could be interpreted by one model. A model for precipitation by reduction of ceramic solid solution (PRCS model) is therefore proposed, which is based on the consideration of the chemical potential and diffusion in the aged samples. This model has two aspects: the macroscopic and microscopic. The macroscopic aspect of PCSR (4.3.4.1) mainly addresses the phase change

and the diffusion profiles which can be further related to the intergranular second phase distribution, while the microscopic aspect of PRCS (4.3.4.2) addresses the intragranular precipitation. The basic ideas of PCSR are stated as followings.

The chemical potentials of oxygen vacancy for Fe (μ_{Fe}), $FeAl_2O_4$($\mu_{FeAl2O4}$) and as-sintered solid solution ($\mu_{(Fe,Al)2O3}$) are all constant, so the corresponding oxygen vacancy concentrations in solid solution should also be fixed.[16] In the PRCS model, region α is defined as a region with chemical potential above μ_{Fe}. Region α contains both Fe and $FeAl_2O_4$ as second phase particles. Region β is defined as region with chemical potential above $\mu_{FeAl2O4}$ but lower than μ_{Fe}, which only contains $FeAl_2O_4$ as the second phase. Region γ is the solid solution alumina without any second phase particles, with chemical potential above $\mu_{(Fe,Al)2O3}$ but lower than $\mu_{FeAl2O4}$.

4.3.4.1 The macroscopic aspect of PRCS model

Figure 4.27 and Figure 4.28 described the macroscopic aspect of PCSR model. As described in section 4.3.2.1, the oxygen vacancy concentration at the gas/solid interface $[V_o^{\cdot\cdot}]_{g/s}$ should be a constant during the aging.

Figure 4.27 (a-b) showed that the PRCS model responsible for samples aged in 4% H_2/N_2 and some samples aged in 1% H_2/N_2, while Figure 4.27(c) and (d) are responsible for most samples aged in 1% H_2/N_2, and samples aged in 4% CO/N_2 and argon. It should be noted that the $[V_o^{\cdot\cdot}]$ profiles in Figure 4.27 followed the error functions to Fick's second law, corresponding to samples which could be regarded as semi-infinite with surface concentration fixed. The $[V_o^{\cdot\cdot}]$ profiles may also follow Fourier solutions to Fick's second law (line (2) in Figure 4.28) in some cases, where the samples are regarded as thin films. In general, within short aging durations, the error function solutions can be applied to the $[V_o^{\cdot\cdot}]$ profiles (line (1) in Figure 4.28), while with sufficiently long aging duration, Fourier

solutions should be applied (line (2) in Figure 4.28). Furthermore, since the precipitation will consume oxygen vacancies, the real $[V_o^{\cdot\cdot}]$ profiles can be pushed leftwards compared with the ideal $[V_o^{\cdot\cdot}]$ profiles.

As stated in 4.3.2.1, it is assumed that the volume fraction of $FeAl_2O_4$ particles in section β is proportional to the $[V_o^{\cdot\cdot}]$ profiles. Since the volume fraction of intragranular particles is far less than that of intergranular particles, the $[V_o^{\cdot\cdot}]$ lines can be regarded as $[V_o^{\cdot\cdot}]_{gb}$ line, where $[V_o^{\cdot\cdot}]_{gb}$ is the oxygen vacancy concentration on the grain boundaries.

The influence of varying processing parameters on the oxygen vacancy concentration lines of PRCS could be categorized into four actions: pushing upwards, downwards, leftwards and rightwards. (Figure 4.29) Generally, the $[V_o^{\cdot\cdot}]$ profiles can be pushed upwards by higher aging temperature, more reducing atmospheres and higher gas flow rate, rightwards by longer aging duration, smaller sample thickness and higher MgO dopant level. It is easy to understand the influences of the chemical composition of atmosphere, temperature and time on the $[V_o^{\cdot\cdot}]$ lines, while the effects of gas flow rates and MgO dopant level are more complicated and explained as followings.

The effect of gas flow rate on $[V_o^{\cdot\cdot}]$ lines can be explained as: at the very beginning of the aging treatment, $[V_o^{\cdot\cdot}]_{g/s}$ in lower gas flow rates (even 10 ml/min) should be the same as in 200 ml/min. However, if the gas flow rate is too slow, as reduction reactions continue, hydrogen in the furnace tube could be gradually used up, which results in a decreased $[V_o^{\cdot\cdot}]_{g/s}$ and hence $[V_o^{\cdot\cdot}]$ lines would be pushed downwards.

It was reported that MgO mostly segregates to grain boundaries [25] and increase ionic conductivity and oxygen vacancy grain boundary diffusivity due to the creation of oxygen vacancies:

$$2MgO \rightarrow 2Mg_{Al}' + V_o^{\cdot\cdot} + 2O_o^x \quad (4.45)$$

Furthermore, the segregation of MgO on grain boundaries would inhibit abnormal grain growth due to a solute drag effect.[26] This confirms the result that a higher amount of MgO dopant results in smaller grain size both before (Figure 4.11) and after aging (Table 4.9). Thus the concentration of grain boundaries in as-sintered samples is increased with higher MgO dopant amount and hence more paths for grain boundary diffusion, i.e grain boundary diffusivity would be further increased. Therefore, higher MgO dopant level could push the $[V_o^{\cdot\cdot}]$ lines rightwards.

The results section indicates that the $[V_o^{\cdot\cdot}]$ lines in H4-1450-20 samples with thickness below/ equal 1.4 mm, should follow Fourier solution which in this case becomes a sine wave after a short duration of aging (Figure 4.28). The $[V_o^{\cdot\cdot}]$ lines therefore would be pushed rightwards with reduced sample thickness.

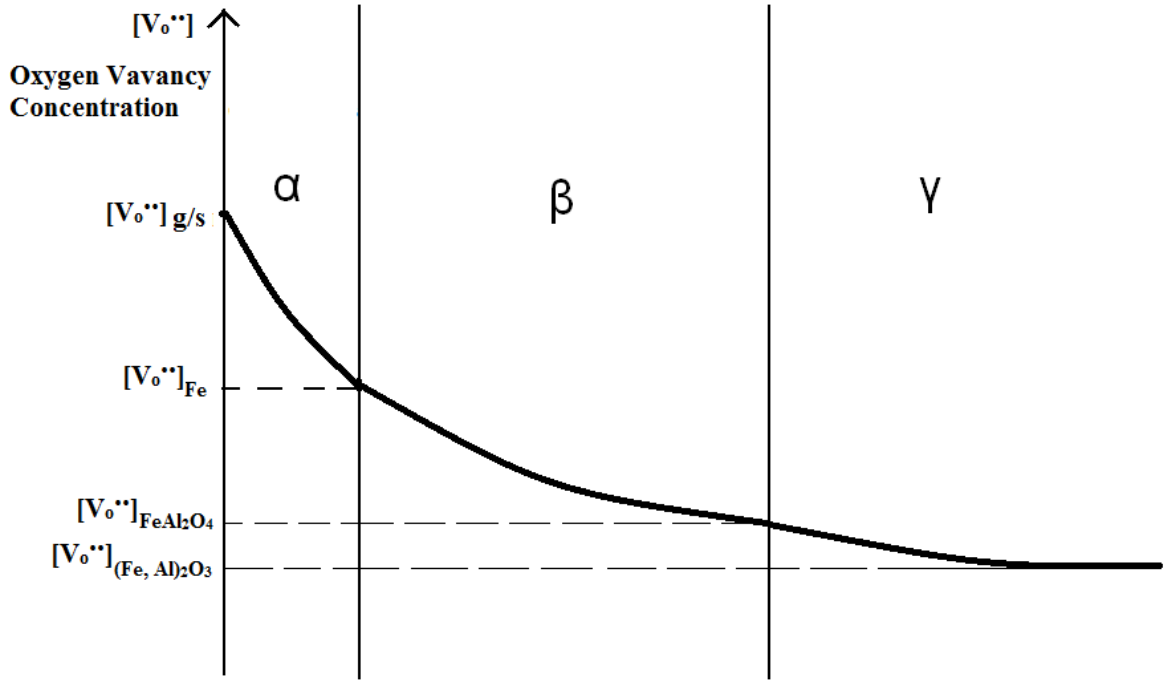

(a)

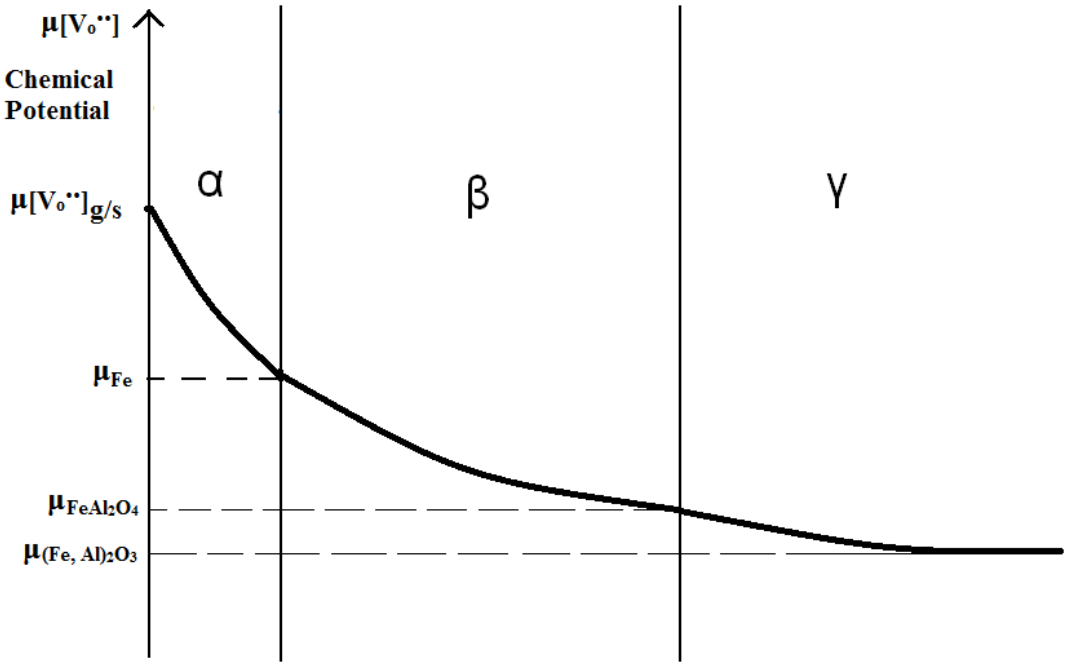
μ[V₀••]
Chemical Potential
α
β
γ
μ[V₀••]g/s
μFe
μFeAl2O4
μ(Fe, Al)2O3

(b)

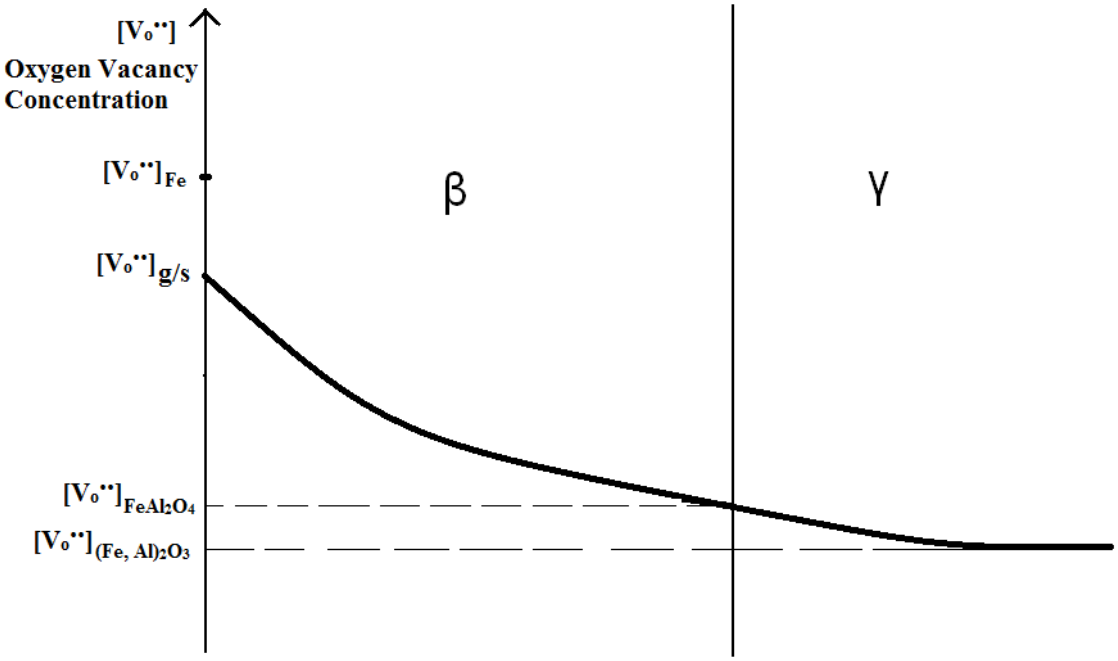
[V₀••]
Oxygen Vacancy Concentration
β
γ
[V₀••]Fe
[V₀••]g/s
[V₀••]FeAl2O4
[V₀••](Fe, Al)2O3

(c)

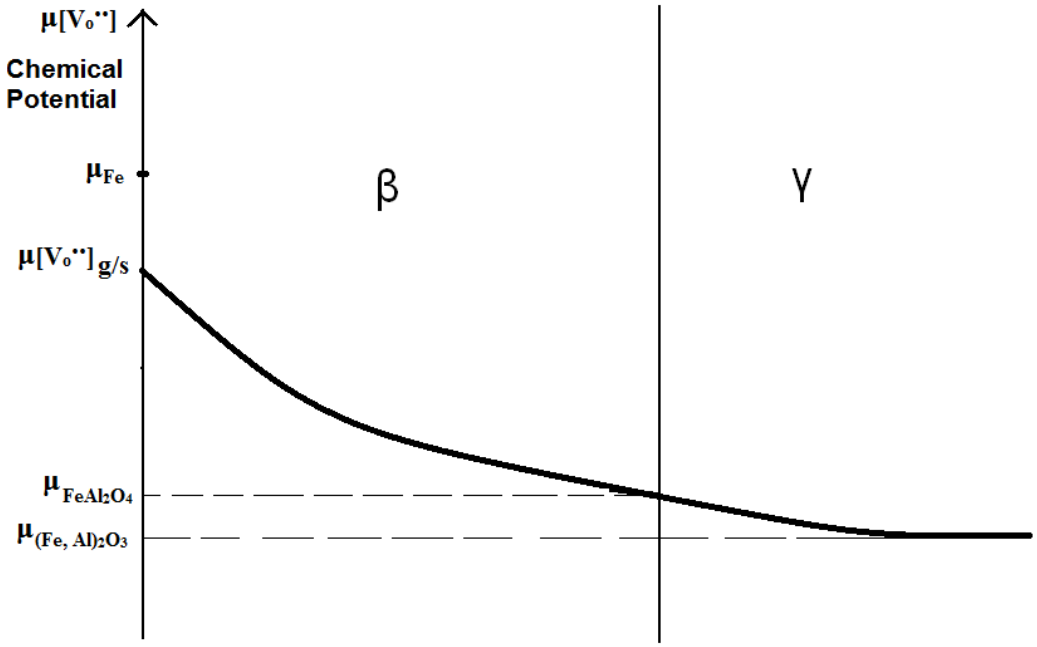

(d)

Figure 4.27 (a) The oxygen vacancy concentration profile in the aged samples under 4% H_2/N_2 and some of the samples aged under 1% H_2/N_2; (b) profile of chemical potential correspond to (a); (c) the oxygen vacancy concentration profile in most of the samples aged under 1% H_2/N_2,the aged samples under 4% CO/N_2 and argon; (d) profile of chemical potential correspond to (c). The thickness of the corresponding samples are all above 2.5mm.

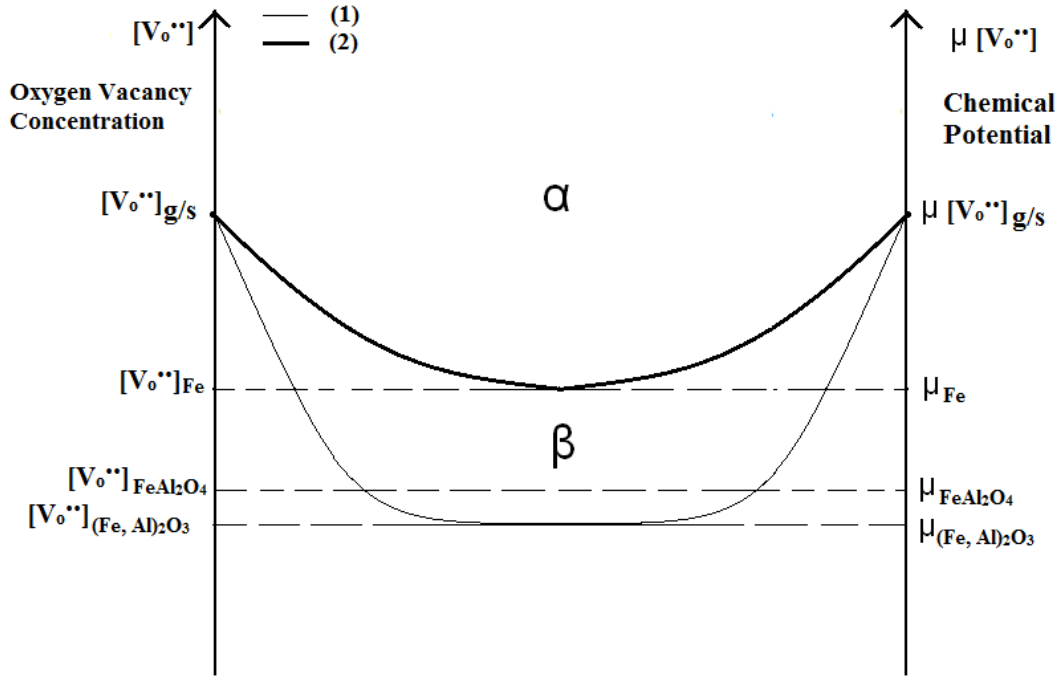

Figure 4.28 The oxygen vacancy concentration and profile of chemical potential in the samples aged under 4% H_2/N_2 where the Fourier solution applies.

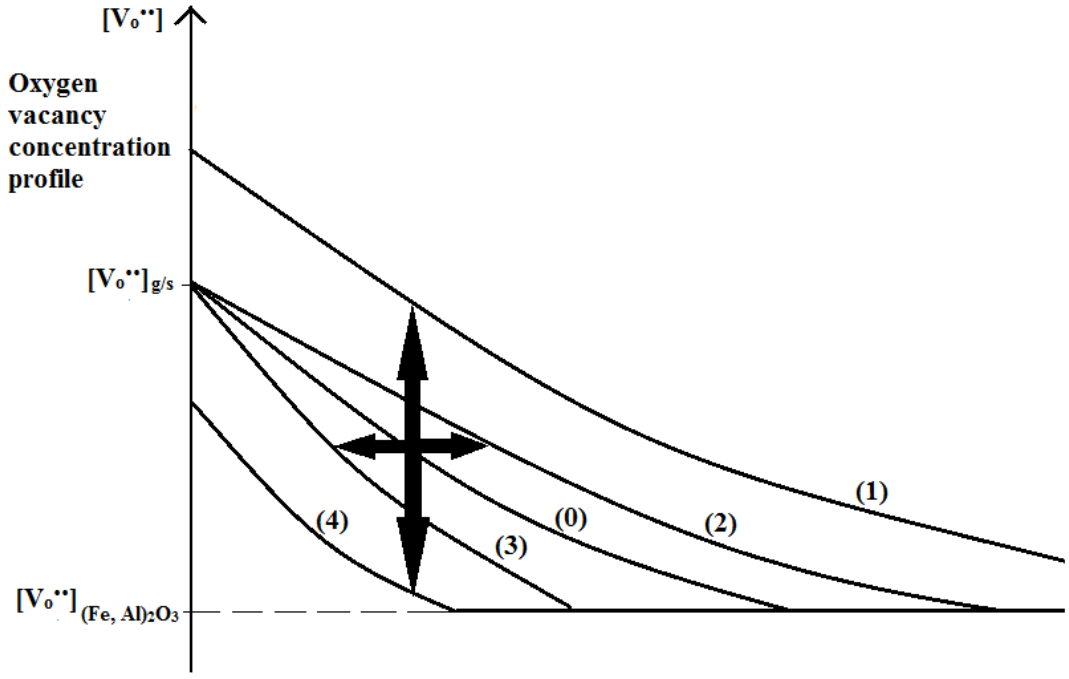

Figure 4.29 'Four actions', the influence of varying processing parameters on the oxygen vacancy lines of PRCS. Line (0) can be pushed upwards to line (1)/rightwards to line (2)/leftwards to line(3)/downwards to line (4).

4.3.4.2 The microscopic aspect of PCSR model: the intragranular precipitation

The accumulation of oxygen vacancies and electrons at grain boundaries will make oxygen vacancy concentration at the grain boundary much higher than in the core of the grains. Thus a chemical potential of oxygen vacancy will be created between the grain core and the grain boundaries, which induce the transportation of oxygen vacancies and electrons into the grains. This may cause the intragranular precipitation.

Referring to Figure 4.26, it can be seen that the intragranular precipitation would not happen if the oxygen vacancy concentration in the grain core $[V_o^{\cdot\cdot}]_{gc}$ is below $[V_o^{\cdot\cdot}]_{FeAl2O4}$. Similarly, if the Fe^{3+} concentration in the grain core $[Fe^{3+}]_{gc}$ is too low, the chemical potential of iron ions would not be sufficiently high for intragranular precipitation. Thus it is reasonable to say that the intragranular precipitation only happens when $[V_o^{\cdot\cdot}]_{gc}$ is above $[V_o^{\cdot\cdot}]_{FeAl2O4}$ and $[Fe^{3+}]_{gc}$ is above $[Fe^{3+}]_{FeAl2O4}$. $[Fe^{3+}]_{FeAl2O4}$ is the Fe^{3+} concentration below which no intragranular particles could precipitate and is a constant.

Given a period of aging time, the intragranular precipitation in the grains can be categorized into three situations, as shown in Figure 4.30:

1. If $[V_o^{\cdot\cdot}]_{gc} < [V_o^{\cdot\cdot}]_{FeAl2O4}$, no intragranular precipitation would happen (quadrant II and III);
2. If $[V_o^{\cdot\cdot}]_{gc} > [V_o^{\cdot\cdot}]_{FeAl2O4}$ and $[Fe^{3+}]_{gc} > [Fe^{3+}]_{FeAl2O4}$, the intragranular precipitation would happen (quadrant I);
3. If r_o $[V_o^{\cdot\cdot}]_{gc} > [V_o^{\cdot\cdot}]_{FeAl2O4}$ and $[Fe^{3+}]_{gc} < [Fe^{3+}]_{FeAl2O4}$, no intragranular precipitation would happen (quadrant IV);

Considering Reaction 4.13, additional definitions can be made:

t is the aging time;

The rate of increase of local oxygen vacancy concentration in the grain core ($[V_o^{\bullet\bullet}]_{gc}$) is written as $\frac{d[V_O^{\bullet\bullet}]_{gc}}{dt}$, it is a positive function of $[V_o^{\bullet\bullet}]_{gb}$ and oxygen vacancy matrix diffusivity;

The rate of decrease of local Fe^{3+} ion concentration in the grain core ($[Fe^{3+}]_{gc}$) is written as $\frac{d[Fe^{3+}]_{gc}}{dt}$, it is a positive function of Fe^{3+} ion matrix diffusivity;

$[V_o^{\bullet\bullet}]_{gb}$ is the oxygen vacancy concentration in the grain boundary;

$[V_o^{\bullet\bullet}]_0$ is the oxygen vacancy concentration in the as-sintered solid solution, which is a constant;

$[Fe^{3+}]_0$ is the Fe^{3+} concentration of the as-sintered solid solution, which is a constant.

Based on the definitions above, two equations can be given:

$$[V_O^{\bullet\bullet}]_{gc} = \frac{d[V_O^{\bullet\bullet}]_{gc}}{dt} \times dt + [V_O^{\bullet\bullet}]_o \tag{4.46}$$

$$[Fe^{3+}]_{gc} = [Fe^{3+}]_O - \frac{d[Fe^{3+}]_{gc}}{dt} \times dt \tag{4.47}$$

Therefore the intragranular precipitation can be simplified as a competition between $\frac{d[V_O^{\bullet\bullet}]_{gc}}{dt}$ and $\frac{d[Fe^{3+}]_{gc}}{dt}$.Furthermore, there is another competition involved in the precipitation of intragranular particles: competition between intergranular and intragranular precipitation. The intergranular and intragranular precipitation are competing for both oxygen vacancies and iron ions. Since the intergranular precipitation will lower the $[V_o^{\bullet\bullet}]_{gb}$, so $\frac{d[V_O^{\bullet\bullet}]_{gc}}{dt}$ will be lowered. Thus the intergranular precipitation will decrease the tendency of intragranular precipitation.

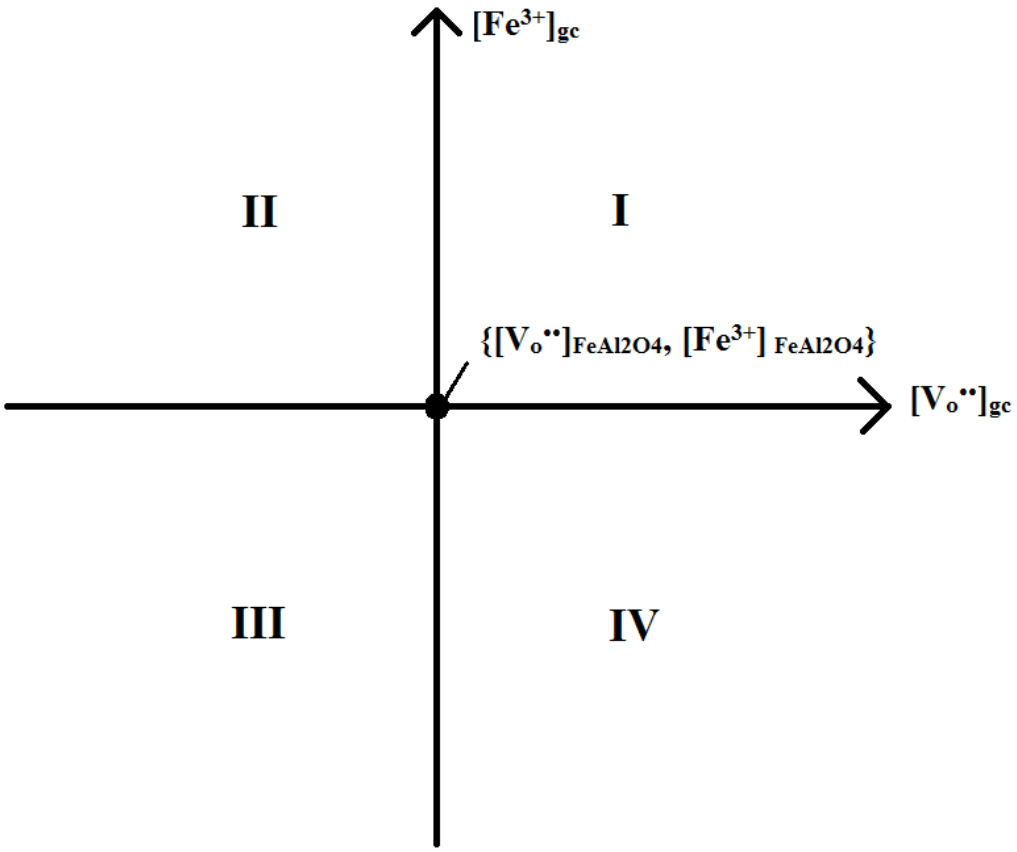

Figure 4.30. Four quadrants describing the oxygen vacancy and iron matrix diffusion situations. The origin is set as $\{([V_o^{\bullet\bullet}]_{FeAl2O4}, [Fe^{3+}]_{FeAl2O4}\}$.

4.3.5 Applications of PRCS model in microstructural developments during aging treatment

4.3.5.1 Formation of the surface layer

In terms of phase, the surface layers of samples aged in both 4% H_2/N_2 (Figure 4.3(b)) and some of the samples aged in 1% H_2/N_2 (Figure 4.9(b)) are in region α as shown in Figure 4.27 (a) and (b). The surface layers of most of the samples aged in 1% H_2/N_2, and samples aged in both 4% CO/N_2 (Figure 4.9(d)) and argon (Figure 4.9(e)) are in region β as shown in Figure 4.27 (c) and (d). This can be explained by different $[V_o^{\bullet\bullet}]_{g/s}$ in the different atmospheres. The thickness of region α is dependent of $[V_o^{\bullet\bullet}]$ lines so higher aging temperature (4.2.3.2), longer aging duration (4.2.3.3), higher gas flow rate (4.2.3.5), higher

MgO dopant level (4.2.3.6) and reduced sample thickness (4.2.3.7) would increase the surface layer thickness.

In terms of intragranular precipitation, only surface layers of samples aged in 4% H_2/N_2 and some of the samples aged in 1% H_2/N_2 contain intragranular particles. This is because [$V_o^{\bullet\bullet}$] lines are pushed upwards in more reducing atmospheres, which leads to high $\frac{d[V_O^{\bullet\bullet}]_{gc}}{dt}$, while $\frac{d[\mathrm{Fe}^{3+}]_{gc}}{dt}$ is independent of atmospheres.

4.3.5.2 The porosity of the surface layer

The porosity of the surface layers compared with the corresponding bulk part in different atmospheres can be explained by phase change. The calculation of volume shrinkage induced by the reduction reactions is shown in Appendix C. As the calculations show, the complete precipitation of $FeAl_2O_4$ leads to a 0.4% volume reduction, and complete precipitation of metallic Fe leads to a 4.5% volume reduction of the sample. Hence the precipitation of metallic Fe could result in a much higher porosity than that caused by $FeAl_2O_4$ precipitation. Furthermore, both the resultant iron metallic particles and $FeAl_2O_4$ particles tend to vaporize at high aging temperatures [27], which would increase the porosity further. Particle pull-out may also lead to apparent porosity, but its effect could be neglected since the bulk part is always much less porous than the surface layer.

In samples aged in 4% CO/N_2, the surface layer is also more porous than the bulk part. It has been reported that Fe_2O_3 will decompose into metallic Fe and oxygen in air when heated above 1450 ℃[28]. Since the surface layer is closer to the reducing atmosphere, it is possible that the $FeAl_2O_4$ particles in the surface layer would also decompose and evaporate into the atmosphere.

No second phase particle was found in the surface layers of samples aged in argon. These surface layers are not obviously more porous than in the bulk parts. This is probably because the $[V_o^{\bullet\bullet}]_{g/s}$ in these samples are so low that the volume fraction of $FeAl_2O_4$ particle produced is very low (only 2 vol% maximum in sample Ar-1450-20), hence the induced volume shrinkage and evaporation of particles would be very low. EDX results also showed that the Fe concentration in the matrix of the surface layer (4.2 ±0.3 wt%) is lower than the solid solution (7 ±0.5 wt%), thus some Fe atoms in the surface should have evaporated to the atmosphere.

4.3.5.3 The structure of the sample bulk

In terms of phase change, the bulk parts of samples aged in all atmospheres only contain $FeAl_2O_4$ particles, and hence are all in region β. The volume fraction of intragranular $FeAl_2O_4$ particles in the bulk part is negligible compared with that of intergranular particles as shown in the results section. Thus the volume fraction of intergranular $FeAl_2O_4$ particles should follow the solutions to Fick's second law for the different cases (section 4.3.2.1).

In terms of intragranular precipitation, the distribution of intragranular particles in the bulk part could be characterized by $P_{bulk}=(P_{nano}- P_{surf})$. Referring to the microscopic aspect of PRCS model, both high $\frac{d[V_o^{\bullet\bullet}]_{gc}}{dt}$ and low $\frac{d[\mathrm{Fe}^{3+}]_{gc}}{dt}$ favour intragranular precipitation.

High $[V_o^{\bullet\bullet}]$ would increase $\frac{d[V_o^{\bullet\bullet}]_{gc}}{dt}$ and hence favours intragranular precipitation, so this is why longer aging durations, smaller sample thickness, more reducing atmospheres and higher MgO dopant would result in an increased P_{bulk}, i.e. the volume fraction of quadrant I in the bulk part is increased. The results section also shows that with elevated aging temperatures, P_{bulk} increases. There are two reasons. The first reason is that at higher temperatures, the $[V_o^{\bullet\bullet}]$ line of the PRCS model would be pushed upwards, which results in a higher $\frac{d[V_o^{\bullet\bullet}]_{gc}}{dt}$. Another

reason is that the average activation energy of matrix oxygen vacancy diffusion in alumina is around 644kJ/mol (as discussed in Chapter 2), which is much higher than that of Fe^{3+} matrix diffusion in alumina reported to be around 300kJ/mol[18]. Thus the increment of Fe^{3+} matrix diffusivity along with temperature increase is much less than that of oxygen vacancy matrix diffusivity, i.e $\frac{d[V_O^{\bullet\bullet}]_{gc}}{dt}$/ $\frac{d[\mathrm{Fe}^{3+}]_{gc}}{dt}$ is increased.

4.3.5.4 The nucleation and growth of intergranular precipitatie

$FeAl_2O_4$ is based on a FCC close-packed oxygen sub-lattice and Fe is a FCC close packed structure, while the solid solution is the corundum structure.[1] This indicates that the phase transformation within grains needs local atomic rearrangements. Furthermore, as stated in the PRCS model, the precipitation of intragranular particles relies on the competition between oxygen vacancy and iron ion matrix diffusion. Therefore, both size and volume fraction of intergranular particles will be much larger than intragranular particles.

a. The nucleation of intergranular precipitation

Although the driving force for precipitation here is provided by the reduction reactions instead of temperature, the kinetics of crystal precipitation follows the same theory. As Porter and Easterling[16] suggested, the heterogeneous nucleation rate of intergranular particles, can be given by an equation of the form:

$$R_{nuc} = \omega C_1 \exp\left(-\frac{\Delta G_m}{kT}\right) \cdot \left(-\frac{\Delta G^*}{kT}\right) nuclei\ m^{-3} s^{-1} \tag{4.48}$$

Where $R_{nuc}$is the nucleation rate of intergranular $FeAl_2O_4$ particles, T is the temperature, k is the Boltzmann constant, C_1 per unit volume is the density of heterogeneous nucleation sites, ω is a factor that includes the vibration frequency of the atoms and the area of the critical nucleus, ΔG_m per atom is the activation energy for atomic migration, ΔG^* is the total free energy change for nucleation. Since the main factor controlling ΔG^* is the driving force, and

the driving force in this project is provided by reduction reactions[16], thus ΔG^* can be related to the concentration of oxygen vacancies and electrons.

Higher $[V_o^{\bullet\bullet}]_{gb}$ provides higher driving force for intergranular particle nucleation, i.e. an increased $exp\left(-\frac{\Delta G^*}{kT}\right)$, hence R_{nuc} would be increased. This is why more reducing atmosphere, longer aging duration, higher gas flow rate, higher MgO dopant level and reduced sample thickness would increase the particle density (Table 4.16) Another reason why the higher particle density caused by higher MgO dopant level is that the smaller grain size caused by higher MgO dopant level could increase the nucleation site density (i.e. a higher C_1).

Referring to Figure 4.31, it can be seen that generally the particle density increased with elevated aging temperature. Although higher temperature could result in lower grain boundary density and hence a smaller C_1, higher aging temperatures can push the oxygen vacancy profiles upwards, hence $(-\Delta G^*)$ is increased. Therefore the increase of $\exp\left(-\frac{\Delta G_m}{\mathrm{kT}}\right)\cdot\left(-\frac{\Delta G^*}{kT}\right)$ with elevated aging temperature overcame the decrease of C_1 and hence resulted in higher R_{nuc}. Nevertheless, at 1550 ˚C, after 5 hours the particle density decreased. This is probably because Ostwald ripening[29] is fast at 1550˚C thus small particles could diffuse fast to the large particles which reduced the particle density.

b. The growth of intergranular precipitation

For unit area of interface to advance a distance, dx, a volume fraction ($1\times\ dx$) must be converted from solid solution containing C_γ moles of Fe^{3+} per unit volume to $FeAl_2O_4$ containing C_β moles of Fe^{2+} per unit volume, i.e $(C_\beta - C_\gamma)dx$ moles of Fe^{2+} must be supplied by Fe^{3+} matrix diffusion.[16] Assume reduction reaction $Fe^{3+} \rightarrow Fe^{2+}$ is sufficiently fast. The flux of Fe^{3+} through unit area in time dt is given by $D_{inter}(\frac{dC}{dx})dt$, where D_{inter} is the Fe^{3+}

inter-diffusion coefficient. Equating these two quantities gives the expression of the growth rate of the precipitate:

$$R_{gro} = \frac{dx}{dt} = \frac{D_{inter}}{C_\beta - C_\gamma} \times \frac{dC}{dx} \quad (4.49)$$

where R_{gro} is the growth rate of intergranular $FeAl_2O_4$ particles. In this project, D_{inter} is dependent on both matrix diffusion of Fe^{3+} and grain boundary mobility. In the early stage of aging when grain boundary migration happens, D_{inter} is mainly dependent on grain boundary migration since it provides faster transport paths for Fe^{3+} to the nuclei. When grain boundary migration is inhibited by particle pinning, D_{inter} is mainly dependent on iron matrix diffusion.

Since the grain boundary migration and Fe^{3+} matrix diffusivity are not directly affected by oxygen vacancy concentration, R_{gro} and hence the particle size are not dependent on $[V_o^{\bullet\bullet}]_{gb}$. This is at least partially the reason why the particle size is independent of chemical composition of atmospheres (Figure 4.9), gas flow rate (Figure 4.10) or sample thickness (Figure 4.13).

At higher temperature, both Fe^{3+} matrix diffusion and grain boundary migration are faster, thus D_{inter} and hence R_{gro} will be both higher. Therefore the particle size increased with elevated aging temperature (Figure 4.31(b)).

Generally, the particle size increased with longer aging duration. At 1450˚C, the particle size varied little after 5 hours' aging. There are two possible reasons. The first reason is that the grain boundary migration was pinned by intergranular particles, thus the provision of Fe^{3+} to the grain boundary was mainly by Fe^{3+} matrix diffusion, which is slower than the grain boundary migration. Secondly, the $\frac{dC}{dx}$ is decreased after 5 hours, because the grain size is larger and hence the diffusion zone width for Fe^{3+} matrix diffusion is longer, thus R_{gro} is slower. Nevertheless, at 1550 ˚C, after 5 hours the particle was still growing because

although particle pinned the moving grain boundaries, the large particles can grow by Ostwald ripening[29].

Although the smaller grain size could shorten the Fe^{3+} matrix diffusion zone width, the grain migration might be stronger and further inhibit the particle size, thus the particles were smaller with higher MgO dopant level.

Table 4.16 Summary of the effect of other processing parameters on the particle density

Processing parameters	The effect of processing parameters on the particle density
Chemical composition of the atmosphere	As Figure 4.9 shows, at 1450℃ the intergranular $FeAl_2O_4$ particle volume fraction increased with more reducing atmospheres but the particle sizes were comparable. This indicates that the particle density increased with more reducing atmospheres.
Gas flow rate	Figure 4.10 showed that the volume fraction of the intergranular $FeAl_2O_4$ particle increased with higher gas flow rate while the particle size was not influenced. This indicates that the particle density increased with higher gas flow rate.
MgO dopant level	Figure 4.12 showed that the volume fraction of the intergranular $FeAl_2O_4$ particle increased with higher MgO dopant level while the particle size decreased with MgO dopant level. This indicates that the particle density increased with higher MgO dopant level.
Sample thickness	Figure 4.13 showed that the volume fraction of intergranular particles increases with reduced sample thickness, while the particle size almost stayed the same. This indicates a higher particle density with reduced sample thickness.

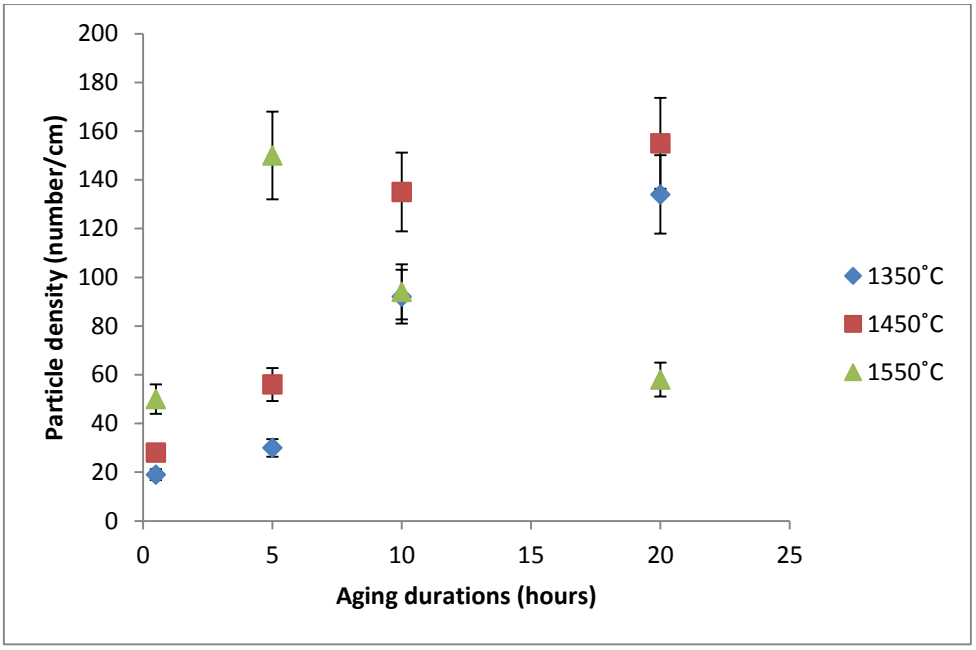

(a)

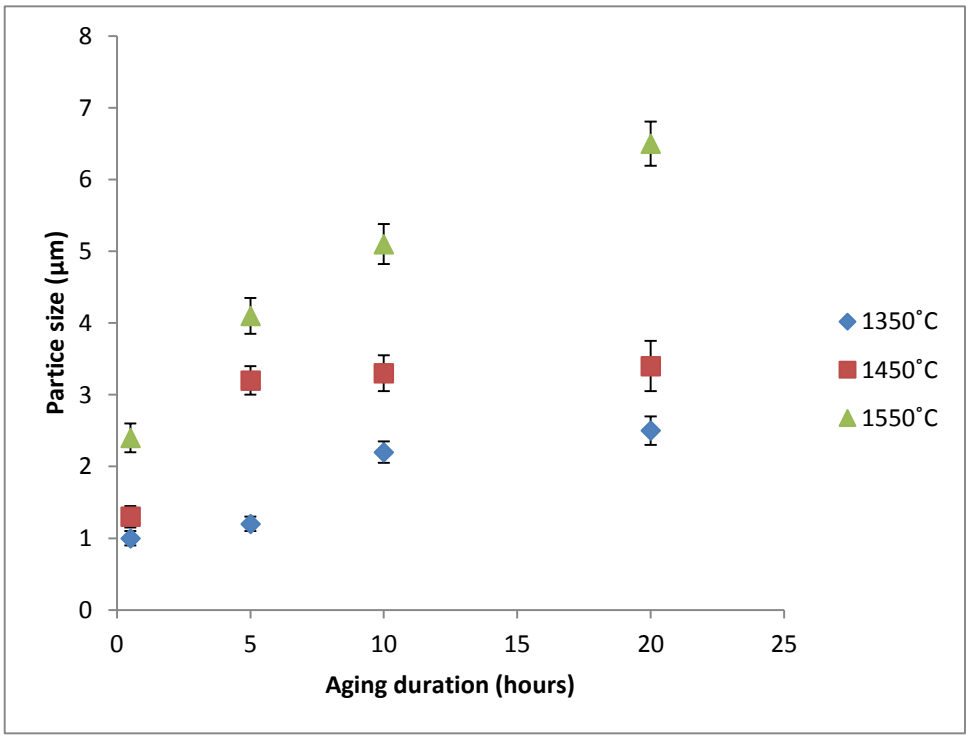

(b)

Figure 4.31 Particle density (a) and particle size (b) against aging time at the 500µm away from g/s interface in samples aged under 4% H_2/N_2 at different aging temperatures.

4.4 Summary

A systematic study on the microstructural evolution of Al_2O_3-10wt% Fe_2O_3 solid solution during aging treatment was made by varying different processing parameters. The thermodynamics, kinetics and mechanisms associated with the microstructural evolution was discussed. A model for precipitation induced by reduction in ceramic solid solution (PRCS model) was proposed to explain the microstructural developments, which matched the experiments results reasonably well. Therefore, model PRCS is suggested to be a useful tool for explaining and predicting the precipitation in ceramic solid solution by reduction reactions.

Appendix A:

Referring to Reaction 4.24, the formation of 2 mol $FeAl_2O_4$ consumes 1mol oxygen vacancies. 2 mols $FeAl_2O_4$ is a reduction product of 392.3 cm^3 solid solution. 392.3 cm^3 solid solution equals 1 mol Fe_2O_3 and 14.1 mol Al_2O_3. Each mol Fe_2O_3 or Al_2O_3 has 3 mols oxygen sites. Therefore the total oxygen sites of 392.3 cm^3 solid solution n(O) can be calculated:

$n(O)=3\times n(Fe_2O_3+Al_2O_3)=13\times(1+14.118)=45.4mol$

Thus the concentration of oxygen vacancies:

$[V_o^{\bullet\bullet}]=\frac{n(Vo^{\bullet\bullet})}{n(O)}/=\frac{1mol}{45.4mol}=2.2\times10^{-2}$

Appendix B:

As reported by Lagelof et al[23], when doped by 500at ppm MgO, the oxygen vacancy concentration in the purest undoped single crystalline alumina is increased from 1.5×10^{-7} to 3.8×10^{-5} (almost 62 times) at 1400 ℃, and oxygen vacancy diffusivity is correspondingly increased from 2×10^{-22} to 1×10^{-20} m^2/s (around 50times).

According to this ratio, the maximum oxygen vacancy diffusivity D_{1400} in the bulk part of samples aged at 1400 ℃ under 4% H_2/N_2 with an oxygen vacancy concentration of 2.2×10^{-2} could be calculated as:

$$\frac{D_{1400}}{7\times10^{-19}\ m^2/s}=\frac{2.2\times10^{-2}}{1.5\times10^{-7}}$$

$$\text{So } D_{1400}\approx 1.0\times10^{-13} m^2/s$$

where the average reported oxygen diffusivity in undoped polycrystalline alumina is about 7×10^{-19} m^2/s, the oxygen vacancy concentration in the purest undoped polycrystalline alumina is around 1.5×10^{-7}.[19] D_{1400} is not far away from 3.25×10^{-13} m^2/s as measured from samples aged at 1400 ˚C in 4% H_2/N_2.

Appendix C

Density data:

$\rho(Al_2O_3)$=4 g/cm^3,

$\rho(FeAl_2O_4)$=4.26 g/cm^3,

$\rho(Al_2O_3$-10wt%$Fe_2O_3)$=4.078 g/cm^3

Molecular weight:

$M(Al_2O_3)$=102 g/mol,

M(FeAl2O4)=174 g/mol,

$M(Fe_2O_3)$=160 g/mol

Set the weight of solid solution is 1600 g,

where $n(Fe_2O_3)=1600\times10\%\div160=1$ mol,

$n(Al_2O_3)=1600\times90\%\div102=14.118$ mol,

V(ss)=$1600 \div 4.078 = 392.3$ cm^3

Case 1: if all $Fe^{3+}$is reduced into Fe^{2+},

n($FeAl_2O_4$)=2mol, so V($FeAl_2O_4$)=$174 \times 2 \div 4.26 = 81.69$ cm^3

V(Al_2O_3)=$102 \times (14.118 - 2) \div 4 = 309$ cm^3

so V(composite)= V($FeAl_2O_4$) + V(Al_2O_3)=390.69 cm^3

so f($FeAl_2O_4$)= $81.69 \div 390.69 = 20.9\%$

Volume shrinkage is 0.4%

Case 2: If Fe^{3+} is all reduced into metallic Fe,

ρ(Fe)=7.8 g/cm^3

n(Fe)=2mol, so V(Fe)=$56 \times 2 \div 7.8 = 14.36 cm^3$

V(Al_2O_3)=$102 \times (14.118) \div 4 = 360 cm^3$

so V(composite)= V(Fe)+ V(Al_2O_3)=374.36 cm^3

Volume shrinkage is 4.5%

In both cases, V(composite) < V(ss)

Reference

[1] Y. M. Chiang, D. P. Birnie, W. D. Kingery, Physical Ceramics, John Wiley & Sons, New York (1996).

[2] T. Butler, In Situ Ceramic Nanocomposites by Solid State Precipitation, MSc Thesis, Oxford University, UK (2011).

[3] A. Mukhopadhyay, R. I. Todd, Microstructure and Mechanical Properties of Alumina Matrix Nanocomposites Produced by Solid State Precipitation, Journal of the European Ceramic Society, 30, 1359-1372 (2010).

[4] K. A. Berry, M. P. Harmer, Effect of MgO Solute on Microstructure Development in Al_2O_3, Journal of the American Ceramic Society, 69, 143–149 (1986).

[5] Y. Ikuma, R. S. Gordon, Effect of Doping Simultaneously with Iron and Titanium on the Diffusional Creep of Polycrystalline Al_2O_3, Journal of the American Ceramic Society, 66, 139-147 (1983).

[6] J. Tartaj, G. L. Messing, Anisotropic Grain Growth in α-Fe_2O_3-doped Alumina, Journal of the European Ceramic Society, 17, 719-725(1997).

[7] B. Phillips, A. Muan, Stability Relations of Iron Oxides: Phase Equilibria in the System Fe_3O_4-Fe_2O_3 at Oxygen Pressures up to 45 Atmospheres, Journal of Physical Chemistry, 64 1451-1453 (1960).

[8] Y. Ikuma, R. S. Gordon, Effect of Doping Simultaneously with Iron and Titanium on the Diffusional Creep of Polycrystalline $A1_2O_3$, Journal of the American Ceramic Society, 66, 139-147 (1983).

[9] H. Y. Lee, S. J. L. Kang, Chemically Induced Grain Boundary Migration and Recrystallization in Al_2O_3, Acta Metallurlical Materialia, 38, 1307–1312 (1990).

[10] J. Gurt Santanach, C. Estournès, A. Weibel, A. Peigney, G. Chevallier, Ch. Laurent, Spark Plasma Sintering as a Reactive Sintering Tool for the Preparation of Surface-Tailored Fe–$FeAl_2O_4$–Al_2O_3 Nanocomposites, Scripta Materialia, 60, 195-198 (2009).

[11] A. Mukhopadhyay, R. I. Todd, Microstructure and Mechanical Properties of Alumina Matrix Nanocomposites Produced by Solid State Precipitation, Journal of the European Ceramic Society, 30, 1359-1372 (2010).

[12] A. Mukhopadhyay, R. I. Todd, Effect of Yttria Doping on the Microstructure and Mechanical Properties of $Al_2O_3/FeAl_2O_4$ Nanocoposites Developed via Solid State Precipitation, Journal of the European Ceramic Society, 30, 2905-2915 (2010).

[13] B. J. McBride, S. Gordon, Computer Program for Calculation of Complex Chemical Equilibrium Compositions and Applications: II. Users Manual and Program Description, NASA Reference Publication, Cleveland (1996).

[14] I. Barin, O. Knacke, Thermochemical Properties of Inorganic Substances, Springer-Verlag, Berlin (1973).

[15] P. A. Rock, Chemical Thermodynamics, University Science Books, Oxford (1971).

[16] D. A. Porter, K. E. Easterling, Phase Transformations in Metals and Alloys, Chapman & Halls, London (2009).

[17] R. H. Doremus, Diffusion in Alumina, Journal of Applied Physics, 100, 101-301 (2006).

[18] B. Lesage, A. M. Huntz,G. Petot-ervas, Transport Phenomena in Undoped and Chromium- or **Y**ttrium Doped Alumina, Radiation Effects and Defects in Solid, 75, 283-299 (1983)

[19] M. O. Dauies, Nasa Technical Notes: Transport Phenomena in Aluminum Oxide, Lewis Research Center, Cleveland (1965).

[20] F. M. Ernsberger, Proton transport in solids, Journal of Non-Crystalline Solids, 38, 557-561 (1980).

[21] W. R. Magro, D. M. Ceperley, C. Pierleoni, B. Bernu, Molecular Dissociation in Hot, Dense Hydrogen, Physical Review Letters, 76, 1240-1243 (1996).

[22] K. R. Jennings, Fundamentals and Applications of Gas Phase Ion Chemistry, Springer, London (1999).

[23] K. P. D. Lagerlof, T. E. Mitchell, A. H. Heuer, Lattice Diffusion Kinetics in Undoped and Impurity Doped Sapphire (α-Al_2O_3): a Dislocation Loop Annealing Study, Journal of the American Ceramic Society, 72, 2159–2171 (1989).

[24] H. P. Cahoon, C. J. Christensen, Sintering and Grain Growth of α-Alumina, Journal of the American Ceramic Society, 39, 337-337 (1956).

[25] J. J. Zuckerman, Inorganic Reactions and Methods: Formation of Ceramics, John Wiley & Sons, London (1999).

[26] H. L. Marcus, M. E. Fine, Grain-Boundary Segregation in MgO-Doped Al_2O_3, Journal of the American Ceramic Society, 55, 568–570 (1972).

[27] W. D. Callister, D. G. Rethwisch, Materials Science and Engineering: An Introduction, John Wiley & Sons, New York (2009).

[28] American Society for Metals International Handbook Committee, American Society for Metals Handbook Volume 03: Alloy Phase Diagrams, American Society for Metals International, New York (1992).

[29] P. W. Voorhees, The theory of Ostwald ripening, Journal of Statistical Physics, 38, 231-252 (1985).

Chapter 5 Mechanical Properties and Wear Resistance of PRABN

5.1 Introduction

The mechanical properties, residual stresses and wear resistances of $Al_2O_3/FeAl_2O_3$ nanocomposites developed by aging in 4% H_2/N_2 are reported, and the relationships between microstructures, mechanical properties and wear resistance are discussed.

The sample identification in this chapter is mostly consistent with Chapter 4, besides R1 is monolithic alumina aged in 4% H_2/N_2 at 1450˚C for 20 hours, and R2 is sample H4-1550-0.5 with all surface layers removed.

5.2 Results

5.2.1. Hardness

The room temperature hardness (H_v) were obtained via Vickers indentation with a load of 5 kg (Figure 5.1). The indentation depths were calculated using the crack length and the angle between opposite faces subjected to a load (136^o). It was found that all the calculated plastic zone depths were less than the surface layer thickness of the nanocomposites. Thus, hardness measured in the aged samples represent the properties of the surface layers of all aged samples.

From Figure 5.2, it can be seen that the incorporation of Fe_2O_3 in solution slightly decreased the hardness of alumina. All aged samples showed a much lower surface hardness than that of the solid solution except samples aged at 1250^o C. One possible reason for the hardness reduction in the surface layer of samples aged at 1350^o C is the higher porosity than the solid solution due to the reduction reactions. Porosity could reduce the area of material under the

indentor, thus could increase the local pressure exerted by the indentor and hence lead to a lower apparent hardness. Indentors could also crush the pores and the destruction of pores could account for the volume reduction, which could result in a larger indentation area and therefore a lower apparent hardness. However, since extensive pullouts happened in the surface layers of samples aged at 1450^{o}C and 1550^{o}C and sample R2 (Figure 4.3(b)), it is difficult to specifically state that the hardness in aged samples decreased with increased aging temperature and time. Furthermore, the hardness of R1 was slightly higher than that of the as sintered monolithic alumina.

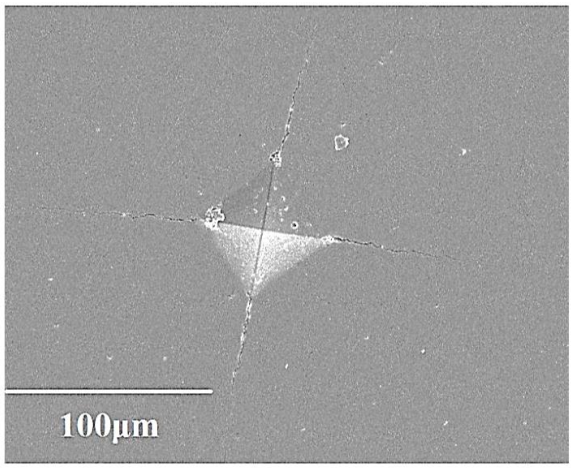

(a)

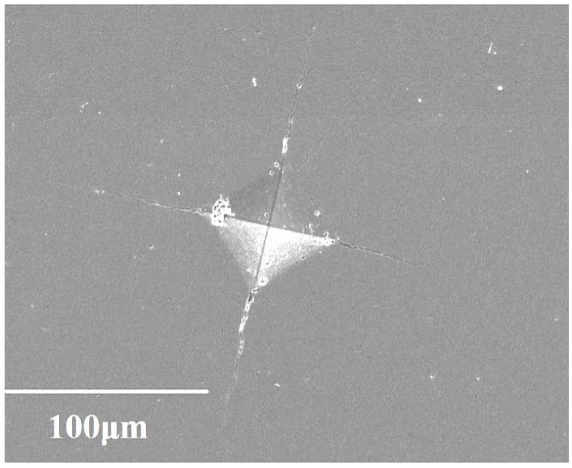

(b)

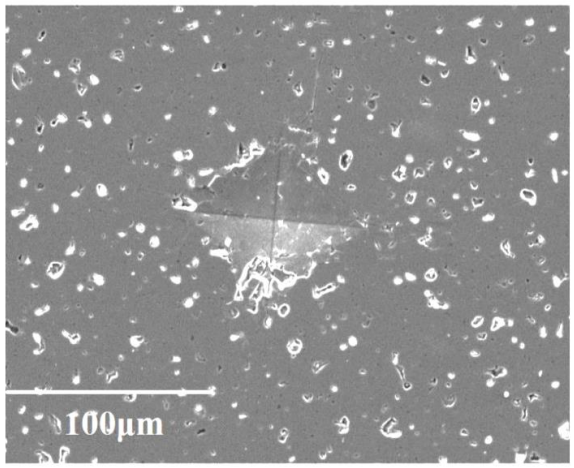

(c)

Figure 5.1 SEM images of indents made by 5kg Vickers' indenter on (a) monolithic alumina; (b) solid solution; (c) sample H4-1550-20.

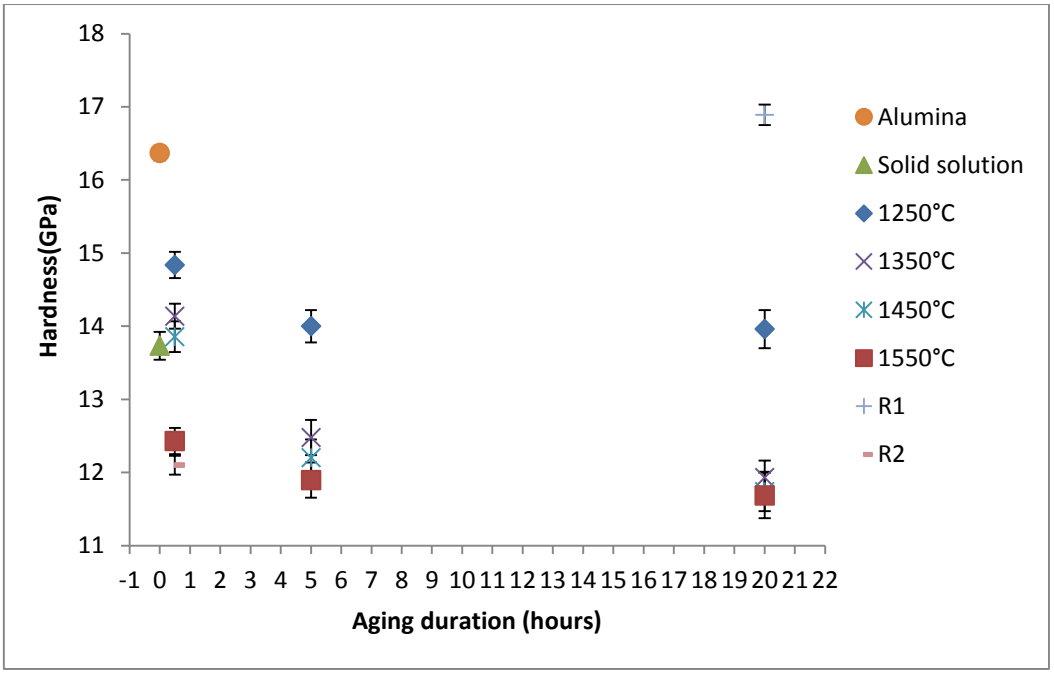

Figure 5.2. Vickers hardness (H_{v5}) as measured with 5kg indentation load for monolithic alumina, solid solution and nanocomposites developed by aging of solid solution with different thermal conditions in 4% H_2/N_2. The surfaces of as-aged samples were slightly polished by 3 μm diamond suspension before indentation so that the subsequent indentation could be seen clearly.

5.2.2. Flexural strength and fracture mode change.

The flexural strengths of the monolithic Al_2O_3, Al_2O_3-Fe_2O_3 solid solution, samples aged with various aging conditions, sample R1 and sample R2 were shown in Figure 5.3. The surfaces subjected to tensile stresses during the four-point bending experiments were lightly ground and polished before aging.

Figure 5.3 showed that the incorporation of Fe^{3+} to Al_2O_3 in solid solution did not result in a significant strength change with respect to monolithic Al_2O_3. Considering the error range, the flexural strength of samples H4-1250-0.5, H4-1250-5 and sample H4-1350-0.5 were comparable to monolithic Al_2O_3, while other aged samples all showed a higher flexural strength than that of monolithic Al_2O_3. From 1250˚C to 1450 ˚C, the flexural strength increased with higher aging temperature with the same aging duration. Within this

temperature range, the flexural strength also increased with longer aging durations at the same aging temperature. When aged at 1550˚C, the flexural strength decreased with longer aging duration. Furthermore, the flexural strength of R1 was much higher than that of any other sample, while the flexural strength of R2 was much lower than that of sample H4-1550-0.5 and is the lowest among all samples.

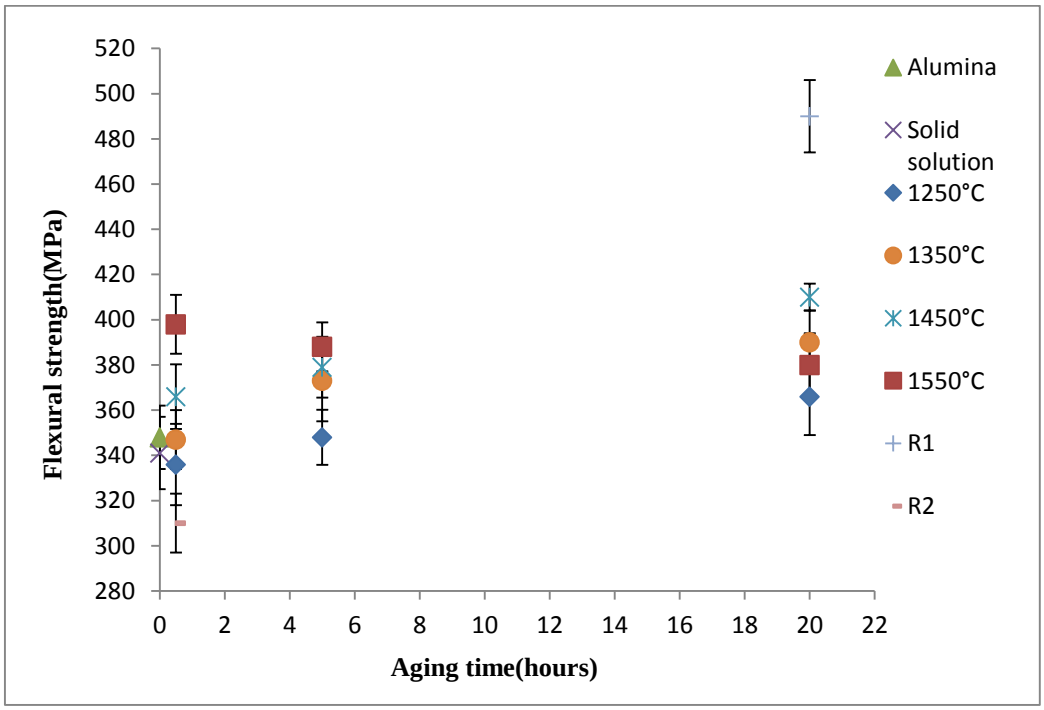

Figure 5.3 Flexural strength of monolithic alumina, solid solution and samples aged under 4% H_2/N_2.

Examination was made through SEM on the fractured surfaces obtained from four point bend testing of as-sintered monolithic Al_2O_3 (Figure 5.4(a)), Al_2O_3-Fe_2O_3 solid solution(Figure 5.4(b)), aged samples (Figure 5.4(c-m)), sample R1 (Figure 5.4(n)). Figure 5.4(a) and Figure 5.4(n) showed that the monolithic Al_2O_3 and sample R1 both exhibited the classical almost completely intergranular fracture mode while Al_2O_3-Fe_2O_3 solid solution showed a mixture of intergranular and transgranular fracture (Figure 5.4(b)). It was found that samples aged at 1250^{o} C showed a clear boundary between transgranular and intergranular fracture mode (Figure 5.4(c-d)). In samples aged at 1250^{o} C the areas showing completely transgranular

fracture mode (Figure 5.4(e-f)) contained intergranular $FeAl_2O_4$ particles without any intragranular particles, while the areas showing mostly intergranular fracture mode (Figure 5.4(g-h)) were still solid solution (similar to Figure 5.4(b)). The fracture surfaces of samples aged above 1250 ℃ showed substantially transgranular fracture (Figure 5.4(i-m)). In Figure 5.4(i), some of the large transgranularly fractured grains in the surface layer contained nanoparticles. Figure 5.4(j) showed a higher magnification BSE-SEM image of the fracture surface near the gas/solid interface of sample H4-1550-5. Holes left by coarser intergranular particles falling out and intact intragranular nanoparticles can be both observed in Figure 5.4(j). Figure 5.4 (k-l) showed the bulk part of H4-1550-5, where the fracture mode was mostly transgranular within the sole presence of intergranular spinel particles. Since intragranular nanoparticles could be in seen in Figure 5.4 (i) which has a lower magnification than that of Figure 5.4 (l), it can be confirmed that there was no intragranular nanoparticles in the bulk part of H4-1550-5 corresponding to Figure 5.4 (l). Therefore, intragranular nanoparticles were not necessary for the fracture mode change.

In conclusion, the fracture mode change of the aged samples from intergranular to transgranular was probably caused by the intergranular particles and/or large grains. In addition, it can be noted that some of the transgranular fracture surfaces are not planar cleavage planes, but contain a few step like features (Figure 5.4(m)). Such step like features can also be observed on the transgranular fracture surfaces of Al_2O_3-SiC nanocomposites containing intragranular SiC nano particles. [1]

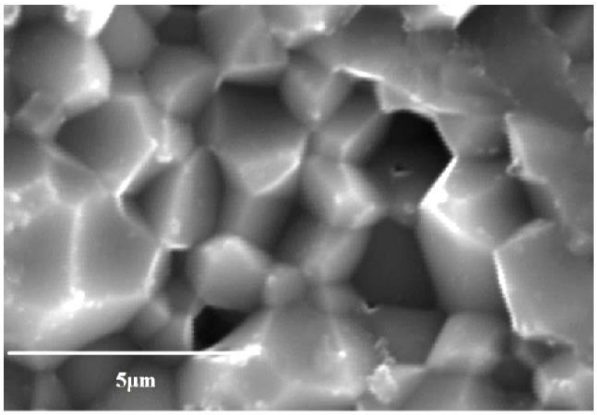

(a)

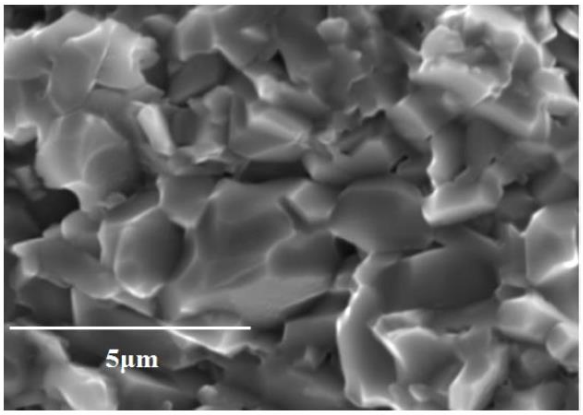

(b)

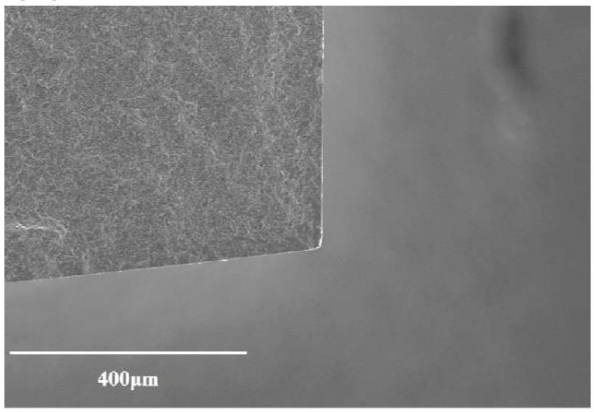

(c)

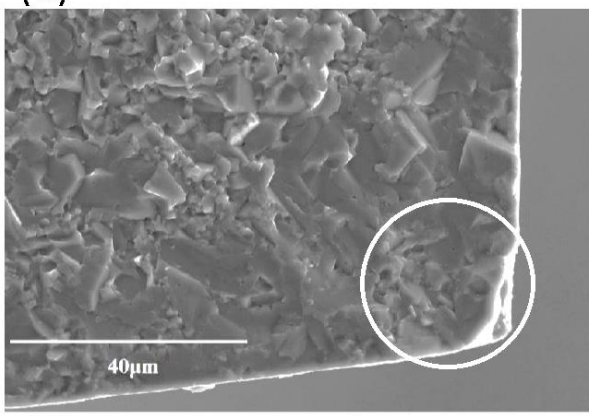

(d)

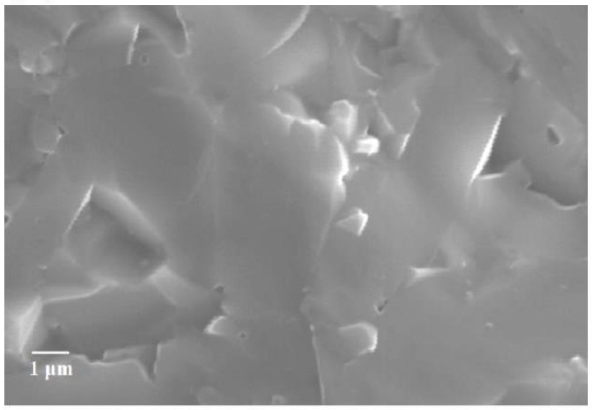

(e)

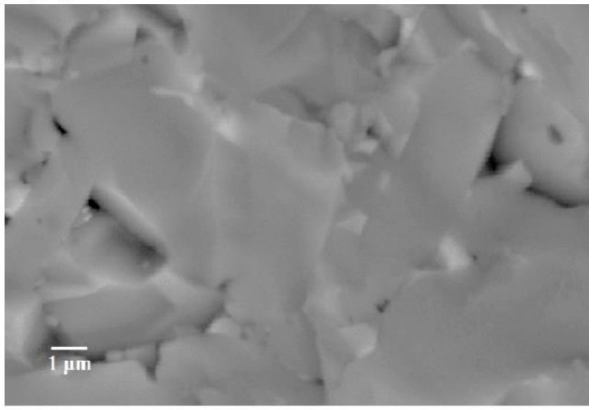

(f)

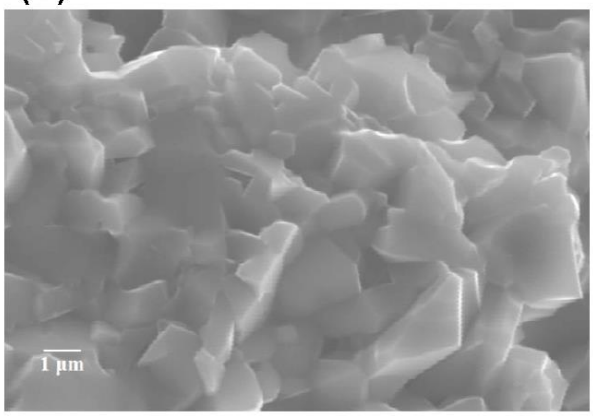

(g)

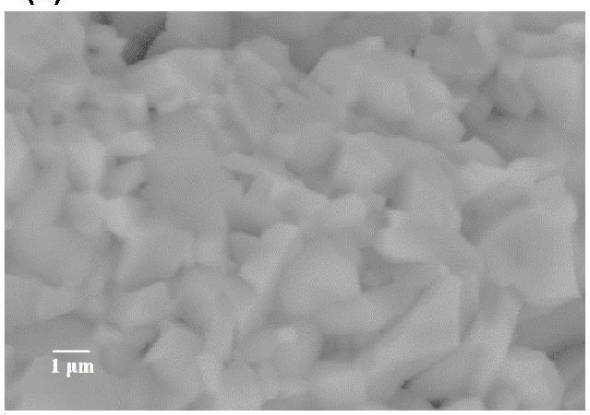

(h)

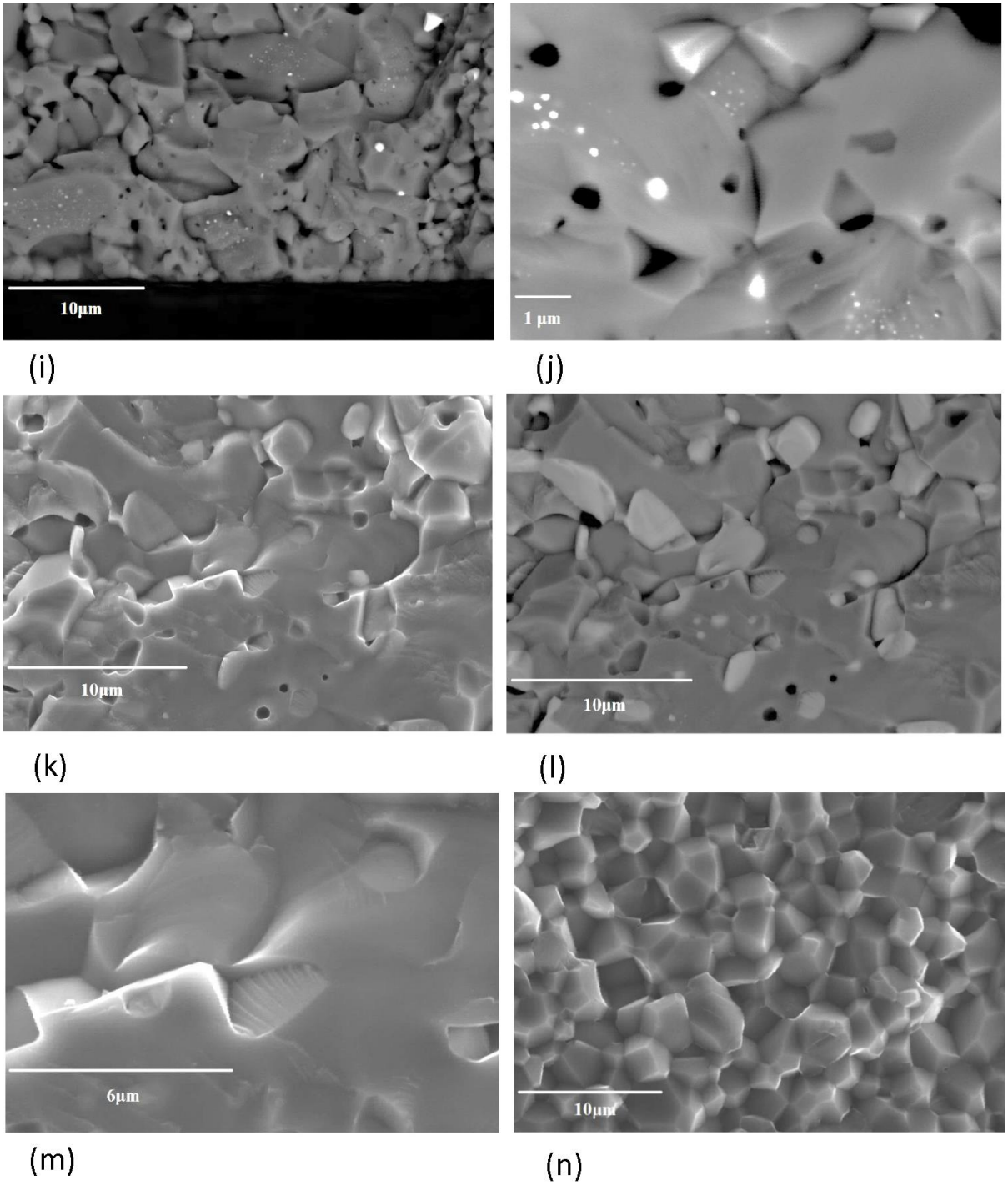

Figure 5.4 SEM-SEI images of fractured surfaces obtained from four point bending tests of (a) monolithic alumina; (b) as sintered solid solution; (c-d) sample H4-1250-5; (e) surface layer of sample H4-1250-5 and (f) SEM-BSE image corresponding to (e); (g) bulk part of sample H4-1250-5 and (h) SEM-BSE image corresponding to (g); (i-j) SEM-BSE image of the surface layer of H4-1550-5; (k,m) bulk part of sample H4-1550-5 and (l) SEM-BSE image corresponding to (k); (n) sample R1.

5.2.3. Fracture origins

It is difficult to identify all fracture origins in all samples due to the uncontrollable machining process and the complicated fracture process, especially when the critical flaws are small. However, the crack branching patterns can lead back to an approximate position where the fracture could have initiated. For example, Figure 5.5(a-f) showed that some relatively large critical flaws with radiating branching pattern around could be found in the corners/on the tensile surfaces of solid solution and some aged samples. Such large flaws (typically 60μm) probably originated from the processing route. However, it is difficult to say all critical flaws in solid solution and some aged samples were large because Figure 5.5(a-f) only represent a fraction of the samples, while in a part of the rest samples no obvious large critical flaws could be found. The branching pattern in Figure 5.5 (g-h) indicated that the fracture origin lies in the edge of the sample (marked by a white circle in Figure 5.5 (h)), though it is difficult to identify the critical flaw. Figure 5.4(c-d) also indicated that the critical flaw was in the corner (marked by a white circle in Figure 5.4(d)).

It has been found that the fracture origins of the monolithic alumina, solid solution and all aged samples were located near/on the corner or the tensile surface. This is at least partially due to the higher stress on the tensile surface and the corners from slight misalignment of the specimen in the testing configure, and the ‘double aging’ in the corners of aged samples which would induce more porosity. Another reason may be the surface defects caused by machining at the corners/tensile surfaces. In other words, the flexural strength represented the strength when failure originates in the surface layers.

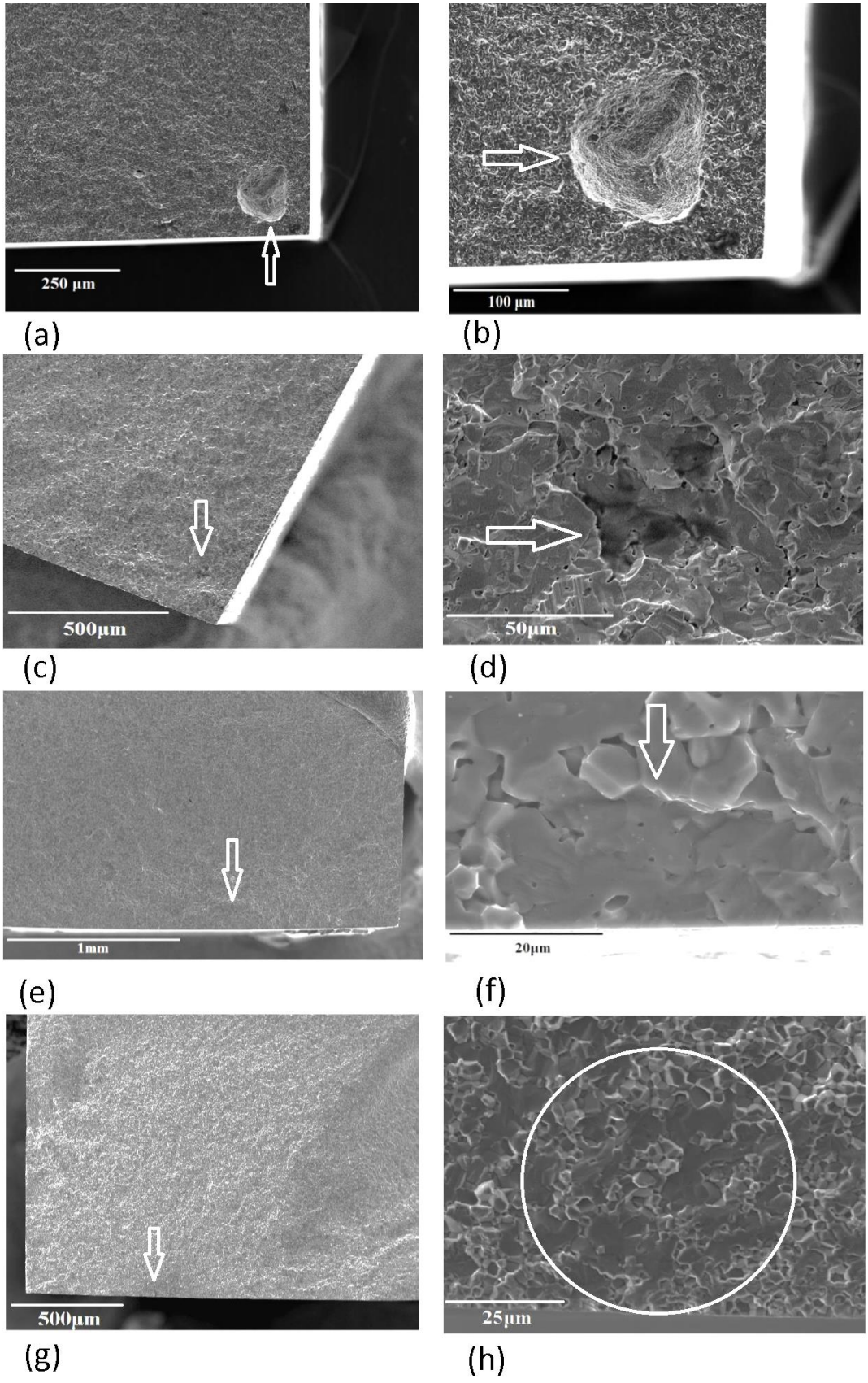

Figure 5.5 SEI-SEM pictures of fracture origins in (a-b) solid solution; (c-d) sample H4-1550-0.5; (e-f) sample H4-1450-20;(g-h) sample R1.

5.2.4. Wear properties and worn surface observation

Topographical observations of the worn surfaces corresponding to the monolithic alumina, solid solution and the nanocomposites developed under different aging conditions were made using SEM. All the worn surfaces comprised two distinct appearances: (1) areas showing material removal by cutting and ploughing by plastic deformation, and (2) areas showing pull-outs by brittle fracture. The worn surfaces of both monolithic alumina and solid solution (Figure 5.6(a,b)) showed a classical feature of extensive pull-out, whereby a significant amount of material was removed by intergranular fracture.

By contrast, the worn surfaces of most samples aged at/above 1350 ˚C (Figure 5.6(c,d)) were smoother than both monolithic alumina and solid solution (Figure 5.6(a,b)), and also showed less pull-outs. Furthermore, higher magnification images (Figure 5.6(e)) showed that these pull-outs were a mixture of intergranular fracture and transgranular fracture features in the samples aged at/above 1350 ˚C. It can be seen that the plastic deformation induced material removal is more prevalent in the aged samples. Unlike other aged samples, the worn surfaces of sample R2 were even rougher than the monolithic alumina, and the corresponding pull-outs were also a mixture of intergranular and intragranular fractures.

Wear crater sizes of all samples were measured during the wear tests and the wear craters produced with a sliding distance of 59 m for all samples were confirmed later via optical microscopy. The wear volumes were calculated using Equation 3.4 in Chapter 3. A plot of the wear volume of selected samples against the product of the sliding distance and the normal load is shown in Figure 5.7. The wear resistance results are shown in Figure 5.8. From Figure 5.8 it can be seen that the wear resistances of monolithic alumina and solid solution were comparable. The results indicate that both aging temperatures and aging time have a significant influence over the wear behaviour of the aged nanocomposites. All aged samples

exhibited a higher wear resistance than monolithic alumina. It can be seen that for specimens aged at the same temperature, with increased aging duration the wear resistance generally increased. When the aging time is 0.5 hour, the wear resistance increased along with higher aging temperature. However, as the aging duration was extended to or above 5 hours, the situation was different. It can be seen that from 1250 ℃ to 1350 ℃, the wear resistance of aged samples increased along with higher aging temperatures. However, from 1350℃ to 1550℃ the wear resistance of aged samples decreased with more elevated aging temperatures. The percentages and sizes of surface pull-out by fracture within the crater region were measured on the SEM images such as pictures in Figure 5.6 and were presented in Figure 5.9 and Figure 5.10. The holes left by pull-outs in the worn surfaces shown in pictures such as Figure 5.6 were identified manually. The area fractions of those identified holes were calculated using ImageJ, which was taken as the pull-out percentage. The sizes of those holes were calculated by ImageJ as equivalent circular area radius. The pull-out percentage results generally agree with the wear resistance results. As shown in Figure 5.9, all aged samples exhibited a lower pull-out percentage compared with the solid solution. Samples aged at 1250℃ gave the highest pull-out percentage among the aged samples but were still less compared with monolithic alumina and un-aged solid solution. Samples aged at 1350℃ gave the lowest pull-out percentage. It can be seen that at the same aging temperature, the pull-out percentage decreased with longer aging durations. From aging temperature 1250℃ to 1350℃, the pull-out percentage decreased as aging temperature was elevated. From aging temperature 1350℃ to 1550℃, the pull-out percentage increased as aging temperature was elevated. As shown in Figure 5.10, most aged samples exhibited a larger pull-out size compared with the solid solution. It can be seen that the pull-out size increased with higher aging temperature and longer aging durations. Furthermore, Figure 5.8 to Figure 5.10 showed

that the wear resistance of R1 was very close to that of the monolithic alumina, while the wear resistance of R2 was clearly poorer than sample H4-1550-0.5.

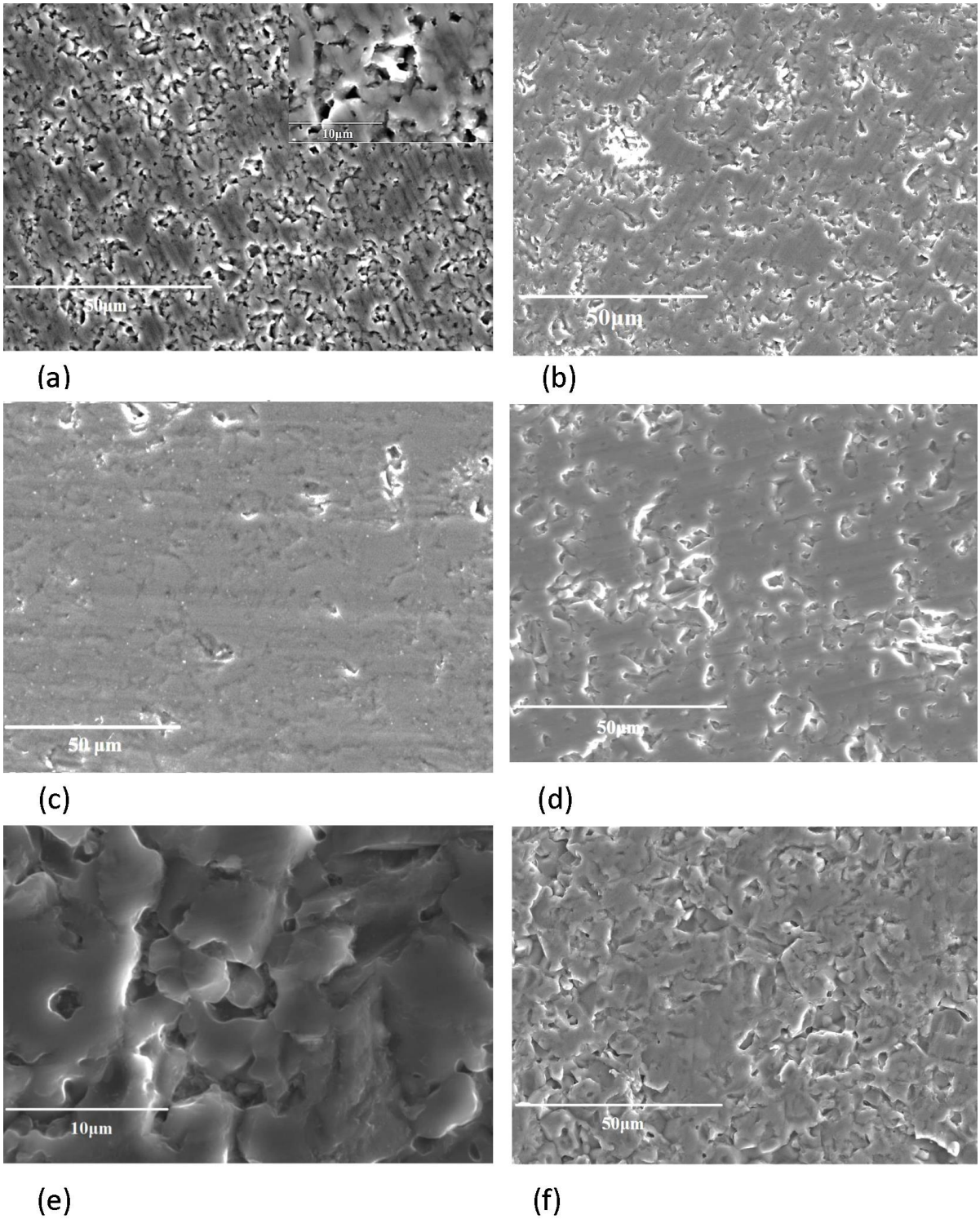

Figure 5.6 SEM images obtained from the worn surfaces of (a) monolithic alumina; (b) solid solution; (c) sample H4-1350-5; (d) and (e) sample H4-1550-5; (f) sample R2.

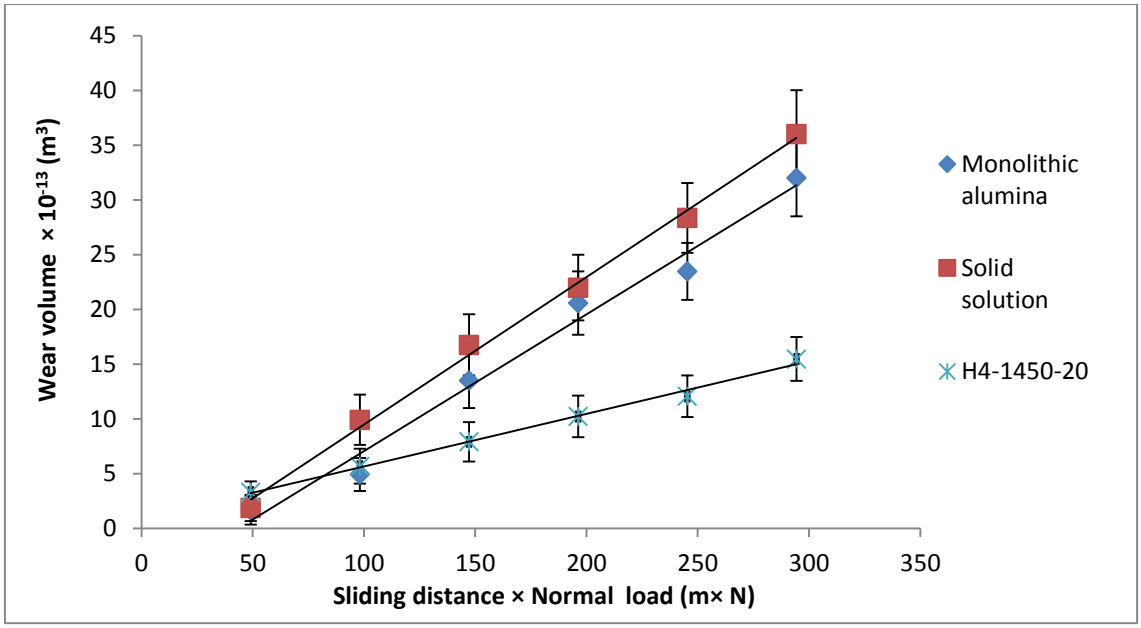

Figure 5.7 Wear volume determined as a function of sliding distance for selected samples. The wear efficient *k* is equal to the slope of the corresponding straight line.

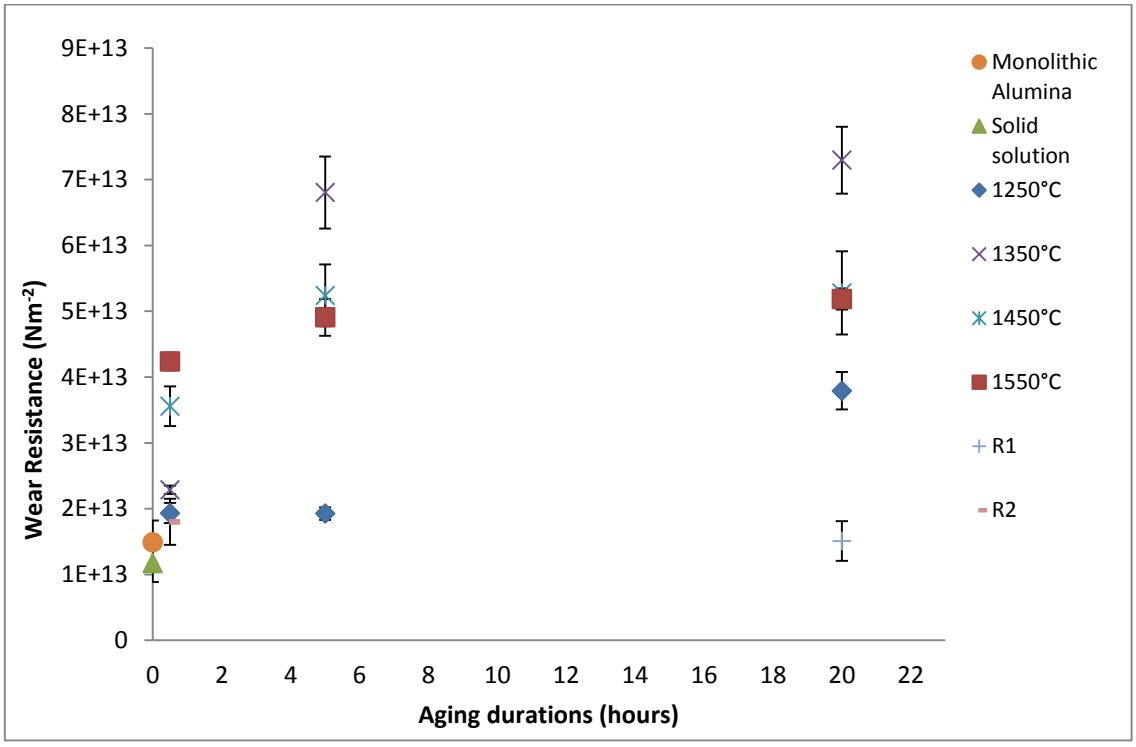

Figure 5.8 Wear resistance of monolithic alumina, the solid solution and samples aged with different conditions.

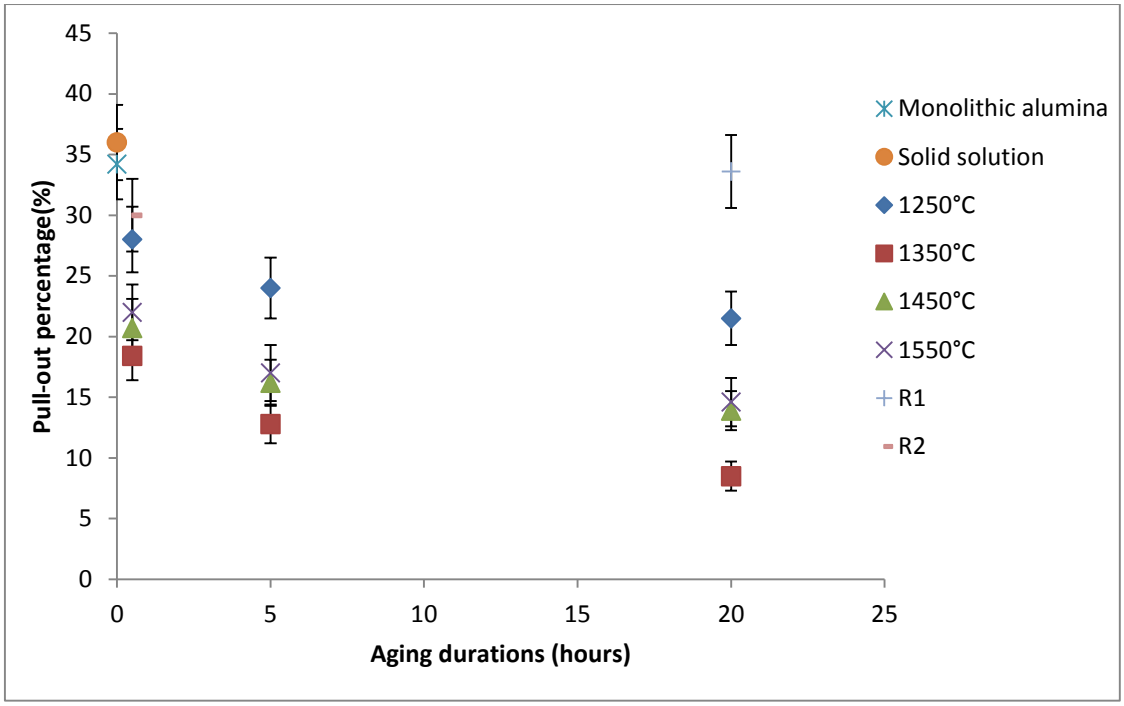

Figure 5.9 Pull-out percentage of worn surfaces of monolithic alumina, solid solution and samples aged at different conditions.

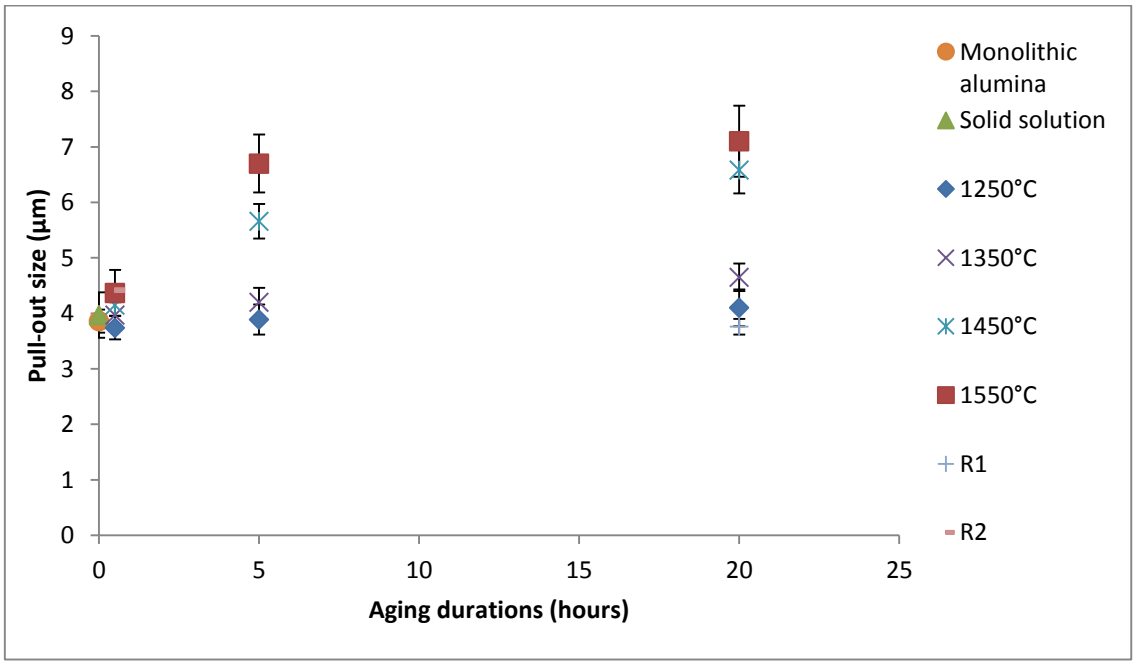

Figure 5.10 Pull out size of worn surfaces of monolithic alumina, solid solution and samples aged with different thermal treatments in 4% H_2/N_2.

5.2.5. Indentation polishing results

Figure 5.11 shows SEM pictures of the indented surfaces following subsequent polishing with 1 μm diamond slurry. The aged samples were indented directly after aging treatment without any previous polishing. The remaining part of the original indentation can be seen in the centre of the picture in each case. In Figure 5.11(a), (b) and (c), the traces of the classical radial cracks can be seen outside the plastic zone, while in Figure 5.11(d), barely any traces of radial cracks can be seen outside the plastic zone. It is clear that in Figure 5.11(a) corresponding to monolithic alumina, a lot of pull-out by brittle fracture has occurred in a clearly defined region corresponding closely to the shape and size of the indentation before the indentation polishing tests. This is taken as the plastic zone beneath the indentation. Similar presence of intensive pull-out in the plastic zone could also be found in the solid solution (Figure 5.11(b)), sample H4-1350-0.5, and samples aged at1250˚C 1450℃ and 1550˚C. By contrast, Figure 5.11(c) shows a reduction in pull-out within the plastic zone in samples aged at 1350℃ for more than 0.5 hours though such pull-out reduction is not significant.

Higher magnification SEM images show that the pull-out induced in the plastic deformation zone, was intergranular in monolithic alumina and solid solution (Figure 5.11(e)), while the pull-outs in the aged samples show a higher proportion of transgranular fracture (Figure 5.11(f)).

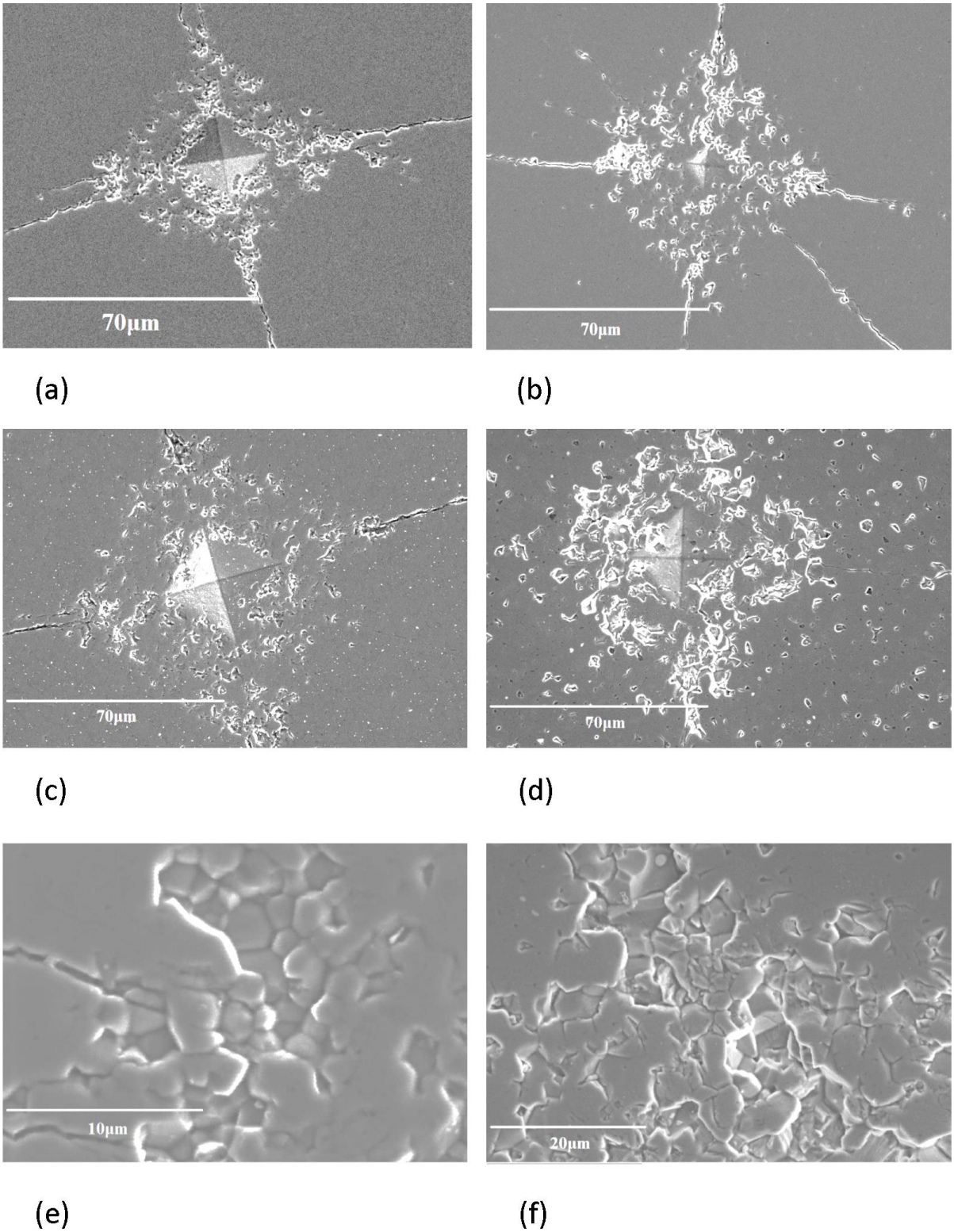

Figure 5.11 Surfaces of (a),(e) monolithic alumina; (b) solid solution; (c)sample H4-1350-5;(d),(f) sample H4-1550-5;

5.2.6. Surface residual stress

Residual stresses arise during cooling from the aging temperature due to the strain mismatch originated by differences in the thermal expansion coefficients (TEC) of the constituents of the layers.[2] The level and sign of the expected residual stresses in a symmetric laminate constituted by two 'effective surface layers' each with thickness t_s and a bulk part with thickness t_b, can be evaluated using the simplified model of a symmetric sandwich structured laminate (Figure 5.12), since all aged samples produced in this project approximated to such a sandwiched structure. The meaning of 'effective surface layer thickness', and how both t_s and t_b were measured have been discussed in section 3.5.3. In this model, it assumed a uniform biaxial distribution of stresses in the bulk plane of each layer and an infinite body in the x and z direction (y is the direction perpendicular to the sample surface). The assumptions are reasonable because no anisotropy is expected and the specimens are much wider and longer than their thickness. Equation 5.1- 5.4 were derived from this model according to the requirement of balanced forces and moments for a static body[2].

$$\sigma_s = -\frac{\varepsilon_M E_s'}{(1+\frac{2\times t_s E_s'}{t_b E_b'})} \tag{5.1}$$

$$\sigma_b = -\frac{\varepsilon_M E_b'}{(1+\frac{t_b E_b'}{2\times t_s E_s'})} \tag{5.2}$$

ε_M is the strain mismatch between layers, given by[3]:

$$\varepsilon_M = \int_T^{T_0} (\alpha_1 - \alpha_2)(dT) \tag{5.3}$$

$$\sigma_s = -\sigma_b \frac{2t_b}{t_s} \tag{5.4}$$

In Equation 5.1 to 5.4, σ_s is the residual stress in the surface layer, σ_b is the residual stress in the bulk part, E_s' is the average biaxial Young's modulus of the effective surface layer, E_b' is

the biaxial Young's modulus of the bulk part, α_1 is the thermal expansion coefficient of the surface layer, $\alpha_2$is the thermal expansion coefficient of the bulk part, T_o is the temperature below which elastic stress develops.

As explained in section 3.5.3, the stresses measured in the bulk parts (σ_{b-uni}) are expected to be uniaxial. However, the surface region must have approximately the same in-plane strain across the cut surface as in the bulk. Therefore, a relationship could be drawn for the measured uniaxial residual stress on the bulk part (σ_{b-uni}) and the real residual stress on the bulk part σ_b:

$$\frac{\sigma_b}{E_b'} = \frac{\sigma_{b-uni}}{E_b} \tag{5.5}$$

$$E_b' = \frac{E_b}{(1-v_b)} \tag{5.6}$$

where $v_b$is the Poisson's ratio of the bulk part, E_b is the average uniaxial Young's modulus of the bulk part. Therefore:

$$\sigma_b = \frac{\sigma_{b-uni}}{(1-v_b)} \tag{5.7}$$

Thus Equation 5.4 could be re-written as:

$$\sigma_s = -\frac{\sigma_{b-uni}}{(1-v_b)} \cdot \frac{2t_b}{t_s} \tag{5.8}$$

Taking sample H4-1350-20 as an example, the measured residual stress distribution in the bulk part was shown in Figure 5.13. It can be seen that the bulk part was in tension. The sharp increase of tensile stress on both sides of the bulk part can be due to relaxation of the surface layer/bulk part interface which increased the local tensile stresses, while the sandwich model[2] predicts a homogeneous stress distribution across the layers. Thus an average tensile stress should be calculated from the constant part of the tensile residual stress profile in the bulk

part (i.e the middle part of the stress profile, from position 1000 μm to 1500 μm away from the gas/solid interface in Figure 5.13). Therefore σ_{b-uni} of sample H4-1350-20 is around 105 MPa. Using Equation 5.8 and values from Table 5.1, the corresponding average residual stress in the surface layer of sample H4-1350-20 was calculated as −532MPa. Using the same method, the residual stress σ_s in the surface layer of most of the aged samples could be calculated and were summarized in Figure 5.14. It should be noted that the samples aged at low temperatures and short durations contained very thin surface layers which might make measurements unreliable, thus only sample H4-1350-20 and samples aged above 1350˚C were investigated.

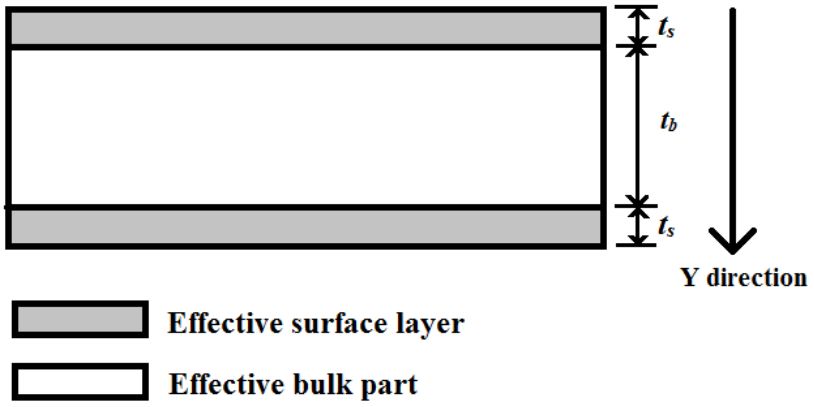

Figure 5.12 Sandwiched structure of laminated composites.

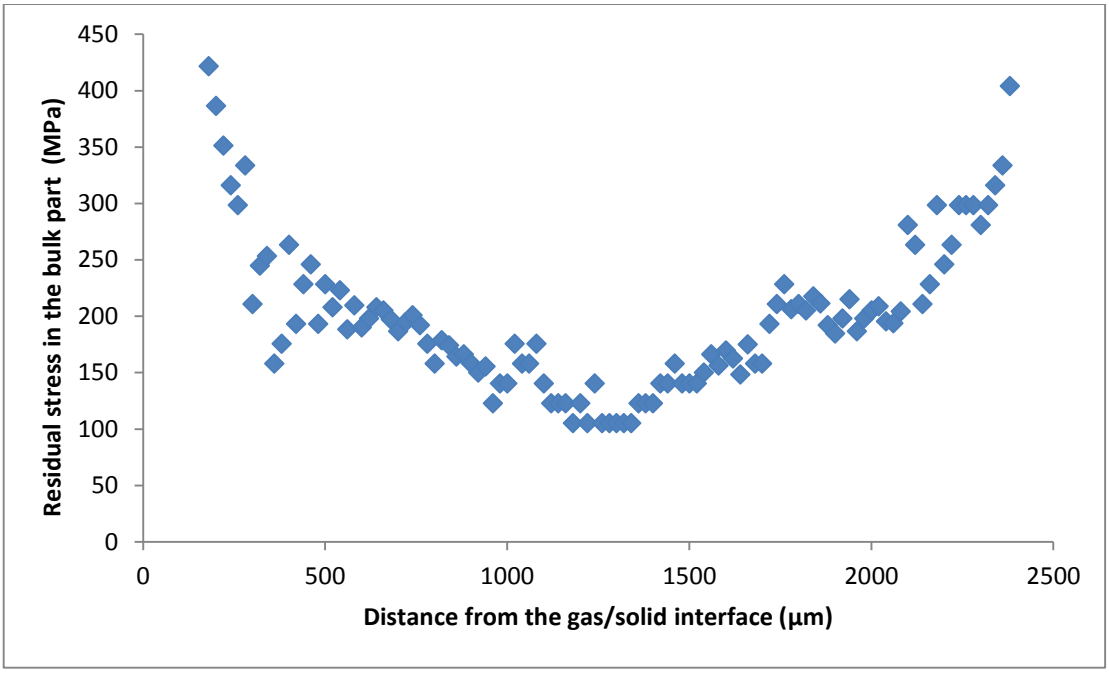

Figure 5.13 Residual stress in the bulk part of sample H4-1350-20.

Table 5.1 Values and sources of material properties used in calculation of residual stress. The values for nanocomposites and solid solution were calculated according to rule of mixture. E is the Young's moduli, α is the thermal expansion coefficient, $\boldsymbol{\nu}$ is the possoin's ratio.

Property	Alumina[4,5]	Fe[6]	$FeAl_2O_4$[7,8]	Fe_2O_3[9]	nanocomposite where f_A = 0.8 and f_S = 0.2	for solid solution
E (GPa)	402	211	222 GPa	359	366 GPa	398
α (K^{-1})	8-9× 10^{-6}	14× 10^{-6}	12-13× 10^{-6}	12-18× 10^{-6}	9.8 × 10^{-6}	9.7× 10^{-6}
ν	0.23	0.29	0.32	0.12	0.25	0.22

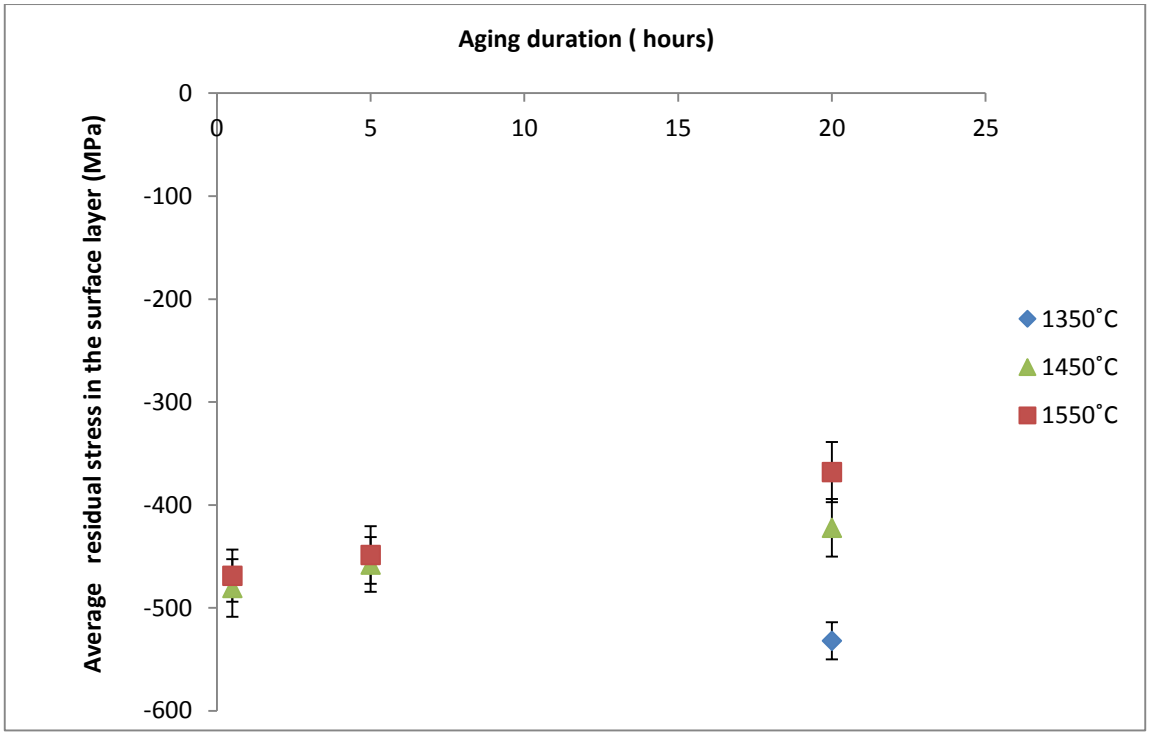

Figure 5.14 Average compressive residual stress in the surface layers of selected samples.

5.3 Discussion

5.3.1. Fracture mode change

A fracture mode change from intergranular to transgranular was observed in the worn surfaces and fracture surfaces of aged samples, while monolithic alumina and the solid solution exhibited mainly the classical intergranular fracture mode. As described in section 5.2.2, both grains surrounded by intergranular $FeAl_2O_4$ particles and large grains exhibited transgranular fracture. This is different from Mukhopadhyay's work, which suggested that only grains containing intragranular particles exhibit transgranular fracture[10]. It should be noted that in Mukhopadhyay's work, the sample aged at 1450^{o} C for 0 hour which only contained a relatively low volume fraction of intergranular $FeAl_2O_4$ particles without any intragranular nanoparticles (Figure 4.6(a) in Mukhopadhyay's work), also showed a mixture of intergranular and transgranular fracture (Figure 4.14(c) in Mukhopadhyay's work). [5,10]

It may be argued that the transgranular fracture could be because of the large grains produced by high temperature and/or long duration aging treatment.[11] However, as shown in Figure 5.4(d-f), the surface layer of sample H4-1250-5 where the grain size is only 3.0±0.3 μm and only intergranular particles exist without any intragranular particles, also showed transgranular fracture. Therefore, the 'coarse grains' were not the only reason for the fracture mode change.

Three more factors could cause fracture mode change. Firstly, if the intergranular particles are stiffer than the alumina matrix, the intergranular cracks can be deflected into grains.[1,12] However, Table 5.1 showed that the stiffness of $FeAl_2O_4$ particles is much lower than that of alumina. The second reason could be the compressive stress on the grain boundaries induced by the intergranular $FeAl_2O_4$ particles, which tends to close the cracks and may help to deflect the cracks into grains so that follow the average direction of crack propagation (ADOCP). Whether this occurs depends on the relative orientation between the grain boundary and the applied stress. The third reason could be a better grain boundary bonding. The contribution to fracture mode change by the latter two reasons are discussed below.

To evaluate the contribution of the second factor to the fracture mode change, one question needs be answered: to what extent can the compressive residual stresses on the grain boundaries in aged samples deflect intergranular cracks into grains?

Due to thermal expansion coefficient (TEC) mismatch between the matrix grains and the $FeAl_2O_4$ particles (Table 5.1)[13,14] the $FeAl_2O_4$ particles should create a compressive hoop stress around the particles, thus compression will be generated in the matrix around the particles after cooling down from high temperature to room temperature. When two neighbouring intergranular $FeAl_2O_4$ particles are connected with a grain boundary, a compressive stress would be exerted on the grain boundary. A simple model can be used to

calculate the residual stress on the grain boundary connecting two neighbouring particles, σ_m. Assuming composites were all made up by the spherical unit shown in Figure 5.15, a is the radius of intergranular particles, b is the outer radius of the matrix surrounding the particle, then the volume fraction of the particles f is given by:

$$f = (\frac{a}{b})^3 \tag{5.9}$$

The grain boundary could be regarded as a cross-section of the spherical unit through its equator because the particles tend to be on the grain boundaries. The requirement that equilibrium is maintained between the residual stresses in the particles σ_p and σ_m demands that:

$$(\pi a^2)\sigma_p + \pi(b^2 - a^2)\sigma_m = 0 \tag{5.10}$$

Therefore:

$$\sigma_m = \frac{-(f^{\frac{2}{3}} \cdot \sigma_p)}{1 - f^{\frac{2}{3}}} \tag{5.11}$$

The strain of the intergranular particles (ϵ_p) and σ_p could be obtained by modifying previous solutions for the same geometry of the current model[4]:

$$\epsilon_p = \frac{-(1 - f^{\frac{2}{3}}) \cdot E_m(1 - 2v_p)(\alpha_m - \alpha_p)\Delta T}{\left(1 - f^{\frac{2}{3}}\right)E_m(1 - 2v_p) + E_p\{f^{\frac{2}{3}} \cdot (1 - 2v_m) + \frac{1}{2}(1 + v_m)\}} \tag{5.12}$$

$$\sigma_p = \frac{E_p \epsilon_p}{1 - 2v_p} \tag{5.13}$$

E_p is the Young's modulus of intergranular particles, E_m is the Young's modulus of the alumina matrix, α_p is the thermal expansion coefficient of the intergranular particles, α_m is the thermal expansion coefficient of the alumina matrix, v_p is the Poisson's ratio of the particles, v_m is the Poisson's ratio of alumina matrix. All these values can be obtained from Table 5.1. Taking the bulk part of sample H4-1450-20 as an example, using a and b

measured from SEM images and Equation 5.11-5.13, σ_m was calculated as 274 MPa for this case.

Using models proposed by Evans et al[15], Cutler and Virkar[16], and Taya et al[17], the mode I and mode II stress intensity factors for an intergranular propagating crack (Figure 5.16) K_I and K_{II} can be given respectively by:

$$K_I = K_o \cos^2 \Psi + 2\sigma_m \sqrt{\frac{2(\lambda - d)}{\pi}} \tag{5.14}$$

$$K_{II} = K_o \sin\Psi \cdot \cos\Psi \tag{5.15}$$

$$K_o = \gamma \sigma_o \sqrt{\pi c} \tag{5.16}$$

Ψ as shown in Figure 5.16 is the angle between the ADOCP and a grain boundary, λ is the average interparticle spacing on grain boundaries, d is the average diameter of intergranular particles, γ is the geometrical factor, σ_o is the tensile stress (Figure 5.16), c is the crack length. Using σ_m =274 MPa and λ and d measured from SEM images, $2\sigma_m\sqrt{\frac{2(\lambda-d)}{\pi}}$ was calculated as -1 MPa·m$^{0.5}$.

When an intergranular crack propagates on grain boundaries as shown in Figure 5.16, the strain energy release rate G should equal the toughness for intergranular fracture in alumina ($G_{c,gb}$) [18]. Taking 9.95 J m^{-2} as a typical value for toughness for intergranular fracture in monolithic alumina: [18,19]

$$G = \frac{K_I^2}{E_m} + \frac{K_{II}^2}{E_m} = (9.95\ \mathrm{J \cdot m^{-2}}) \tag{5.17}$$

Therefore K_o, K_I *and* K_{II} can be obtained for different Ψ.

With a fixed Ψ, if an intergranular crack could be deflected into grains with an angle θ to the grain boundary (Figure 5.16), the corresponding strain energy release rate $G'(\theta)$ must be

larger than the toughness for transgranular fracture of alumina ($G_{c,g}$). Using the Irwin crack tip solutions, the following equations can be obtained:[18]

$$K_I' = K_I \cdot \cos^3\frac{\theta}{2} - 3K_{II} \cdot \sin\frac{\theta}{2} \cdot \cos^2\frac{\theta}{2} \tag{5.18}$$

$$K_{II}' = K_I \cdot \sin\frac{\theta}{2} \cdot \cos^2\frac{\theta}{2} + K_{II} \cdot \cos\frac{\theta}{2}[1 - 3\sin^2\frac{\theta}{2}] \tag{5.19}$$

$$G'(\theta) = \frac{(K_I')^2}{E_m} + \frac{(K_{II}')^2}{E_m} \tag{5.20}$$

K_I' is mode I stress intensity factor for a crack with θ, K_{II}' is mode II stress intensity factor for a crack with θ . $G'(\theta)$ is clearly a function of θ, and numerical analysis of Equation 5.20 showed that $G'(\theta)$ has a maximum value $G'(\theta)_{max}$ with θ between 0 and 90 º. $G'(\theta)_{max}$ of pure alumina and the bulk part of sample H4-1450-20 could be obtained with different Ψ and is plotted in in Figure 5.17.

Taking 15.75 J m^{-2} as a typical value for toughness for transgranular fracture in monolithic alumina[18,19], crack deflection into the grains from the grain boundary would happen only if $G'(\theta)_{max}$ is larger than 15.75 J m^{-2}. Figure 5.17 and calculations showed that intergranular cracks in alumina would continue propagating intergranularly with angles Ψ less than 43.5 º but would deflect into grains with angles Ψ larger than 43.5 º. In other words, 43.5 ºwas the critical angle Ψ_{crit} for fracture mode change from intergranular to transgranular in monolithic alumina. With the compressive residual stress on the grain boundaries in sample H4-1450-20 as calculated before, Ψ_{crit} was 29.5 º, i.e. Ψ_{crit} was reduced by 14 º($G'(\theta)_{maxg}$ in Figure 5.17). However, this still could not completely explain the observed complete transgranular fracture in the composites.

Figure 5.17 also suggested that with Ψ above 75 º, the intergranular cracks in monolithic alumina will continue propagating intergranularly, and with Ψ above 60 º the intergranular cracks in sample H4-1450-20 will continue propagating intergranularly. However, both of

these may rarely happen since most of the grain boundaries of alumina and aged samples have a Ψ less than 60 º[4,10-26], and the following calculations will show that intergranular cracks in alumina/aged samples will never propagate with a Ψ larger than 70 º. Figure 5.18 shows the situation where a crack propagating in the direction parallel to ADOCP encounters an individual alumina grain. In this case, Equation 5.14 and 5.15 could be re-written as:

$$K_I = K_o \tag{5.21}$$

$$K_{II} = 0 \tag{5.22}$$

Therefore, Equation 5.18 - 5.20 could be written as:

$$K_I' = K_I \cdot \cos^3 \frac{\Psi}{2} \tag{5.23}$$

$$K_{II}' = K_I \cdot \sin \frac{\Psi}{2} \cdot \cos^2 \frac{\Psi}{2} \tag{5.24}$$

$$G'(\Psi) = \frac{(K_I')^2}{E_m} + \frac{(K_{II}')^2}{E_m} = \frac{(K_o)^2}{E_m} \cdot \cos^4 \frac{\Psi}{2} \tag{5.25}$$

The requirement that this crack will follow ADOCP and continue propagating transgranularly demands that:

$$G = \frac{K_I^2}{E_m} = G_{c,g} = \frac{K_{c,g}^2}{E_m} \tag{5.26}$$

i.e.
$$K_o = K_{c,g} \tag{5.27}$$

$K_{c,g}$ is the critical stress intensity for transgranular fracture in monolithic alumina.

The requirement that this crack will be deflected onto the grain boundary which has an angle of Ψ to ADOCP demands:

$$G'(\Psi) = \frac{(K_o)^2}{E_m} \cdot \cos^4 \frac{\Psi}{2} = G_{c,gb} = \frac{(K_{c,gb})^2}{E_m} \tag{5.28}$$

i.e.
$$\cos^2 \frac{\Psi}{2} = \frac{K_{c,gb}}{K_o} \tag{5.29}$$

$K_{c,gb}$ is the critical stress intensity of intergranular fracture in monolithic alumina.

Since $K_{c,gb}$ is a constant and Ψ varies between 0^o and 90^o, Ψ in Equation 5.29 reaches a maximum Ψ_{max} when K_o reached its maximum. Equation 5.27 shows that the crack will continue propagating parallel to ADOCP when K_o equals $K_{c,g}$, which means the maximum value of K_o is $K_{c,g}$.

Therefore:
$$\cos^2 \frac{\Psi_{max}}{2} = \frac{K_{c,gb}}{K_{c,g}} \quad (5.30)$$

Taking $\frac{K_{c,g}}{K_{c,gb}}$ as 1.5[11], $\Psi_{max}=70^o$. In other words, Ψ will not be larger than 70º. Therefore, intergranular cracks in alumina/aged samples will never propagate with a Ψ larger than 70º.

It should be admitted that the models here are only approximate because they only considered the 2D fracture process while the real fracture is in three dimensions, thus models here might have over-simplified the calculations. However, the current models at least provided some information that the compressive residual stress on the grain boundaries could deflect intergranular cracks into grains to some extent but could not explain the complete fracture mode change alone.

Although the particle pull-outs during polishing suggest that the intergranular $FeAl_2O_4$ particles were not well-bonded, the chemical change on the grain boundaries after aging treatments might strengthen the grain boundary bonding and hence provides an additional mechanism responsible for fracture mode change in the aged samples. Such chemical change might result in a change in the relative toughnesses for intergranular and transgranular fracture. This is possible because section 5.2.2 showed that the incorporation of Fe_2O_3 in alumina did change the complete intergranular fracture into a mixture of both intergranular and transgranular though intergranular fracture was still dominant. As Yahya and Todd reported[20], doping with only 0.12 wt% Carbon results in the fracture mode change from intergranular to completely transgranular in pure alumina. Bedu-Amissah et al [21] also noted that the grain boundary diffusion of Cr in alumina was changed by doping with 100 ppm

yittrium. Therefore it is possible that subtle chemical change in grain boundaries would change the grain boundary properties of alumina which might further cause the observed fracture mode change in this project. However, to answer this question future investigations using methods such as microcantilever tests to measure the toughnesses for intergranular and transgranular fractures of alumina grains and atomistic modelling to study the atomic bonding are needed.

In conclusion, it is probable that several multiple mechanisms are simultaneously operative in changing the fracture mode, which includes ‘coarse grains’, compressive residual stress on the grain boundaries and chemistry change on the grain boundaries after aging.

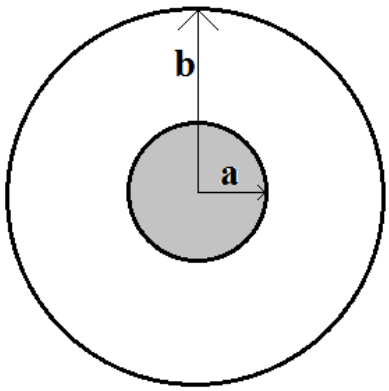

Figure 5.15 Schematic showing the spherical units forming the composites .

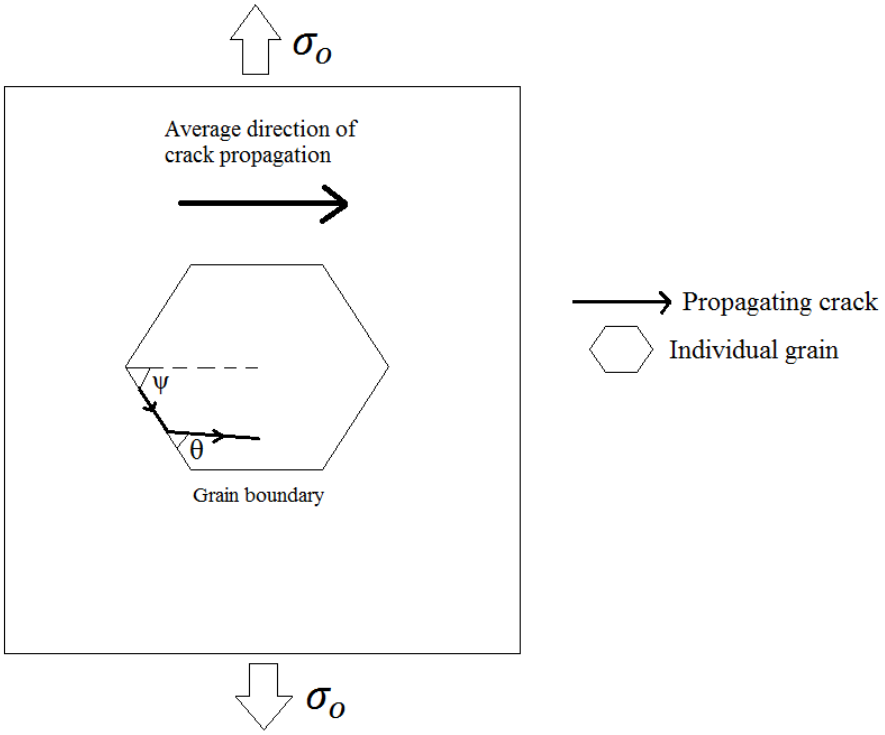

Figure 5.16 Model for crack deflection in alumina.

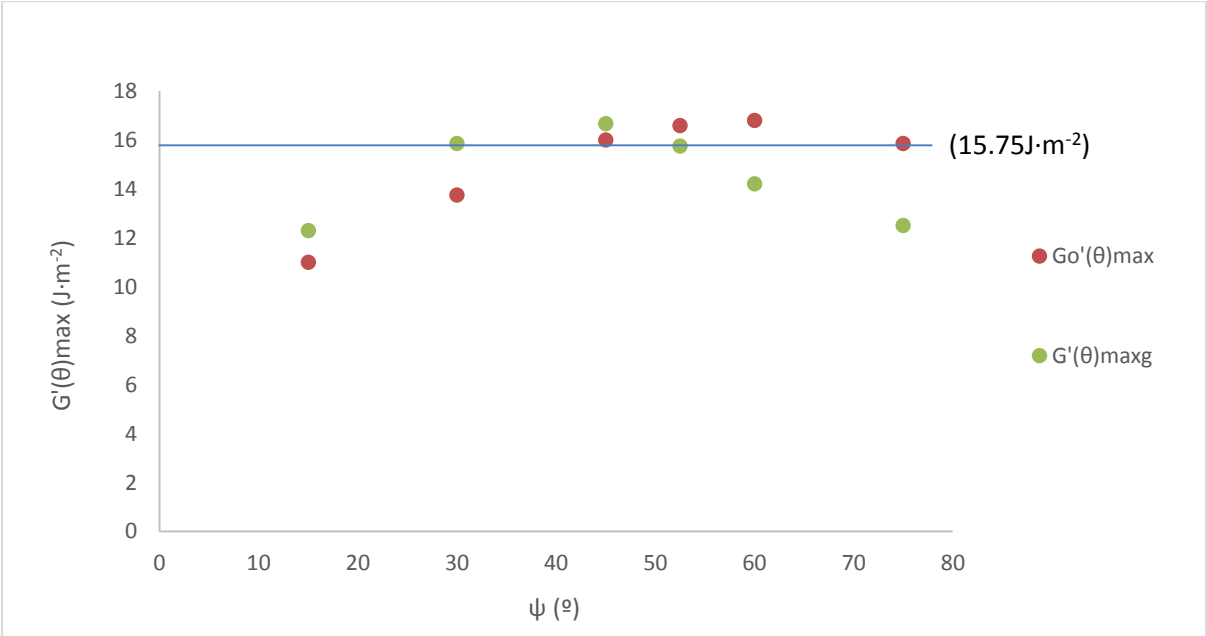

Figure 5.17 $\boldsymbol{G'(\theta)_{max}}$ values of alumina ($\boldsymbol{G_o'(\theta)_{max}}$)and the bulk part of sample H4-1450-20 ($\boldsymbol{G'(\theta)_{maxg}}$).

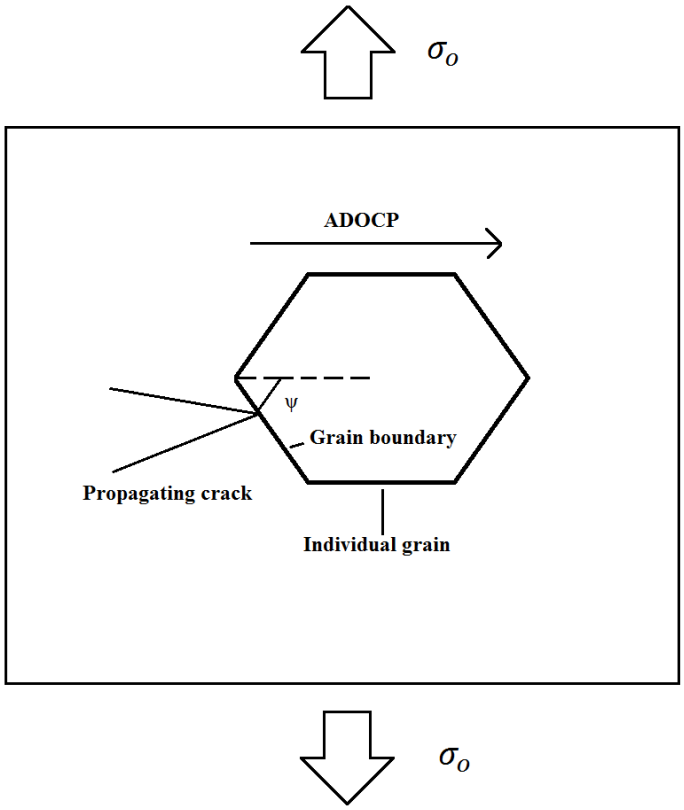

Figure 5.18 Schematics showing that a propagating crack encounters an individual grain.

5.3.2. Origin of the residual stress in the surface layer

Referring to Table 5.1, it can be seen that the thermal expansion coefficients of both $Al_2O_3/FeAl_2O_4$ nanocomposites and solid solution are higher than that of monolithic alumina. It was reported in Chapter 4 that in samples aged at high temperatures, the chemical concentration of Fe atoms in both the surface layer and bulk part areas near the surface layer is much lower than in the majority of bulk part due to the evaporation, thus the TEC of the bulk part should be higher than that of the surface layer. Since compressive stresses would develop on the outer layer when the outer layers of laminates present lower thermal strains than the internal ones, there must be residual compressive stress in the surface layer. Although the phase transformation during the aging would also introduce residual stress in the materials, such stress must relax at the high temperatures, thus its effect would be minor here.

In the absence of curvature, the residual stress at the surface layer σ_s can be calculated using the model proposed for sandwich structured laminate composites in section 5.3.2 and Table 5.1. Both Young's moduli and thermal expansion coefficients were estimated from Table 5.1 using rules of mixtures. Since the layers actually consist of graded compositions, average compositions were estimated from the microstructures and the corresponding Young's moduli were estimated from Table 5.1 using rules of mixtures. The surface layers also have graded porosities, thus an average porosity p was estimated and the Young's modulus of the layer was further modified using Equation 5.8[22].

$$E = E_o(1 - 1.9 \cdot p + 0.9 \cdot p^2) \tag{5.31}$$

where E is the Young's modulus of the material surface with porosity p, $E_o$is the Young's modulus of the same material surface without any porosity and p is the porosity.

Using Equation 5.1 to 5.4 and the values from Table 5.1, $\Delta T = T_o - T = 1330^{\circ}C$, t_b=2.0 mm and t_s=0.25 mm, the theoretical residual stress in the surface layer and bulk part of sample H4-1350-20 can be obtained:

$$\sigma_s = -441\text{MPa} \tag{5.32}$$

$$\sigma_b = 110.25\ \text{MPa} \tag{5.33}$$

Using the same methods, the theoretical residual stress in the surface layer of the other aged samples can also be obtained and the values are summarized in Figure 5.19. Comparing Figure 5.14 with Figure 5.19, the measured average residual stress in the surface layer showed good agreement between theory and experiments, although the experimental value is always more compressive than the theoretical values. One possible reason is that TEC values used in the theoretical calculations may not perfectly suit the aged samples. The TEC values reported by different researchers showed a large scatter, partially because of the fact that the range of measurement is different. Thus the TEC error may have been magnified in the calculation. Therefore the real ε_M might have been underestimated in the theoretical

calculation, and hence the compressive residual stress in the surface layer could be underestimated.

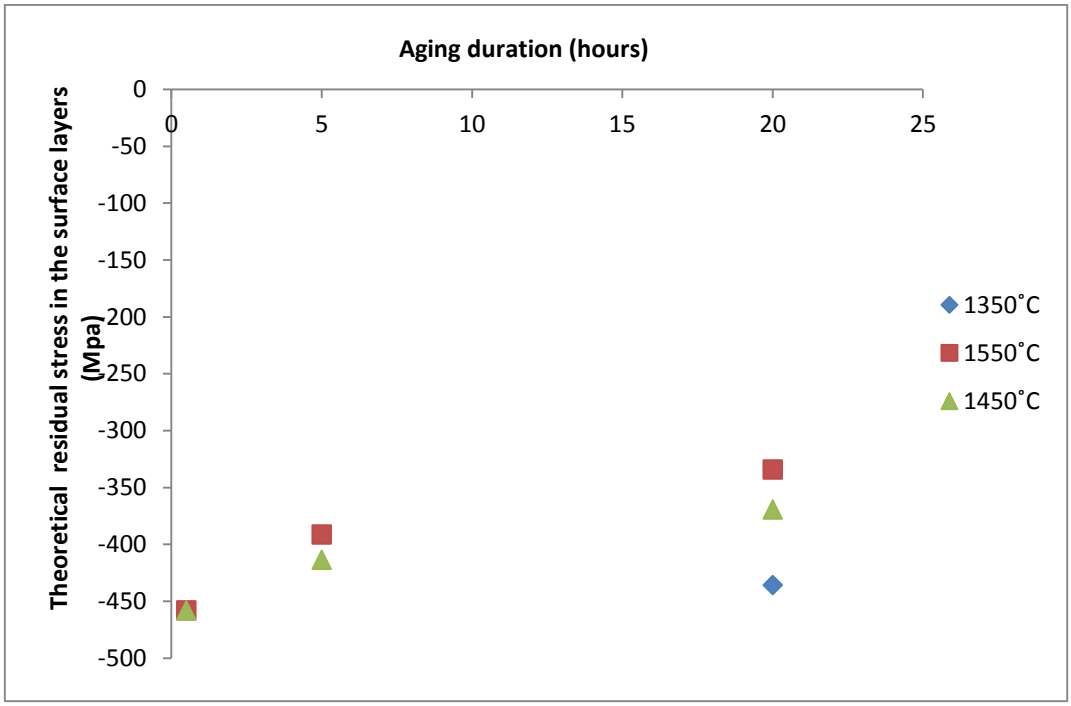

Figure 5.19 Theoretical compressive residual stress in the surface layers of selected samples.

5.3.3. Relationship between microstructure and mechanical properties

5.3.3.1. Fracture Toughness

The hardness results suggested that the porosity probably did decreased the hardness of the aged composites, thus any indentation fracture toughness measured would probably be affected by porosity. Although the Vickers indentation fracture toughness test (VIF) seems the only standard method for characterizing fracture toughness of the surface layers in this project since other methods such as single edge V-notch beam (SEVNB) could only measure the fracture toughness of the bulk parts, the credibility of the Vickers indentation fracture toughness test has been questioned for long time.[23] Furthermore, the microstructures of surface layers varied between samples owing to the variation of precipitates and porosity, which makes the measurements of indentation fracture toughness not a convincing parameter

for the comparison of the crack propagation resistance. Due to the uncertainties above, any modelling based on the indentation fracture toughness data would be speculative. Therefore, currently no credible fracture toughness data has been obtained due to the shortage of credible fracture toughness characterization techniques for the surface layers.

Generally, there are three factors that could influence the fracture toughness of aged samples. The first one is porosity. Since toughness was reported as proportional to $(1-\text{porosity})$, fracture toughness should be proportional to $\sqrt{(1-\text{porosity})}$.[24] The porosity observed in the surface layer of sample H4-1450-20 is around 4%, thus fracture toughness decrease in sample H4-1450-20 due to porosity is 2%, which is minor. The second factor is the precipitates. $FeAl_2O_4$ has a lower fracture toughness (around 1.5 MPa·$m^{0.5}$)[25] than alumina. Taking sample H4-1450-20 as an example, the $FeAl_2O_4$ particle volume fraction in the surface layer was around 3%, thus the fracture toughness decrease by $FeAl_2O_4$ was 2%. Fe particles in the surface layer could also decrease the fracture toughness but the effect should be negligible because the volume fraction of Fe in the surface layer of sample H4-1450-20 is very low (a rough estimation is 0.5%) compared with $FeAl_2O_4$. Particle bridging is probably not working in this project because the pull-outs of particles during polishing indicated a weak particle/matrix bonding.

The third factor is the fracture mode change. Using the models in section 5.3.1, the maximum fracture toughness increase by fracture mode change could be estimated. Assuming a crack is propagating in the direction parallel to ADOCP, therefore:

$$K_{II} = 0 \tag{5.34}$$

$$G = \frac{K_I^2}{E_m} \tag{5.35}$$

If the crack is deflected by a grain boundary with an angle of Ψ to the ADOCP:

$$K_I' = K_I \cdot \cos^3 \frac{\Psi}{2} \tag{5.36}$$

$$K_{II}' = K_I \cdot \sin \frac{\Psi}{2} \cdot \cos^2 \frac{\Psi}{2} \tag{5.37}$$

The requirement for crack to be deflected onto a grain boundary with an angle of Ψ to the ADOCP is that:

$$G'(\Psi) = \frac{(K_I')^2}{E_m} + \frac{(K_{II}')^2}{E_m} = \frac{(K_{c,gb})^2}{E_m} \tag{5.38}$$

i.e.
$$\frac{K_I}{K_{c,gb}} = \cos^{-2} \frac{\Psi}{2} \tag{5.39}$$

Taking Ψ from 0 to 70° as stated in section 5.3.1 that no intergranular cracks in alumina/aged samples will propagate with a Ψ larger than 70°, the average ratio of $\frac{K_I}{K_{c,gb}}$ is 1.15 ($\frac{\overline{K_I}}{K_{c,gb}}$, $\overline{K_I}$ is the average applied mode I stress intensity factor for intergranular crack). The deflection factor f_d proposed by Hansson et al[26] in section 2.1.2.2 can be obtained now:

$$f_d = \frac{\frac{\overline{K_I}}{\overline{K_{c,gb}}}}{\frac{K_{c,g}}{\overline{K_{c,gb}}}} = \frac{\overline{K_I}}{\overline{K_{c,gb}}} = \frac{1.15}{1.58} = 0.73 \tag{5.40}$$

Also the ratio of fracture toughness increase due to fracture mode change over the original fracture toughness could be calculated as:

$$\frac{K_{c,g} - \overline{K_I}}{\overline{K_I}} = \frac{1}{f_d} - 1 = \frac{1.58}{1.15} - 1 = 0.37 \tag{5.41}$$

Since sample H4-1450-20 showed a transgranular fracture, the fracture toughness of sample H4-1450-20 can be increased up to 37% by fracture mode change.

Therefore, the fracture toughness in H4-1450-20 is expected to be increased by up to 33% (37%-2%-2%) and the main contribution to the fracture toughness increase is probably by the fracture mode change. However, a more accurate fracture toughness characterization for the

surface layers of the aged samples is needed to measure the real fracture toughness change in the aged samples, since the model used here only represents 2D situation while the real fracture is in 3D situation, hence the calculations here can be over-simplified.

5.3.3.2. Flexural Strength

The strength of monolithic alumina aged in 4% H_2/N_2 at 1450 ˚C for 20 hours (sample R1) is significantly higher than any other sample, including sample H4-1450-20 which was the strongest of the aged composites. One possible explanation could be crack healing during the aging treatments in monolithic alumina. However, it is difficult to say whether crack healing is working in the aged samples because some aged samples showed a relatively large critical flaws which can be hardly crack healed (section 5.2.3).

There are generally two factors that could decrease the strength of the aged samples. One is the porosity. Porosity adjacent to the critical flaws could increase the flaw size and hence reduce the strength. The reported fracture toughness for the solid solution[5] is around 3.3 $MPa{\cdot}m^{0.5}$ and the flexural strength of the solid solution measured here is 340 MPa, thus the critical flaw size in the monolithic alumina can be calculated as 74μm using the following equation:[27]

$$K_{IC} = \frac{2\sigma}{\sqrt{\pi}}\sqrt{a} \tag{5.42}$$

K_{IC} is the mode I critical stress intensity factor at the tip of a penny-shaped crack with critical radius a in an infinite body under uniaxial tension σ. The the average diameter of porosity in the surface layer of sample H4-1450-20 is around 4.2μm, so the critical flaw size of sample H4-1450-20 could be increased to 78.2μm. Furthermore the porosity in sample H4-1450-20 could reduce the fracture toughness by 2% as stated in section 5.3.3.1. Therefore the strength reduction by the porosity in sample H4-1450-20 can be calculated using Equation 5.42 as 4.7%, which is minor compared with the observed strength increase in sample H4-1450-20.

The other factor is the $FeAl_2O_4$ particles. The pull-outs during polishing indicated a weak interface between spinel particles and the matrix. This could also increase the critical flaw size when $FeAl_2O_4$ particles are adjacent to the critical flaws. The average $FeAl_2O_4$ particle diamter in the surface is 3.8μm, hence the critical flaw size of sample H4-1450-20 could be increased to 77.8μm. As stated in section 5.3.3.1, the $FeAl_2O_4$ particles in sample H4-1450-20 could reduce the fracture toughness by 2%. Thus using Equation 5.42 the total strength reduction caused by $FeAl_2O_4$ particles is around 4.4%. Therefore, the strength reduction of sample H4-1450-20 compared with that of the solid solution by porosity and $FeAl_2O_4$ particles is 9.1% of actual strength in total.

There are generally three factors that could increase the strength of the aged samples. As discussed in section 5.3.3.1, the models in section 5.3.1 predict an increase in fracture toughness up to 37% and hence an increase in strength up to 37%. The second is the porosity. Porosity in the surface layers of sample H4-1450-20 was around 4%, so using Equation 5.31 the maximum Young's modulus reduction on the surface layers of all aged samples would be 7.5% and hence the same value for the strength increase in sample H4-1450-20.[28,29] The third factor could be the compressive residual stress in the surface layer. As discussed in 5.3.2, aging treatments would promote the compressive residual stress in the surface layer of aged samples. Such compressive stress could arrest surface cracks and hence increase the flexural strength.[30,31] This mechanism might help explain why the strength of composites aged at 1550˚C decreased with longer aging duration. It is because the compressive residual stress in the surface layer is decreased with longer aging duration at 1550˚C, as shown in section 5.2.6. The measured compressive residual stress in sample H4-1450-20 was around 420MPa and hence is expected to increase the strength by 124%. Therefore the strength of sample H4-1450-20 is expected to be increased by 168.5% in total by the three factors as discussed above compared with that of the solid solution.

In summary, the strength of sample H4-1450-20 is expected to be 159.4% (168.5%−9.1%) higher than that of the solid solution. However, the measured strength increase in sample H4-1450-20 was around 22%, which was far lower than the increase predicted. Although it is not very clear yet why the measured strength increase in sample H4-1450-20 is much less than the predicted increase, it is probable that the compressive residual stress is the most important strengthening mechanisms in the aged sample because it predicts the highest strength increase compared with other factors discussed above. The flexural strength results here are similar to the flexural strength measured by Mukhopadhyay and Todd[10], but the measured surface compressive residual stress gives different strengthening mechanisms from Mukhopadhyay and Todd[10]'s story because most of Mukhopadhyay and Todd[10]'s samples have no surface layers and exhibited an uniform microstructure.

5.3.4. Relationship between microstructure and wear behaviour

Both the wear resistance results (Figure 5.8) and pull-out results (Figure 5.9) revealed an improved wear resistance and reduced pull-out in samples aged above 1350˚C. The factors that contribute to improved wear resistance can be categorized into two types: reduction in pull-out formation rate and reduction in pull-out size[32] It was found that the surface layers of all aged composites have larger or comparable pull-out size than that of solid solution, so the improved wear resistance of aged samples should be attributed to a reduction in pull-out formation rate. This could be a result of compressive residual stress in the surface layer and suppression of crack initiation. Although the wear resistance of sample R2 is about 1.5 times that of the solid solution, it is far less wear resistant than sample H4-1550-0.5. Therefore, the mechanism for improved wear resistance of aged samples should lie on the surface layer.

5.3.4.1. Influence of compressive residual stress in the surface layer

It has been demonstrated that residual compressive stress in the surface layer of a sample leads to an improvement in wear resistance.[33] As discussed in section 5.3.2 and demonstrated

in section 5.2.6, a compressive residual stress would be developed in the surface layer due to the evaporation of Fe atoms. In samples aged at/above 1350˚C, the hardness are similar and pull-out percentage is below 20%, the effect of hardness could be neglected here.

The rate at which cracks are initiated depends upon very high stress concentrations at the head of twins and dislocations, thus it seems unlikely to be affected significantly by the residual stresses with several hundred MPa measured here. However, the effective value of the pull-out formation rate may be reduced by the arrest of cracks normal to the surface under the action of the compressive residual stresses. Furthermore, as described in section 5.2.1, the hardness was decreased in the aged composites. Thus the hardness of the aged samples would degrade the wear resistance.

Since the residual stress results in section 5.2.6 conforms well to the results of wear resistance, it is probable that the compressive residual stress in the surface layer is the main reason for the wear resistance improvements in the aged composites

5.3.4.2. Crack initiation suppression by intragranular particles

The results of the indentation polish test (section 5.2.5) showed some suppression of brittle fracture (both intergranular and transgranular fracture) and concomitantly grain pull-out during wear in samples aged at 1350˚C. However, it only plays a minor role in improving the wear resistance because such pull-out reduction in the plastic zone is not significant.

The intergranular pull-outs produced in both alumina and solid solution were only confined to the plastic zone of the indentation. This indicates that plastic deformation might be responsible to some extent for the initiation of cracks resulting in pull-outs. As Ortiz Merino and Todd suggested, cracks can be suppressed because intragranular particles could block the formation of long twins and/or dislocation pileups during plastic deformation in alumina, and

concomitantly reduce their lengths and the stress concentration at their tips. [32,34]. The stress concentrations at the heads of twins and pileups have been proved to be capable of initiating cracks in alumina, and would increase with the length of the twin or pileup. [34,35,36] Thus it is possible that the suppression of crack initiation by the intragranular second phase particles in the surface layer partially contributes to the pull-out suppression in samples aged at 1350˚C for more than 0.5 hours, though the effect is not significant.

However, intensive pull-outs were observed in the plastic deformation zone of samples aged at/above 1450˚C. These pull-outs were transgranular. Although there were intragranular second phase particles in the surface layer of samples aged at/above 1450˚C for more than 0.5 hour, not all the grains in the surface layer contain intragranular particles, and the coarse grains tend to initiate transgranular fracture during plastic deformation[11]. Therefore no crack initiation suppression contributes to the improved wear resistance of samples aged at/above 1450˚C compared with solid solution.

In conclusion, it is probable that the compressive residual stress in the surface layer is the main reason for the improved wear resistance.

5.4 Summary

This chapter showed improved flexural strength and significantly increased wear resistance of aged composites compared with the monolithic alumina and solid solution. Therefore it is desirable to obtain well designed surface layers in the aged samples. Comparing with the aged samples in Mukhopadhyay and Todd's reports[5], sample H4-1350-5 offers a better chance for industrial wear resistant application since the aging temperature is reduced and the aging duration is much shorter.

The ‘Microstructure-Mechanical Property’ relationships of samples processed in this project were discussed. It was suggested that the the compressive residual stress in the surface layer could be the most important mechanism for the increased strength and the main reason for the significantly improved wear resistance of the aged samples. The possible reasons for the observed fracture mode change in the aged samples were proposed and discussed. The factors that could influence fracture toughness of the aged samples were proposed and discussed.

This project provides a new method for fabricating functionally graded materials (FGM). Although the wear resistance mainly derived from the ‘layered structure’ since the microstructures of the aged samples are gradually changing from the gas/solid interface to the core of the samples, it is unlikely that the interface between surface layer and the bulk part would suffer the ‘delamination’ problem that most laminated materials would suffer when the surface stresses are large.

Reference:

[1] S. Jiao, M. L. Jenkins, R. W. Davidge, Electron Microscopy of Crack/Particle Interactions in Al_2O_3/SiC Nanocomposites, Journal of Microscopy, 185, 259–264 (1997).

[2] A. J. Sanchez-Herencia, C. Baudin, Ceramic Laminates with Tailored Residual Stress, Boletin de la Sociedad Espanola de Ceramica y Vidrio, 48, 311-320 (2009).

[3] S. Ho, C. Hillman, F. F. Lange, Z. Suo, Surface Cracking in Layers under Biaxial, Residual Compressive Stress, Journal of the American Ceramic Society, 78, 2353-2359 (1995).

[4] R. I. Todd, M. A. M. Bourke, C. E. Borsa, R. J. Brook, Neutron Diffraction Measurements of Residual Stresses in Alumina/SiC Nanocomposites, Acta Materialia, 45, 1791-1800 (1997).

[5] A. Mukhopadhyay, R. I. Todd, Relationship between Microstructure and Abrasive Wear Resistance of Al_2O_3–$FeAl_2O_4$ Nanocomposites Produced via Solid-State Precipitation, Journal of the European Ceramic Society, 31, 339-350 (2011).

[6] H. M. Ledbetter, Reference database: Elastic Properties of Metals and Alloys, Journal of Physical Chemistry (1973).

[7] D. Tromans, Fracture Toughness and Surface Energies of Minerals: Theoretical Estimates for Oxides, Sulphides, Silicates and Halide, Minerals Materials, 15, 1027-1041 (2002).

[8]T. Fujimura, S. I. Tanaka, In-situ High Temperature X-ray Diffraction Study of Fe/Al_2O_3 Interface Reactions, Journal of Materials Science, 34, 425-429 (1999).

[9] D. Chicot, J. Mendoza, A. Zaoui, G. Louis, V. Lepingle, F. Roudet, J. Lesage, Mechanical Properties of Magnetite (Fe_3O_4), Hematite (α-Fe_2O_3) and Goethite (α-FeO OH) by Instrumented Indentation and Molecular Dynamics Analysis, Materials Chemistry and Physics, 129, 862-870 (2011).

[10] A. Mukhopadhyay, Fabrication and Properties of Oxide Nanocomposites Containing Uniformly Dispersed Second Phase, DPhil Thesis, Oxford University, UK (2010).

[11] W. D. Kingery, H. K. Bowen, D. R. Uhlmann, Introduction to Ceramics, John Wiley & Sons, New York (1976).

[12] S. Jiao, M.L. Jenkins, R.W. Davidge, Interfacial Fracture Energy-Mechanical Behaviour Relationship in Al_2O_3/SiC and Al2O3/TiN Nanocomposites, Acta Materialia, 45,149-156(1997).

[13] M. Taya, S. Hayashi, A. S. Kobayashi, H. S. Yoon, Toughening of a Particulate-Reinforced Ceramic-Matrix Composite by Thermal Residual Stress, Journal of the American Ceramic Society, 73, 1382–1391 (1990).

[14] L. Gao, H. Z Wang, J. S. Hong, H. Miyamoto, K. Miyamoto, Y. Nishikawa, S. D. D. L. Torre, Mechanical Properties and Microstructure of Nano-SiC–Al_2O_3 Composites Densified by Spark Plasma Sintering, Journal of the European Ceramic Society, 19, 609-613 (1999).

[15] A. G. Evans, A. H. Heuer, D. L. Porter, The Fracture Toughness of Ceramics, Proceedings of 4th International. Conference of Fracture, **1**, 529-556 (1977).

[16] R. A. Cutler and A. V. Virkar, The Effect of Binder Thickness and Residual Stresses on the Fracture Toughness of Cemented Carbides, Journal of Material Science, **20**,3557-3573 (1985).

[17] M. Taya, S. Hayashi, A. S. Kobayashi, and H. S. Yoon, Toughening of a Particulate-Reinforced Ceramic-Matrix Composite by Thermal Residual Stress. Journal of the American Ceramic Society, 73, 1382-1391(1990).

[18] B. Lawn, Fracture of Brittle Solids, Cambridge University Press, Cambridge (1993).

[19] S. M. Wiederhorn, Fracture of Sapphire, Journal of the American Ceramic Society, 52, 485-491(1969).

[20] N. A. Yahya, R. I. Todd, Influence of C Doping on the Fracture Mode and Abrasive Wear of Al2O3, Journal of the European Ceramic Society, 32, 4003-4007 (2012).

[21] K. Bedu-Amissah, J. M. Rickman, H. M. Chan, M. P. Harmer, Grain-Boundary Diffusion of Cr in Pure and Y-Doped Alumina, Journal of the American Ceramic Society, 90, 1551-1555 (2007).

[22] R. W. Davidge, Mechanical Behaviour of Ceramics, Cambridge University Press, Cambridge (1980).

[23] G. D. Quinn, R. C. Bradt, On the Vickers Indentation Fracture Toughness Test, Journal of the American Ceramic Society, 90, 673–680 (2007).

[24] R. W. Rice, Grain Size and Porosity Dependence of Ceramic Fracture Energy and Toughness at 22 ℃, Journal of Materials Science, 31, 1969-1983(1996).

[25] D. Tromans, J. A. Meech, Fracture Toughness and Surface Energies of Minerals: Theoretical Estimates for Oxides, Sulphides, Silicates and Halides, Minerals Engineering, 15,1027–1041 (2002).

[26] T. Hansson, R. Warren, J. Wasén, Fracture Toughness Anisotropy and Toughening Mechanisms of a Hot-pressed Alumina Reinforced with Silicon Carbide Whiskers, Journal of the American Ceramic Society, 76, 841–848 (1993).

[27] N. Perez, Fracture mechanics, Kluwer Academic Publishers, Boston (2004).

[28] K. K. Phani, S. K. Niyogi, Young's Modulus of Porous Brittle Solids, Journal of Materials Science, 22, 257-263 (1987)

[29] F. P. Knudsen, Effect of Porosity on Young's Modulus of Alumina, Journal of the American Ceramic Society, 45, 94–95 (1962).

[30] W. J. Clegg, Materials Science: Controlling Cracks in Ceramics, *Science*, 5, 1097-1099 (1999).

[31] M. P. Rao, A. J. Sánchez-Herencia, G. E. Beltz, R. M. McMeeking, F. F. Lange, Laminar Ceramics that Exhibit a Threshold Strength, Science, 286, 102-105 (1999).

[32] J. L. Ortiz Merino, R. I. Todd, Relationship between Wear Rate, Surface Pullout and Microstructure during Abrasive Wear of Alumina and Alumina/SiC Nanocomposites, Acta Materialia, 53, 3345–3357 (2005).

[33] G. de Portu, L. Micele, G. Pezzotti, Laminated Ceramic Structures from Oxide Systems, Composites: Part B, 37, 556-567 (2006).

[34] A. Limpichaipanit, R. I. Todd, The Relationship between Microstructure, Fracture and Abrasive Wear in Al_2O_3/SiC Nanocomposites and Microcomposites Containing 5 and 10% SiC, Journal of the European Ceramic Society, 29, 2841-2848 (2009).

[35] M. V. Swain, Microscopic Observations of Abrasive Wear of Polycrystalline Alumina, Wear, 35, 185-189 (1975)

[36] F. Guiberteau, N. P. Padture, B. R. Lawn, Effect of Grain Size on Herztian Contact Damage in Alumina, Journal of the American Ceramic Society, 77, 1825-1831(1994).

Chapter 6 Conclusions and Future work

6.1 Conclusions

The present work was based on two objectives with respect to the Al_2O_3-$FeAl_2O_4$ nanocomposites developed in reducing atmospheres. The first objective of this project was to investigate the thermodynamics, diffusion kinetics and mechanisms for microstructural development during aging treatment. The second objective was to justify the 'microstructure-mechanical properties' relationship of samples aged to produce a surface layer able to improve the mechanical and tribological properties of the ceramics. More specifically, based on the observations and the current analysis, the following conclusions have been made.

6.1.1. Thermodynamics, kinetics and mechanisms

a) A single phase homogeneous solid solution of 10 wt% Fe_2O_3 in Al_2O_3 can be developed in air with pressureless sintering at 1450˚C for 5 hours.

b) Aging in non-oxidising atmospheres (4% H_2/N_2, 1% H_2/N_2, 4% CO/N_2 and Argon) at various temperatures between 1250˚C-1550˚C for different durations up to 20 hours resulted in a layered microstructure consisting of a surface layer and the bulk section with different microstructure. It was found that the components of the surface varied according to the atmosphere, while the bulk part in all aged samples contained $FeAl_2O_4$ as the sole second phase particles.

c) Aging within the temperature range 1350˚C -1550 ˚C in 4 % H_2/N_2 resulted in the formation of intragranular nano-sized Fe and/or $FeAl_2O_4$ particles, along with intergranular micron-sized Fe and/or $FeAl_2O_4$ particles in the surface layer of the aged samples.

d) Varying the processing parameters, i.e MgO dopant level, gas flow rate and sample thickness, could influence the microstructures after aging.

e) The thermodynamics of the reduction reaction were calculated and discussed relating to the second phase formation during aging treatment.

f) Apparent oxygen vacancy diffusivity and apparent Fe^{3+} matrix diffusivity were measured and compared with the literature values. Three reasons were proposed for the extremely high apparent oxygen vacancy diffusivity compared with the literature values of oxygen vacancy grain boundary diffusivity. The apparent Fe^{3+} matrix diffusivity was in a good agreement with the literature values of Fe^{3+} matrix diffusivity.

g) Based on the thermodynamics, the diffusion kinetics and essential mechanisms that were discussed, a model for precipitation induced by reductions in ceramic solid solution (PRCS model) was proposed to explain the microstructural developments during aging treatments. The macroscopic aspect of PRCS model was mainly used to explain the microstructural developments along with the distance from the gas/solid interface and the nucleation and growth of intergranular particles during aging treatment, while the microscopic aspect of the model was mainly used to explain the preicpitation of intragranular particles. It has been found that the microstructures after aging in this project conform well to PRCS model. Therefore, PRCS model is suggested to be a useful tool for explaining and predicting the precipitation induced by reductions in ceramic solid solution

h) It has been found that the high aging temperature, long aging duration, more reducing atmosphere, high gas flow rate, high MgO dopant amount and reduced sample thickness favour larger sample thickness and the precipitation of Fe metallic particles and intragranular particles.

6.1.2. Microstructure-mechanical properties relationship in aged samples

a) The incorporation of Fe_2O_3 in alumina as a solid solution led to lower hardness than that of monolithic alumina. One possible reason for the lower hardness of samples aged in 4% H_2/N_2 at 1350° C than that of the solid solution could be the higher porosity.

b) The fracture toughness of the aged samples is expected to be increased to some extent, though there is currently no credible fracture toughness data yet.

c) The samples aged in 4% H_2/N_2 at temperature within the range 1350˚C - 1550˚C possessed higher flexural strength and improved wear resistance, compared with the solid solution and monolithic alumina.

d) The fracture mode change from intergranular to transgranular in the aged samples was believed to be a result of three reasons: 'coarse grains', compressive residual stress on the grain boundaries and chemistry change on the grain boundaries after aging.

e) A compressive residual stress was found in the surface layers of the aged samples due to a CTE mismatch between the surface layer and bulk part.

f) The compressive residual stress in the surface layer was suggested to be the main source of the improved strength of aged samples and wear resistance.

g) This project provided a new method for fabricating functionally graded materials (FGM). Since the microstructure of the aged samples gradually changes from the gas/solid interface to the core of the samples, it is unlikely that the interface between the surface layer and the bulk part would suffer a 'delamination' problem as most laminate materials suffer when the interlaminar stresses are high.

6.2 Future Work

The following work is suggested to be undertaken in the near future.

a) Investigations using TEM/HRTEM could be performed to further understand the nucleation and growth of intragranular particles during aging treatments.

b) Detailed chemical elementary investigation may be performed to study the chemical element distribution during aging treatments.

c) Investigations using methods such as microcantilever tests to measure the toughnesses for intergranular and transgranular fractures of alumina grains and atomistic modelling to study the atomic bonding are needed to answer the question whether chemical changes on the grain boundaries influence the fracture mode change.

d) New tests may be designed to obtain reliable fracture toughness data for the surface layers of the aged samples.

e) Short time aging treatment followed by consolidation treatments may be investigated to obtain a less porous surface containing intragranular particles.

f) Refractory particles could be added to the solid solution to pin the grain growth during both sintering and aging treatments.

g) The possible reasons behind the improved flexural strength for the surface layers of the aged samples may be elucidated further by in detail TEM observations of foils carefully prepared from near the fracture surfaces.

h) The possible reasons behind the improvement in the wear resistance and the sub-surface damage for the surface layers of those aged samples could be further investigated by in detail TEM observations of foils carefully prepared from near the as worn surfaces.